Karlsruher Institut für Technologie

Institut für Angewandte Materialien

Oberflächenanalytische Ansätze zur zuverlässigen Charakterisierung von Lithium-Ionen-Batterie-Elektroden

Surface Analytical Approaches to Reliably Characterize Lithium-Ion Battery Electrodes

Zur Erlangung des akademischen Grades einer

DOKTORIN DER INGENIEURWISSENSCHAFTEN (DR.-ING.)

bei der Fakultät für Maschinenbau

Karlsruher Institut für Technologie (KIT)

angenommene

DISSERTATION

von

M.Sc. Raheleh Azmi

Tag der mündlichen Prüfung: 02.10.2018

Hauptreferent: Prof. Dr. M. J. Hoffmann

Korreferent: Prof. Dr. H. Ehrenberg

Abstract

Active materials of Li-ion batteries can potentially be characterized using X-ray photoelectron spectroscopy (XPS) regarding quantitative chemical state elucidation. This work presents a novel multiplet splitting approach for XPS characterization of active cathode materials in order to improve the results in comparison to peak barycenter or single symmetric Voigt profile approaches. The investigated cathode materials are composed of at least two first-row transition metals, such as Mn, Co, and Ni, which are known to show multiplet splitting in their core level 2p spectra. As a prerequisite, special care was taken with respect to air sensitivity, contamination during sample handling and transport, and to probable method-induced sample damages. The achieved 2p templates, in particular, address the complex peak structures consisting of significant multiplet splitting, shake-up and plasmon loss features, and additional overlaps with Auger and photoelectron peaks stemming from other elements. The consideration of all these features is indispensable for a reliable quantification. To separate from topography effects and contributions of the electrode's binder and carbon black in powder electrodes, the developed template procedure in a first attempt was successfully transferred to novel magnetron sputtered Li-Ni-Co-Mn-O thin-films, designed for all-solid-state Li-ion batteries. In a systematically study, the approach was expanded to the pure active powder materials of newly developed $LiNi_{0.8-y}Mn_yCo_{0.2}O_2$ ($0 \leq y \leq 0.4$) compound series (NMC). Here the template approach enables the unambiguous elucidation of the transition metals' oxidation states; even gradual changes in the Ni^{2+}/Ni^{3+} ratio depending on the Ni content in the different compounds of the NMC series can clearly be evidenced. Consecutively, the developed new fitting procedure was extended to the spectra from pristine electrodes made of this series' compounds in combination with binder and carbon black. Here it could clearly be evidenced, that not the active material's dilution but its inhomogeneous distribution across the electrode might hamper the quantitative chemical state elucidation due to poor intensity. In principle, even cycled electrodes can be successfully and reliably characterized with respect to their quantitative chemical states when utilizing the developed template approach.

The general applicability of the new template approach was evidenced by the application of the developed procedures to spectra of different novel transition metal powder compounds comprising various combinations of Co, Ni, or Mn and additional dopants, such as Cu, Fe, Ru, Ti, and Zn. This successful justification opens-up the possibility of reliable XPS characterization of transition metal compounds within the high diversity of materials development. As a prerequisite, the fundamental elucidation of the XPS core level multiplet splitting behavior of every additional transition metal has to be done carefully prior to the desired characterization.

Zusammenfassung

Aktive Materialien von Lithium-Ionen-Batterien können potenziell mittels Röntgenphotoelektronen-Spektroskopie (XPS) hinsichtlich der quantitativen Analyse der Oxidationszustände charakterisiert werden. Diese Arbeit stellt einen neuartigen Multiplett-Splitting-Ansatz für die XPS-Charakterisierung von aktiven Kathodenmaterialien vor, um die Ergebnisse im Vergleich zu Peak-Baryzentrum- oder einzelnen symmetrischen Voigt-Profilansätzen zu verbessern. Die untersuchten Kathodenmaterialien bestehen nämlich aus mindestens zwei Übergangsmetallen der ersten Reihe wie Mn, Co und Ni, von denen bekannt ist, dass sie in ihren 2p-Rumpfniveau-Spektren Multiplett-Splitting zeigen. Besonderes Augenmerk wurde dabei auf die Luftsensitivität, die Kontamination während des Probenhandlings und -transports sowie auf die möglichen methodeninduzierten Schädigungen gelegt. Die entwickelten 2p-Templates berücksichtigen insbesondere die komplexen Peakstrukturen, die aus signifikanten Multiplett-Splitting, Shake-up- und Plasmonenanregung-Verlustpeaks bestehen, wie auch zusätzliche Auger- und Photoelektronen-Peak-Überlappungen anderer Elemente. Die Berücksichtigung all dieser Merkmale ist für eine zuverlässige Quantifizierung unbedingt erforderlich. Zur Trennung von Topographieeffekten und Beiträgen des Bindemittels und des Leitrußes in Pulverelektroden wurde das entwickelte Template-Verfahren in einem ersten Versuch erfolgreich auf neuartige magnetrongesputterte Li-Ni-Co-Mn-O-Dünnschichten angewendet, die für Feststoff-Lithium-Ionen-Batterien ausgelegt sind. In einer systematischen Studie wurde dann der Ansatz auf die reinen aktiven Pulvermaterialien der neu entwickelten $LiNi_{0.8-y}Mn_yCo_{0.2}O_2$ ($0 \leq y \leq 0.4$) Serie (NMC) erweitert. Hier ermöglicht der Template-Ansatz die eindeutige Aufklärung der Oxidationszustände der Übergangsmetalle. Selbst graduelle Veränderungen des Ni^{2+}/Ni^{3+}-Verhältnisses in Abhängigkeit vom Nickelgehalt in den verschiedenen Verbindungen der NMC-Serie lassen sich eindeutig nachweisen. Anschließend wurde das neu entwickelte Fitting-Verfahren auf die Spektren von frisch präparierten Elektroden, bestehend aus den Pulvermaterialien dieser Serie gemischt mit Bindemittel und Leitruß, erweitert. Hier konnte eindeutig nachgewiesen werden, dass nicht der geringere Anteil an aktivem Material in den Elektroden sondern seine inhomogene Verteilung über die Elektrode die quantitative Oxidationszustandsanalyse aufgrund geringer Peak-Intensität behindern könnte. Prinzipiell lassen sich mit dem entwickelten Template-Ansatz auch zyklierte Elektroden hinsichtlich ihrer Oxidationszustände erfolgreich und zuverlässig quantitativ charakterisieren.

Die allgemeine Anwendbarkeit des neuen Template-Ansatzes wurde durch die Anwendung der entwickelten Verfahren auf Spektren verschiedener Pulver aus neuartigen Übergangsmetallverbindungen, bestehend aus Co, Ni oder Mn und zusätzlichen Dotierelementen

wie Cu, Fe, Ru, Ti und Zn, belegt. Dieser erfolgreiche Nachweis eröffnet die Möglichkeit einer zuverlässigen XPS-Charakterisierung von Übergangsmetallverbindungen im Rahmen der hohen Vielfalt der Werkstoffentwicklung. Voraussetzung dafür ist, dass die grundsätzliche Aufklärung des Multiplett-Splittings des Rumpfniveaus jedes weiteren Übergangsmetalls vor der gewünschten Charakterisierung sorgfältig durchgeführt wird.

Table of Contents

List of Figures

List of Tables

List of Abbreviation

1D	one-dimensional
2D	two-dimensional
3D	three-dimensional
BE	binding energy
BSE	backscattering electrons
CAE	constant analyzer energy
DEC	diethyl carbonate
DMC	dimethyl carbonate
EAL	effective attenuation length
EC	ethylene carbonate
EDS	energy dispersive X-ray spectroscopy
E_p	pass energy
ESB	energy selective backscattered detector
EV	electric vehicles
FWHM	the full width at half maximum
HAS	hemispherical sector analyzer
HOMO	Highest Occupied Molecular Orbital
ICP-OES	inductively coupled plasma optical emission spectroscopy
IMFP	inelastic mean free path
KE	kinetic energy
LIB	Li-ion battery
LMIG	Liquid Metal Ion Gun
LNMO	$LiNi_{0.5}Mn_{1.5}O_4$
LUMO	Lowest Unoccupied Molecular Orbital
NMC	Li-Ni-Mn-Co-O layered cathode compounds
NMC442	$LiNi_{0.4}Mn_{0.4}Co_{0.2}O_2$
NMC532	$LiNi_{0.5}Mn_{0.3}Co_{0.2}O_2$
NMC622	$LiNi_{0.6}Mn_{0.2}Co_{0.2}O_2$
NMC712	$LiNi_{0.7}Mn_{0.1}Co_{0.2}O_2$
NMC802	$LiNi_{0.8}Co_{0.2}O_2$
PVDF	polyvinylidene difluoride
RSF	relative sensitivity factor
SE	secondary electrons
SEI	solid-electrolyte interphase
SEM	scanning electron microscope
ToF-SIMS	Time-of-Flight Secondary Ion Mass Spectrometry
VTM	vacuum/Ar transport modules
XPS	X-ray photoelectron spectroscopy

1. Introduction

Nowadays Li-ion batteries (LIBs) are an indispensable part of daily life. Since their commercialization in 1991 by Sony Corporation, they are dominantly used in most of the portable electronic devices especially in smartphones and laptops causing a revolution in personal digital electronics [1]–[3]. Moreover, in recent years LIBs gained another expanding market namely in electrifying road transportation by mass production of electric vehicles (EVs) like Tesla Model 3 and BMW i3 [4], [5]. Furthermore, in order to achieve the environmental sustainability, the electricity that powers EVs must be renewable, green and clean. Therefore, the batteries are prospective stationary energy storage candidates to be employed to buffer the intermittent and fluctuating supply of green and clean energy from renewable sources like wind and solar [5]. The large range of power and energy density provided by Li-ion batteries enables them to be used in such a wide variety of applications. Despite the commercial success of Li-ion batteries, there are still some drawbacks such as high cost, degradation of performance at high temperatures, not being safe if charged rapidly at low temperatures, possible venting and fire when crushed, which reduce the customer acceptance for EVs [6], [7]. Therefore, still intensive research and development activities are focusing on novel materials to progress the next generation Li-ion batteries.

In all states of the LIBs development as well as in evaluating degradation mechanisms involved in battery deterioration, surface analytical methods are essential to characterize the pristine materials as well as the surfaces and interfaces of deployed electrodes. For this purpose, X-ray photoelectron spectroscopy (XPS) is one of the pivotal spectroscopic techniques to provide quantitative information on chemical binding states in a non-destructive manner. In consequence, XPS is widely used in today's battery materials development both to identify decomposition products mainly on negative electrode surfaces and to elucidate the cathode's active material's oxidation states at different battery cycling states. Composition and origin of the anode's solid electrolyte interphase (SEI) are rather complicated and, therefore, XPS and time-of-flight secondary ion mass spectrometry (ToF-SIMS) results are still controversially discussed [8]–[14]. However, in the case of the first-row transition metals, which are commonly used in LIB's cathodes, the analytical potential of XPS is not widely utilized in its entirety. Obviously, the major reason for this fact is mainly due to the complex multiplet splitting, peak overlaps and additional shake-up and plasmon features in the respective 2p XP spectra, although fundamental studies are available mainly by the work of Biesinger et al. [15], who considered a semi-empirical approach combining the analysis of high purity oxide/hydroxide reference samples and theoretically calculated free-ion multiplet

structures of core 2p vacancy levels by Gupta and Sen [16], [17]. Aside presenting only raw data sets and solely assigning expected oxidation states [18]–[24], simplifying approaches such as reducing the complex multiplet splitting to single Voigt peak shapes, are often used [21], [25]–[28], which, in consequence, could lead at least to uncertainties in the quantitative chemical information. Only a few groups worldwide present attempts of multiplet fitting procedures during XPS characterization of LIB active materials [29], [30].

The aim of this work is to advance the multiplet-splitting approach for binary systems systematically towards more complex systems to interpret the XP spectra of real systems of various LIB active materials containing multiple transition metals. If necessary, complementary time-of-flight secondary ion mass spectrometry (ToF-SIMS), as well as scanning electron microscopy (SEM), will be applied to achieve a comprehensive characterization. As a major result, detailed parameter sets for XPS multiplet deconvolution will be available providing a powerful tool to reliably characterize compounds comprising various combinations of transition metals regarding quantitative chemical state evaluation even beyond the LIB materials.

The starting point to achieve this goal is the development of templates to deconvolute XP spectra of first-row transition metals using pure reference materials and a simple model system, comprising of magnetron sputtered Li-Co-Ni-M-O thin-films, to exclude any intensity minimizing effects due to topography and dilution by carbon black and binder. A crucial prerequisite is the comprehensive study of the probable contamination during sample handling and transport from synthesis to analysis and, moreover, method-induced decomposition of the samples during the different characterization steps. Strategies have to be developed to avoid potential artifacts arising from such influences [31].

The elaborated multiplet templates will be applied to a pure powder system series tuning systematically the stoichiometry of Mn, Co, and Ni to develop a strategy to overcome problems arising from Auger and photoelectron peak overlaps and finally to prove the applicability of the template approach to elucidate chemical state changes due to stoichiometry variation [32]. The achieved procedures will be applied to realistic LIB electrode systems (pristine and test-cycled) to elaborate ways to overcome the dilution of the active material associated with the necessary carbon black and binder materials.

In order to prove the general applicability of the new template approach, the developed procedures shall be applied to different novel transition metal powder compounds comprising various combinations of Co, Ni, or Mn and additional dopants, such as Cu, Fe, Ru, Ti, and Zn [33]–[36].

A successful justification will open-up the possibility of reliably characterize transition metal compounds within the high diversity of materials development.

2. Theoretical background

In this chapter, the theoretical background of this work will be introduced. In the first part, the used surface analytical methods to evaluate the Li-ion batteries will be introduced. In particular, XPS will be described in more detail, as the main focus of this work is to develop multiplet fitting approaches for photoelectron spectra of first-row transition metal materials used in LIBs. In the second part, the fundamentals of Li-ion battery will be outlined, and the important analytical challenges will be discussed.

2.1. X-ray photoelectron spectroscopy (XPS)

X-ray photoelectron spectroscopy (XPS) is a very important and widely used surface-sensitive quantitative analytical technique to obtain information about the chemical and electronic state of the elements within the topmost surfaces of materials. XPS is based on the photoelectric effect using characteristic X-rays and measuring the kinetic energy of the emitted photoelectrons originating from the XPS sampling depth of about 6-10 nm of the material's surface.

Historically, XPS can be traced back to the discovery of the photoelectric effect in the 1880s when Heinrich Hertz [37] described that electrically isolated metallic objects, held under vacuum, exhibited an enhanced ability to spark when exposed to light. This Hertz effect also allowed the derivation of the ratio of Plank's constant over electronic charge (h/e) and the work function (ϕ) of the respective metal when altering the energy of the irradiation source. In 1905, Albert Einstein explained this effect as arising from the transfer of energy from photons ($E_{photon} = {}^{hc}/_{\lambda}$) to electrons bound in the atoms of the respective metallic objects. In case the transferred energy is greater than the binding energy of electrons in an atom, these particular electrons will be emitted [38]. For this explanation and for the introduction of the photon concept (a package of energy with zero rest mass), Einstein was awarded the 1921 Nobel Prize in Physics [39].

The experimental and instrumental development for the use of the photoelectric effect as an analytical method to characterize chemical bonding states in near-surface layers was largely driven by Kai Siegbahn in the 1960s. In cooperation with Siegbahn, a small group of engineers at Hewlett-Packard in the USA produced the first commercial monochromatic XPS instrument in 1969. In 1981 Kai Siegbahn was awarded the Nobel Prize in Physics for the development of the XP spectroscopy [40].

2.1.1. The physical principle of XPS

The principle of XPS is based on the emission of core and valence electrons of the surface atoms, excited by characteristic X-rays (standard sources are MgKα = 1253.6 eV and AlKα = 1486.6 eV). The number of the emitted electrons and their kinetic energies (KEs) are then measured by a hemispherical electron energy analyzer in order to obtain element-characteristic chemical information via the photoelectron's binding energy BE. This excitation process is illustrated schematically in Figure 2-1.

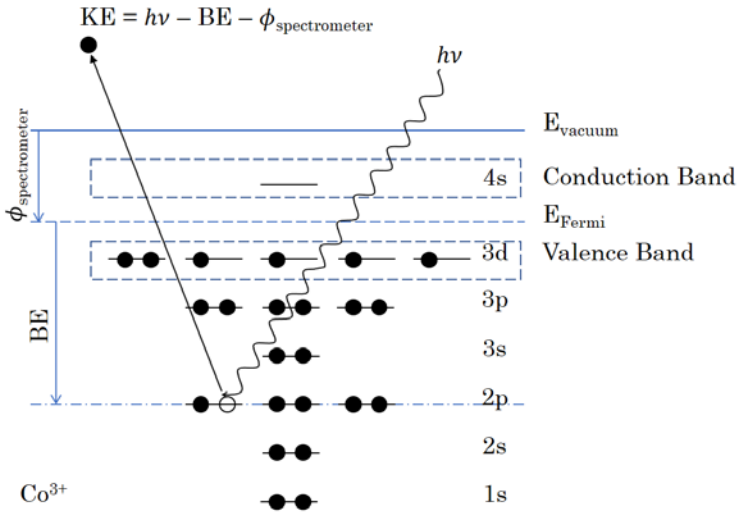

Figure 2-1: Schematic electron energy diagram for a Co^{3+} cation (as free ion) showing the absorption of a photon and resultant ejection of a 2p core level photoelectron.

The KE and BE of the photoelectron are related via the Equation 2-1:

$$KE = h\nu - BE - \phi_{spectrometer} \qquad \text{Equation 2-1}$$

where $h\nu$ represents the energy of the absorbed photon and $\phi_{spectrometer}$ is the work function of the spectrometer. $\phi_{spectrometer}$ represents the energy necessary to remove an electron from the spectrometer on the assumption that a conductive sample in physical contact with the instrument is analyzed.

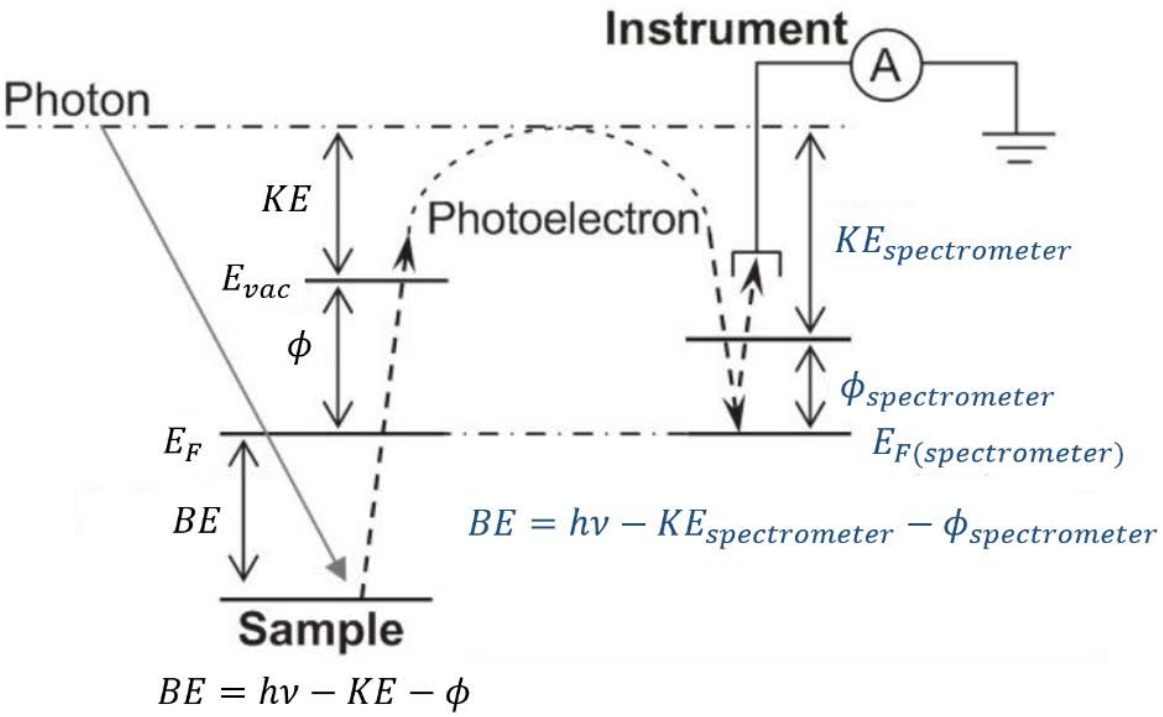

Figure 2-2: The relation between the work function ϕ, the Fermi level E_F, and the kinetic energy KE of a photoelectron in relation to the sample and the instrument.

The relevant contributions to the work function are shown schematically in Figure 2-2. Provided the sample is in conductive contact with the spectrometer, the work function of the spectrometer $\phi_{spectrometer}$ usually dominates ϕ_{sample}. In case of insulating sample surfaces, the method-induced local charge up has to be compensated by energy referencing to internal standards, e.g. to adventitious carbon originating from atmospheric contact.

The two main contributions to the binding energy, BE, in Equation 2-1 are the binding energy of the electron and the chemical shift. The binding energy of the photoelectron depends on the electron configuration of the respective element in its elementary state and the resulting shielding of the nuclear charge. Therefore, the BEs derived from Equation 2-1 are not only characteristic for each element but also for its chemical environment. Since all electrons with a binding energy less than incident photon energy do appear in the XP spectrum, the outcome is the complete electronic structure of an element quite accurately as depicted exemplarily for Pb [41] in Figure 2-3.

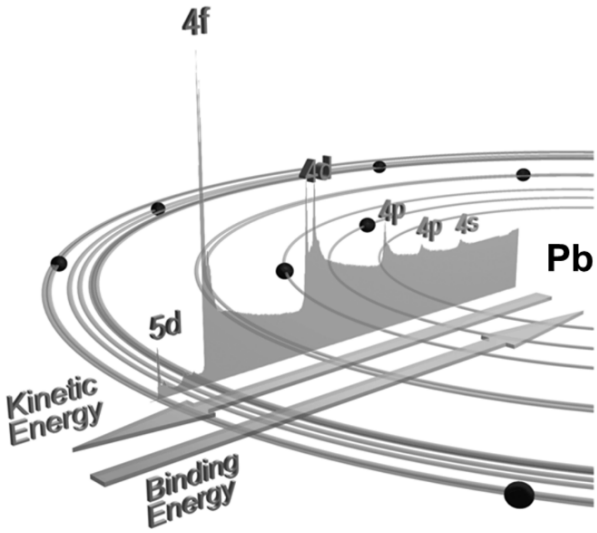

Figure 2-3: Photoelectron spectrum of lead superimposed on its schematic electronic structure. (adapted from reference [41])

2.1.2. The depth of analysis in XPS

Generally, soft X-rays are used to excite electrons in XPS have energies in the range of 1-2 keV and can penetrate several micrometers into the surface. However, the probability that a photoelectron can escape from the surface parallel to the surface's normal without losing its KE is given by Beer-Lambert relationship shown in Equation 2-2:

$$I_d = I_0 e^{-d/\lambda} \qquad \text{Equation 2-2}$$

Here I_d is photoelectron intensity originating from atoms at a depth d, I_0 is the photoelectron intensity from an infinitely thick uniform substrate and λ is the photoelectron inelastic mean free path (IMFP). IMFP represents the average distance that a photoelectron can travel without undergoing inelastic scattering. The IMFP is dependent on both the material properties and the photoelectron kinetic energy. Assuming a gaussian probability distribution and by considering photoelectrons emitting at 90° to the sample surface (i.e. parallel to the surface's normal), it can be shown that 95 % of the photoelectrons will emanate from a depth of around 3λ. Seah and Dench developed an empirical formula (Equation 2-3) for the calculation of the dependency of IMFP on the photoelectron's kinetic energy based on experimentally determined values [42] (see Figure 2-4):

$$\lambda_M = \frac{538}{E_{Kin}^2} + 0.41\sqrt{aE_{Kin}}$$ Equation 2-3

λ_M = IMFP in monolayers

E_{Kin} = kinetic energy

a = thickness of the monolayer

Typical IMFPs for the metal 2p core photoelectrons for transition metals and their oxides are calculated to be in the order of 1.1-1.8 nm (when using AlKα excitation) resulting in an information depth between 3.3-5.4 nm for these systems [39].

The photoelectrons generated from deeper layers of the sample experience an energy loss through inelastic collisions and contribute at most to the background of an XP spectrum. For quantification, a homogeneous layer structure is assumed, and in order to correct the energy-dependency of the escape-depths of the photoelectrons, their respective IMFP has to be taken into account.

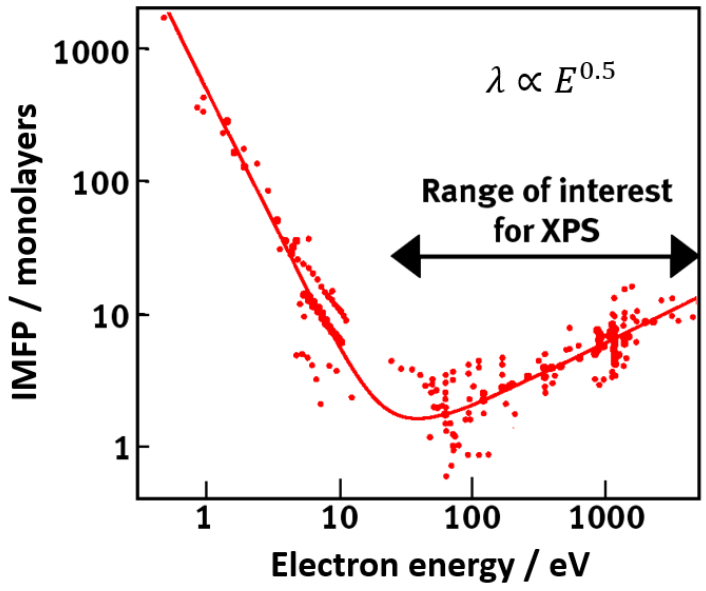

Figure 2-4: Dependency of the IMFP on the photoelectron's kinetic energy. (adapted from reference [43])

2.1.3. Thermo Fisher Scientific K-Alpha instrumentation

All XPS analysis completed as part of this work is performed using Thermo Fisher Scientific K-Alpha and K-Alpha+ spectrometers, East Grinstead, UK. Figure 2-5 (a) shows a simplified layout of the main components of the K-Alpha XPS instruments.

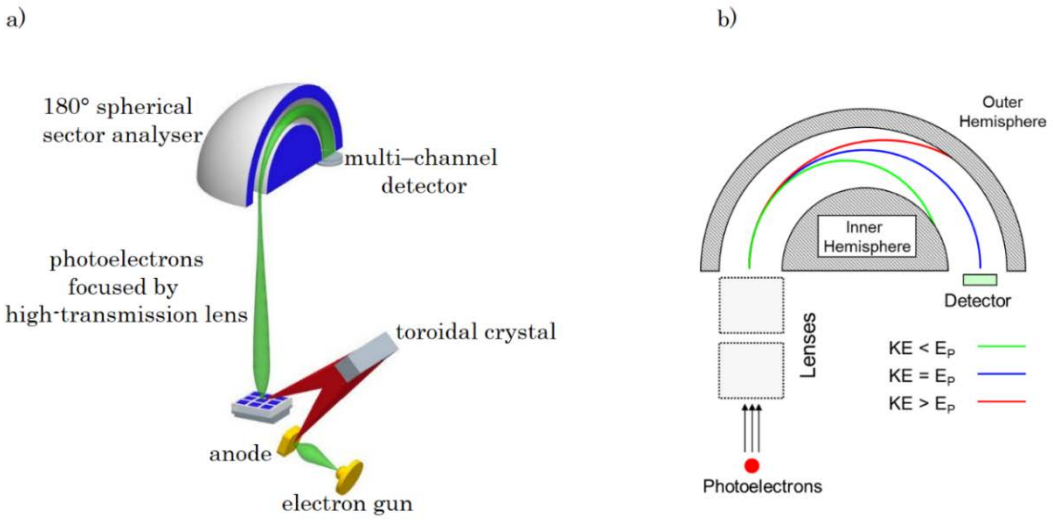

Figure 2-5: a) Simplified layout of the main components of a K-Alpha XPS instrument comprising monochromatic and micro-focused AlKα X-ray source, electron transfer lens, hemispherical electron energy analyzer, and multichannel detector [44] and b) Schematic diagram of a hemispherical electron energy analyzer with electron transfer lens [44].

The base pressure in the analytical chamber is typically near 10^{-9} mbar prior to the introduction of the samples. This ultra-high vacuum is prerequisite to minimize scattering of the low energy photoelectrons by residual gas molecules and, more importantly, to avoid sample contamination by fast adsorption processes compared to the necessary measuring time. The monochromatic AlKα X-ray source provides spot sizes between 30-400 µm. Photoelectrons ejected from a sample surface are focused by high transmission lenses with a ±30° acceptance angle towards the entrance slit of an electron energy analyzer (hemispherical sector analyzer, HSA), see Figure 2-5a. To achieve a constant XPS energy resolution, the HSA is operated in constant analyzer energy (CAE) mode. Here the photoelectrons are accelerated or retarded to a fixed pass energy (E_p) and the CAE's hemisphere voltages are scanned across the complete energy range, illustrated in Figure 2-6. The applied potentials define the energy range for the kinetic energy that photoelectrons must have in order to pass through the analyzer. Photoelectrons with a lower energy than the set energy

range describe a circular orbit with a smaller radius than the radius of the analyzer and hit the inner hemisphere. Photoelectrons with too high kinetic energy hit the outer hemisphere (see Figure 2-5b). Once the electrons exit the HSA they enter a channel plate detector of 128 channels acting as small channel electron multipliers (channeltrons) to amplify the input photoelectron signal by a factor of up to 10^8 and thus make it electrically measurable.

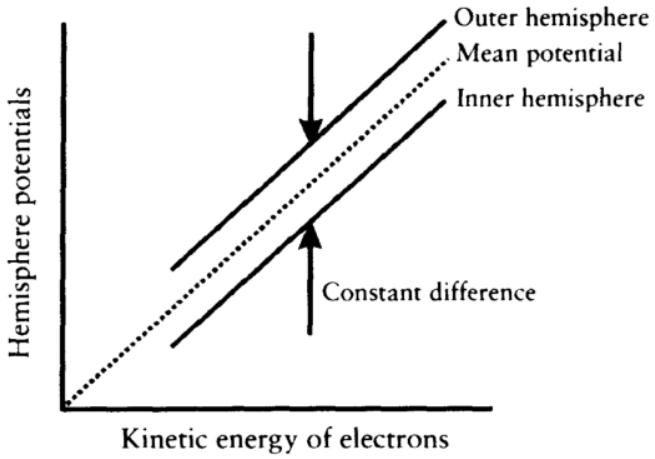

Figure 2-6: Operation of an HSA in the constant analyzer energy mode to achieve constant energy resolution across the complete XPS energy range. (adapted from reference [41])

The analyzer's transmission function is defined as the fraction of the total number of photoelectrons collected at the sample surface that passes through the HSA into the detector. The transmission function is dependent on the HSA entrance slit width, HSA radius, the defined pass energy, and the initial KE of the photoelectrons. The absolute energy resolution (ΔE) of the instrument is defined by the full width at half maximum (FWHM) of the Ag $3d_{5/2}$ photoelectron peak. The absolute resolution increases with decreasing pass energy. However, the increase in spectral resolution results in a loss of intensity due to a higher dispersion of the electrons around the exit slit. These effects are illustrated in Figure 2-7.

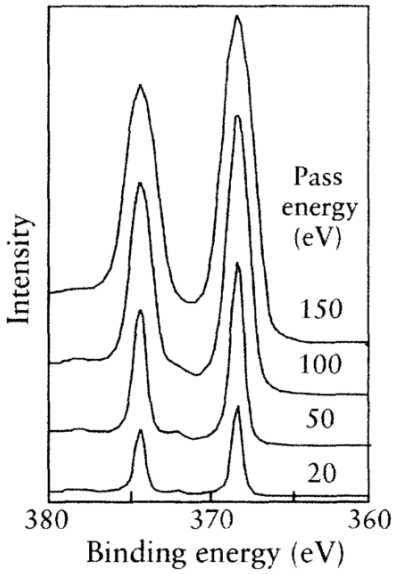

Figure 2-7: Illustrating the effect of pass energy upon the Ag 3d high-resolution spectrum. (adapted from reference [41])

The combination of monochromatic AlKα irradiation with the described HSA provides an ultimate energy resolution of < 0.5 eV FWHM of the Ag $3d_{5/2}$ photoelectron peak.

To avoid local charge-up of insulating materials (resulting in energy shifts and peak broadening) XPS instruments are usually equipped with a neutralization system using low energy electrons or, better, dual beams of low energy electrons and Ar ions (K-Alpha instruments).

2.1.4. Features of XPS spectra

XPS spectra are conventionally plotted as a function of photoelectron intensity vs. binding energy BE. Survey spectra (wide scans) are collected using a high pass energy (> 120 eV), a high energy step (1.0 eV) and a large BE window (> 1200 eV). These spectra have in consequence low resolution; however, the large BE range allows for the identification of the all elements present in the sample. A survey spectrum of $LiCoO_2$ powder containing a small carbon and sodium impurity is exemplarily depicted in Figure 2-8. Aside from the desired photoelectron peaks also the X-ray-induced Auger electron peaks (description see below) can be identified in Figure 2-8.

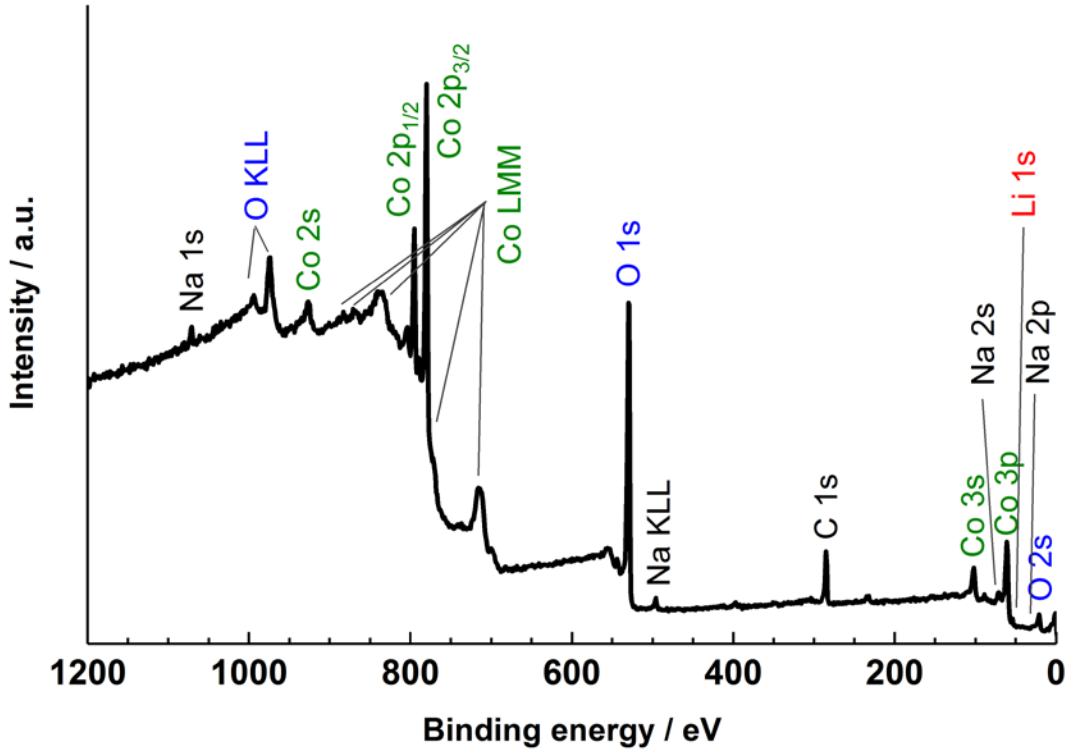

Figure 2-8: Survey spectrum of $LiCoO_2$ powder including the assignments of all photoelectron and Auger peaks.

At higher BEs (> 600 eV) an increase in the spectral background is observed that arises from the detection of photoelectrons having undergone one or more energy loss events while escaping the surface (see Equation 2-1).

After having identified the elemental content, measuring high energy resolution spectra provide the chemical state information. These spectra are typically collected at a low pass energy (10-50 eV), a low energy step width (0.1-0.05 eV) and BE windows ranging from 10-40 eV. As an example, the Co 2p high-resolution spectrum from $LiCoO_2$ powder is presented in Figure 2-9.

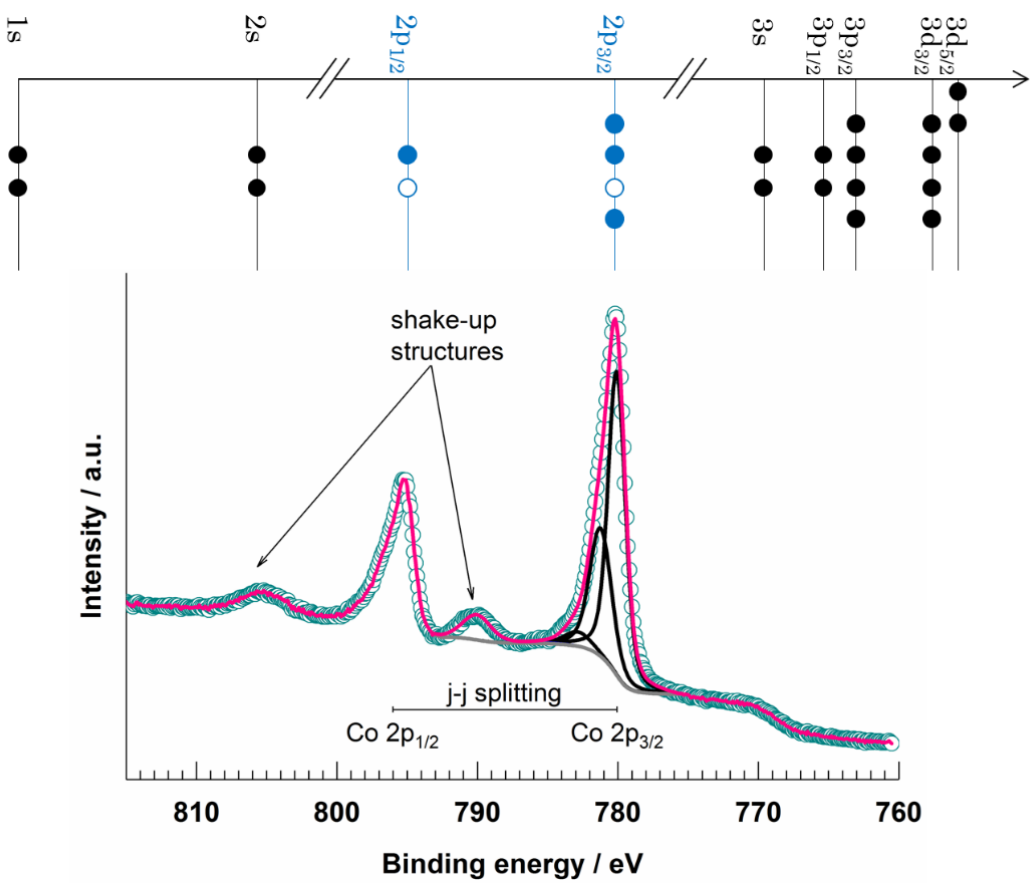

Figure 2-9: High energy resolution Co 2p spectrum of $LiCoO_2$ powder (bottom) and schematic electronic structural features arising from j-j coupling and shake-up satellites (top).

The peak shape and intensity for each core level photoelectron peak is defined by the principal quantum number n, the angular momentum quantum number l, and the electron spin angular momentum quantum number s. Following the photoionization from an orbital where $l = 0$ (i.e. 1s shell) a singlet photoelectron peak is observed since only one final state is possible. For orbitals where $l > 0$ (i.e. 2p shells), the orbital angular momentum and spin angular momentum of the remaining electron can couple either in parallel (lower energy) or anti-parallel (higher energy), resulting in two possible final states. This gives rise to a doublet structure defined by the following relationship:

$$j = (l \pm s) \qquad \text{Equation 2-4}$$

where j is the total angular momentum quantum number. This phenomenon is referred to as spin-orbit or j-j coupling (see Figure 2-9, top). In the case of the 2p spectral line, j values of 3/2

($2p_{3/2}$) and 1/2 ($2p_{1/2}$) are obtained. The separation between the doublet peaks increases with atomic number (Z) and is scaled by a factor of $1/r^3$, with r representing the radius of the orbital from which the photoelectron has been ionized. The relative electron populations of the respective doublet peaks are defined by $2j + 1$ resulting in a $2p_{3/2}$:$2p_{1/2}$ ratio of 2:1. The doublet splitting (an initial state process) is illustrated schematically for Co 2p photoelectron peak in Figure 2-9. The energetic splitting of the two doublet peaks depends on the strength of the spin-orbit coupling. In general, the energetic splitting increases by increasing atomic number (Z) and given the atomic number (i.e. for an element) by increasing principal and angular quantum numbers (n and l), p > d > f.

The line width FWHM of a photoelectron peak is determined by both the natural line broadening (sample dependent) and spectrometer broadening. The natural line broadening results directly from the lifetime of the corresponding near-nuclear electron vacancy. The lifetime can be determined by Heisenberg's uncertainty principle [45]:

$$\Delta E . \Delta t \approx \frac{h}{2\pi}$$ Equation 2-5

h = Planck's constant

ΔE = energy uncertainty

Δt = time uncertainty

For an element, the line width increases in the following row: f > d > p > s, and can be described using a Lorentz function. The spectrometer-related broadening is dependent on the excitation source used and the respective spectrometer. This contribution to the peak shape is Gaussian and is more determinative for the measured FWHM of the photoelectrons. There are further very sample specific contributions to the line width, such as defects and vibration effects of the final state that are not going to be explained here.

The 2p spectra for transition metal cations having unpaired d electrons are further complicated by additional fine structures resulting from multiplet splitting (a final state process). These structures arise from the parallel or anti-parallel coupling of the spin angular momentum of an unpaired core electron with the spin angular momentum of unpaired 3d valence electrons (spin-spin-coupling). Exchange interactions between electrons with parallel spins are lower in energy than the interactions between electrons with anti-parallel spins, producing a doublet structure. Additional

contributions from atomic relaxation and ligand interactions also contribute to the multiplet structures observed. Figure 2-10 adapted from reference [46] illustrates how the multiplet splitting affects Mn 3s spectrum.

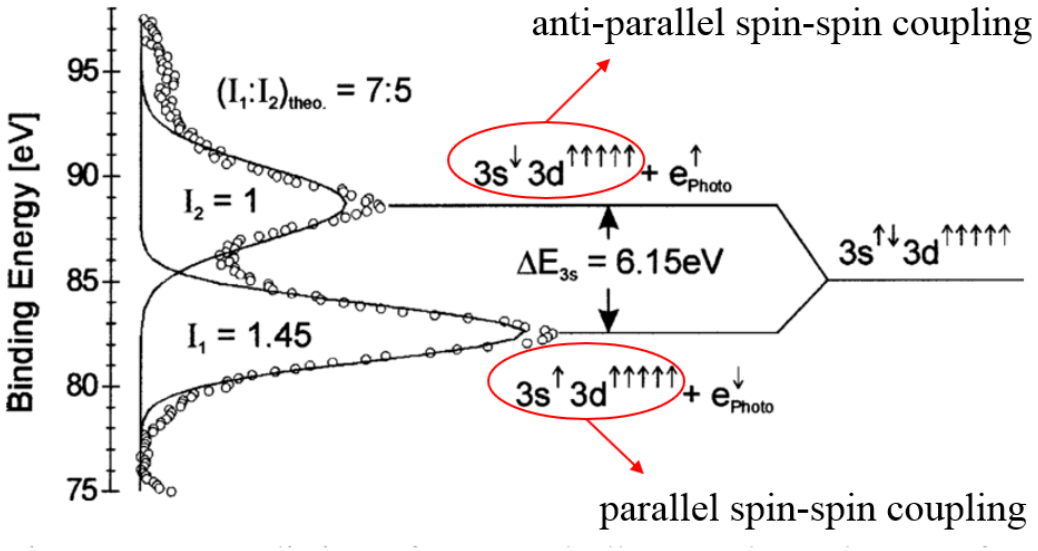

Figure 2-10: Illustration of the spin-spin coupling effect on the Mn 3s splitting of a MnO bulk crystal. (adapted from reference [46])

Additional spectral loss features common to many transition metals are shake-up and/or shake-off peaks appearing at higher BE than the main photoelectron peak (see Figure 2-9). Shake-up peaks arise from simultaneous loss of a photoelectron and excitation of a valence electron to a higher unoccupied bound state. Shake-off peaks are similar in origin only instead of the valence electron being excited to an unoccupied energy level it is lost to the continuum, resulting in a doubly ionized final state. The observed BE of the shake-off peaks is much higher than shake-ups. These satellite peaks sometimes help greatly in the identification of oxidation states, for example, Co^{3+} and Co^{2+} are mainly identified by presence or absence of characteristic Co^{2+} satellite at around 786 eV (see Chapter 4.2.2).

In the mid-1970s Gupta and Sen (GS) used a Hartree-Fock free ion method to model the 2p core line final states for many of the transition metals [16], [17]. Their models achieved a good approximation of the observed line shapes for most transition metals. These approximations are the basis of the peak fitting approaches of binary oxides in the other works such as Biesinger et al. [15].

The line shape of the photoelectron peaks collected for pure metal surfaces tends to have an asymmetric character that tails off to higher BE. The degree of asymmetry of the core line peak for any metal is related to its density of states at the Fermi level. In metals, the valence and conduction bands overlap and as a result, electrons are easily promoted above the Fermi level to any number of unoccupied energy levels. Moving valence electron density away from the nucleus effectively strengthens the attractive force of the nucleus on the core electrons, resulting in higher BE for the respective photoelectrons.

Some metal spectra also exhibit plasmon loss features, which arise from photoelectrons that have excited oscillations in valence electrons while passing through the surface. These collective oscillations require specific amounts of energy leading to KE losses and the appearance of characteristic peaks at higher BE. The oscillations are quantized and therefore the plasmon peaks repeat in constant energy distances with decreasing intensity.

For a correct quantification, the shake-up, shake-off, and plasmon loss peaks must be taken into account and be added to the intensity of the main peaks.

Besides the emission of characteristic X-rays as a relaxation process after photoelectron emission which is used in energy dispersive X-ray spectroscopy (EDS), the second relaxation route is the Auger electron emission depicted in Figure 2-11. The two described relaxation processes are in competition with each other and depend on the atomic number of the respective element. With increasing atomic number, X-ray emission is preferred. Auger peaks additionally occur in the photoelectron spectrum and can provide additional information for the distinction of chemical states e.g. between metallic Zn and ZnO [33], [47]. As the Auger electron emission is independent of the primary excitation energy, Auger peaks can be shifted on the XPS binding energy scale by changing the X-ray excitation energy (i.e. AlKα / MgKα) to overcome cross-talks of photoelectron an Auger electron peaks.

In case of using such non-monochromatic X-ray sources, satellite peaks originating from $K\alpha_{3,4}$ X-ray excitation also appear in the XPS spectra, which should be subtracted for quantification purposes.

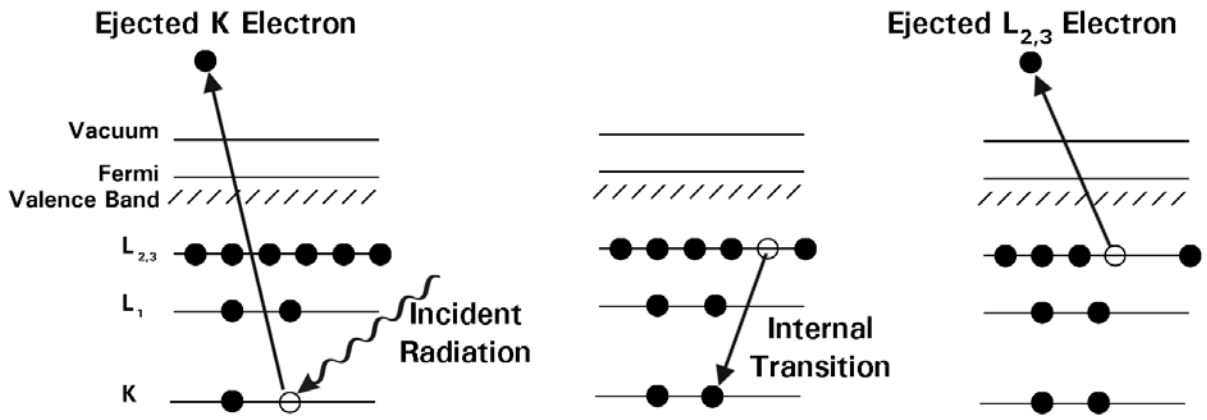

Figure 2-11: Illustration of X-ray-induced Auger electron emissions.

2.1.5. Chemical shift

The chemical shift refers to the small changes in the photoelectron binding energy of an atom based on its local bonding environment and/or chemical state. These binding energy differences can be explained qualitatively using the charged sphere model. In this model, the individual atoms of a surface are considered to be hard spheres having a valence charge q at a fixed radius of r. Inside the sphere, the charge distribution is considered to be uniform and as a result, any change in the valence charge density will shift the BE of all core electrons by:

$$\Delta BE = q/r \qquad \text{Equation 2-6}$$

For example, the oxidation of metallic Cr to Cr^{3+}, i.e. the loss of 3 valence electrons results in the remaining electrons being held more tightly by the nucleus of the atom and in consequence an increase in BE is observed.

To be able to get the benefit of the quantitative XPS chemical state identification the experimental multiplets must be fitted by one or more Voigt functions, a convolution of Lorentz and Gaussian functions, taking into account the contributions of sample and spectrometer. The quality of the fits is described by the Abbe criterion and Chi-square. The mathematical details can be found in the related literature [48], [49]. For a consistent evaluation, physically reasonable FWHM should be kept constant and the number of fitted peak components should be chemically relevant. For the used K-Alpha instruments intense peaks and/or peaks clearly evidenced by the peak shape have a

binding energy uncertainty of around ±0.1 eV. In case of weak peaks and no direct justification by the peak shape, the uncertainty should be set to ±0.2 eV. The assignment of chemical bonds is always controlled with standard reference values or literature values.

2.1.6. XPS quantification

From the XPS narrow scans the quantitative chemical composition of a surface can be determined using the following formula:

$$X_A = \frac{\frac{I_A}{S_A}}{\sum_n \frac{I_n}{S_n}} \qquad \text{Equation 2-7}$$

where X_A, I_A, and S_A represent the atomic concentration (in at. %), the peak area and the relative sensitivity factor (RSF) for element A, in a surface having n elements. Any contributions from the energy loss background to the photoelectron peak intensities are removed using a subtraction algorithm. The photoelectron peak intensity I_A depends on various parameters covered by the following integral [50]:

$$\begin{aligned} I_A = & \\ & \sigma_A^X D(E_A) \\ & \times \int_{\gamma=0}^{\pi} \int_{\varphi=0}^{2\pi} L_A(\gamma) \\ & \times \int_{y=-\infty}^{\infty} \int_{z=-\infty}^{\infty} J_0(xy)\, T(xy\gamma\varphi E_A) \\ & \times \int_{z=0}^{\infty} N_A(xyz) \exp\left[-\frac{z}{\lambda_M(E_A)\cos\theta}\right] dx\, dy\, dz\, d\varphi\, d\gamma \end{aligned} \qquad \text{Equation 2-8}$$

σ_A^X = cross-section for emission of a photoelectron from the relevant inner shell per atom of A

$D(E_A)$ = detection efficiency for each electron transmitted by the electron spectrometer

γ = angle between analyzer and X-ray source (see Figure 2-12)

φ = Azimuth on sample surface between X-ray and analyzer (see Figure 2-12)

$L_A(\gamma)$ = angular asymmetry of the intensity of the photoemission from each atom

$J_0(xy)$ = X-ray photon flux intensity at the point (x, y) on the sample

$T(xy\gamma\varphi E_A)$ = transmission function of the analyzer

$N_A(xyz)$ = atom density of the A atoms at (x, y, z)

θ = angle of emission of the photoelectron with respect to the sample normal (see Figure 2-12)

$\lambda_M(E_A)$ = photoelectron inelastic mean free path in the matrix M

An illustration of the relevant instrument's geometry is shown in Figure 2-12. Most of the parameters are determined and fixed by the instrument except mainly the cross-section for photoionization σ_A^X, which represents the probability a specific photoelectron emission will occur and the energy dependent inelastic mean free path $\lambda_M(E_A)$ (IMFP). The Thermo Scientific software Avantage utilizes photoionization cross-sections of Scofield [51] and the TPP-2M [52] formalism for the calculation of IMFPs. For the C 1s orbital, the Scofield factor is set to 1.0 for AlKα [51]. Relative to this, a factor of 0.061 is calculated for lithium. Consequently, the quantifications of lithium may be subject to a large resulting error.

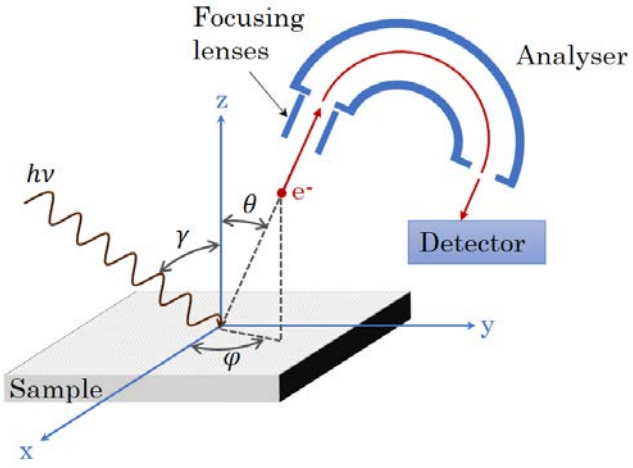

Figure 2-12: Illustration of XPS instruments geometry.

For homogeneous samples, the specified integral (I_A) can be solved in closed-form solution. By converting the equation according to the atom density of the A atoms, $N_A(xyz)$, and summarizing the known parameters into a constant K, the simplified equation below is obtained:

$$N = I_A / K \qquad \text{Equation 2-9}$$

The quantification takes place in a relative approach which eliminates the unknown parameters such as the non-measurable X-ray photon flux $J_0(xy)$. Therefore, the indication of the existing concentration of species is always relative to the total proportion as already pointed out in the Equation 2-7.

A precondition for a successful quantification is an exact subtraction of the spectral background from the peak areas under consideration. The background subtraction must be done by means of a function to separate the contributions of inelastically scattered photoelectrons. Common functions are the ones defined by Shirley [51] or Tougaard [53]. The Shirley background is iteratively adjusted between two manually defined points resulting in a step-shaped background. The adaptation of the Tougaard background is done by a weighted calculation of the measured energy dependent function. Here is the energy dependence of photoelectrons according to the inelastic scattering cross section considered [53].

Fulfilling the assumption of a homogenous sample with a flat surface, a quantification error of approx. ±10 % is to be expected.

2.1.7. XPS sputter depth profiling

Sputter depth profiling is alternating Ar^+ ion beam etching for materials removal and XPS analyses, revealing subsurface information which provides quantified elemental information as well as layer thicknesses. The surface is etched by a raster-scanned ion beam over a defined area of the sample. During the profile acquisition, the acceptance area of the transfer lens or the source-defined monochromator beam should be located at the center of the sputtered area to ensure that the analyzed area is situated on the flat bottom of the sputter crater. In case of insulators, an equilibration period should be allowed between the ion etch part of the cycle and the data acquisition. This allows the sample's surface potential to return to its steady state before data collection. The sputter yield determines the rate at which material is removed from the sample during a sputter depth profile, and mainly on the material to be removed and the incidence angle,

as well as the mass and the energy of the primary ion. More details regarding the fundamental sputter processes are discussed in the ToF-SIMS chapter.

Although sputter depth profiling works well in obtaining information from deeper layers with a depth resolution of approximately 5-10 nm; but, material removal via ion using high energy Ar^+ ion etching (1-5 keV) usually causes damages to the sample's surface (bond breaking, local warming, etc) and in consequence the chemical information on the new top-most layers are completely lost resulting in elemental distribution information only. A big step forward regarding sputter depth profiling while preserving the chemical information was the recently introduced gas cluster ion sources, especially for organic materials. Using e.g. Ar_{2000}^+ clusters at 8 keV energy achieves the extremely low energy of 4 eV per single particle at high particle densities. Overall, this leads to a gentler sputtering process to characterize organic samples such as polymers in a roughly nondestructive manner for the underlying layers of the material. Moreover, tuning cluster sizes and energy the current development is also going towards the application to inorganic materials aiming at nondestructive surface cleaning as well as depth profiling.

Figure 2-13 shows an example of XPS sputter depth profiling using monoatomic Ar ions, on an r.f. magnetron sputter deposited Li-Ni-Mn-Co-O thin-film deposited on Al substrate after annealing of the system. The chemical shift of the O 1s and Al 2p indicate the formation of Al_2O_3 at the substrate (the deposition condition is given in Chapter 3.4.1)

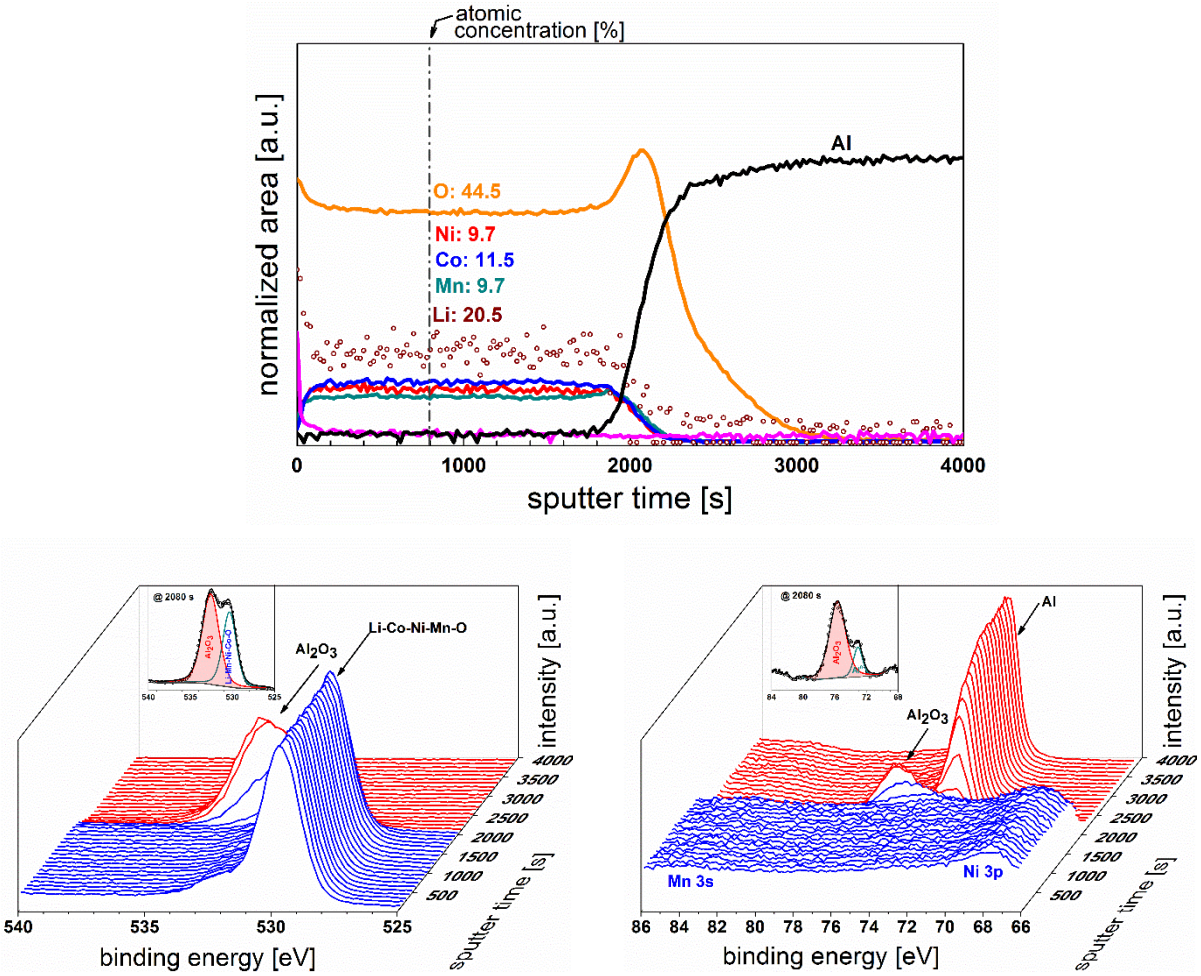

Figure 2-13: XPS depth profile of an r.f. magnetron sputter deposited Li-Ni-Mn-Co-O thin-film deposited on Al substrate after annealing of the system (top); XP spectra of O 1s (bottom left) and Al 2p (bottom right) energy region.

2.2. Time-of-flight secondary ion mass spectrometry (ToF-SIMS)

Time-of-Flight Secondary Ion Mass Spectrometry (ToF-SIMS) is the complementary surface analytical technique to XPS that is extremely sensitive to the outermost surface layers (sampling depth around 1 nm) and, therefore, analogous to XPS an excellent ultra-high vacuum is necessary within the analysis chamber (e.g. 10^{-10} mbar). The detection limit of ToF-SIMS is much lower than that of XPS and is in the order of ppm and ppb. In particular, ToF-SIMS is highly sensitive for the lithium, and, therefore, in a complementary approach with XPS can overcome the extremely poor XPS sensitivity for Li. Also, in addition to XPS, ToF-SIMS is able to detect all elements of the periodic table including their isotopes. Due to the raster-scanned pulses of the probing e.g. Bi^+

ion beam, fast chemical/molecular images can be provided easily with a spatial resolution of around 4 µm containing always the complete information in each point.

2.2.1. Fundamentals of ToF-SIMS

The probing beam in ToF-SIMS is a focused pulsed beam of energetic (25-30 keV) primary ions, which initiate the ejection of non-volatile secondary ions, molecular ion fragments and neutral atoms from the uppermost layers (1-2 nm) of the sample. The actual removal of material from the surface is the result of collision cascades or correlated atomic motions in the solid, which are initiated by the primary ion imprinting on the sample surface. The ejected particles are mostly neutrals, only around 5 % are positively or negatively charged secondary ions in the size range from single atoms, clusters of atoms and molecular fragments which subsequently are extracted to entrance slit of the time-of-flight detector mass spectrometer, having all the same kinetic energy (e.g. 2 keV) at the starting point and then are mass separated by measuring their flight time within the analyzer. Since every individual primary ion pulse generates an entire mass spectrum, not only integral spectra of the analyzed area are obtained, but also images of the lateral distribution of the secondary ions [54].

While the technique is apparently destructive, the use of an extremely low dose of primary ions in static SIMS (static limit = 10^{13} ions/cm^2) allows, on a random impact basis, obtaining molecular information in a quasi-non-destructive manner. The emitted particles arise from an area less than 10 nm^2 and are remote from the next point of analytical impact. Thus, each spectral information arises from a pristine surface.

The basic SIMS equation is presented in Equation 2-10 showing the secondary ion current for a selected ion.

$$I_m = I_p Y_m \alpha^+ \theta_m \eta \qquad \text{Equation 2-10}$$

where I_m is the secondary ion current of a species m, I_p is the primary ion flux, Y_m is the sputter yield of neutral and charged particles of the species m per incident primary ion, α^+ (or α^-) is the ionization probability that the sputtered particle will be a positive or negative ion, θ_m is the fractional concentration of the species m in the surface layer and η is the transmission of the analysis system.

The sputter yield Y_m is a function of the mass and energy of primary ion and also its angle of incidence (in the case of the ToF-SIMS.5 instrument: 45° to the surface normal). The ionization probabilities (α^+ and α^-) vary dramatically across the elements and are very sensitive to the electronic state of the surface. The secondary ion yield ($Y_m\alpha$) can therefore vary by several orders of magnitude for different elements and be very matrix sensitive. SIMS is therefore inherently non-quantitative, i.e. there is no simple relationship between the concentration of a given mass, θ_m, and its peak intensity, I_m. However, if a standard calibration material is available, the quantification might be possible.

2.2.2. Instrumentation of ToF-SIMS

Typically, a ToF-SIMS instrument as schematically shown in Figure 2-14 consists of the following main components: a pulsed liquid metal ion beam source (e.g. Bi^+, Bi_3^+, etc.) providing the primary probing beam, several ion beam sources (Cs^+, O_2^+, Ar^+, gas cluster ions) for materials removal during sputter depth profiling, an effective charge compensation system providing low energy electrons, and finally, the time-of-flight mass analyzer.

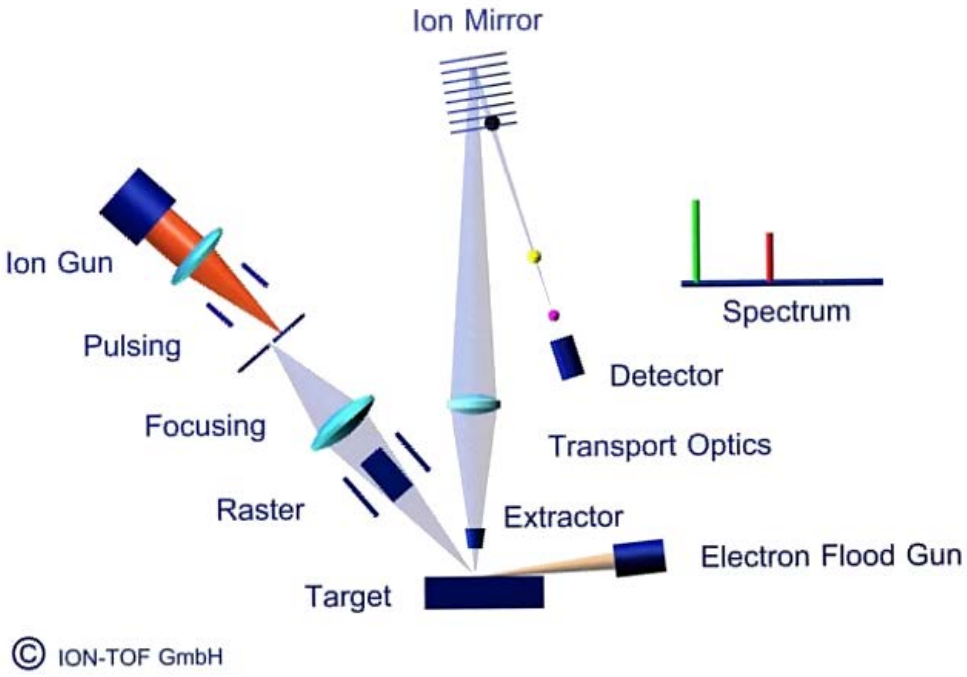

Figure 2-14: Schematic view of a typical ToF-SIMS instrument (adapted from ION-TOF GmbH, Münster, Germany).

2.2.2.1. Bismuth liquid metal ion gun (LMIG)

In today's modern ToF-SIMS instruments mainly Bismuth sources are used due to the additional advantage of making small Bi_x^+ (x=1-7 and multi-charged) clusters available and increasing the material dependent secondary ion yield compared to formerly used Ga or Au sources. When characterizing organic samples, for example, using Bi-cluster ions, the yield of bigger molecular species is significantly higher than that using Bi^+ and sample damage can be minimized to areas close to the surface. In addition, high and constant primary ion currents can be achieved with such a Bismuth source. In this work, mainly the Bi_n^{z+} source is used, which is a liquid metal ion source (LMIS). Hated liquid metal in LMIGs typically wets a tungsten needle tip where the opposing forces of surface tension and an electric field produce the cup-shaped Taylor cone. Herewith a virtual point emitter is achieved with a diameter of approximately 10 nm ideal to achieve small spot sizes on the probed topmost surfaces.

In addition, short primary ion beam pulses are required to achieve a high mass resolution. For mass analysis using a time-of-flight analyzer, all ions need to have a precisely defined starting time so that the ions can enter the analyzer via the extractor field with a minimized time blur. The higher the pulse rate of the primary ion source, the more accurate is the starting time of the emitted ions and the higher is the mass resolution to be achieved. The respective "high-current bunched mode" of ION-TOF's ToF-SIMS.5 instrument provides e.g. 0.7 ns Bi_1^+ and 1.0 ns Bi_3^+ ion pulses at 25 keV energy, respectively, and a lateral resolution of approximately 4 µm. This mode allows very high mass resolutions ($r=m/\Delta m$) in the range of approximately 10000 to be achieved.

For chemical mapping of the cathode surfaces the so-called "delayed extraction" mode is utilized which combines high lateral resolution based on a well-focused long pulse primary beam with a high spectral resolution. These features are achieved by delaying the onset of the extraction pulse with respect to the primary ion impact. Therefore, no longer the duration of the primary ion pulse but the fast increase of the secondary ion extraction field defines the starting timing of the time-of-flight separation. It should be considered that due to the delay between impact and emission, some of the light and fast secondary ions have already drifted out of the extraction zone between the surface and the extraction lens. Therefore, species below a mass to charge ratio of m/q = 20 cannot be detected in this mode [54].

2.2.2.2. Time-of-flight mass analyzer

Besides double-focusing sector field analyzers and quadrupole analyzers, SIMS mainly uses time-of-flight (ToF) analyzers. Sector field analyzers provide high mass resolution, but the

transmission is usually poor so that in consequence strong extraction fields are necessary. In quadrupole analyzers, only small extraction fields are required, but the achievable mass resolution is very low. The ToF analyzer combines both positive aspects. For the desired high mass resolution, only moderate extraction fields are required for a high transmission. The principle of the flight time analyzer is based on the separation of masses with respect to their mass to charge ratio (m/q) over their flight time in a field-free drift route.

In particular, the ions ejected from the surface are electrostatically extracted into the ToF analyzer accelerating all ions of a given polarity to the same nominal kinetic energy ($q.U_a$). These secondary ions then enter the field-free drift region of the analyzer with different velocities (v) dependent on their mass to charge ratio (m/q); with the smallest ions reaching the detector first, see Equation 2-11:

$$E_{kin} = \frac{mv^2}{2} = q.U_a \qquad \text{Equation 2-11}$$

The velocity of the charged particle will not change since it moves in a field-free drift section of length L_d to the detector. The resulting time-of-flight t is then:

$$t = \frac{L_d}{v} = L_d\sqrt{\frac{m}{2q.U_a}} \qquad \text{Equation 2-12}$$

Therefore, the secondary ions' flight time is proportional to the square root of their mass or their mass to charge ratio:

$$t \propto \sqrt{\frac{m}{q}} \qquad \text{Equation 2-13}$$

A channeltron detector is typically used to amplify the ion signal, which is similar to the electron multiplier used in XPS. Thus, a set of flight times will give a set of mass values that can be plotted as a mass spectrum. A major strength of the time-of-flight mass spectrometer is the parallel detection of ions, which means that always the complete mass spectrum is available for every measured point [55], [56].

2.3. Lithium-ion batteries

Lithium-ion batteries (LIBs) are currently the main focus of research and development in portable electronics and electric vehicles field thanks to the high energy and power density, as well as long cycle life that they can provide. The combination of a very low atomic mass and the most negative equilibrium potential in the electrochemical scale make lithium a very interesting element in the field of the energy storage. The advantage of storage systems based on lithium is obvious from a Ragone chart (see Figure 2-15) [57], [58]. In this chapter, the fundamental working principle of a LIB and the characteristics of the main compounds used for the positive electrodes are discussed.

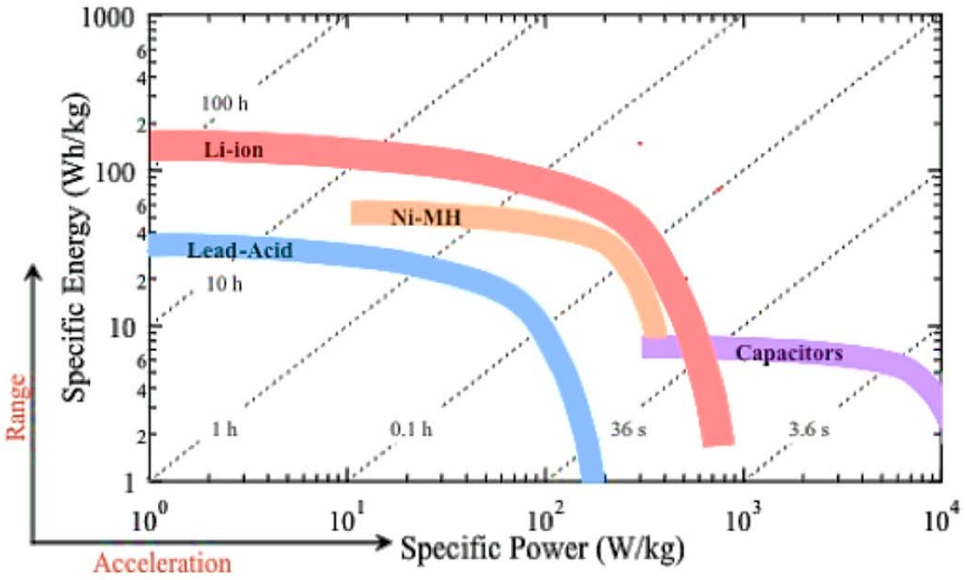

Figure 2-15: Ragone chart of the main secondary battery systems. (adapted from reference [58])

LIBs are complex systems based on the electrochemical process of lithium intercalation; both, bulk and surface properties of the materials are important for the final performance of the system. The Li-ion cells consist of at least three components; namely two electrodes immersed in an ion conducting, but electron insulating electrolyte, which are connected only by an external circuit containing a device, thus the electron and ion transport are completely separated [59]. The two electrodes are typically constructed from two different materials, thus establishing a potential difference between them. The electrode with the lower potential during discharge reaction, at which an oxidation reaction takes place, is called anode or negative electrode, whereas the other

one, at which reduction occurs, is named cathode or positive electrode. During cell operation, driven by the potential difference, electrons flowing in the external circuit are able to perform electric work. Charge balance occurs by Li ions which travel across the electrolyte from one electrode to the other. In most cases, the electrolyte is liquid, but ceramic or polymer electrolytes are also applied [60]. To prevent a direct contact between the electrodes, which can cause short-circuit, a physical separation is necessary for liquid-based systems. Therefore, a porous membrane, called separator, is soaked in the electrolyte between the electrodes and enables diffusion of the electro-active species (i.e. Li ions).

The redox activity in LIBs is carried out in immobile redox centers in the electrodes, thus, Li^+ ions are incorporated or released only for charge balancing reasons while keeping their charge, in other words, the negative and positive electrodes are host materials which can accommodate/release Li^+ ions in/from the structure. This process is called intercalation and is intrinsically a reversible process. For this reason, LIBs are commonly rechargeable and by application of an external current, the reverse reaction can take place so that oxidation occurs at the positive and reduction at the negative electrode. A schematic cross-section of a LIB together with the ionic and electronic flow during both charge and discharge reactions is depicted in Figure 2-16 with commonly used liquid electrolyte as well as graphite and $LiCoO_2$ as anode and cathode, respectively.

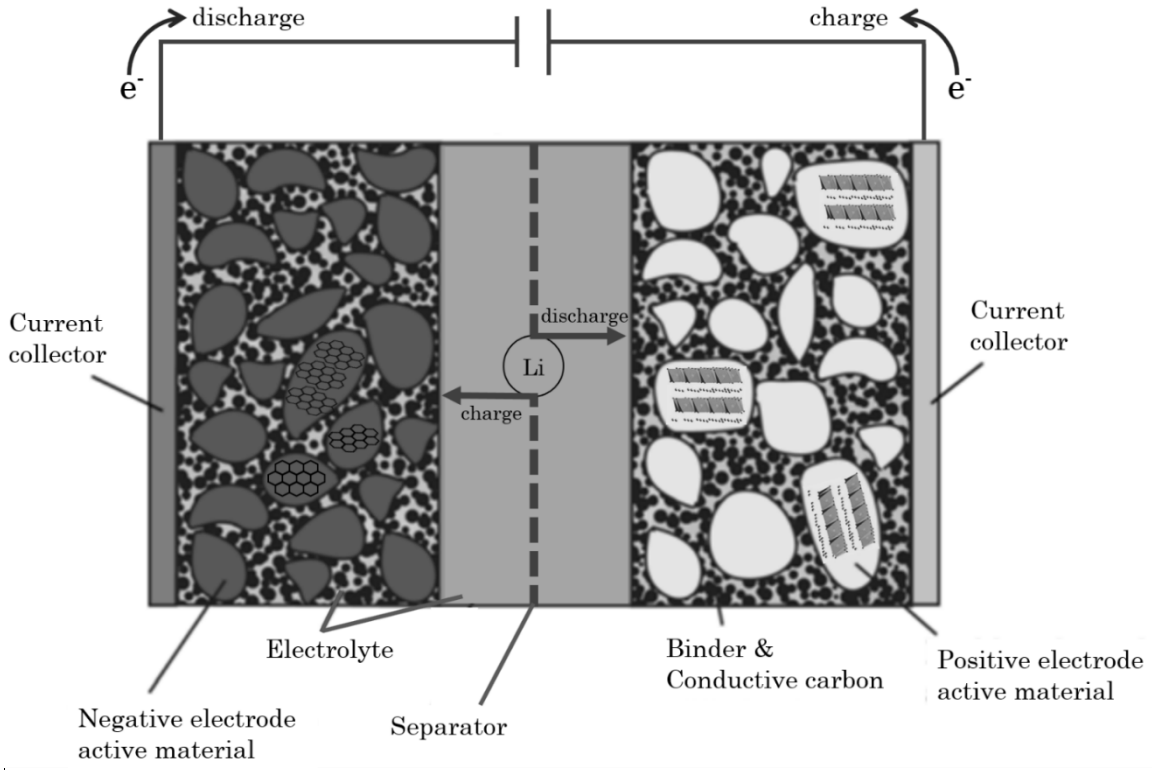

Figure 2-16: Schematic cross-section of a Li-ion battery showing the ionic and electronic flow during charge and discharge reactions, as well as major components of a Li-ion cell.

The choice of electrodes in LIBs depends upon their electrochemical potential values (μ_A for the anode and μ_C for the cathode in Figure 2-17) as well as their positions relative to the HOMO-LUMO (Highest Occupied Molecular Orbital and Lowest Unoccupied Molecular Orbital, respectively) energy gap (Eg) of the electrolyte. For a stable cell, μ_A must be lower in energy than the LUMO of the electrolyte, otherwise the electrolyte will be reduced, and on the other hand, μ_C should be higher in energy than the HOMO of the electrolyte to inhibit the oxidation of the electrolyte, as shown in Figure 2-17 [61]. An alternative scenario, that is already used in LIBs, is to design anode (and cathode) with a stable passivating solid electrolyte interface (SEI) layer that self-heals rapidly when broken by the changes in electrode volume that occur in a charge/discharge cycle; the SEI layer must also permit a fast Li^+ ion transfer between the electrode and the electrolyte without blocking electron transfer between the active particle and the current collector [61]. Hence, to achieve high energy storage density LIBs, it is important to develop low-cost, environmentally benign cathode materials with a maximum electrochemical potential difference to the anode as well as high lithium intercalation ability within the stability window of the electrolyte.

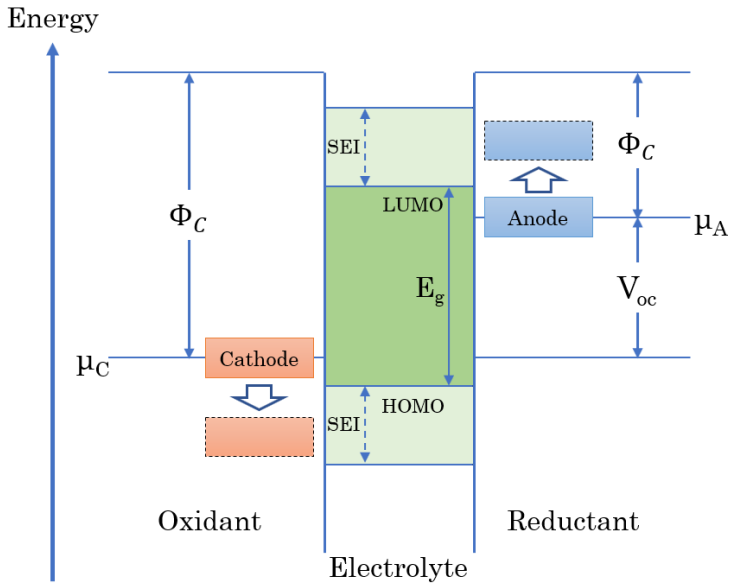

Figure 2-17: Relative energy diagram of electrode potentials and the electrolyte energy gap in LIBs. (adapted from reference [61])

In a LIB cell, the reactions take place at the electrode/electrolyte interfaces. An example of these reactions with typically used graphite (negative) and $LiCoO_2$ (positive) electrodes is provided in

Equation 2-14 (forward direction means the thermodynamically spontaneously occurring reaction) [5]:

$$Li^+ + e^- + C_6 \rightleftharpoons LiC_6 \quad \text{(negative electrode)}$$
$$2LiCoO_2 \rightleftharpoons Li^+ + e^- + 2Li_{0.5}CoO_2 \quad \text{(positive electrode)} \qquad \text{Equation 2-14}$$

On the negative electrode, Li^+ ions intercalate into the graphite via a reversible reaction (Equation 2-14) in which Li^+ ions from the electrolyte penetrate into the interlayer distance between the graphene sheets of graphite [62]. At maximum, one lithium ion per six carbon atoms can be stored [62]. Although μ_A of graphite lies well above the LUMO of a carbonate electrolyte (like typical $LiPF_6$ in ethylene carbonate / dimethyl carbonate (EC/DMC) electrolyte), the formation of a thin, amorphous SEI layer during the initial charge of the graphite provides a kinetic stability for reversible Li intercalation on subsequent charge/discharge cycles [61].

On the positive electrode, mostly inorganic transition-metal oxides or sulfides, capable to incorporate lithium ions, are used, such as $LiCoO_2$ compound (see Equation 2-14) which is most widely used in commercial LIBs [5].

2.3.1. Active materials for LIB cathodes

Typically, the active materials for positive electrodes in LIB are compounds based on transition metals which can release lithium ions from the structure by oxidation of the transition metal cations [63]. To obtain a high rate capability and high reversibility, it is important that the crystal structure of the active material remains unaltered during Li^+ intercalation, i.e. the Li^+ can diffuse rapidly into the structure. Moreover, to obtain high enough specific energy density, it is necessary that at least one Li^+ per transition metal can be intercalated/de-intercalated in the structure. Finally, the electronic conductivity of the compounds is important. If it is too low, conductive additives (mainly carbonaceous) need to be added to the electrode composition, thus the specific energy is lowered. In this case, the electrochemical reaction can occur only in those regions where the three phases (conductive additives, active material, and electrolyte) are in direct contact.

The extensively investigated cathode materials (with Li insertion chemistry [64]) are subdivided into three categories based on their crystal structure; namely the layered $LiMO_2$, the spinel LiM_2O_4, and the olivine $LiMPO_4$ (M = Ni, Mn, Co) [65] as shown in Figure 2-18. The important members and characteristics of each category are discussed below in more detail.

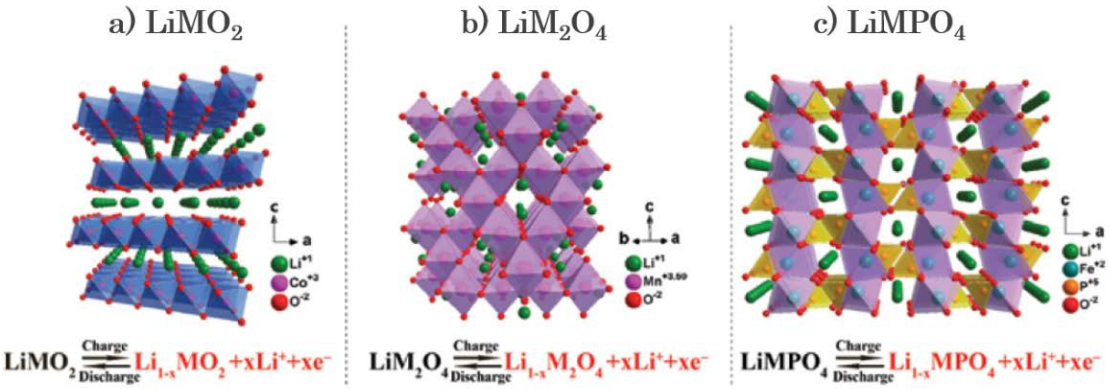

Figure 2-18: Crystal structures of three important classes of cathode materials: a) layered $LiMO_2$, b) spinel LiM_2O_4, and c) olivine $LiMPO_4$. (adapted from reference [65])

2.3.1.1. Layered cathode materials

Layered oxides denoted by the general formula $LiMO_2$, where M can be one or more transition metals, form an ordered rock-salt structure (see Figure 2-18a) with Li and M cations on alternate crystallographic planes, are capable of reversible lithium intercalation in two-dimensional (2D) pathways. Normally, the removal of lithium from ordered $LiMO_2$ leaves a metastable compound, and M cations stable in tetrahedral sites either move into the partially occupied Li-layer or transform the structure to spinel on the removal of half of the lithium. Moreover, a well-ordering of Li and M atoms in the initial $LiMO_2$ is required. As already mentioned, the layered structured $LiCoO_2$ cathode material is the prominent member of this category [61]. The complete removal of the Li^+ ions from $LiCoO_2$ results in changes of crystal structure, where, oxygen layers rearrange in a hexagonal close-packed cell and form CoO_2 which is electrochemically inactive with respect to Li^+ intercalation. Since the removal of more than half of lithium results in an increase of the amount of the irreversible specific charge, the maximum practical specific capacity of $LiCoO_2$ is 137 mAh/g with a plateau potential of 3.9 V versus Li^+/Li while its theoretical capacity is 274 mAh/g upon full charge [5]. In addition to its low practical capacity, other noticeable disadvantages of the $LiCoO_2$ are related to the safety of the battery, and the toxicity and the high costs of cobalt. The safety issues of $LiCoO_2$ originates mainly its intrinsic instability in the delithiated state. At temperatures above 200 °C delithiated Li_xCoO_2 disproportionates into $LiCoO_2$ and CoO_2, the latter reacts into Co_3O_4 by releasing oxygen. In combination with flammable electrolytes, an overheating at high charge levels results in an ongoing exothermal reaction, known as “thermal runaway” [66].

A relatively low-cost alternative for $LiCoO_2$ could be $LiNiO_2$ which has the same layered structure of the cobalt equivalent. Its practical capacity is as high as 190-210 mAh/g, however, its commercialization in the pure state as a battery cathode is hindered for a variety of reasons: such as difficult preparation process, poor thermal stability, and since always an excess of nickel is found in the lithium layer (cation mixing of Li^+ and Ni^{2+}), which causes a reduction of the diffusion coefficient and consequently the power capability [63], [65]. Moreover, the delithiated compound seems to be unstable and therefore dangerous in contact with organic solvents [63]. The usage of low-cost and environmental friendly layered $LiMnO_2$, which has a high practical capacity of ~200 mAh/g, is also hampered by Mn dissolution caused by the Jahn-Teller distortion of Mn^{3+} (which induces distortion and collapse of the host lattice, more detail in [67]) and oxygen evolution at a high charging potential, leading to the loss of the active material and serious safety issues [63]. To combine the advantages of $LiCoO_2$, $LiNiO_2$, and $LiMnO_2$, the $LiNi_{1-x-y}Mn_xCo_yO_2$ ternary system, has been systematically investigated and expected to replace $LiCoO_2$ in the near future [5], [65], [68]. The common abbreviation for such materials is NMC or NCM with numbers indicating the decimals of the elements (e.g. NMC532: $LiNi_{0.5}Mn_{0.3}Co_{0.2}O_2$). According to the literature [68], [69], the Ni^{2+}/Ni^{3+} and/or Ni^{3+}/Ni^{4+} redox couples provide the majority of the reversible capacity; Co reinforces the layered ordering with improved rate capability and additional capacity from the $Co^{3+/4+}$ redox reaction; Mn, on the other hand, remains electrochemically inert in the tetravalent state and stabilizes the local structure, especially at the highly delithiated state. The Jahn-Teller effect associated with Mn^{3+} is not a concern for $LiNi_{1-x-y}Mn_xCo_yO_2$ [68]. Although NMC materials with Ni ≥ 60 % showed higher capacity, the degradation that occurs at the particle surface during electrochemical operation leads to a rapid capacity fading and hinders their widespread commercialization as cathode materials for LIBs. This is in part due to their higher operating voltage (up to 4.3-4.5 vs. Li^+/Li) compared to the conventional $LiCoO_2$, which is dangerously close to the oxidation stability limits of most known nonaqueous liquid electrolytes. Also, Ni^{4+} ions are highly reactive and accelerate the electrolyte decomposition and low thermal stabilities [69]. Additionally, the formation of microcracks on NMC, via rapid changes in the crystallographic parameter at the end of charge and often notable after extensive cycling (i.e. > 500 cycles), considerably worsens the surface degradation and further limits NMC cycle life [68], [69]. The evolution of the surface chemistry of NMC materials initiates technically long before the electrochemical operation in LIBs [68]. Theoretically, manganese and cobalt are present in the NMC structure as Mn^{4+} and Co^{3+} respectively, while nickel is observed as a mixing of Ni^{2+} and Ni^{3+} [70]. A native film of Li_2CO_3 (and additionally LiOH) is usually present on the particle surface, introduced during materials manufacturing, processing, and storage [68]. This is because that an excess amount of Li salt is necessary for the

lithiation heat treatment process for the precursors to crystalize in the highly ordered layered structure. As a result, the residual Li_2O on the surface of the final products inevitably reacts with moisture and CO_2 in the air to form LiOH and Li_2CO_3 [68]. Furthermore, given the acidic chemical nature of most commercialized electrolytes with fluorinated anions (e.g. PF_6^-), this native film is corroded away instantly upon contact with the electrolyte components, and largely replaced by compounds such as LiF, Li_xPF_y, and $Li_xPO_yF_z$; gaseous products such as CO_2 and alkane are also produced during the process. These spontaneous reactions greatly contribute to the eventual complex surface species on the NMC particle surface, in terms of both the chemical composition and morphology [68]. Therefore, clearly, the unique ability of XPS in the identification of the chemical state of transition metals as well as involved degradation mechanisms is very demanded in research and development of NMC materials.

2.3.1.2. Spinel cathode materials

Spinel oxides with the general formula of LiM_2O_4, where M-cations occupy the octahedral sites and lithium predominantly occupies the tetrahedral sites in a cubic-closed-packed O^{2-} lattice (as shown in Figure 2-18b), provide a three-dimensional (3D) Li^+ diffusion pathways [65], [71]. Therefore, mainly $LiMn_2O_4$ and $LiMn_{1.5}Ni_{0.5}O_2$, have shown great potential for high-rate LIB applications [65]. $LiMn_2O_4$ spinel compound is a low-cost and environmental friendly cathode material. The average oxidation state of the manganese in $LiMn_2O_4$ compounds is critical to obtain an effective cycle life. In case the oxidation state of the manganese is 3.58 or higher, like in the $Li_{1+x}Mn_{2-x}O_4$ compounds, the dissolution of the manganese is minimized and the spinel compound has a longer cycle-life-time [72]. However, often Mn dissolution via disproportionation ($2Mn^{3+} \rightarrow Mn^{2+} + Mn^{4+}$) and Jahn–Teller distortion from the cubic to tetragonal phase, hinder the practical application of the spinel $LiMn_2O_4$ [65], [73]. The substitution of Mn by Ni in $LiMn_{1.5}Ni_{0.5}O_2$ can increase the mean oxidation state of the Mn ions for a more stable structure and eliminate the Jahn-Teller distortion. The oxidation potential for Ni^{2+} to Ni^{4+} can reach up to 4.7 V (vs. Li^+/Li), making $LiNi_{0.5}Mn_{1.5}O_2$ a promising high-voltage cathode material. Nevertheless, the stability of the present electrolytes and active materials makes it difficult to accommodate these high-voltage cathodes [65]. The Ni-doped Mn spinel with the composition $LiNi_{0.5}Mn_{1.5}O_4$ (LNMO) is a highly promising cathode material which shows an impressive electrochemical performance like large reversible capacity at a high operating voltage around 4.7 V where the reversible $Ni^{2+} \rightleftharpoons Ni^{4+}+2e^-$ redox reactions take place. In the ideal $LiNi_{0.5}Mn_{1.5}O_4$ spinel, the oxidation state of Ni and Mn are +2 and +4, respectively, and no Mn ions exist in the trivalent state, which is well-known as Jahn-Teller ion causing structural instability. However, usually, a small amount of Mn^{3+} remains

in the compound as a result of oxygen deficiency after the high-temperature synthesis process. Cation doping on LNMO spinels by 3d or 4d cations can enhance the reachable capacity, cycling stability at high C-rates, the electrical conductivity and the structural stability [74].

2.3.1.3. Olivine cathode materials

The olivine-type $LiMPO_4$ (M = Fe, Mn, Co, Ni) compound provide a one-dimensional (1D) pathway for the diffusion of Li^+ ions (see Figure 2-18c). The attractive $LiFePO_4$ compound is a low cost and environmentally benign material. $LiFePO_4$ offers a number of advantages compared to $LiCoO_2$, such as stability, excellent cycle life, and temperature tolerance (−20 to 70 °C). The stability of $LiFePO_4$ originates largely from the fact that both the lithiated $LiFePO_4$ and the fully delithiated $FePO_4$, exist as minerals triphylite and heterosite, respectively [66]. However, $LiFePO_4$ has a problem of poor electronic (10^{-10} S/cm) and ionic conductivity (10^{-8} cm^2/sec), as well as relatively low capacity (theoretically 170 mAh/g). An additional issue is a one-dimensional pathway for lithium ion diffusion which can easily be blocked by defects and impurities [5], [75].

3. Experimental

This chapter describes the utilized spectrometers, devices, materials and chemicals together with the experimental conditions.

3.1. X-ray photoelectron spectroscopy (XPS)

X-ray photoelectron spectroscopy was performed using a K-Alpha and/or a K-Alpha+ XPS instrument by Thermo Fisher Scientific, East Grinstead, UK. All samples were analyzed using a micro-focused, monochromated AlKα X-ray source. The diameter (short axis of the ellipse) of the measuring area was 400 µm. To compensate local charging, a combination of low-energy electrons (8 eV) and low-energy argon ions (1-10 eV) was directed to the sample using the instruments neutralization system. Sputter depth profiles were measured in an alternating process via topmost surface removal by ion beam etching and intervening spectral recording. The argon ion beam was raster-scanned over the sample with ion energies in the range of 500-2000 eV at a 30° angle of incidence, and a raster-area of 2×4 mm^2. The quantitative multiplet evaluation was done by fitting the spectra using Voigt functions (convolution of Gauss and Lorentz functions), whereby the determination accuracy for the binding energy is ±0.2 eV. The Lorentz to Gauss ratio was set to 70:30 (deviations are explained in the respective parts of the results and discussion chapter). The quantification was carried out considering the transmission function of the analyzer, the cross sections for the photoionization according to Scofield [51] and the effective attenuation lengths (EAL) for the photoelectrons. EALs were calculated using TPP-2M formalism [52]. The correction of the background of the spectra was done by fitting a Shirley function [76]. All spectra were referenced to either 285.0 eV of the C 1s component for aliphatic carbon (C-C, C-H bonds) or 284.4 eV of the graphitic C 1s component, controlled by the known binding energy levels of the photoelectron peaks of copper, silver, and gold. Data acquisition and processing were performed using the Thermo Avantage software [77]. In order to exclude atmospheric contact during sample handling, sample transport was done over double welded containers in a polymer coated aluminum composite (leak rate 0.006 $Ls^{-1}m^{-2}$) or by an especially designed transfer vessel with vacuum slide and flange technique. The sample was mounted in a glovebox directly attached to the spectrometer (Glove Box Technology, St. Ives, UK, dewpoint ≤ -80 °C, O_2 < 1ppm).

3.2. Time-of-flight secondary ion mass spectrometry (ToF-SIMS)

Time-of-flight secondary ion mass spectrometry (ToF-SIMS) was performed on a TOF-SIMS.5 instrument (ION-TOF GmbH, Münster, Germany) equipped with a bismuth cluster liquid metal primary ion source and a nonlinear time-of-flight analyzer (reflectron assembly).

For surface spectra, the settings were chosen so that the primary ion dose does not exceed the static limit of 1×10^{-11} primary ions/cm^2. For each sample, spectra were recorded in positive and negative polarity at two different measuring positions. The primary ion beam was scanned over a field of view of 500×500 µm^2 at a resolution of 128×128 pixels. The achievable lateral resolution is in a range of 4 µm.

For sputter depth profiles and high mass resolution, the bismuth source was operated in the "high current bunched" mode and provided a 0.7 ns (Bi_1^+) or 1.0 ns (Bi_3^+) pulsed primary ion beam at an acceleration voltage of 25 keV. The time-of-flight analyzer provides a mass spectrum in the range of 0-800 m/z for a cycle time of 100 µs. The materials removal was performed using a 1 or 2 keV Cs^+ ion beam at a raster-scanned area of 400×400 µm^2. The measuring range for sputtering depth profiles with a field of view of 100×100 µm^2 at a resolution of 256×256 pixels was adjusted in the center of the Cs sputter crater.

For the acquisition of ToF-SIMS images the "delayed extraction" mode was applied which combines high lateral resolution based on a well-focused long pulse primary beam with a high spectral resolution. The primary ion beam was scanned over a field of view of 50×50 µm^2 at a resolution of 512×512 pixels. The maximum achievable lateral resolution is in a range of 100 nm for very flat samples.

The mass scale for negative polarity spectra was calibrated to $^6Li^-$, C^-, C_2^- C_3^-, and C_4^-. Positive polarity spectra were calibrated using $^6Li^+$, $^6Li_2^+$, C^+, Na^+, K^+, Ni^+. For sputter depth profiles, a selection of MCs^+ clusters (e.g. Cs_2^+, Cs_2F^+, $CsLi^+$) was also used to calibrate the mass scale.

The charge compensation was not used since the electrodes show enough conductivity for ToF-SIMS measurements. The working pressure in the analysis chamber was in the range of 10^{-8} to 10^{-9} mbar for all measurements. For air-sensitive electrodes, the sample assembly was carried out under argon protective gas atmosphere inside a glovebox. The sample transfer into the load-lock of the spectrometer was performed utilizing the special transfer vessel of ION-TOF GmbH.

3.3. Scanning electron microscopy (SEM)

Scanning electron microscopy was performed using a Zeiss Merlin (Carl Zeiss SMT AG, Oberkochen) scanning electron microscope (SEM) equipped with a Schottky field emission source. The SEM provides primary electron beam width energies in the range of 0.02-30 keV. The interaction of primary electron beam with the electrons of the sample produces many backscattered electrons (BSE) when elastically scattered, as well as secondary electrons (SE) and characteristic X-rays when inelastically scattered. For SEM images the SE and BSE are detected with an SE detector and an energy selective backscattered (ESB) detector, respectively. Details and advantages of the ESB technique, e.g. for characterizing binder and carbon black, are explained elsewhere [78]. For the topographical contrast in electron micrographs, secondary electrons were used as they are generated only in the surface near regions (≤ 50 nm). The backscattered electrons provide the materials contrast in the images, due to the dependence of the backscattering coefficient on atomic number (Z), i.e. the backscattering coefficient increases with the increase of the atomic number. Hence, the brighter regions displayed in the BSE images correspond to those of the species with higher Z elements [79].

3.4. Material synthesis

Most of the materials used in this work are synthesized by colleagues from IAM-ESS, IAM-AWP, and IAM-KWT institutes of KIT. Some reference materials are bought from specified companies. The synthesis route used by the material developers are presented in the next chapters.

3.4.1. Synthesis of thin Li-Ni-Mn-Co-O films

Thin Li-Ni-Mn-Co-O films (cf. Chapter 4.3.1) were deposited on silicon substrates by r.f. magnetron sputtering from a $Li_{1.18}(Ni_{0.39}Mn_{0.19}Co_{0.35})O_{1.97}$ ceramic target. The support of Marc Strafela, IAM-AWP, is gratefully acknowledged and the deposition process in detail is described in reference [31].

Thin Li-Ni-Mn-Co-O films were deposited on silicon substrates by r.f. magnetron sputtering in a Leybold Z550 PVD coating facility using a $Li_{1.18}(Ni_{0.39}Mn_{0.19}Co_{0.35})O_{1.97}$ (π PI-KEM Ltd.) ceramic target with a diameter of 76 mm and a thickness of 6.4 mm. The target to substrate distance was 55.5 mm. All films were deposited by using 100 W r.f. target power at 7 Pa working gas pressure in a pure argon atmosphere. The film thickness was adjusted between 200 nm and max. 1 µm and measured by means of a Tencor P-10 profilometer. Before deposition, the base chamber pressure was below 10^{-5} Pa. The substrates were ultrasonically cleaned in acetone at room temperature and

subsequently sputter etched directly before deposition. Finally, all films were annealed at 600 °C in an Argon/Oxygen atmosphere (Argon/Oxygen = 80/20) at 10 mPa to trigger reorganization and crystallization of the material. In order to avoid any thin-film contamination, the samples were transferred inert from the deposition chamber to a glovebox with a pure argon atmosphere.

3.4.2. Synthesis of the $LiNi_{0.8-y}Mn_yCo_{0.2}O_2$ ($0 \leq y \leq 4$) powder series

Single phase $LiNi_{0.8-y}Mn_yCo_{0.2}O_2$ samples with y = 0, 0.1, 0.2, 0.3 and 0.4 were synthesized by the sol-gel process using metal acetates and adipic acid as the chelating agent. The support of Maryam Masoumi, IAM-AWP, is gratefully acknowledged and the details of the synthesis are given in references [32], [80].

These samples are abbreviated as NMC442, NMC532, NMC622, NMC712, and NMC802 for $LiNi_{0.4}Mn_{0.4}Co_{0.2}O_2$, $LiNi_{0.5}Mn_{0.3}Co_{0.2}O_2$, $LiNi_{0.6}Mn_{0.2}Co_{0.2}O_2$, $LiNi_{0.7}Mn_{0.1}Co_{0.2}O_2$, and $LiNi_{0.8}Co_{0.2}O_2$ stoichiometries, respectively.

For synthesis, the stoichiometric amounts of $Li(CH_3COO)\cdot 2H_2O$, $Mn(CH_3COO)_2\cdot 4H_2O$, $Ni(CH_3COO)_2\cdot 4H_2O$ and $Co(CH_3COO)_2\cdot 4H_2O$, and adipic acid were dissolved in distilled water. The amounts of the nickel, manganese and cobalt acetates were chosen based on the designated stoichiometry of the sample, while 3 mol% extra lithium acetate is added to compensate the lithium loss during high-temperature heat treatment which is common for these type of materials [81]. The amount of adipic acid was chosen to yield an acid to total metal ion ratio of 1:1. The origin and purities of the starting chemicals are listed in Table 3-1. The *pH* value of the resulting mixed solution at room temperature was adjusted to approximately 6.5 by ammonium hydroxide. The solution was heated at 80–90 °C while constantly stirred for 5-6 hours to obtain a viscous gel. The gel was dried in a drying oven at 120 °C for 1 days. The ground precursor was fired in alumina crucibles with silica lining for 10 hours at 500 °C with a heating rate of 2 $K\cdot min^{-1}$ in air using a box furnace to remove the organic content. The pre-calcinated sample was ground and placed in an alumina crucible for final calcination for 15 hours. The final calcination temperature was 900 °C for the samples with y = 0.2, 0.3, and 0.4, and 850 °C for the sample with x = 0.1, as well as 725 °C and 800 °C for the sample with y = 0. The samples were quenched in the air by removing from the hot furnace.

Table 3-1: Used commercial starting chemicals for the synthesis of the $LiNi_{0.8-y}Mn_yCo_{0.2}O_2$ ($0 \leq y \leq 4$) powder series.

raw material	chemical formula	source	mass fraction purity
Lithium acetate dihydrate	$Li(CH_3COO)\cdot 2H_2O$	*Alfa Aesar*	≥ 99.9 %
Manganese (II) acetate tetrahydrate	$Mn(CH_3COO)_2\cdot 4H_2O$	*Merck KGaA*	≥ 99.0 %
Nickel acetate tetrahydrate	$Ni(CH_3COO)_2\cdot 4H_2O$	*Sigma-Aldrich*	≥ 99.0 %
Cobalt acetate tetrahydrate	$Co(CH_3COO)_2\cdot 4H_2O$	*Merck KGaA,*	≥ 99.0 %
Adipic acid	$C_6H_{10}O_4$	*Merck Schuchardt OHG*	≥ 99.0 %

[a] Purity expressed in mole fraction

3.4.3. Preparation of electrodes of $LiNi_{0.8-y}Mn_yCo_{0.2}O_2$ ($0 \leq y \leq 4$) and their electrochemical characterization

To obtain the electrodes, powders of $LiNi_{0.4}Mn_{0.4}Co_{0.2}O_2$, $LiNi_{0.5}Mn_{0.3}Co_{0.2}O_2$, and $LiNi_{0.6}Mn_{0.2}Co_{0.2}O_2$ annealed at 900 °C and $LiNi_{0.7}Mn_{0.1}Co_{0.2}O_2$ and $LiNi_{0.8}Co_{0.2}O_2$ annealed respectively at 850 °C and 800 °C was used. The electrode preparation by Maryam Masoumi, IAM-AWP, and performing electrochemical cycling by Liuda Mereacre, IAM-ESS, is gratefully acknowledged.

To obtain cathodes for electrochemical characterizations, the pristine $LiNi_{0.8-y}Mn_yCo_{0.2}O_2$ ($0 \leq y \leq 4$) powders (80 wt.%) have been ground with carbon black (10 wt.%, TIMCAL, Super C65) and PVDF (10 wt.%, Solef 6020, Solvay) and NMP (Alfa Aesar) resulting in a slurry, which was then coated on aluminum foil (20 µm) with a wet thickness of 150 µm. This film was then vacuum dried at 80 °C for 24 h and discs were punched out with a diameter of 13 mm. The mass loadings of the electrodes were on average 4.9 mg composite. The electrodes were pressed (8 T, 30 s) and dried at 110°C in vacuum before assembly. Coin cells (2032) were assembled in an argon-filled glovebox (MBraun) with a lithium foil (MTI, 15.6 mm diameter, 250 µm thickness) as anode, 180 µL electrolyte and two layers of Celgard 2325 as separator. All cells were cycled with a VMP3 multi-channel potentiostat (Bio-Logic, France) at 25 °C. The electrolyte used for cells cycled in the voltage range of 3.0-4.2 V was LP30 (1 M $LiPF_6$ in EC:DMC (50:50, wt.%), BASF), and the cells are cycled at C-rate of C/10. The cells were disassembled in the charged and

the discharged state for each stoichiometry. The cell potential over time and the resulting specific capacity is shown in Figure 3-1 and Figure 3-2 respectively.

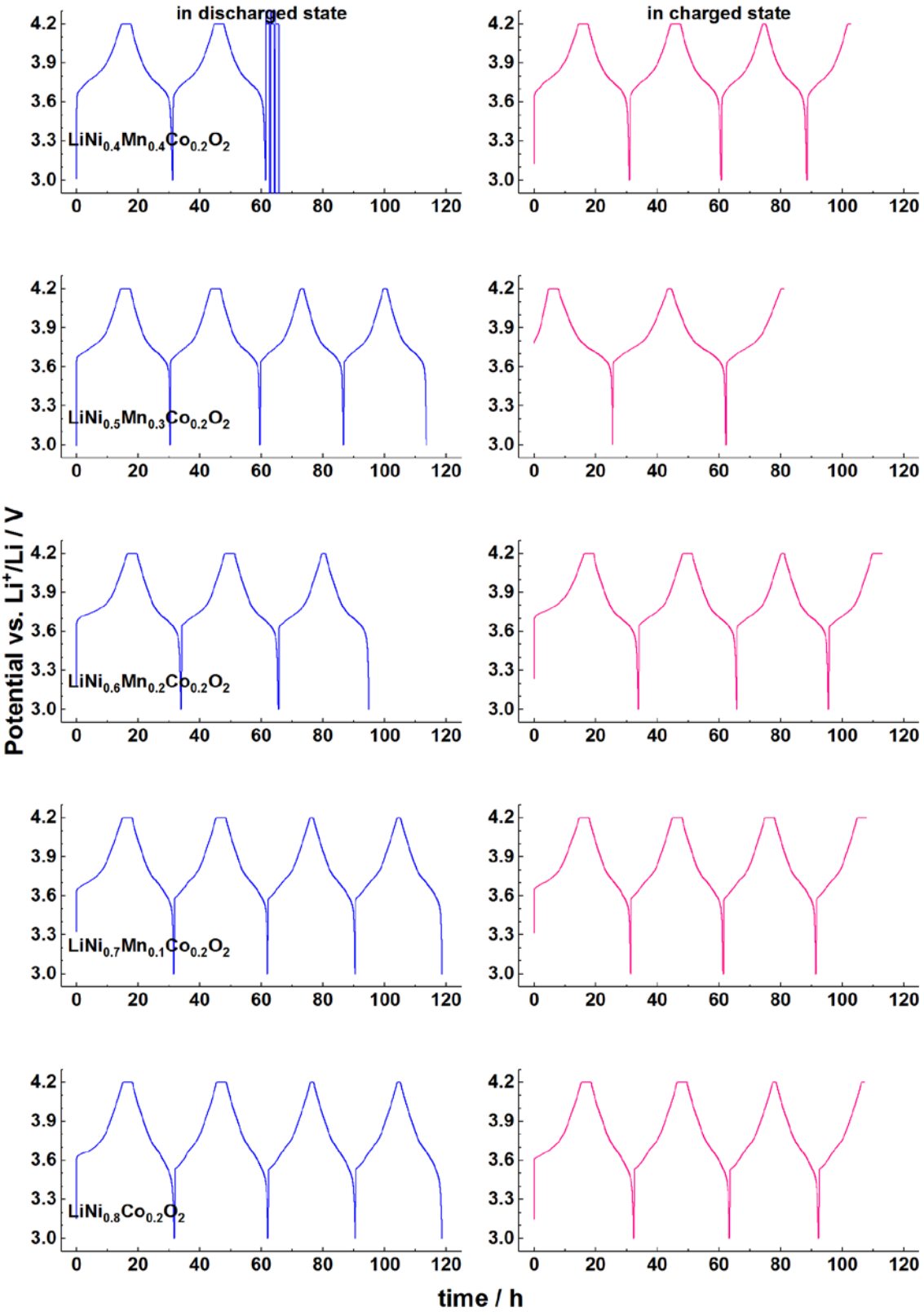

Figure 3-1: The potential over time graphs for the $LiNi_{0.8-y}Mn_yCo_{0.2}O_2$ ($0 \leq y \leq 4$) electrodes in discharged (left) and charged (right) state.

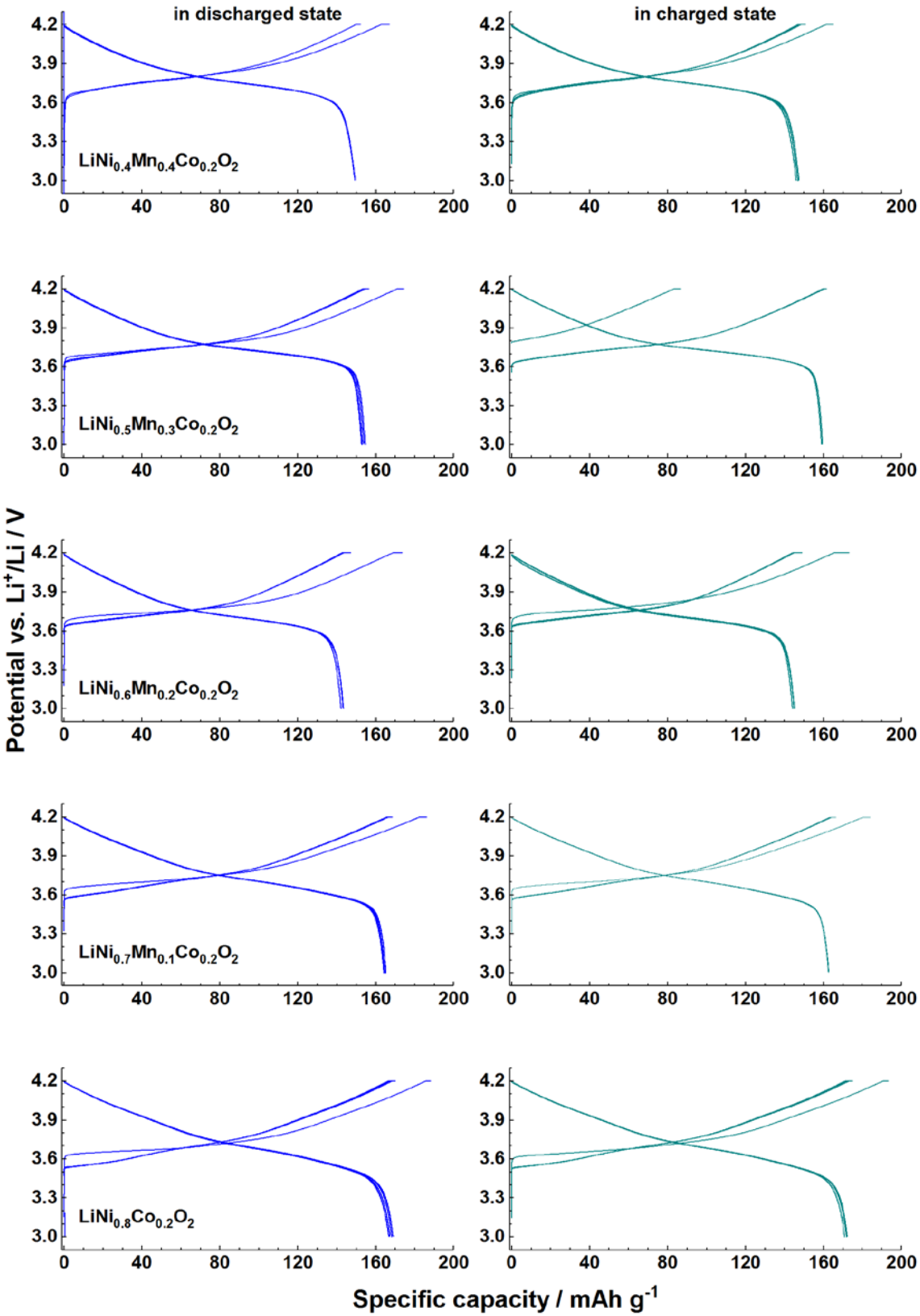

Figure 3-2: The potential over specific capacity for the $LiNi_{0.8-y}Mn_yCo_{0.2}O_2$ ($0 \leq y \leq 4$) electrodes in discharged (left) and charged (right) state.

3.4.4. Synthesis of Co, Cu, and Fe doped $LiNi_{0.5}Mn_{1.5}O_4$ powders

The $LiNi_{0.4}M_{0.2}Mn_{1.4}O_4$ (M = Cu, Co, Fe) spinel cathode materials were synthesized using the citric acid-assisted sol-gel method with final calcination at a temperature of 1000 °C. Synthesis details are to be found in reference [82] and the materials delivery by Aishwarya Bhaskar, IAM-ESS, is gratefully acknowledged.

The $LiNi_{0.5}Mn_{1.5}O_4$ and $LiNi_{0.4}M_{0.2}Mn_{1.4}O_4$ (M = Cu, Co, Fe) materials were synthesized by a citric acid-assisted sol-gel method. $LiCH_3COO{\cdot}2H_2O$, $Mn(CH_3COO)_2{\cdot}4H_2O$, $Ni(CH_3COO)_2{\cdot}4H_2O$ and Iron acetate anhydrous, Cobalt (II) acetate tetrahydrate or copper acetate monohydrate (II) precursors were dissolved in a mixture of citric acid and ethylene glycol (1:4 mol mol^{-1}) by heating at 90 °C. Subsequently, the solution was heated up to 180 °C to evaporate the excess ethylene glycol from the mixture and to get a transparent gel. The obtained gel was pre-calcined at 400 °C for 5 h to remove the carbon. After cooling down to the room temperature, the mixture was ground in a mortar and then pre-annealed at 600 °C for 24 h in the air with intermittent grinding. Until this step, the heating rate was 300 $°Ch^{-1}$. Finally, each material composition was annealed at 1000 °C with a heating rate of 600 $°Ch^{-1}$ and holding time < 1 min and cooled down to the room temperature slowly in the furnace to obtain the final products.

3.4.5. Synthesis of Ru/Ti-doped $LiNi_{0.5}Mn_{1.5}O_4$ (LNMRTO) powders

A three-step synthesis was used to produce the ruthenium/titanium doped spinels, i.e. two spray-drying steps followed by calcination, with an intermediate grinding step. The used precursor materials were metal acetates of lithium, nickel and manganese ($Li(OOCCH_3){\cdot}2H_2O$, (Alfa Aesar); $Ni(OOCCH_3)_2{\cdot}4H_2O$, and $Mn(OOCCH_3)_2{\cdot}4H_2O$ (Sigma Aldrich)) as well titanium isopropoxide ($Ti[OCH(CH_3)_2]_4$, (Merck) and ruthenium acetate solution, $(Ru(OOCCH_3)_3$, (Umicore). Synthesis details are to be found in reference [83], and the delivery of Ru-, Ti-doped $LiNi_{0.5}Mn_{1.5}O_4$ powders by Andres Höweling, IAM-KWT, is gratefully acknowledged.

Two types of powder materials were investigated by XPS. The as-prepared material is denoted as $LNMRTO_{AP}$ (Ru-, Ti-doped). The second type was calcined again using an additional temperature program (1000 °C without dwell time followed by 800 °C for 10 h). This particular material is denoted as $LNMRTO_{HT}$.

3.4.6. Synthesis of mesoporous spinel-type MCo_2O_4 (M = Co, Zn, and Ni) rods

The spinel-type MCo_2O_4 (M = Co, Zn, and Ni) mesoporous rods were fabricated by a simple solvothermal approach without the assistance of surfactants as described in detail in reference [33]. The materials delivery by C. R. Mariappan, National Institute of Technology, Kurukshetra, India, is gratefully acknowledged.

$NiCo_2O_4$ mesoporous rods were prepared by mixing 1 mmol $Ni(SO_4)_2 \cdot 7H_2O$ (Loba Chemie) and 2 mmol $CoSO_4 \cdot 7H_2O$ (Loba Chemie) and dissolving this mixture in ethylene glycol (EG) and deionized water (3:1 v/v ratio) under magnetic stirring. $H_2C_2O_4$ (3 mmol, Loba Chemie) was added to this solution slowly under continuous stirring for about 1 h at room temperature (RT). The final mixture was poured into an autoclave (Teflon-lined stainless steel) with a volume of 100 mL and hydrothermally treated at 140 °C for 24 h in an oven. The products were collected by centrifugation, washed with deionized water several times, and dried in air at 80 °C for 10 h. The $ZnCo_2O_4$ rods were prepared by mixing 2 mmol $CoSO_4 \cdot 7H_2O$ and 1 mmol $Zn(SO_4)_2 \cdot 7H_2O$ (Loba Chemie), and the Co_3O_4 mesoporous rods were synthesized by taking 3 mmol $CoSO_4 \cdot 7H_2O$, while the other steps were identical to those of the $NiCo_2O_4$ rods. Finally, the product precursors were heated at 450°C for 2 h with a heating rate of 5°C min^{-1} and cooled down slowly to RT.

3.4.7. Synthesis of 3D highly porous $Zn_{0.2}Ni_{0.8}Co_2O_4$ microspheres

3D highly porous spinel-type $Zn_{0.2}Ni_{0.8}Co_2O_4$ microspheres are synthesized by a hydrothermal method and a post-calcination approach as described in detail in reference [34]. The materials delivery by C. R. Mariappan, National Institute of Technology, Kurukshetra, India, is gratefully acknowledged.

To obtain the highly porous $Zn_{0.2}Ni_{0.8}Co_2O_4$ microspheres, initially, 0.8 mmol of $NiCl_2 \cdot 6H_2O$ (Merck), 0.2 mmol of $ZnCl_2 \cdot 6H_2O$ (Sigma-Aldrich) and 2 mmol of $CoCl_2 \cdot 6H_2O$ (Merck) were dissolved in 15 mL deionized water (DI). Then 1 mmol of urea and 15 mg of polyvinyl pyrrolidone (Alfa Aesar) were added to the solution under magnetic stirring at room temperature for 1 h. A homogeneous pink solution was obtained, which was then transferred to a Teflon-lined stainless-steel autoclave with a capacity of 100 ml. The autoclave was tightly sealed and maintained at 120 °C for 12 h. The obtained precursor was collected by centrifugation, washed with deionized water and ethanol several times, and dried in air at 80 °C for 10 h. Based on thermogravimetric results, the collected product precursors were finally annealed at 350 °C for 2 h in the air in order to obtain the mesoporous $Zn_{0.2}Ni_{0.8}Co_2O_4$ microspheres.

3.4.8. Reference materials

The diverse sources of the pure materials, used for reference measurements, are compiled in Table 3-2. The materials delivery by Arlimin Industries (Fort Collins, CO, USA) is gratefully acknowledged.

Table 3-2: Details of the raw materials and other chemicals used for reference measurements in the present work.

Raw material	Used in:	source	Mass fraction purity
Mn_2O_3	Figure 4-6, & Figure 4-7	*Sigma-Aldrich*	≥ 99.99 %
$Co(OH)_2$	Figure 4-9	*Alfa Aesar*	≥ 99.9 %
NiO	Figure 4-10	*Alfa Aesar*	≥ 99.0 %
$NiSO_4$	Figure 4-10	*Sigma-Aldrich*	≥ 99.99 %
PVDF	Figure 4-14	*Solef 6020, Solvay*	
Ni_2O_3	Figure 4-10	*Arlimin*	

4. Results and discussion

The central aim of this work is to develop procedures to reliably deconvolute XPS multiplets of primary first-row transition metals in Li-ion batteries by starting with simple model systems to exclude any intensity minimizing effects. One essential prerequisite for success here was the comprehensive study of the probable contamination during sample handling and transport from synthesis to analysis and moreover, method-induced degradation of the samples during the different measurements. The resulting tool of multiplet fitting templates from both above-mentioned studies subsequently was applied to pure powder system series, tuning systematically the stoichiometry of e.g. three first-row transitions metals (namely Mn, Co, and Ni), to develop a strategy to overcome problems arising from photo- and Auger electron peak overlaps as one main challenge. The achieved procedures were checked on realistic LIB electrode systems (pristine and test-cycled) to elaborate ways to overcome the dilution of the active material associated with the necessary carbon black and binder materials. Finally, the developed procedures were applied to different novel powder compounds planned for LIB electrodes in order to prove the general applicability of the new template approach which then opens up the possibility of reliably characterize transition metal compounds within the high diversity of materials development even beyond LIBs.

4.1. Method development and method-induced artifacts

In order to obtain a good level of repeatability and reproducibility for the data, it is necessary to audit the specific aspects and artifacts of applied characterization methods on the particular material under study. Therefore, the following chapters present the observation of method-induced effect for surface analysis of LIB cathodes.

4.1.1. Sample handling and transport

Since Li-ion battery materials are highly sensitive to ambient air and humidity, one essential prerequisite for any surface analytical characterization is the safe sample handling and transport under vacuum and conditioned Ar atmosphere, respectively. For this purpose, an Ar glovebox is directly connected to the load lock of the K-Alpha XPS instrument in surface analysis laboratory of IAM-ESS institute at KIT. This glovebox is the central unit to introduce samples into the established surface characterization infrastructure and to get access to all spectrometers (XPS, ToF-SIMS, SEM/EDS) via commercially available or self-constructed vacuum/Ar transport modules (VTM). One central issue prior to the sample characterization is to check the influence

of every single handling or transport step onto the sample surfaces with respect to possible contamination- or transport-induced degradation. In particular, the reaction with the glovebox atmosphere as well as with the residual gas of the spectrometers has to be checked out carefully to avoid artifacts.

For this purpose, a pure Li foil was used which, for the different tests, was sputter-etched with monoatomic Ar^+ within the analysis chamber of the glovebox K-Alpha XPS instrument. The results of all critical steps are compared in Figure 4-1 and Figure 4-2.

Directly after sputter etching, the very weak O 1s peak at 530.9 eV attributed to Li_2O is due to an unavoidable reaction of highly reactive metallic Li (Li 1s = 55.0 eV) with the residual gas and, therefore, proves the cleanliness of XPS instrument's analysis chamber (Figure 4-1 and Figure 4-2a). However, after a further 10 min. storage in the analysis chamber an increase of this component by a factor of 9 must be considered (Figure 4-1 and Figure 4-2b) which is due to the residual gas at a base pressure of 5×10^{-9} mbar. This finding is corroborated by the corresponding Li 1s peak at 56.3 eV.

During the exposure to the glovebox atmosphere for 8 min. a freshly etched Li surface almost completely reacts to LiOH (Li 1s = 57.6 eV, O 1s = 534.1 eV, 56.1 %), Li_2CO_3 (Li 1s = 57.6 eV, O 1s = 534.1 eV, 5.4 %), and Li_2O (Li 1s = 56.4 eV, O 1s = 531.1 eV, 29.7 %) species (Figure 4-1 and Figure 4-2c). In consequence, even the standard glovebox oxygen and water content, which is below 1 ppm, might affect reactive topmost surfaces. Moreover, the additionally detected weak fluorine content (Li 1s = 57.6 eV, F 1s = 687.8 eV, LiF 0.4 %) originates from other gloveboxes used for materials synthesis and/or battery cycling and here contaminated the spectrometer glovebox' atmosphere. However, this can be overcome by using fresh Li surfaces to getter the fluorine contamination.

In all cases of the above-mentioned experiment, the binding energy is referenced to metallic lithium and therefore a local charge-up of about 2.4 eV of topmost layer components must be considered. Such charging is often observable when using electrically conducting substrates together with insulating topmost layers [84]. However, due to the lack of adventitious carbon on several surfaces the standard energy referencing to the C 1s peak of hydrocarbons at 285.0 eV binding energy could not be applied properly. Taking charging into account, all binding energies of the detected Li compounds are in a good agreement with the literature [11], [85], [86].

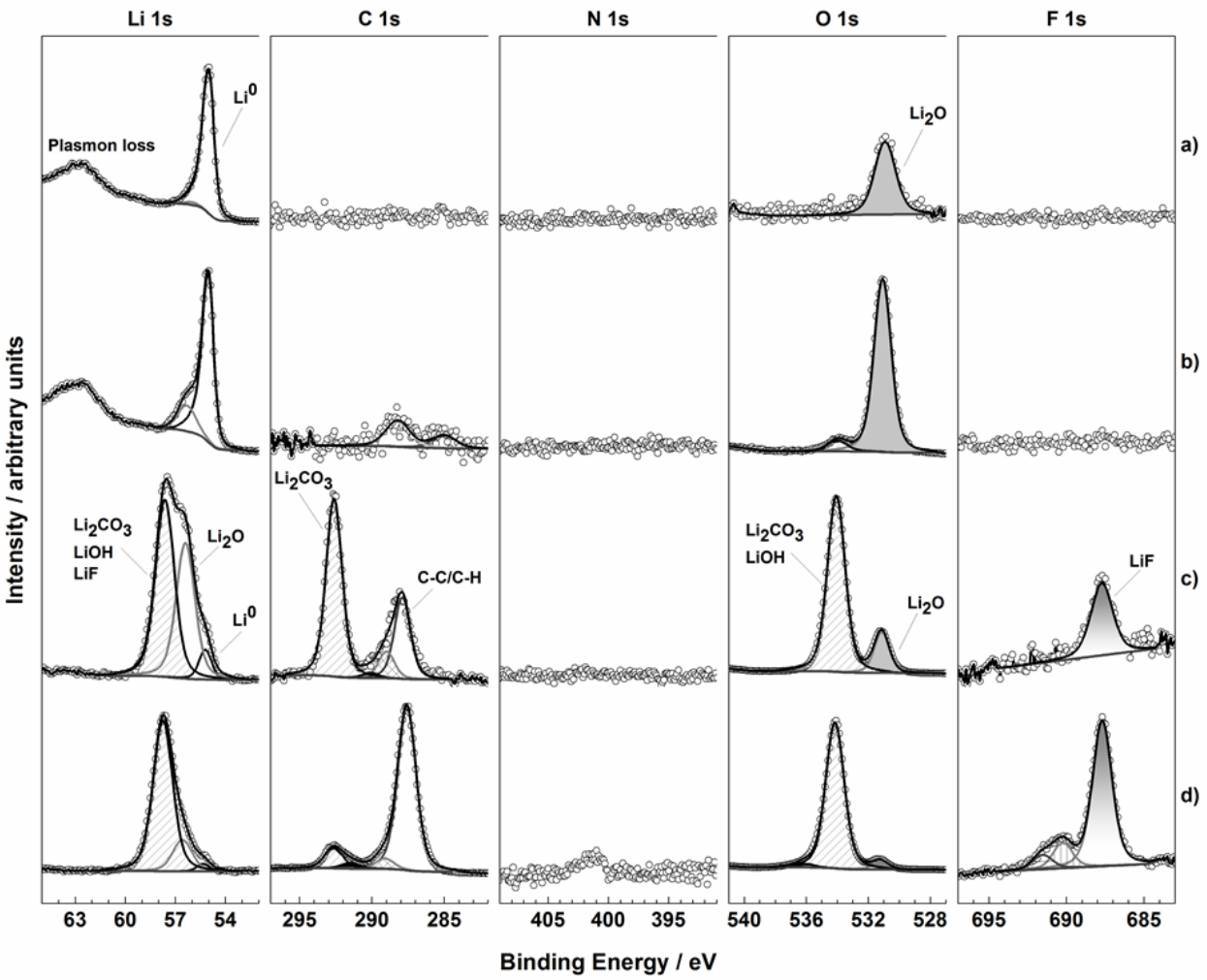

Figure 4-1: Li 1s, C 1s, N 1s, O 1s, and F 1s XP spectra of a pure Li foil after different steps during sample transport; a) directly after Ar^+ sputter etching in the analysis chamber, b) stored in the analysis chamber for 10 min. after Ar^+ sputter etching, c) stored for 10 min in the glovebox after Ar^+ sputter etching, d) transported via vacuum transport module after Ar^+ sputter etching and assembling in the glovebox.

In the case of VTM transfers, it is necessary to evacuate the module within the antechamber of the glovebox. This procedure leads to a dramatic increase of hydrocarbons on sample surfaces stemming from exhaust gases of standard oil-pumps used for such antechambers (Figure 4-1 and Figure 4-2d). In particular, when focusing on (volatile) solid electrolyte interphase (SEI) components this can easily lead to artifacts, e.g. when cooling samples to LN2 (Liquid Nitrogen) temperature. In consequence, the oil pump was exchanged with a dry working membrane pump to exclude such contaminations. However, contamination originating from other glovebox systems (materials development, battery testing, etc.) cannot completely be avoided. In many cases of inorganic materials, the Ar-cluster ion sources of the XPS and ToF-SIMS instruments can carefully

be utilized for sputter cleaning while preserving the chemical information of the surfaces of interest.

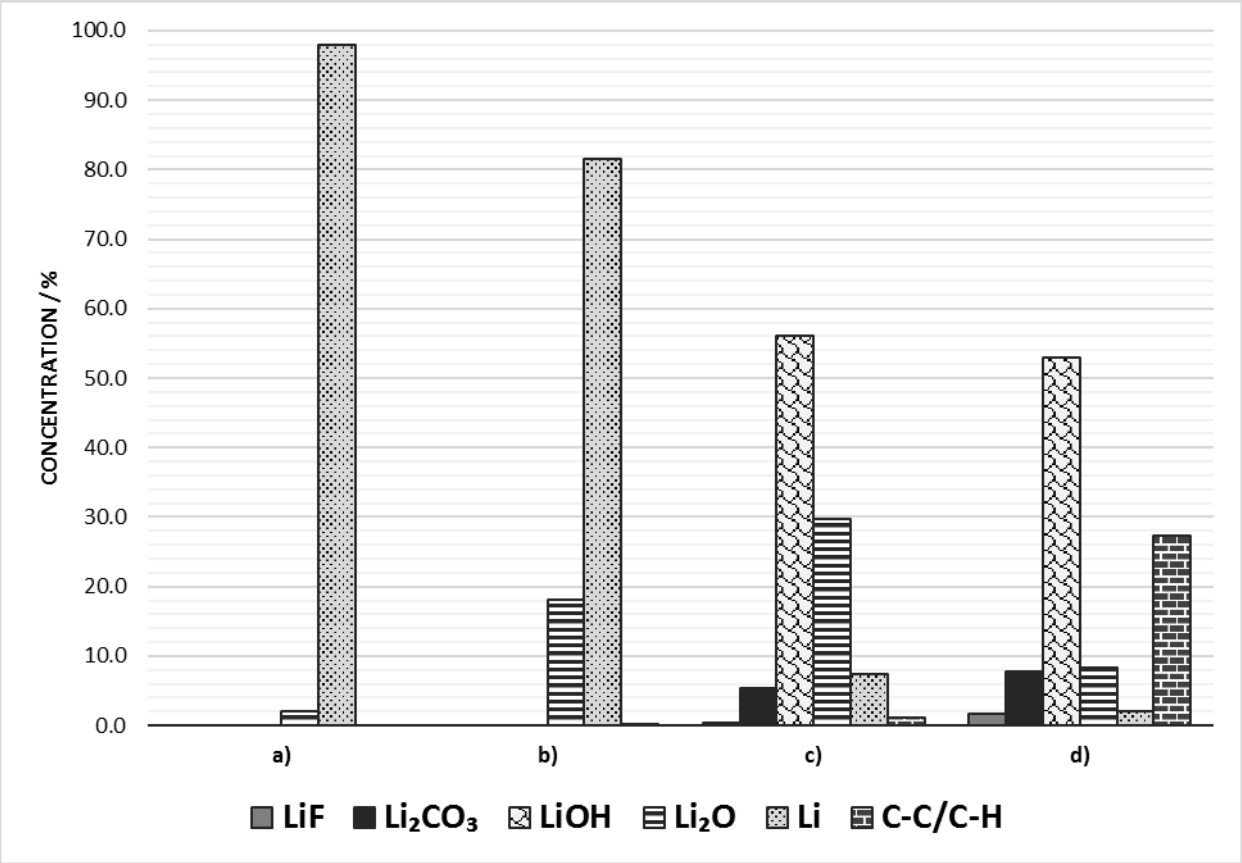

Figure 4-2: Comparison of the amount of topmost surface contamination on a pure Li foil after different steps during sample transport. (Quantification is based on XPS data.); a) directly after Ar^+ sputter etching in the analysis chamber, b) stored in the analysis chamber for 10 min. after Ar^+ sputter etching, c) stored for 10 min in the glovebox after Ar^+ sputter etching, d) transported via vacuum transport module after Ar^+ sputter etching and assembling in the glovebox.

4.1.2. Verification of X-ray sensitivity of 3d transition metal elements in LIB cathode materials

Pronounced X-ray-induced reduction (mainly based on X-rays and/or secondary electrons) of some 3d transition metal compounds, as one of the major radiation damage processes, is already known from different studies [87], [88]. Systematic data indicate that the degree of reduction in a given compound does not depend on temperature, vacuum pressure or X-ray flux, but is a function of only the integrated X-ray dose [89]. In other words, long X-ray exposure can reduce or degrade transition metal compounds. Since LIB cathodes mainly consist of transition metal compounds, the possible X-ray-induced damage should be inspected.

In order to examine X-ray damage on LIB cathode materials during a typical measurement time on K-Alpha XPS instrument, four different transition metals, namely Ni, Mn, Co, and Ti from diverse powder cathode compounds, iteratively exposed to X-rays. Each iteration giving rise to a spectrum in Figure 4-3 consists of 10 scans which takes 2 min to obtain. Between each iteration, there is a gap of 1 min, and 15 iterations are done in total. Therefore, the samples are exposed to X-ray for 45 min which is a typical time for one measurement. It is obvious from Figure 4-3 that the peak barycenter for the above-mentioned transition metals does not shift more than 0.4 eV during the described experimental condition. In conclusion, the LIB cathode materials are not generally affected by X-ray exposure. Otherwise the sensitive elements have to be measured at first on a fresh surface to minimize X-ray exposure (low dose), or the option of K-Alpha by utilizing short acquisition time at different points and collapsing the data, should be taken into consideration assuming, however, homogeneous and uniform elemental distribution across the total measured area.

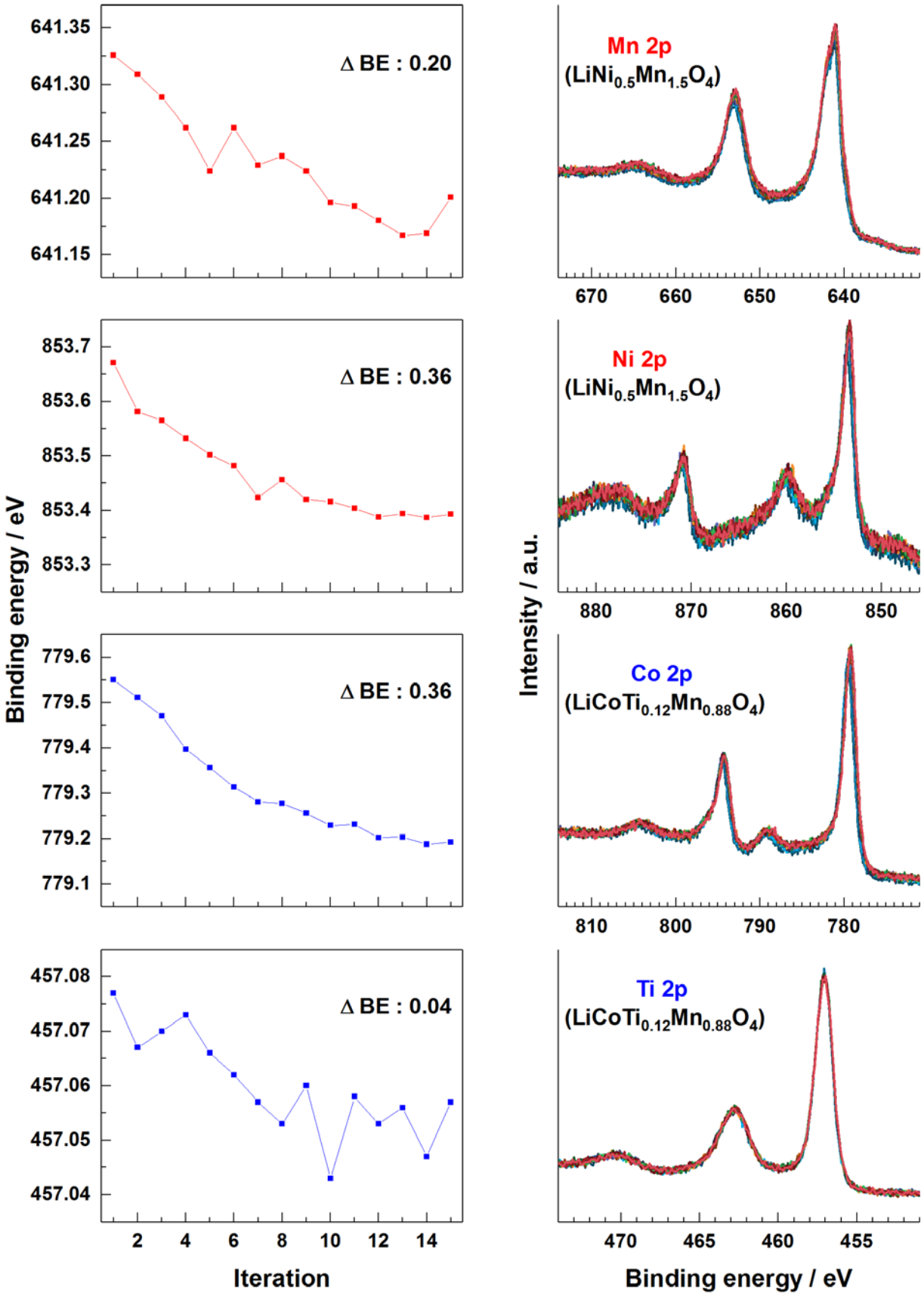

Figure 4-3: X-ray sensitivity of 3d transition metal elements in LIB cathode materials.

4.1.3. Verification of degradation by the spectrometer's neutralization system

The interaction of electrons with materials, and especially beam sensitive structures such as polymers, [90], [91] biological materials, [92] or semiconductors, [93] causes different types of radiation damage, e.g., atomic displacement, electrostatic charging, sputtering, radiolysis, and knock-on damage [94]. These mechanisms operate at different length scales; at sub-nanometer length scales, knock-on damage and atomic displacement can result in degradation of crystal lattices, while morphology changes due to heating, electrostatic charging, and sputtering are visible at nanometer and micrometer length scales [94].

Since LIB cathode materials are electrically insulating or semiconducting (low electronic conductivity), the emission of photoelectrons causes a positive charge to accumulate at the surface. As a result, the peaks in the spectrum shift to higher binding energies and will be broadened. For this reason, it is necessary to neutralize the surface charge-up by an external source. The used K-Alpha XP spectrometer utilizes a dual beam source (flood gun) to produce both the focused low energy electron beam and the large area ion-flux, to neutralize the charge on the surface. Again, it is important to analyze and understand the probable beam damage to facilitate the study of LIB cathodes materials with a minimum number of artifacts.

Therefore, the XP spectra of different elements of $LiCo_{0.12}Ti_{0.88}MnO_4$ powder with and without utilizing the flood gun were measured and are shown in Figure 4-4. From these spectra can easily be concluded that the neutralizing system has effectively compensated the charging, and no major damage to the sample peaks is detectable.

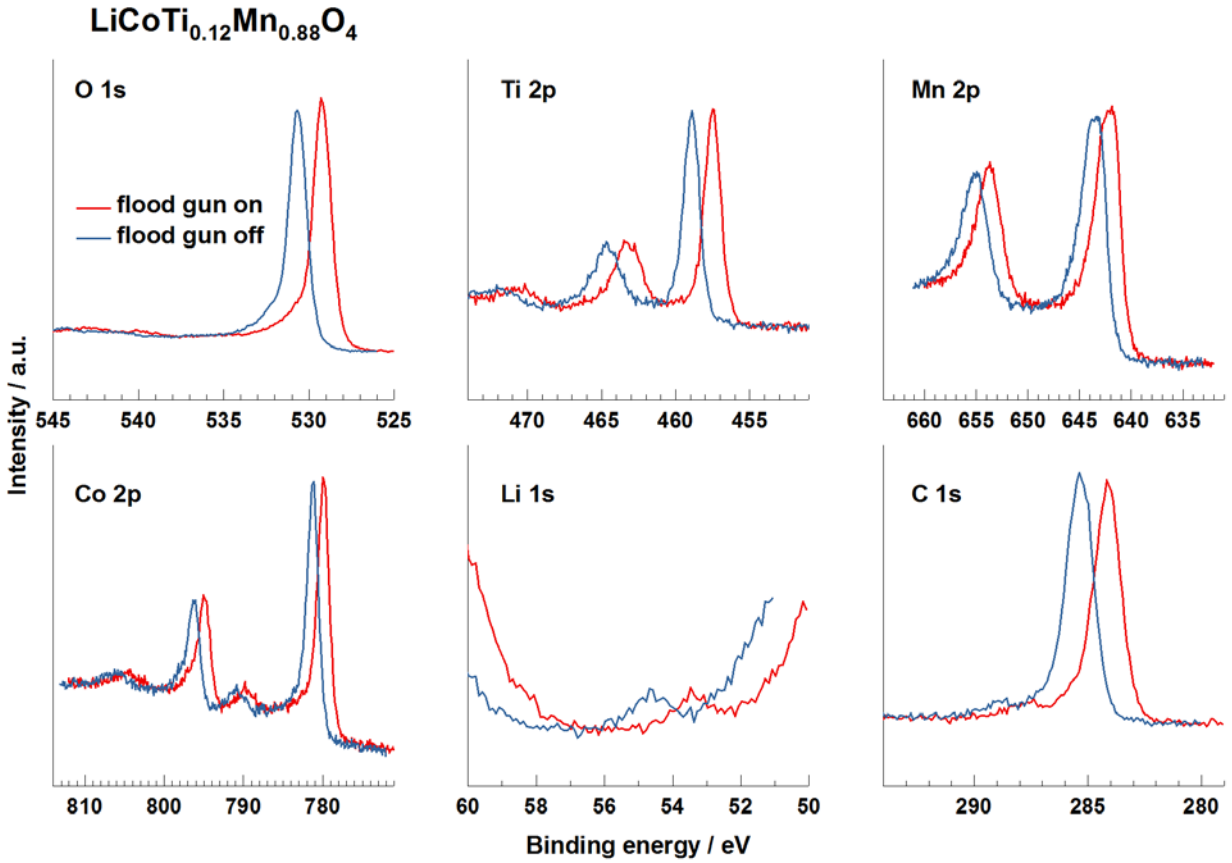

Figure 4-4: Samples' sensitivity to flood gun utilization.

4.1.4. Verification of probable degradation by Ar^+ ion bombardment during sputter depth profiling

It is well known that conventional monoatomic XPS sputter depth profiling induces large scale damages to the surface and subsequent changes in the surface chemistry of the analyte, due to the large projected range of the incident Ar^+ ions which is mostly greater than the sampling depth of XPS [95]. As expected, this is also the case for the LIB cathodes as it is obvious from Figure 4-5 for reduction of Co and Mn ions in $LiCo_{0.12}Ti_{0.88}MnO_4$ and ZrF_4 coated $LiNi_{0.5}Mn_{1.5}O_4$ powder materials. This, in consequence, limits the usage of sputter depth profiling regarding in-depth chemical state information for these materials. The changes in the chemical state of Mn and Co can easily be tracked by considering the broadening of Mn $2p_{3/2}$ peak, the shift of Mn 3p peak to lower binding energies, the increasing of the splitting of Mn 3s peak and arising of the Co^{2+} characteristic satellite at around 786 eV. More detailed information about the identification of different oxidation states of Mn and Co is provided in Chapter 4.2.1 and Chapter 4.2.2.

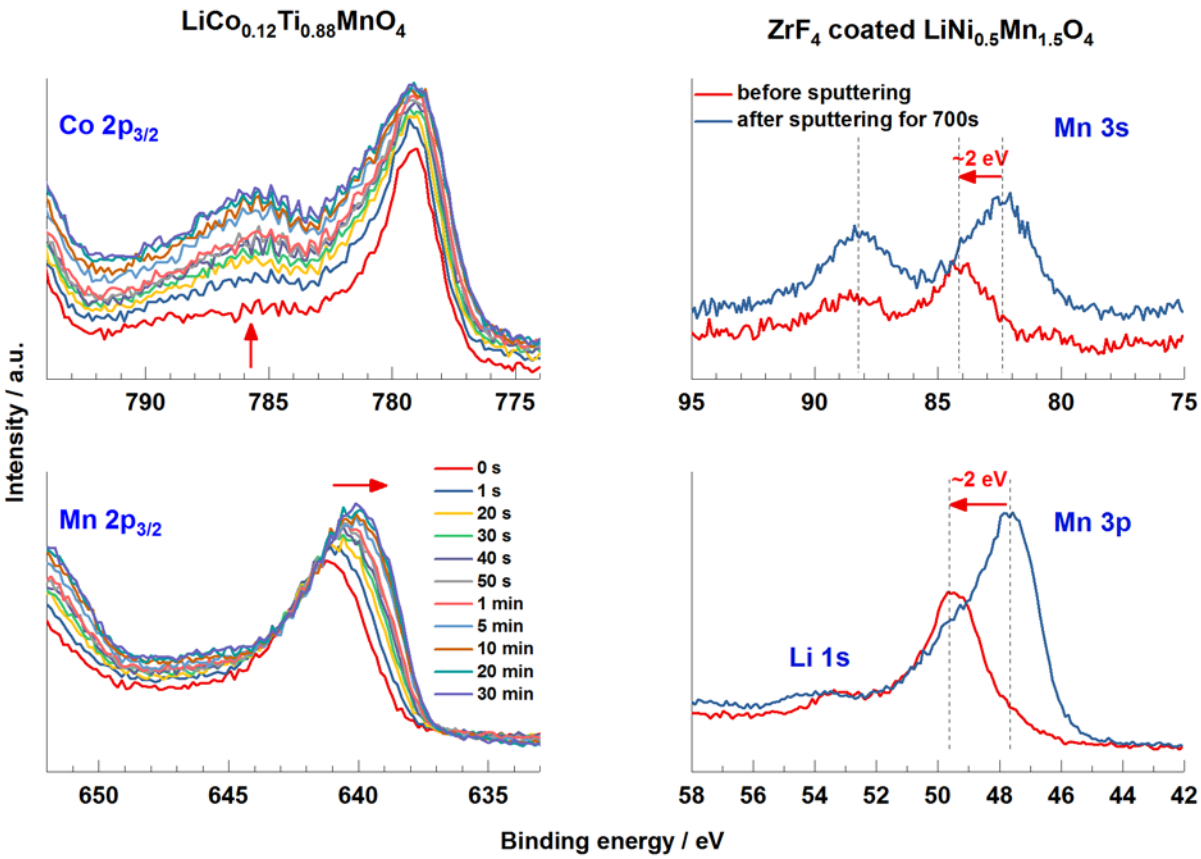

Figure 4-5: Sputter-induced damage to the $LiCo_{0.12}Ti_{0.88}MnO_4$ and ZrF_4 coated $LiNi_{0.5}Mn_{1.5}O_4$ powder cathode materials.

4.2. XPS characterization of reference materials

In order to achieve a precise XPS fitting procedure for first-row transition metal components in LIB materials, it is essential to adapt and develop peak templates for the different transition metal spectra considering the complex photoelectron multiplet splitting and shake-up satellites structures from pure single metal compounds like the respective oxides of Mn, Co, Ni or e.g. $LiMnO_2$ thin-films. The results of this attempt to summarize and reevaluate the characteristic features of frequently used first-row transition metal elements in LIB cathodes is presented in the following chapters.

4.2.1. XPS characterization of Mn compounds

The elucidation of different chemical states of Mn ions, solely based on Mn 2p spectra is hampered by the fact that the binding energy range for the 2p core-level electrons of Mn^{2+}, Mn^{3+}, and Mn^{4+} ions at the peak maxima is only about 1 eV. Moreover, these high spin Mn ions with unpaired

electrons in their 3d valence level show complex multiplet splitting in the final state of the photoionization, resulting in a broad envelope peak for 2p XP spectra, and therefore making it difficult to resolve the separate contributions [96]–[99]. These features can clearly be seen in the Mn 2p spectra of a Mn_2O_3 reference material in Figure 4-6 (top left). The envelope of this multiplet can be simplified only by using a single peak with a high energy tailing, similar to e.g. graphite [100]. In consequence, diminishing the Mn $2p_{3/2}$ multiplet to a symmetric Voigt peak shape to distinguish between different oxidation states might lead to misinterpretation. This is obvious when comparing non-fitting (using peak barycenter only), simplified fitting, and multiplet fitting approach for the Mn $2p_{3/2}$ peak area as shown in Figure 4-7. The depicted comparison unambiguously proves that non-fitting and simplified fitting indeed lead to fundamental failures with respect to oxidation states of first-row transition metals and, therefore, it is indispensable to consider the multiplet splitting during peak evaluation in any case.

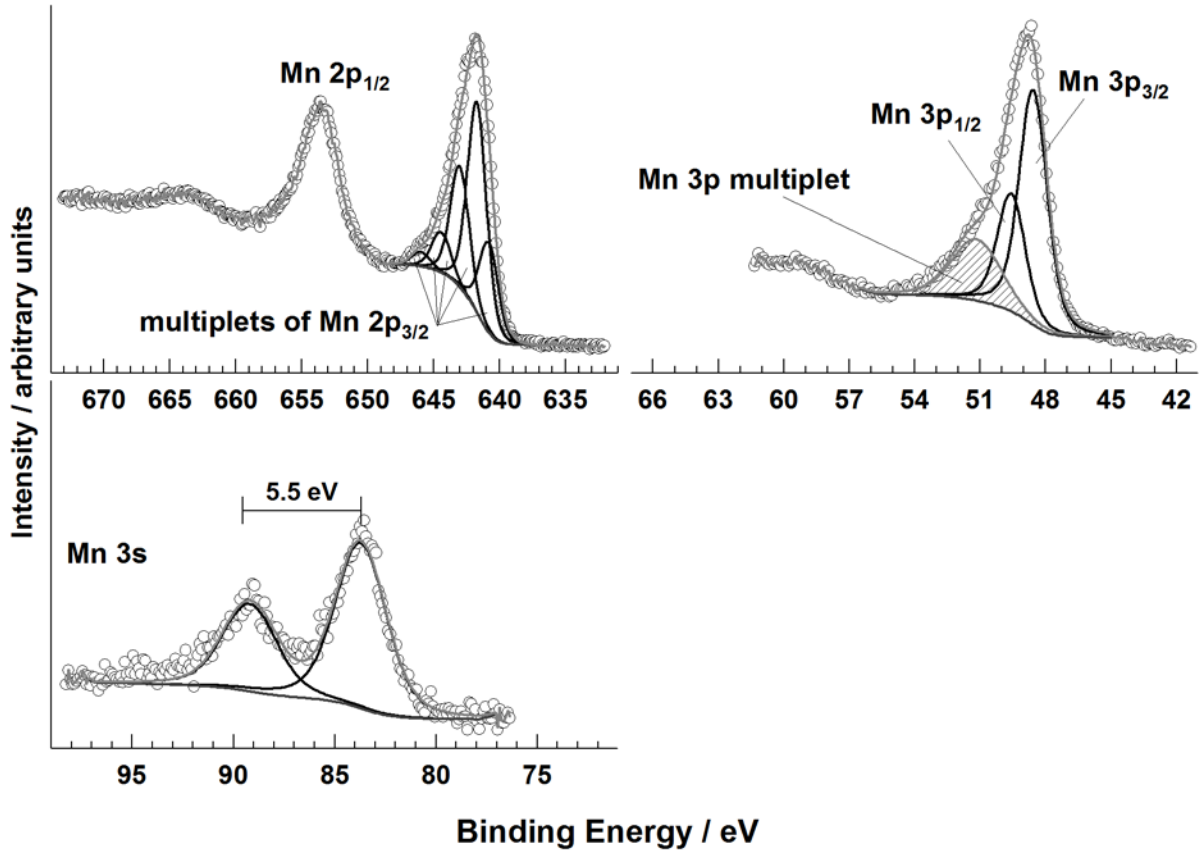

Figure 4-6: Mn 2p (top, left) Mn3p (top, right), and Mn 3s (bottom) XP spectra of pure Mn_2O_3 powder. The area of the shaded curve in Mn 3p spectrum is 20 % of the total fitted Mn 3p area.

For the determination of Mn oxidation states in battery materials, therefore, the peak fitting procedure of M. C. Biesinger et al. was adapted in a first attempt [15]. Their approach is primarily developed for pure oxides and hydroxides of Mn and is based on calculated multiplet structures of Mn^{2+}, Mn^{3+}, and Mn^{4+} free ions [16], [17], [101], revealing four to five adjacent multiplet lines for the Mn $2p_{3/2}$ photoelectron peak at 0.7-1.2 eV binding energy distances.

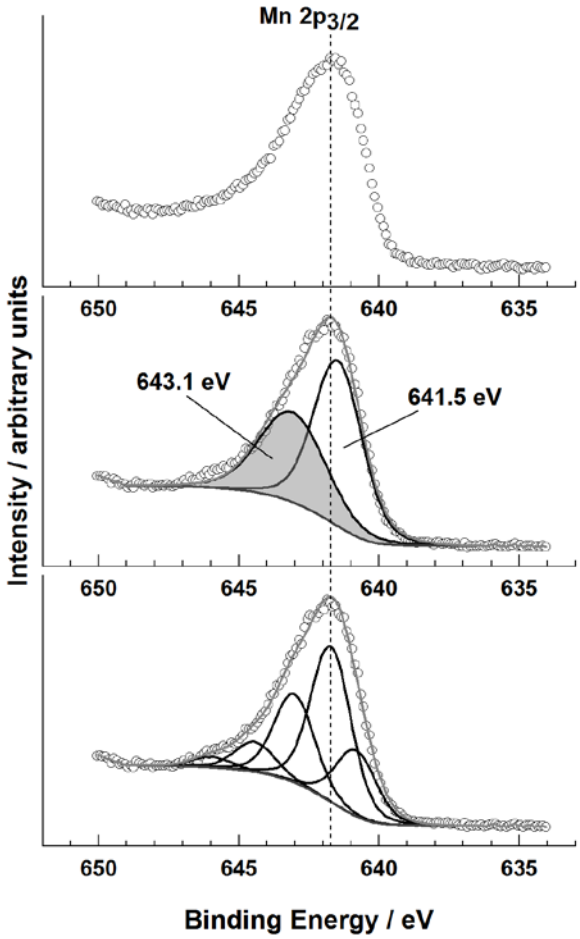

Figure 4-7: Different approaches to evaluate Mn $2p_{3/2}$ spectra: barycenter approach (top), simplified fitting using solely one symmetric Voigt peak to describe a single oxidation state (middle), and peak fitting considering the multiplet splitting (bottom).

Moreover, even considering solely the Mn $2p_{3/2}$ multiplet splitting, it is still challenging to impossible to distinguish between different chemical states. To achieve a reliable assignment, it is crucial to take additionally the Mn 3s splitting energy as well as the Mn 3p binding energy into account. In particular, the Mn 3s splitting energies of 4.5, 5.5, and 6.5 eV are respectively correlated to Mn^{4+}, Mn^{3+}, and Mn^{2+} ions and, therefore, the splitting of about 5.5 eV shown in

Figure 4-6 for pure Mn_2O_3 powder clearly corroborates the assignment to the Mn^{3+} state [23], [46], [102].

According to the literature, the Mn 3p spectrum can be deconvoluted into peaks originating from ^5P and a broad peak from ^7P as depicted in Figure 4-8 adapted from references [103], [104].

a) b)

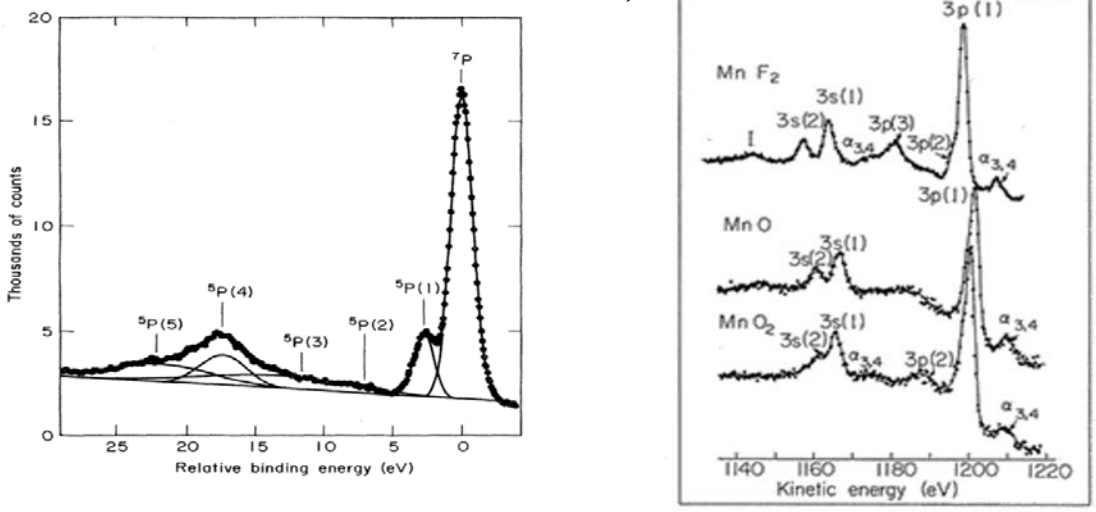

Figure 4-8: a) Fitted Mn 3p XP spectrum of MnF_4 adapted from reference [104], the very broad peaks probably represent several states. The Binding energy of the ^7P peak is 46.76 eV relative to the top of the valence band. the spectrum is acquired by monochromated AlKα X-rays; b) Mn 3p and Mn 3s spectra of MnF_4, MnO, and MnO_2 adapted from reference [103] acquired by MgKα X-rays.

This is also justified by the reference spectra of pure Mn_2O_3 powder depicted in Figure 4-6. Consistently, the binding energy of the Mn $3p_{3/2}$ peak of pure Mn_2O_3 powder at 48.4 eV can be attributed to Mn^{3+} ions, cf. Figure 4-6, as for spinel materials Mn 3p binding energies are to be found at around 47.5 eV for Mn^{2+}, 48.5 eV for Mn^{3+}, and 50.0 eV for Mn^{4+} [21], [105]. In conclusion so far, to reliably elucidate Mn oxidation states it is essential to take Mn 3s, Mn 2p, and Mn 3p into account.

4.2.2. XPS characterization of Co compounds

Similar to Mn 2p it is difficult to distinguish between Co^{2+} and Co^{3+} binding states based only on energy shifts of the respective multiplet components [15], [106], [107]. However, together with the corresponding distinct shake-up satellite structure, the respective oxidation states can be clearly identified.

Co ions in $LiCoO_2$ are agreed as a good reference for the Co^{3+} oxidation state. Although no satellite structure and no multiplet splitting is theoretically expected for Co^{3+} ions in octahedral coordination due to its t_{2g}^6 e_g^0 valence state [106], the fitting of Co 2p spectra from $LiCoO_2$ shown in Figure 4-9 reveal a weak peak at 790.1 eV which is mainly attributed to the Co^{3+} satellite in the literature [108]–[113]. Moreover, the main Co $2p_{3/2}$ peak can be fitted with three components at 780.1, 781.2, and 782.9 eV.

The unique footprint of Co^{2+} ions in Co 2p spectra is their characteristic satellite at around 5.5 eV higher than the main peak. This satellite appears in oxide as well as in hydroxide compounds as shown for the reference measurements of $Co(OH)_2$ in Figure 4-9 and for CoO oxide in many literatures such as the work of Biesinger et al. [15]. Essentially, however, for the peak fitting of mixed state of Co^{2+} and Co^{3+} chemical state, it must be considered that in contrast to the usual high binding energy shifts with increasing oxidation states, the binding energy of Co^{3+} core level photoelectrons is lower than that of Co^{2+}, which is mainly due to final relaxation energies and Madelung Potential terms [114]–[116].

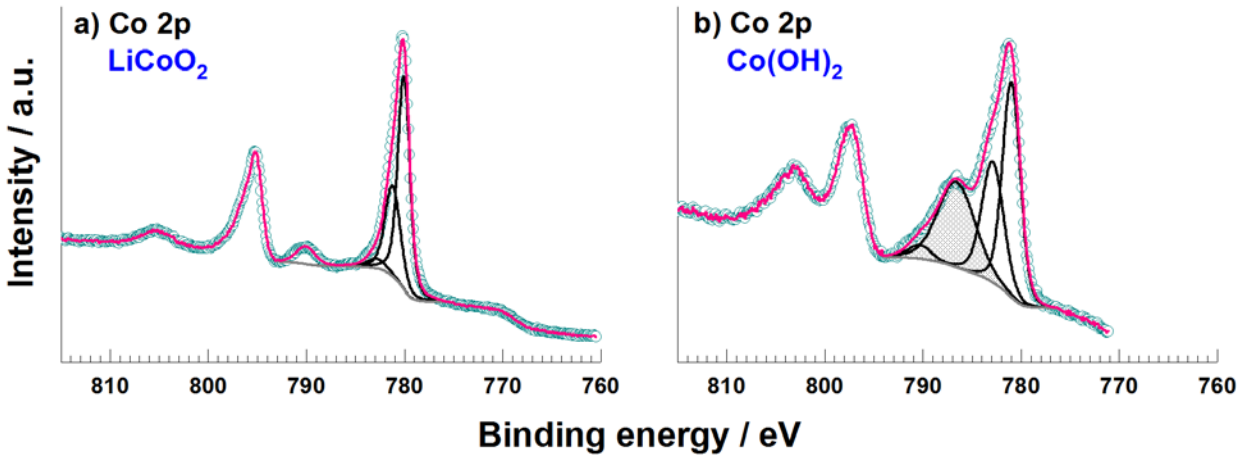

Figure 4-9: Co 2p spectra of $LiCoO_2$ and $Co(OH)_2$ revealing characteristic features of Co^{3+} and Co^{2+} oxidation states respectively.

4.2.3. XPS characterization of Ni compounds

The identification of Ni oxidation states again is very challenging due to a pronounced influence of its chemical binding partners on the respective Ni 2p binding energy. In particular, even the Ni 2p main peak barycenter for Ni^{2+} shifts from NiO at 854.7 eV to $Ni(OH)_2$ at 855.3 eV [117]. On the other hand, probable standard materials for Ni^{3+} like Ni_2O_3 and $LiNiO_2$ are not

well-characterized and, moreover, are found to be stabilized by the formation of defects or hydroxides leading to mixed Ni^{2+}/ Ni^{3+} oxidation states [118]. In consequence, Grosvenor et al. utilized γ-NiOOH as a reference material for Ni^{3+} to present a reasonable peak fitting procedure for the chemical states of Ni compounds which is based on the Gupta and Sen [16], [17] multiplet envelopes for Ni^{2+} and Ni^{3+} free ions [117]. Despite the above-stated problems for using NiO, $NiSO_4$, Ni_2O_3, and $LiNiO_2$ as reference material, the Ni 2p spectra of these materials are measured and depicted in Figure 4-10a to Figure 4-10d and Figure 4-11c respectively.

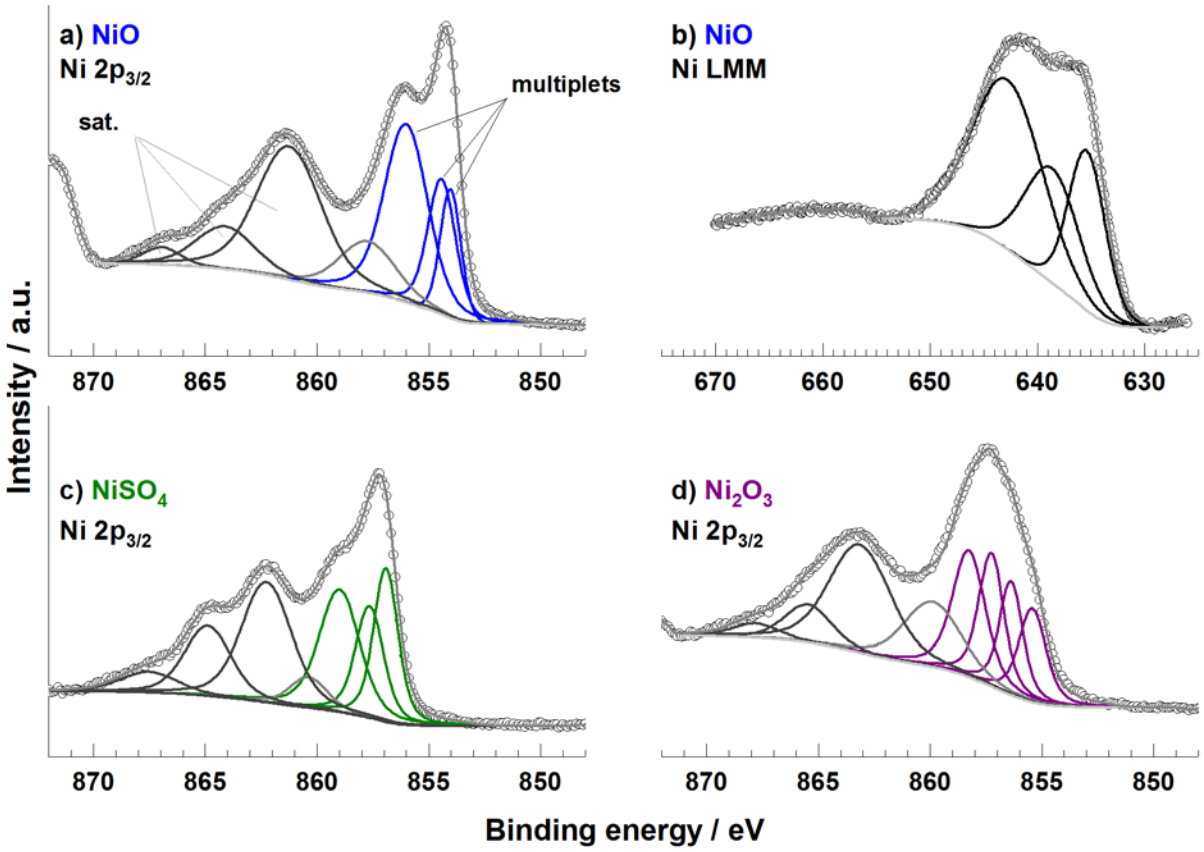

Figure 4-10: Ni $2p_{3/2}$ (a) and Ni LMM (b) XP spectra of pure NiO, the area ratio between Ni 2p / Ni LMM is 1.8. Ni $2p_{3/2}$ spectra of $NiSO_4$ (c) and Ni_2O_3 (d) for comparison of nominal Ni^{2+} and Ni^{3+} oxidation states, respectively. The peak fitting parameters of Ni LMM (b) spectra are given in Table 4-5.

Regarding XPS characterization of more complex materials such as Li-Ni-Mn-Co-O systems it has to be additionally considered that when using AlKα excitation the respective Ni LMM X-ray-induced Auger contribution at around 640 eV overlaps with Mn 2p spectra and Ni LMM at around 780 eV slightly overlaps with Co 2p spectrum which are depicted in Figure 4-10b and

Figure 4-11c, respectively. The interference of Co LMM with Ni 2p spectra here can be neglected because of more than 10 eV difference of peak position, as it is clearly shown in Figure 4-11d. The interference of Mn LMM spectra with Ni 2p spectra, however, depends mainly on their relative concentration. For example, the nominal ratio of Mn/Ni = 3 in spinel $LiNi_{0.5}Mn_{1.5}O_4$ demands considering Mn LMM peak in fitting of Ni spectra in Figure 4-49 whereas the Mn LMM Auger from $LiNi_{0.8-y}Mn_yCo_{0.2}O_2$ ($0 \leq y \leq 0.4$) compound series is weak enough (even for the highest ratio of Mn/Ni = 1) that does not need to be included in Ni 2p peak fitting cf. Figure 4-22.

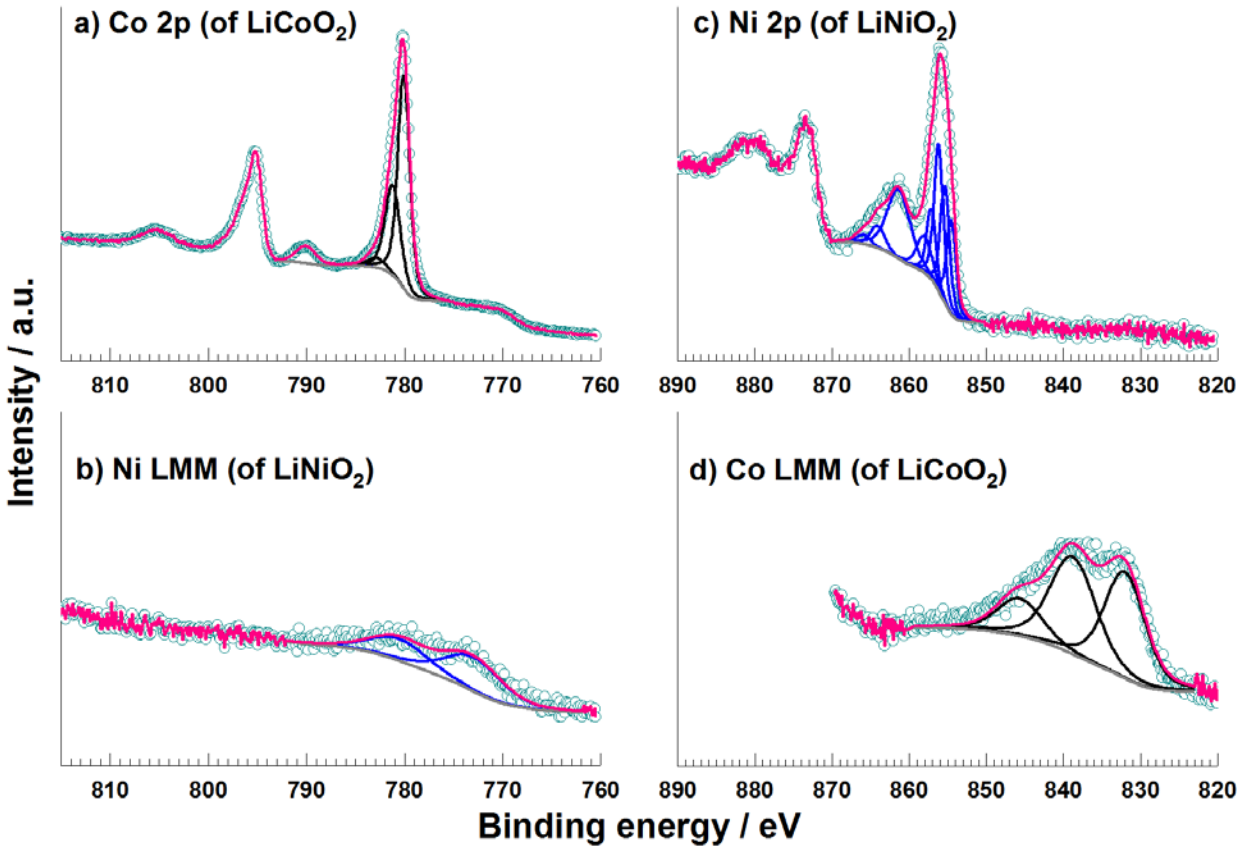

Figure 4-11: a) Co 2p spectra of $LiCoO_2$ powder material, the weak contribution of the Auger peaks Co $L_3M_{23}M_{45}$ (^1P) at 777 eV and Co $L_3M_{23}M_{45}$ (^3P) at 771 eV do not influence the Co 2p multiplet and therefore were not included in the fitting approaches; b) Very weak Ni $L_3M_{23}M_{23}$ contributions to the Co 2p energy range at 772.0 eV and 779.6 eV stemming from $LiNiO_2$ powder material were not included into the fitting approach; c) Ni 2p spectra of $LiNiO_2$; d) Co $L_3M_{23}M_{23}$ Auger peak contributions to the Ni 2p energy range at 831 eV and 838 eV stemming from $LiCoO_2$; The peak parameters for $LiCoO_2$ and $LiNiO_2$ are compiled in Table 4-4 and Table 4-6, respectively.

4.2.4. XPS characterization of Li compounds

A central issue beside the very poor photoionization cross section for Li 1s is the fact that at least all LIB materials comprising first-row transition metals, more or less hamper the quantitative chemical state evaluation of Li due to the strong overlaps of the respective 3p peaks with the Li 1s energy range, as illustrated in Figure 4-12 as well as already shown for Zr, Pt and Au containing samples [51], [103], [119].

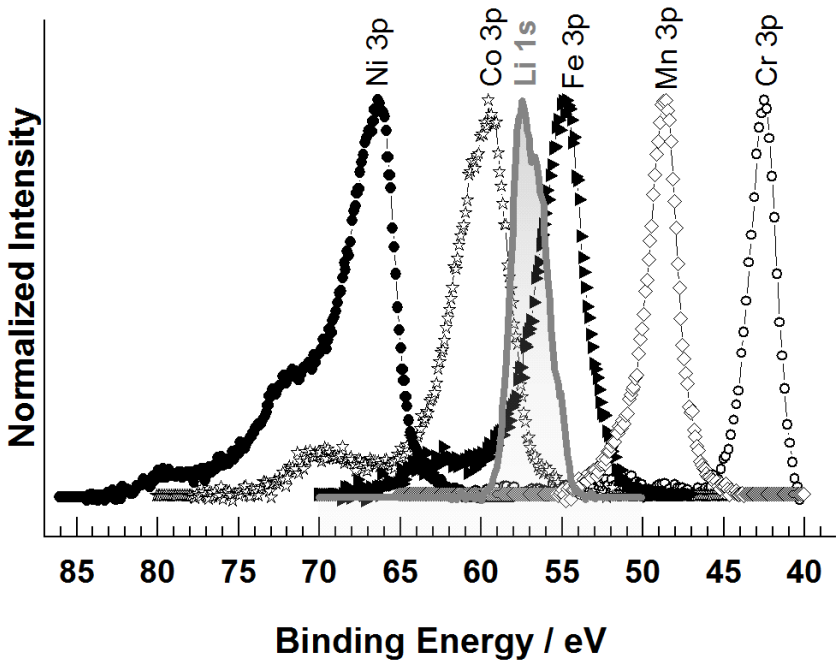

Figure 4-12: XP 3p spectra of first-row transition metals contributing to the Li 1s binding energy range. For a better visualization, all spectra are normalized to maximum intensity. Due to the poor photoionization cross-section coefficient, Li 1s peaks even at high Li concentration will be strongly overlapped by the 3p peak shapes of the respective transition metals.

In consequence, the advantage of Mn 3p peaks to corroborate the Mn 2p results (as described in Chapter 4.2.1) turns into a disadvantage regarding the binding energy evaluation and quantification of Li due to the strong overlap of Li 1s with the Mn 3p illustrated exemplarily in Figure 4-13 for Li-Mn-O thin-film. To overcome this interference, the promising approach is to apply a Mn 3p peak template of pure Mn_2O_3 powder reference material (see Figure 4-6) to the Li 1s region of e.g. Li-Mn-O thin-films in Figure 4-13, considering the overall manganese contribution and a weak

Li 1s peak with an FWHM of 1.3 eV was added to fill-up the experimental multiplet resulting in a binding energy of 54.5 eV assigned to intercalated Li in Li-Mn-O systems [120].

4.2.5. XPS characterization of Li-Mn-O thin-films

In order to prove the applicability to more complex systems, the fitting procedures for Mn and Li elements described in Chapter 4.2.1 and Chapter 4.2.4 were applied to spectra of a pure Li-Mn-O r.f. magnetron sputter-deposited thin-film. The spectra were deconvoluted using multiplets comprising only the Mn^{3+} state as shown in Figure 4-13.

To increase intensities, the as-received film was Ar-cluster ion etched prior to the measurement to remove contamination, as described in Chapter 2.1.7. The corresponding binding energies, full widths at half maximum (FWHM), and peak areas together with the atomic concentrations of all elements are compiled in Table 4-1.

In particular, the Mn 3s splitting of about 5.5 eV shown in Figure 4-13b clearly corroborates the Mn^{3+} state and, consistently, the binding energy of the Mn $3p_{3/2}$ peak at 48.4 eV can be attributed doubtlessly to Mn^{3+} ions, cf. Figure 4-13c and Table 4-1. Similarly the strong overlap of Li 1s and Mn 3p peaks in Figure 4-13, can be solved by using the Mn 3p peak template of pure Mn_2O_3 powder reference material to fit the spectra alongside the guidelines described in Chapter 4.2.4. Together with a single Li 1s peak with an FWHM of 1.3 eV at 54.5 eV binding energy attributed to intercalated Li in Li-Mn-O systems the complete multiplet can doubtlessly be assigned [120].

Moreover, the corresponding major O 1s peak at 530.1 eV binding energy in Figure 4-13d justifies that these findings are in a good agreement with the literature [120], [121]. The weak components at higher binding energies are assigned to residual contamination.

Nevertheless, it is obvious that an increased uncertainty has to be assumed for quantification underpinned by the deviation from the expected $LiMnO_2$ stoichiometry, cf. Table 4-1. However, this will remain a problem for at least all LIB materials comprising first-row transition metals due to the more or less strong overlaps of the 3p peaks within the Li 1s energy range, as described in Chapter 4.2.4.

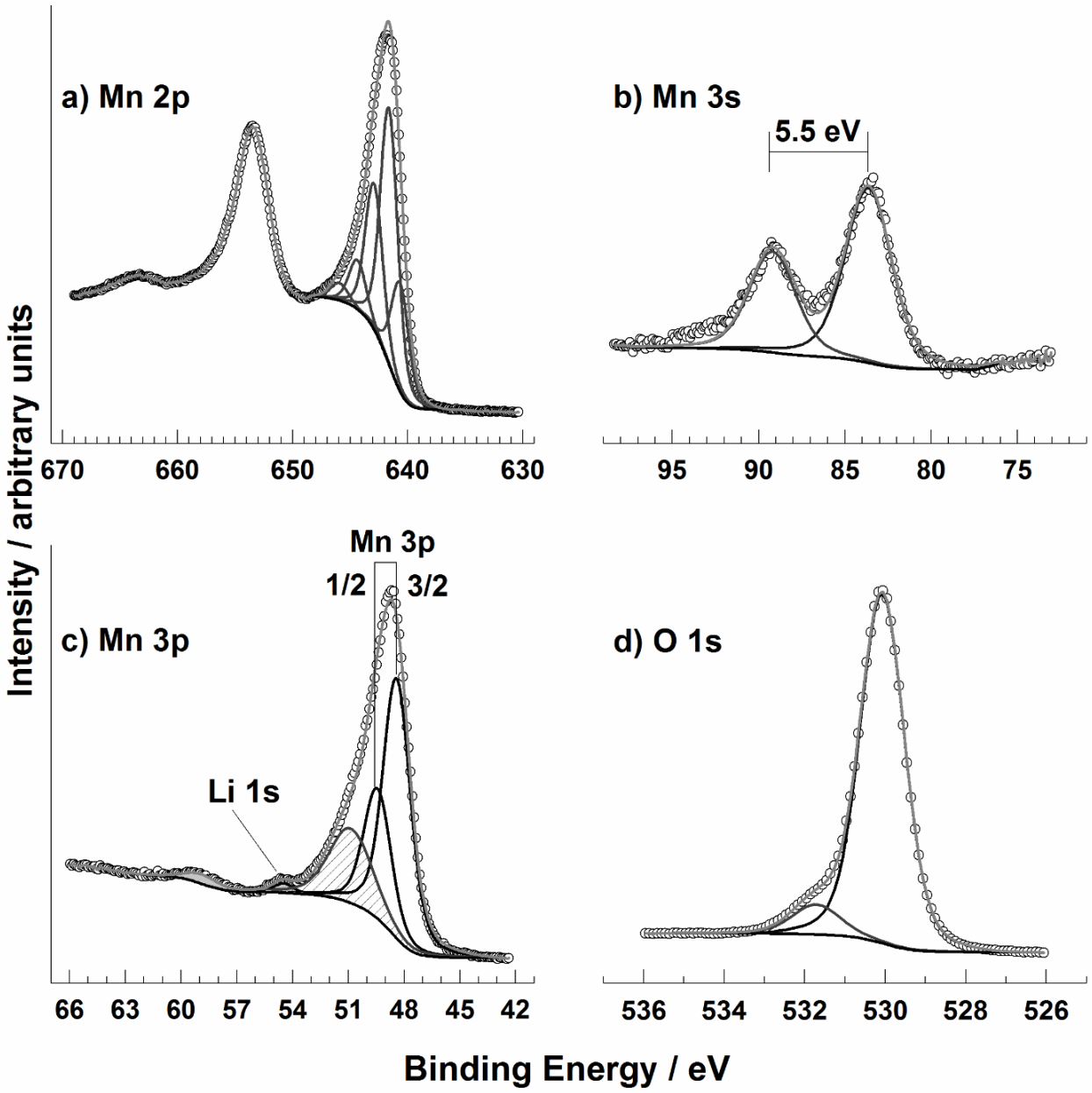

Figure 4-13: XP spectra of an r.f. magnetron sputter deposited Li-Mn-O thin-film. In particular, the multiplet fits for Mn $2p_{3/2}$ (a), Mn 3s (b), and Mn 3p (c), as well as the corresponding O 1s peak (d), are depicted. The corresponding peak fitting parameters are compiled in Table 4-1.

Table 4-1: XPS peak fitting parameters for the characterization from an r.f. magnetron sputter deposited Li-Mn-O thin-film after Ar-cluster ion etching. The binding energy results are in a good agreement with literature values [15], [46].

	Photoelectron	Mn $2p_{3/2}$ (Mn^{3+})	Mn 3p	Li 1s	O 1s	C 1s
Peak 1	BE / eV	640.7	48.4	54.5	530.1	285.0
	FWHM / eV	1.8	1.8	1.3	1.3	2.0
	%	18.9	50.2			
Peak 2	BE / eV	641.6	49.4		531.7	289.6
	FWHM / eV	1.8	1.8		1.4	2.0
	%	44.3	25.1			
Δ Peak / eV		1.0	1.5			
Peak 3	BE / eV	642.9	50.9			
	FWHM / eV	1.8	2.8			
	%	25.3	22.6			
Δ Peak / eV		1.3	8.0			
Peak 4	BE / eV	644.4	58.9			
	FWHM / eV	1.8	2.1			
	%	8.5	2.1			
Δ Peak / eV		1.5				
Peak 5	BE / eV	646.0				
	FWHM / eV	1.8				
	%	3.0				
Δ Peak / eV		1.6				
Atomic concentration / %	Li-Mn-O thin-film	31.0		9.3	53.7	
	Surface contamination				5.2	0.9

4.2.6. XPS characterization of pure PVDF

A final important reference material, polyvinylidene difluoride (PVDF) was comprehensively characterized by XPS (cf. Figure 4-14), as it is commonly the main binder material used to produce electrodes of LIBs. In particular, the strong F KLL Auger peaks stemming from the fluorine of PVDF and shown in Figure 4-14d will strongly interfere with main photoelectron peaks of transition metals, specifically with Ni 2p spectra. This has to be taken into account by an additional template when evaluating the respective 2p spectra of LIB electrodes.

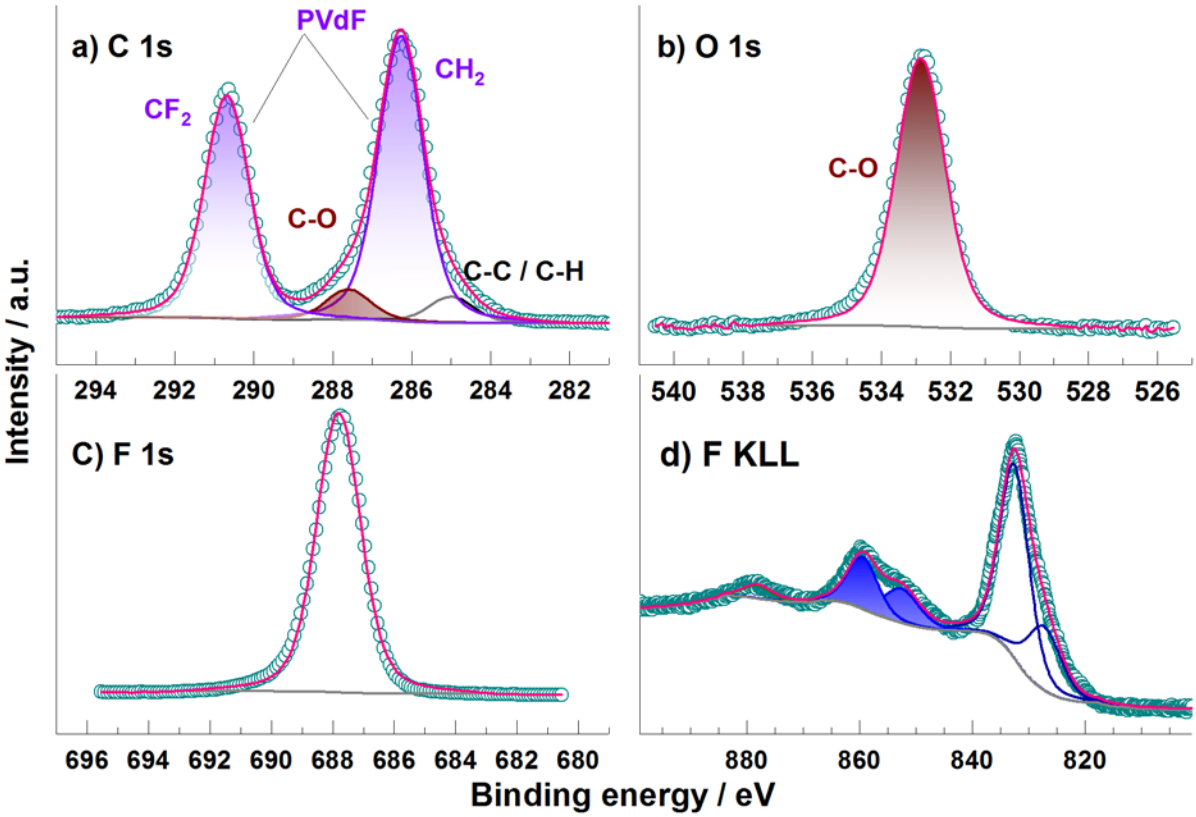

Figure 4-14: C 1s (a), O 1s (b), F 1s (c), and F KLL (d) spectra of PVDF, the blue shaded F KLL peaks in d) cross-talk with Ni 2p peaks.

4.3. XPS characterization of Li-Ni-Mn-Co-O cathode materials

After having comprehensively XPS characterized the necessary reference materials the next step towards application to LIB electrodes active materials is to transfer the findings to pure r.f. magnetron sputter deposited Li-Ni-Mn-Co-O thin-films. This intermediate step is necessary to test and further develop the templates achieved in Chapter 4.2 on model NMC systems representing compounds in the focus of LIB's main interest, while still separating from topography influences. Subsequently, these findings will be applied to pure powder NMC systems to integrate morphology effects but still avoiding intensity problems by diluting with carbon black and binder materials.

4.3.1. Thin-films of the Li-Ni-Mn-Co-O system

The additional complexity arising from peak overlaps due to the presence of three transition metals in the recently developed r.f. magnetron sputtered Li-Ni-Mn-Co-O thin-films, designed for

all-solid-state Li-ion batteries, [31] is comprehensively discussed in this chapter. The respective material synthesis is given in Chapter 3.4.1.

In a first attempt, the knowledge from previous chapters accordingly was transferred to these even more complex Li-Ni-Mn-Co-O thin-films. However, the main challenges arising are due to the additional overlaps between photoelectron and AlKα X-ray-induced Auger peaks of the different transition metals. In particular, the Mn 2p region shown in Figure 4-15 is strongly overlapped by intense Ni LMM Auger peaks. To reliably estimate the overlapping Ni LMM Auger contributions, a Ni LMM template from pure NiO standards was applied using the separated line at 637.3 eV to define the relative intensities, cf. Figure 4-10b and Table 4-3. Herewith the remaining Mn 2p peak sufficiently can be fitted with combined MnO_2 and Mn_2O_3 multiplets, justified by the splitting energy of the Mn 3s peak of about 4.8 eV shown in Figure 4-15. The subsequent quantification reveals a mixed oxidation state of Mn^{4+} and Mn^{3+} with a concentration ratio of about 1.6:1. Note that the experimental alternative, to shift the Auger peaks by changing the X-ray source to MgKα excitation, is not provided by the K-Alpha instrument. Nevertheless, the template approach allows to doubtlessly separate the Mn 2p photoelectron peaks from the cross-talking Ni LMM Auger contribution.

The Co 2p spectrum of the Li-Ni-Mn-Co-O thin-film surface is shown in Figure 4-15 and the respective peak fitting parameters are compiled in Table 4-3. The peak at 779.2 eV is attributed to the main peak of the Co^{3+} multiplet and the one at 779.9 eV to Co^{2+}, cf. Table 4-3, considering that in cobalt oxides the binding energy of Co^{3+} core level photoelectrons is lower than that of Co^{2+}, cf. Chapter 4.2.2 [114]–[116]. The peak at 781.6 eV is attributed to a second component of the Co^{2+} multiplet, and the characteristic Co^{2+} satellite at 785.9 eV supports this assignment [106], [107]. The additional weak peak at 789.3 eV cannot be attributed unambiguously, however, it originates most probably from Co^{3+} as reported for $LiCoO_2$, [113], [118] and shown in Figure 4-9. In conclusion, also for the Co 2p spectra, it is essential to consequently utilize multiplet fitting to achieve reliable results, in particular with respect to the unusual binding energies for Co^{2+} and Co^{3+} ions.

In accordance to the characterization of Ni ions described in Chapter 4.2.3, the Grosvenor et al. [117] method to characterize Ni ions was applied to the spectra of the novel Li-Ni-Mn-Co-O thin-film system and the results are depicted in Figure 4-15. The respective fitting parameters are compiled in Table 4-3. In particular, pure Ni^{2+} and Ni^{3+} multiplet templates were applied to the Ni spectrum of the Li-Ni-Mn-Co-O system to check their potential coexistence. According to the Gupta et al. findings and corroborated by respective reference data of pure NiO shown in Figure

4-10, the presence of the only Ni^{2+} has finally be concluded, based on the multiplet components at 853.6 and 854.4 eV and at least the too low intensity of the component at around 855.3 eV which is not expected for Ni^{3+} [117]. Obviously also for Ni, it is inevitable to apply multiplet fitting to distinguish between the different chemical states of Ni.

As an interim conclusion, the suggested multiplet fitting approach using templates for the different transition metal XPS peaks in LIB materials comprising photoelectron as well as Auger electron peaks and additional loss features allows the chemical characterization of complex stoichiometries even in a quantitative manner. This is justified by the comparison of XPS quantification results on the current Li-Ni-Mn-Co-O thin-film system and the recently presented corresponding ICP-OES (inductively coupled plasma optical emission spectroscopy) data in Table 4-2 [122]. As already mentioned above, here it has to be considered, that XPS quantification regarding LIB materials is primarily hampered by the extremely low cross-section for the Li 1s photoionization, [51] leading to an increased uncertainty in lithium quantification. Moreover, the results originating from a surface sensitive method are here compared with those stemming from a bulk method. Taking this into account, the results are in a very good agreement. Finally, a mixed oxidation state of Mn^{4+} and Mn^{3+} with a 1.6:1 ratio could be proved for Mn in Li-Ni-Mn-Co-O thin-film system, and similarly a Co^{2+} to Co^{3+} ratio of 5.5:1 whereas Ni only appears in the Ni^{2+} state.

Table 4-2: Chemical composition at the surface of the Li-Ni-Mn-Co-O system after Ar-cluster ion sputter cleaning compared to respective ICP-OES data [122].

	Li	Ni	Mn	Co	O
XPS atomic concentration (%)	23.2 (±2.0)	8.0 (±1.0)	5.1 (±0.5)	12.0 (±1.0)	51.6 (±3.0)
ICP-OES atomic concentration (%)	27.1 (±1.4)	8.9 (±0.5)	4.6 (±0.3)	7.8 (±0.4)	51.6 (±2.7)

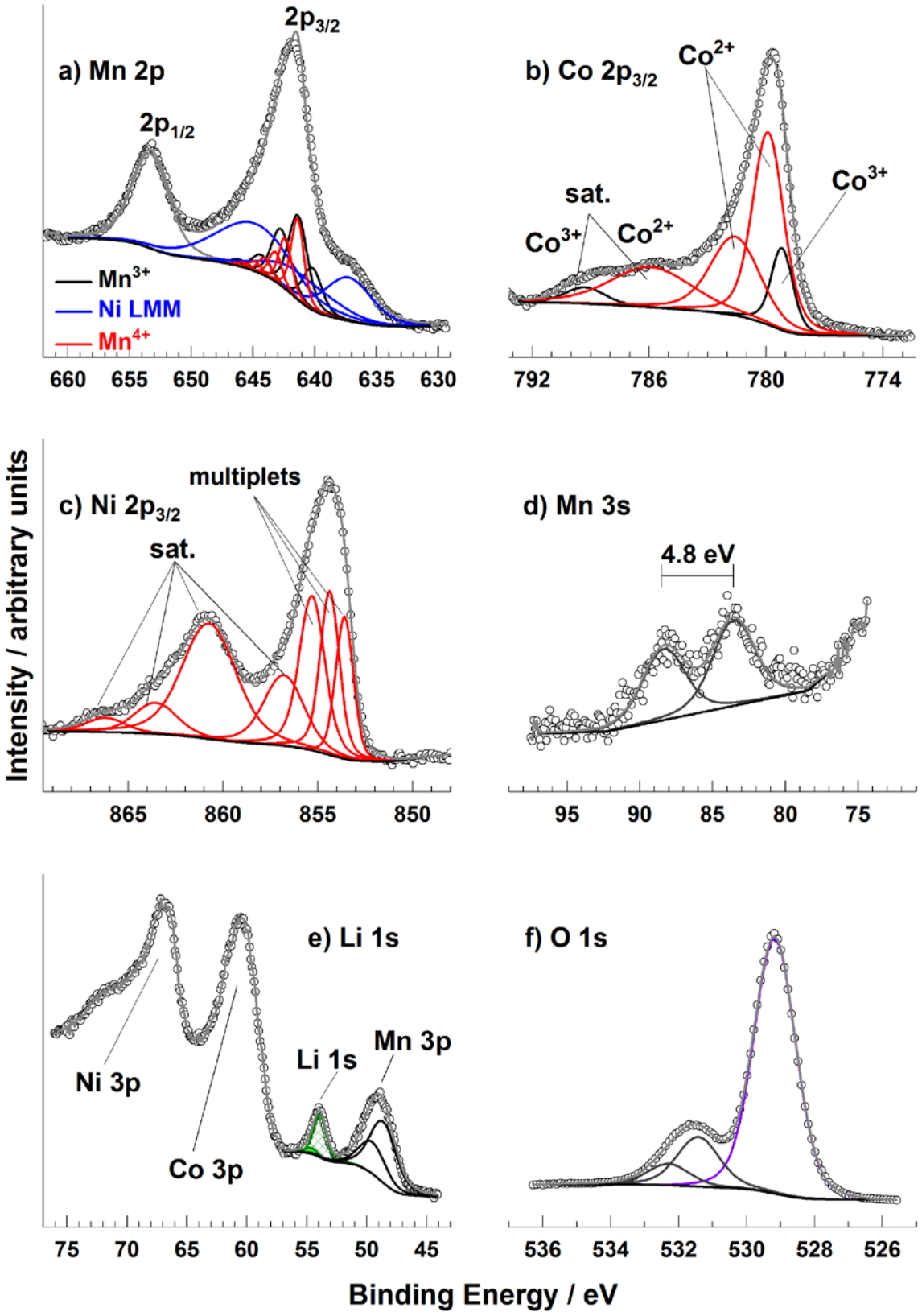

Figure 4-15: XP spectra of an r.f. magnetron sputter deposited Li-Ni-Mn-Co-O thin-film. In particular, the multiplet fits for M $2p_{3/2}$ component of the spin-orbit coupling for Mn (a), Co (b), and Ni (c) are shown as well as the Mn 3s (d), Li 1s (e), and O 1s (f) peaks. The corresponding peak fitting parameters are compiled in Table 4-3.

Table 4-3: XPS peak fitting parameters for the characterization from an r.f. magnetron sputter deposited Li-Ni-Mn-Co-O thin-film after Ar-cluster ion etching. The binding energy results are in a good agreement with literature values [15], [46].

	Photo-/Auger-electron	Mn $2p_{3/2}$ (Mn^{3+})	Mn $2p_{3/2}$ (Mn^{4+})	Ni LMM	Co $2p_{3/2}$ (Co^{3+})	Co $2p_{3/2}$ (Co^{2+})	Ni $2p_{3/2}$
Peak 1	BE / eV	640.2	641.4	637.3	779.2		853.6
	FWHM / eV	1.8	1.2	4.5	1.3		1.1
	%	20.1	41.8	27	72.9		11.6
Peak 2	BE / eV	641.4	642.4	641		779.9	854.4
	FWHM / eV	1.8	1.2	6.3		1.9	1.2
	%	40.3	26.5	24		45.5	15.3
	Δ Peak BE / eV	1.2	1	2.4		0.7	0.8
Peak 3	BE / eV	642.7	643.2	644.8		781.6	855.3
	FWHM / eV	1.8	1.2	7.6		3	1.6
	%	27.1	15.3	49		29.4	19.3
	Δ Peak BE / eV	1.4	0.8	4.7		1.7	0.9
Peak 4	BE / eV	644.3	644			785.9	856.8
	FWHM / eV	1.8	1.2			5	2.5
	%	9.2	9			25.1	13.8
	Δ Peak BE / eV	1.6	0.8			4.3	1.5
Peak 5	BE / eV	646.1	644.8		789.3		860.8
	FWHM / eV	1.8	1.2		2.4		3.4
	%	3.3	4.8		27.1		30.5
	Δ Peak BE / eV	1.7	0.8		3.4		4
Peak 6	BE / eV		645.8				863.6
	FWHM / eV		1.2				2.7
	%		2.6				6.5
	Δ Peak BE / eV		0.9				2.8
Peak 7	BE / eV						866.2
	FWHM / eV						2.5
	%						2.9
	Δ Peak BE / eV						2.6

4.3.2. Pure powders of the $LiNi_{0.8-y}Mn_yCo_{0.2}O_2$ ($0 \leq y \leq 0.4$) system

Following the central aim of this work, this chapter presents the next step towards quantitative chemical state elucidation of Li-ion battery electrodes using newly developed $LiNi_{0.8-y}Mn_yCo_{0.2}O_2$ ($0 \leq y \leq 0.4$) cathode powder materials. In this regard, templates for the complex peak structures consisting of significant photoelectron multiplet splitting, shake-up satellites, and additional Auger and photoelectron peak overlaps developed on the NMC thin-film system in Chapter 4.3.1 were adapted for the powder material. In particular, the stoichiometries indicated on the tie-line depicted in the $LiNiO_2$-$LiMnO_2$-$LiCoO_2$ Gibbs triangle shown in Figure 4-16 were systematically studied to demonstrate the herewith possible XPS elucidation of the oxidation state changes according to stoichiometry. In case of the bulk stoichiometric $LiNi_{0.8-y}Mn_yCo_{0.2}O_2$ ($0 \leq y \leq 0.4$) compounds, the total charge of transition metals needs to be 3+ to achieve charge neutrality. In particular, the oxidation states of 3+ and 4+ are expected for Co and Mn, respectively, whereas the oxidation state of Ni is expected to change between Ni^{2+} and Ni^{3+} by variation of the stoichiometry [123]–[127].

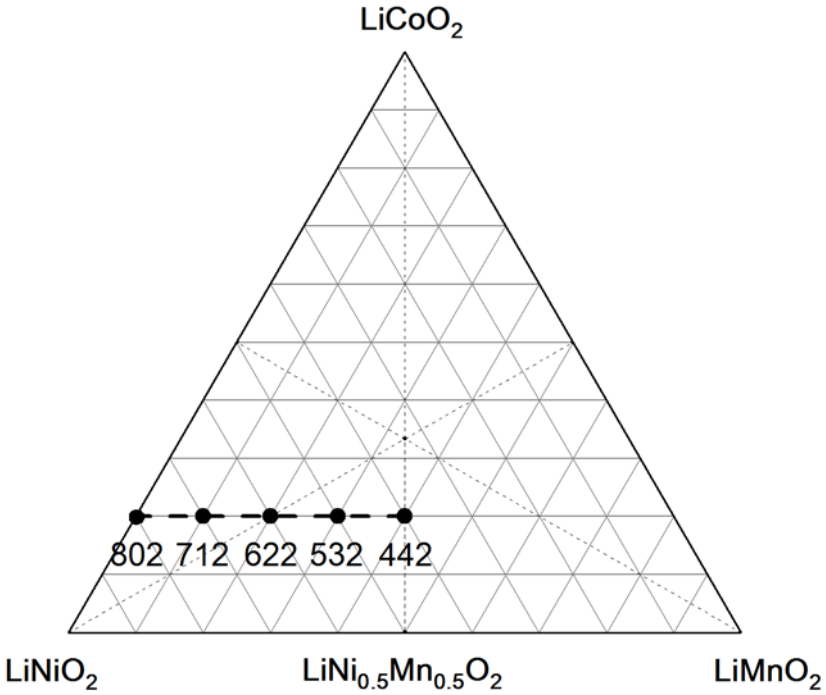

Figure 4-16: Gibbs triangle for the $LiNiO_2$-$LiMnO_2$-$LiCoO_2$ (NMC) system showing the $LiNi_{0.8-y}Mn_yCo_{0.2}O_2$ series (dashed tie-line) and the compositions investigated experimentally (black circles) in the present study.

4.3.2.1. Characterization of Cobalt in $LiNi_{0.8-y}Mn_yCo_{0.2}O_2$ ($0 \leq y \leq 0.4$) powders

The Co 2p spectra of the $LiNi_{0.8-y}Mn_yCo_{0.2}O_2$ ($0 \leq y \leq 0.4$) are shown in Figure 4-17 and the respective peak fitting parameters are compiled in Table 4-4. According to the absence of the characteristic shake-up satellite structure of Co^{2+} at around 6 eV higher than the main peak, [31] and to the similarity of the spectra of three-valent Co ions in $LiCoO_2$, cf. Figure 4-9, it can be concluded that solely Co^{3+} is present in all samples. The main peak at 780.4 eV is attributed to the Co^{3+} multiplet and the peak at 790.1 eV is considered to be a satellite peak of the Co^{3+} chemical state which appears ~10 eV higher than the main peak, although no satellite structure is theoretically expected for Co^{3+} ions in octahedral coordination due to its t_{2g}^6 e_g^0 valence state [31]. The area of this satellite is 11 to 18 % of the main peak. (for more detail about XPS characterization of Co ions see Chapter 4.2.2.)

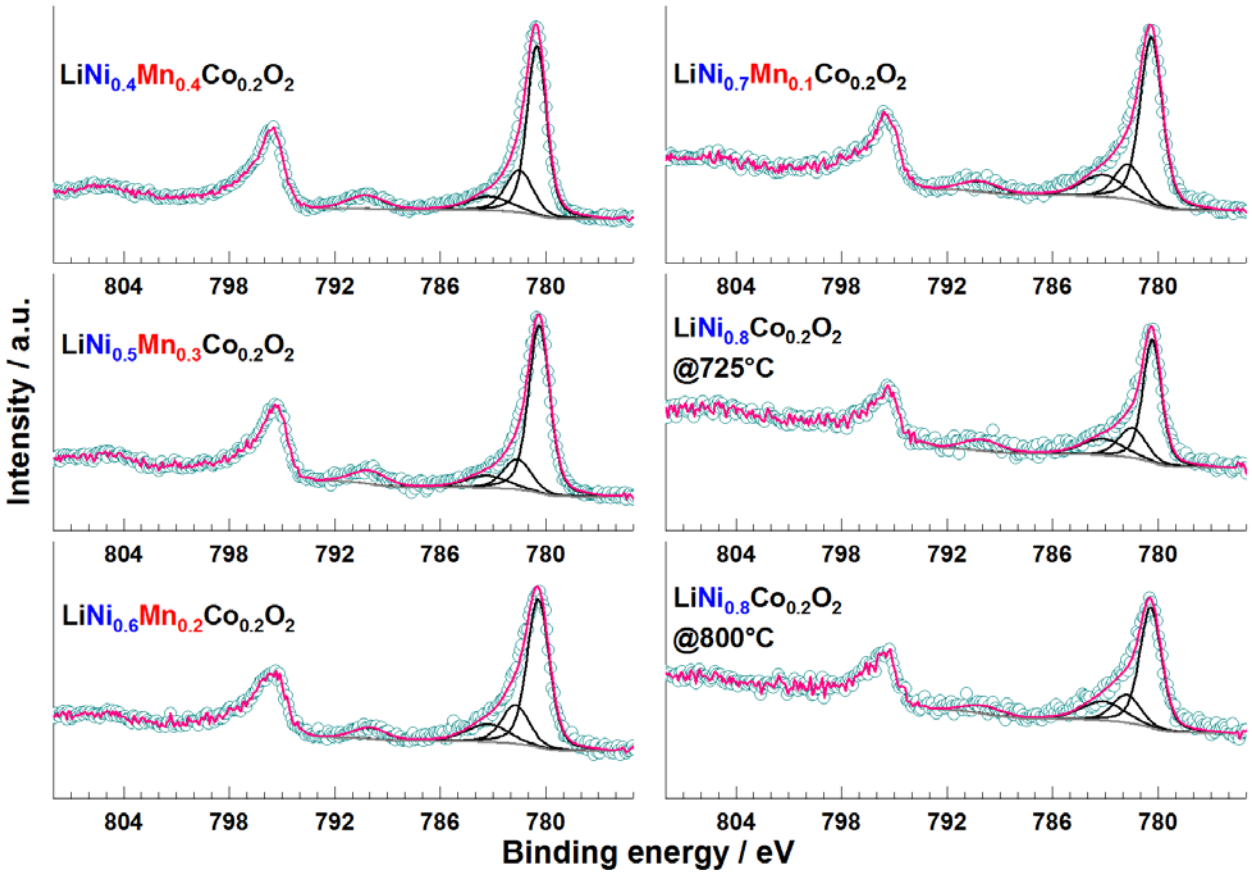

Figure 4-17: Co 2p spectra of the $LiNi_{0.8-y}Mn_yCo_{0.2}O_2$ ($0 \leq y \leq 0.4$) compounds.

4.3.2.2. Characterization of Manganese in $LiNi_{0.8-y}Mn_yCo_{0.2}O_2$ ($0 \leq y \leq 0.4$) powders

The elucidation of different chemical states of Mn ions in NMC compounds based on Mn 2p spectra is hampered not only by the complexities described in Chapter 4.2.1 but also by an overlapping Ni LMM Auger peak. As the experimental alternative to shifting the Auger peaks by changing the X-ray source to MgKα excitation is not provided by the K-Alpha+ instrument, the Ni LMM Auger contribution was estimated on the two Mn free samples with the nominal stoichiometry of $LiNi_{0.8}Co_{0.2}O_2$. The respective template then was applied to the Mn 2p spectra of the other four samples containing Mn. For the determination of the Mn oxidation states, the multiplet splitting approach developed for r.f. magnetron sputtered Li-Ni-Mn-Co-O thin-films directly was applied to peaks of the powder system, cf. Chapter 4.3.1.[31] The results are shown in Figure 4-18 and the corresponding peak parameters are compiled in Table 4-5.

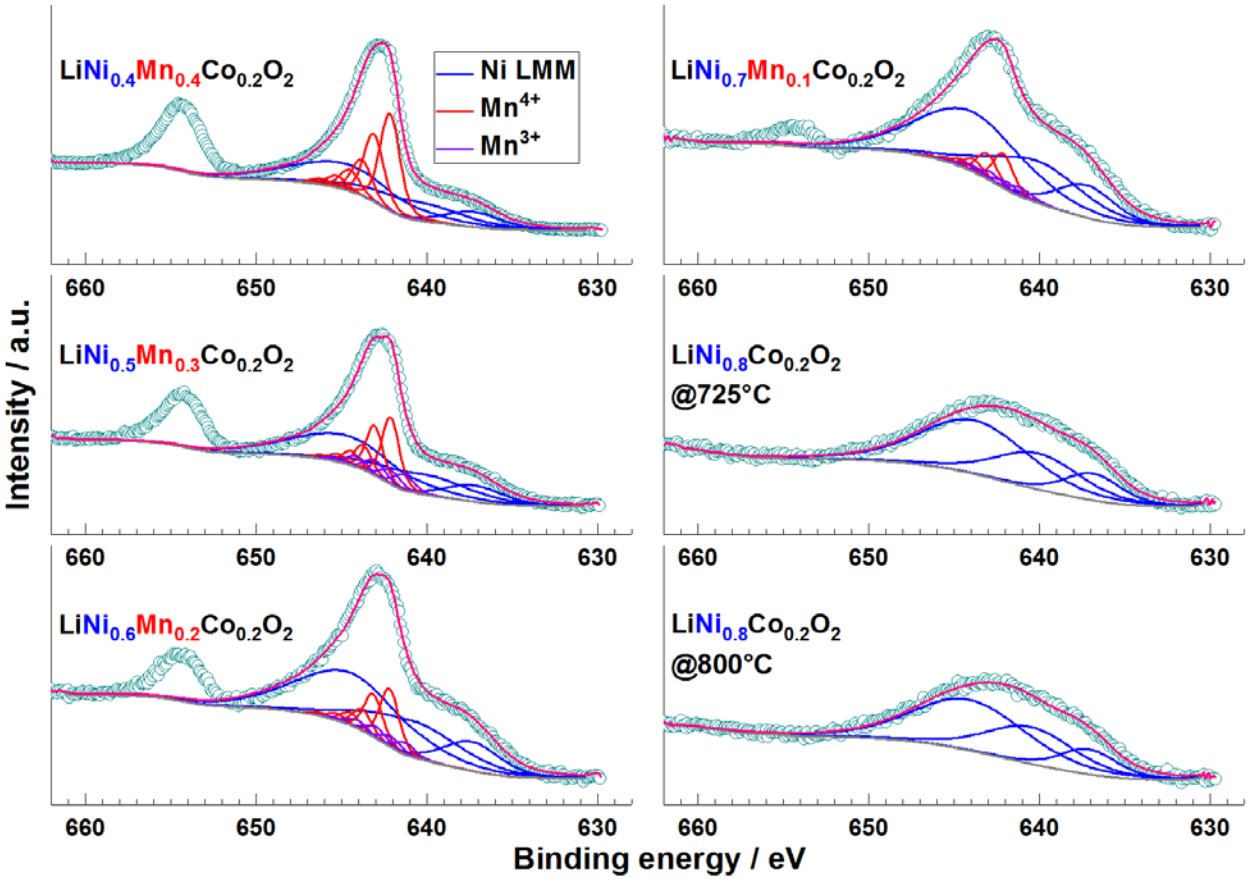

Figure 4-18: Mn 2p spectra of the $LiNi_{0.8-y}Mn_yCo_{0.2}O_2$ ($0 \leq y \leq 0.4$) compounds.

To achieve a reliable chemical state elucidation again it is needed to take additionally the Mn 3s splitting energy as well as the Mn 3p binding energies into account (cf. Chapter 4.2.1). The Mn 3s splitting energy of 4.5, 4.8 and 4.8 eV determined for $LiNi_{0.4}Mn_{0.4}Co_{0.2}O_2$, $LiNi_{0.5}Mn_{0.3}Co_{0.2}O_2$,

and $LiNi_{0.6}Mn_{0.2}Co_{0.2}O_2$ nominal stoichiometries proves the existence of around 30 % Mn^{3+} of the overall Mn content (see Table 4-5) [23]. However, the splitting energy of 5.4 eV determined for $LiNi_{0.7}Mn_{0.1}Co_{0.2}O_2$ has a higher uncertainty because of its low intensity, cf. Figure 4-19.

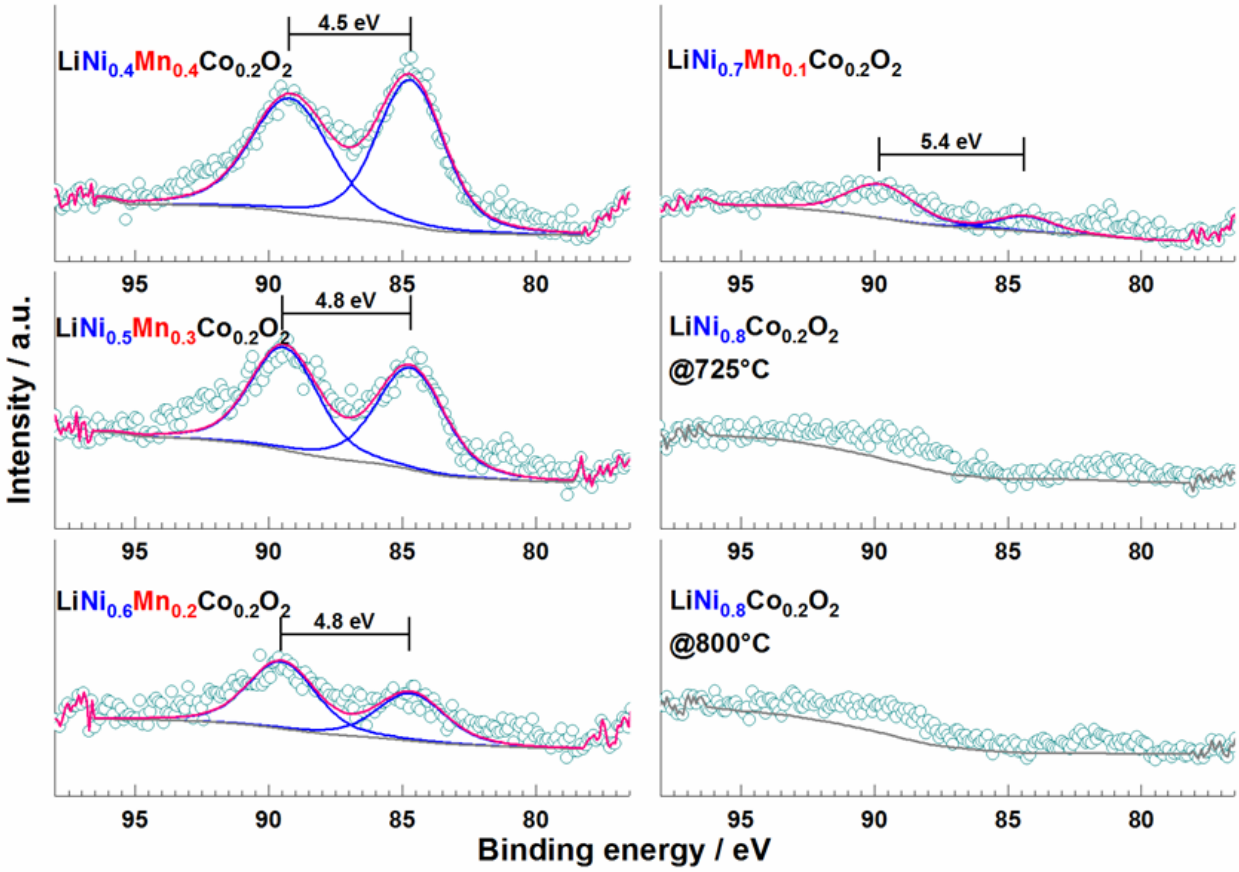

Figure 4-19: Mn 3s spectra of $LiNi_{0.8-y}Mn_yCo_{0.2}O_2$ ($0 \leq y \leq 0.4$) compounds.

Finally, the deconvolution of the Mn 3p multiplet in Figure 4-20 supports these results, as the main peaks at ~48.6 eV and at ~49.8 eV are related to Mn^{3+} and Mn^{4+}, respectively [31] (cf. Chapter 4.2.1). The calculated Mn^{3+} percentage from Mn 2p, Mn 3s, and Mn 3p spectra are compiled in Table 4-5, where the similarity of the Mn^{3+} content arising from deconvolution of different Mn photoemission peaks proves the proper quantification of the Mn^{3+} and Mn^{4+} ratio.

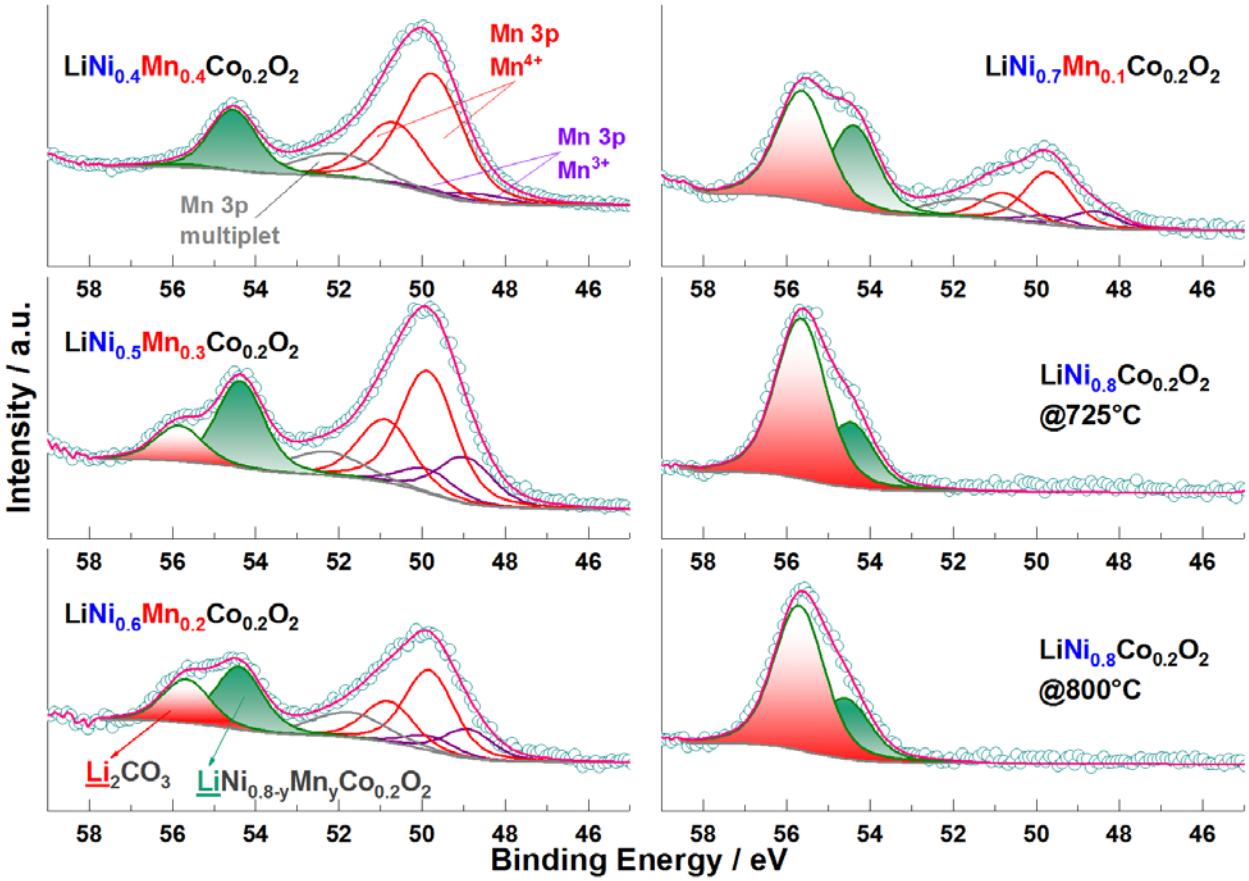

Figure 4-20: Mn 3p and Li 1s spectra of the $LiNi_{0.8-y}Mn_yCo_{0.2}O_2$ ($0 \leq y \leq 0.4$) compounds.

4.3.2.3. Characterization of Nickel in $LiNi_{0.8-y}Mn_yCo_{0.2}O_2$ ($0 \leq y \leq 0.4$) powders

As already stated in previous chapters, in particular, Chapter 4.2.3, the identification of Ni oxidation states is very challenging. In this particular case, however, a $LiNiO_2$ reference material, synthesized in the same way as the $LiNi_{0.8-y}Mn_yCo_{0.2}O_2$ ($0 \leq y \leq 0.4$) compounds, was used for Ni^{3+} identification and the respective Ni 2p spectrum is depicted in Figure 4-11, Chapter 4.2.3.

Already the simplifying comparison of the Ni $2p_{3/2}$ peak maxima for all $LiNi_{0.8-y}Mn_yCo_{0.2}O_2$ ($0 \leq y \leq 0.4$) compounds indicates a change of the oxidation state from Ni^{2+} to Ni^{3+} based on a high energy shift with increasing Ni content, cf. Figure 4-21. This is supported by the results for the chemical state of Co and Mn in $LiNi_{0.8}Co_{0.2}O_2$ and $LiNi_{0.4}Mn_{0.4}Co_{0.2}O_2$ which are 3+ and 4+, respectively, thus the chemical state of Ni needs to be 3+ and 2+, respectively, to achieve charge neutrality in the stoichiometric compounds. In consequence, multiplet templates for pure Ni^{3+} and Ni^{2+}, based on the work of Grosvenor et al. [117] who utilized γ-NiOOH and $Ni(OH)_2$ as reference materials for Ni^{3+} and Ni^{2+}, were applied to the Ni 2p spectra of $LiNi_{0.8}Co_{0.2}O_2$ and

$LiNi_{0.4}Mn_{0.4}Co_{0.2}O_2$, respectively and the results are compiled in Table 4-6. The Ni 2p multiplets for all other available stoichiometries on the tie-line within these threshold compositions (Figure 4-16) were then fitted with both the templates for Ni^{2+} and Ni^{3+} to prove the expected Ni^{2+}/Ni^{3+} ratio, cf. Figure 4-22.

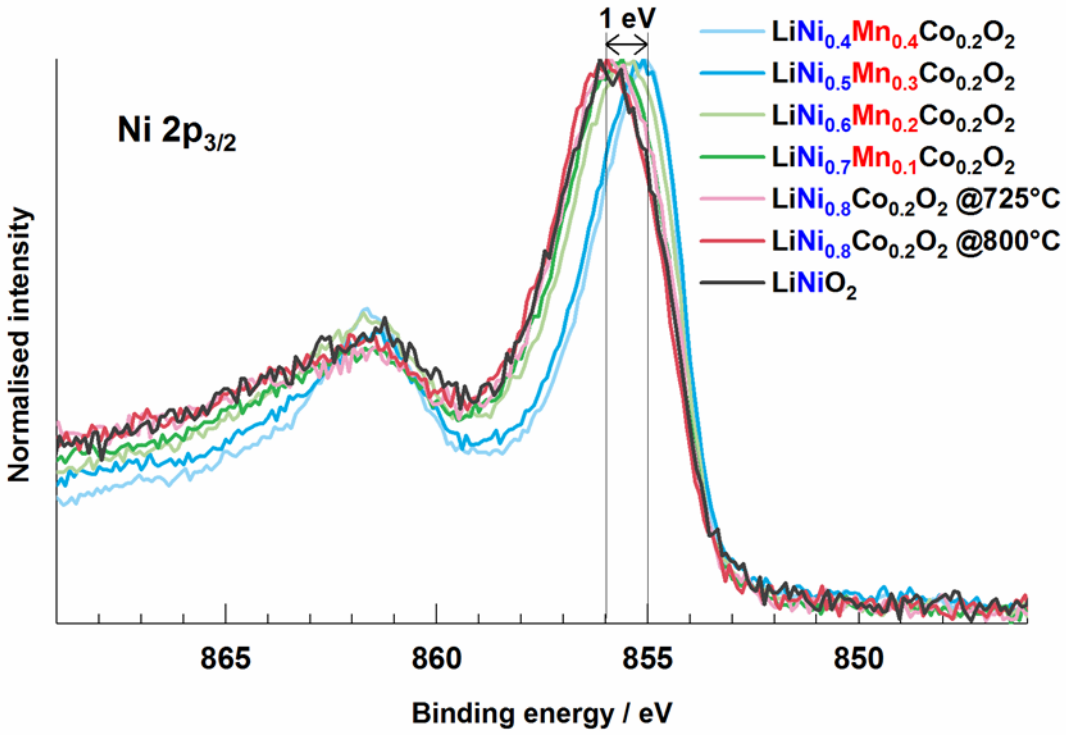

Figure 4-21: overlay of Ni $2p_{3/2}$ spectra of $LiNi_{0.8-y}Mn_yCo_{0.2}O_2$ ($0 \leq y \leq 0.4$) compounds.

As another interim conclusion, it can be drawn out that the template approach enables the unambiguous elucidation of the transition metals oxidation states, even gradual changes in the Ni^{2+}/Ni^{3+} ratio depending on the Ni content in the studied novel $LiNi_{0.8-y}Mn_yCo_{0.2}O_2$ ($0 \leq y \leq 0.4$) compound series can clearly be evidenced.

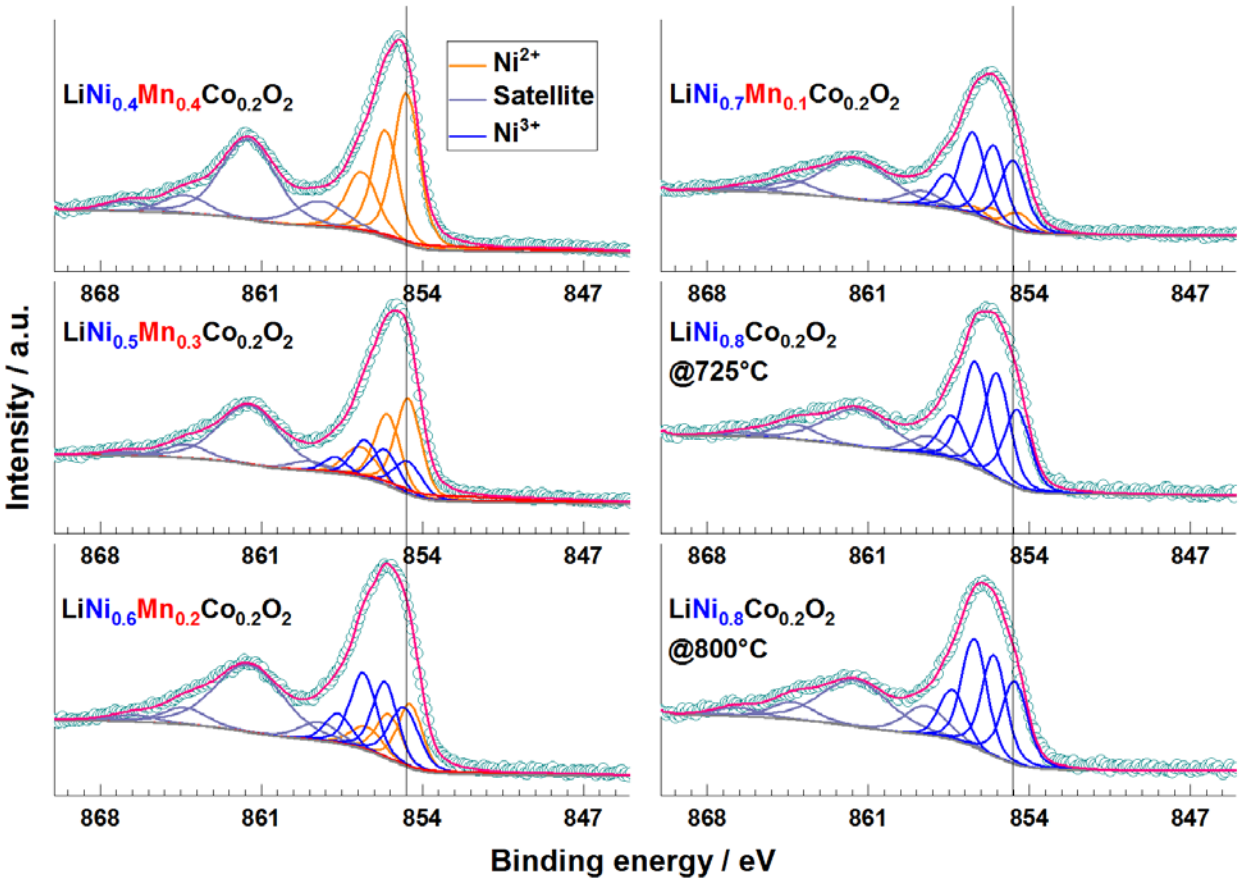

Figure 4-22: Ni $2p_{3/2}$ spectra of the $LiNi_{0.8-y}Mn_yCo_{0.2}O_2$ ($0 \leq y \leq 0.4$) compounds.

4.3.2.4. XPS quantification of $LiNi_{0.8-y}Mn_yCo_{0.2}O_2$ ($0 \leq y \leq 0.4$) powders

The strong overlaps of the 3p peaks of transition metals (particularly Mn 3p) with the Li 1s energy range, hampers the precise binding energy determination and quantification of Li, cf. Figure 4-20. Nevertheless, based on the Mn-free $LiNi_{0.8}Co_{0.2}O_2$ sample two different Li components were identified, namely at 54.5 eV binding energy for Li which is assigned to intercalated Li in $LiNi_{0.8-y}Mn_yCo_{0.2}O_2$ ($0 \leq y \leq 0.4$) compounds and at 55.7 eV binding energy for Li assigned to Li_2CO_3. The presence of Li_2CO_3 is supported by the C 1s and O 1s spectra, exemplarily shown for the $LiNi_{0.6}Mn_{0.2}Co_{0.2}O_2$ compound in Figure 4-23. The O 1s peak at 529.7 eV in all O 1s spectra (cf. Figure 4-23b) is assigned to the oxygen found in the lattice structure of the $LiNi_{0.8-y}Mn_yCo_{0.2}O_2$ ($0 \leq y \leq 0.4$) compounds whereas the peaks at higher binding energies are assigned to Li_2CO_3 at 532.2 eV and other contaminations like SiO_2 and SO_4^{2-}, C-O (at 533.3 eV) and C=O (at 531.3 eV) containing compounds which are most probably originating from the annealing and grinding steps and from slight precursor impurities, respectively, cf. Figure 4-23 Herewith, the contribution of contamination layers can readily be separated from the NMC compounds' composition.

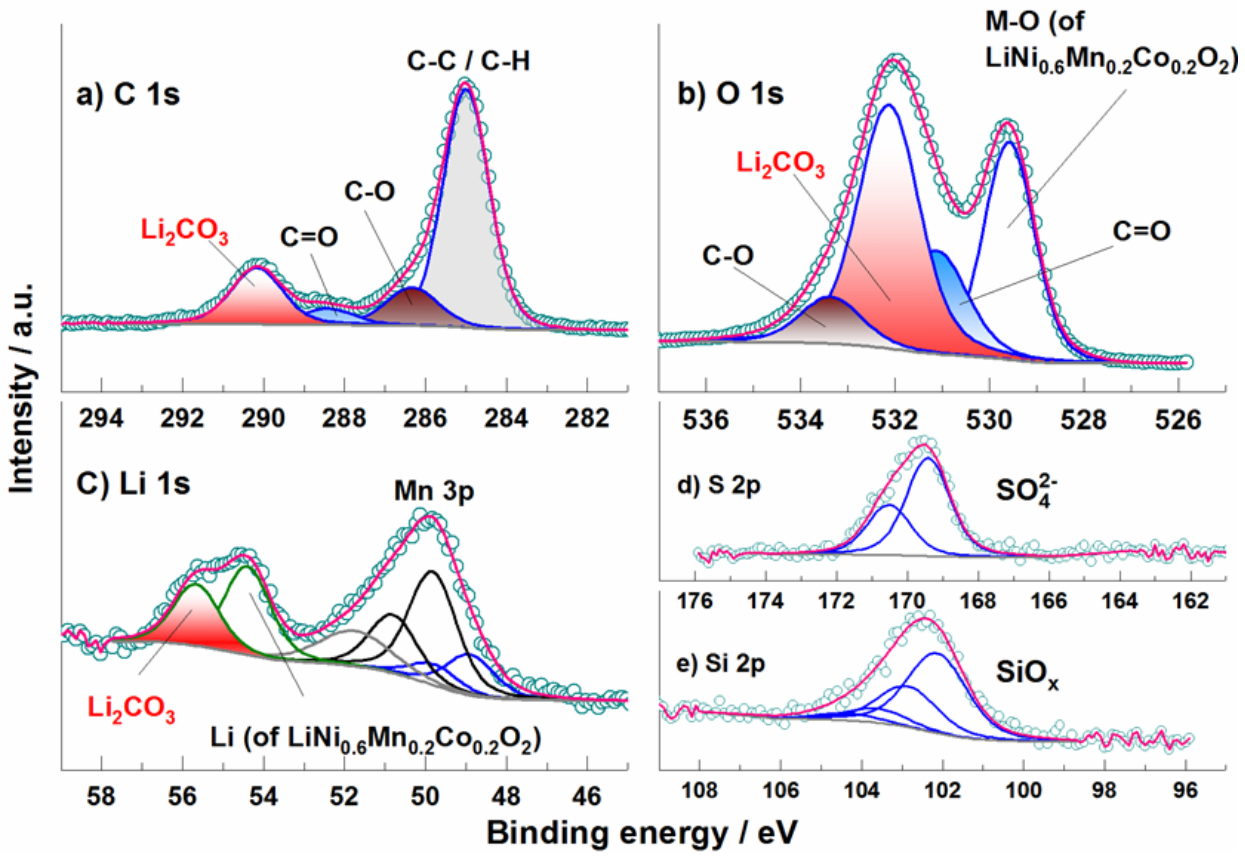

Figure 4-23: C1s, O 1s, Li 1s, S 2p, and Si 2p of spectra of the $LiNi_{0.6}Mn_{0.2}Co_{0.2}O_2$ powder.

The resulting transition metal contents are in good agreement with ICP-OES findings as compared in Figure 4-24 and reflect well the targeted stoichiometry of the compounds. Moreover, the Ni^{2+} fraction finally was determined to be 100 %, 62 %, 35 %, 13 %, and 0 % of the total Ni ions by increasing the Ni content in the sample series. As a conclusion, the quantification of the oxidation states of Ni in each sample as well as the identification of the oxidation states of Co and Mn, reveals the total oxidation state of the transition metals to be between 2.97 and 3.17, which is in good agreement with the expected theoretical value of 3, to achieve charge neutrality of the compounds.

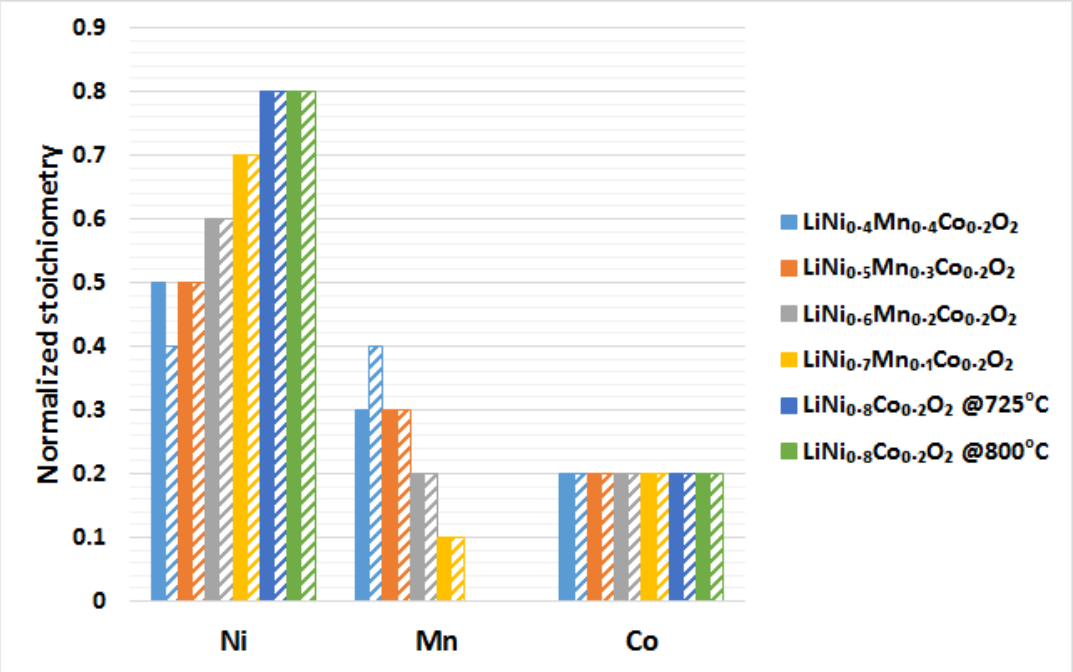

Figure 4-24: XPS quantification data (solid columns) in comparison to ICP-OES measurements (shaded columns) for the characterized NMC compounds, the XPS results are normalized to Co=0.2.

Table 4-4: Fit parameters for Co $2p_{3/2}$ spectra of $LiNi_{0.8-y}Mn_yCo_{0.2}O_2$ ($0 \leq y \leq 0.4$) compounds.

	Photoelectron Co $2p_{3/2}$ (Co^{3+})	$LiCoO_2$	$LiNi_{0.4}Mn_{0.4}Co_{0.2}O_2$	$LiNi_{0.4}Mn_{0.4}Co_{0.2}O_2$	$LiNi_{0.6}Mn_{0.2}Co_{0.2}O_2$	$LiNi_{0.7}Mn_{0.1}Co_{0.2}O_2$	$LiNi_{0.8}Co_{0.2}O_2$ @ 725 °C	$LiNi_{0.8}Co_{0.2}O_2$ @ 800 °C
Peak 1	BE / eV	780.9	780.5	780.4	780.4	780.4	780.3	780.4
	FWHM / eV	1.5	1.3	1.4	1.5	1.5	1.3	1.5
	%	57	60	66	60	62	54	59
Peak 2	BE / eV	781.2	781.5	781.6	781.7	781.7	781.5	781.8
	FWHM / eV	1.9	1.9	1.9	1.9	1.9	1.9	1.2
	%	31	21	15	19	16	19	17
	Δ Peak / eV	1.1	1	1.3	1.3	1.3	1.2	1.4
Peak 3	BE / eV	782.9	783.2	783.4	783.3	783.2	783.1	783.1
	FWHM / eV	2.2	2.8	2.8	2.8	2.8	2.8	2.8
	%	4	11	10	14	15	17	18
	Δ Peak / eV	1.6	1.7	1.7	1.6	1.5	1.7	1.3
Peak 4	BE / eV	790.1	790.2	790	790	790.2	790	790
	FWHM / eV	2.4	2.4	2.3	2.2	2.5	2.5	2.5
	%	8	9	9	7	7	10	7
	Δ Peak / eV	7.2	7	6.7	6.7	7	6.9	6.8

Table 4-5: Fit parameters for Mn $2p_{3/2}$ spectra of $LiNi_{0.8-y}Mn_yCo_{0.2}O_2$ ($0 \leq y \leq 0.4$) compounds.

Photoelectron	$Mn2p_{3/2}$	$LiNi_{0.4}Mn_{0.4}Co_{0.2}O_2$			$LiNi_{0.5}Mn_{0.3}Co_{0.2}O_2$			$LiNi_{0.6}Mn_{0.2}Co_{0.2}O_2$			$LiNi_{0.7}Mn_{0.1}Co_{0.2}O_2$		
		Mn^{3+}	Mn^{4+}	Ni LMM	Mn^{3+}	Mn^{4+}	Ni LMM	Mn^{3+}	Mn^{4+}	Ni LMM	Mn^{3+}	Mn^{4+}	Ni LMM
Peak 1	BE / eV	640.8	642.2	637.3	641.3	642.1	637.2	641.3	642.2	637.4	641.1	642.1	637.3
	FWHM / eV	1.3	1.4	4	1.4	1.2	4	1.4	1.3	4	1.6	1.4	4
	%	23.8	40.5	15.5	26.3	39.8	15.6	26.3	39.8	15.6	26.3	39.8	15.6
Peak 2	BE / eV	641.4	643.1	640.7	642.1	643.1	640.3	642.1	643.2	640.8	641.9	643.1	640.2
	FWHM / eV	1.3	1.4	6.4	1.4	1.2	6.5	1.4	1.3	6.5	1.6	1.4	6.3
	%	23.8	28.3	31	23.7	29.5	31.3	23.7	29.5	31.3	23.7	29.5	31.2
	Δ Peak / eV	0.6	1	3.4	0.8	1	3.1	0.8	0.9	3.4	0.8	1	2.9
Peak 3	BE / eV	642.1	643.8	644.6	643	643.7	644.6	643	643.8	644.4	642.8	643.9	643.9
	FWHM / eV	1.3	1.4	8	1.4	1.2	7.9	1.4	1.3	7.7	1.6	1.4	7.6
	%	28.5	15	53.5	26.3	14.7	53.1	26.3	14.7	53.1	26.3	14.7	53.1
	Δ Peak / eV	0.7	0.7	3.9	0.9	0.7	4.3	0.9	0.6	3.6	0.9	0.8	3.8
Peak 4	BE / eV	643	644.5		644.1	644.4		644.1	644.5		644	644.6	
	FWHM / eV	1.3	1.4		1.4	1.2		1.4	1.3		1.6	1.4	
	%	17.3	8.9		18.4	8.8		18.4	8.8		18.4	8.8	
	Δ Peak / eV	0.9	0.7		1.1	0.7		1.1	0.7		1.1	0.7	
Peak 5	BE / eV	644.3	645.3		645.4	645.2		645.4	645.3		645.2	645.4	
	FWHM / eV	1.3	1.4		1.4	1.2		1.4	1.3		1.6	1.4	
	%	6.7	4.9		5.3	4.8		5.3	4.8		5.3	4.8	
	Δ Peak / eV	1.3	0.8		1.3	0.8		1.3	0.8		1.3	0.8	
Peak 6	BE / eV		646.2			646.1			646.2			646.3	
	FWHM / eV		1.4			1.2			1.3			1.4	
	%		2.4			2.4			2.4			2.4	
	Δ Peak / eV		0.9			0.9			0.9			0.9	
Mn^{3+}/Mn_{total}	out of Mn 3p	6			25			22			19		
	out of Mn 3s	0			25			35			95		
	out of Mn 2p	0			30			26			32		

Table 4-6: Fit parameters for Ni $2p_{3/2}$ spectra of $LiNi_{0.8-y}Mn_yCo_{0.2}O_2$ ($0 \leq y \leq 0.4$) compounds.

Photoelectron Ni $2p_{3/2}$		$LiNiO_2$	$LiNi_{0.8}Co_{0.2}O_2$ @ 800 °C	$LiNi_{0.8}Co_{0.2}O_2$ @ 725 °C	$LiNi_{0.7}Mn_{0.1}Co_{0.2}O_2$		$LiNi_{0.6}Mn_{0.2}Co_{0.2}O_2$		$LiNi_{0.5}Mn_{0.3}Co_{0.2}O_2$		$LiNi_{0.4}Mn_{0.4}Co_{0.2}O_2$
		Ni^{3+}	Ni^{3+}	Ni^{3+}	Ni^{2+}	Ni^{3+}	Ni^{2+}	Ni^{3+}	Ni^{2+}	Ni^{3+}	Ni^{2+}
Peak 1	BE / eV	854.6	854.6	854.5	854.5	854.7	854.5	854.8	854.6	854.6	854.7
	FWHM / eV	1.4	1.3	1.3	1.3	1.3	1.3	1.5	1.3	1.4	1.3
	%	13	15.4	16.1	3.9	15.1	9.6	10.7	18.5	6.9	25.3
Peak 2	BE / eV	855.4	855.5	855.4	855.6	855.6	855.5	855.6	855.5	855.6	855.6
	FWHM / eV	1.4	1.3	1.3	1.3	1.3	1.3	1.3	1.3	1.3	1.4
	%	17	17.6	21.3	2.8	15.9	7.1	11.6	13.7	7	18
	Δ Peak / eV	0.8	0.9	0.9	1.1	0.9	0.9	0.8	0.9	1	0.9
Peak 3	BE / eV	856.2	856.4	856.3	856.4	856.5	856.4	856.6	856.7	856.5	856.6
	FWHM / eV	1.4	1.3	1.3	1.3	1.3	1.6	1.3	1.6	1.3	1.6
	%	21	18.8	21.9	1.9	18.1	4.6	12.3	7.4	7.6	12.2
	Δ Peak / eV	0.8	0.8	0.9	0.8	0.9	1	0.9	1.2	0.9	1
Peak 4	BE / eV	857.1	857.4	857.4	857.6		857.7		857.8		
	FWHM / eV	1.4	1.3	1.3	1.3		1.3		1.3		
	%	10	8.7	9	7.5		4.8		3.1		
	Δ Peak / eV	1	1	1	1.1		1.1		1.3		
Peak 5	BE / eV	858	858.5	858.4	858.7		858.5		858.9		858.4
	FWHM / eV	2.3	2.1	2	2		2.1		2		2.6
	%	8	8.6	5.6	4.9		4.6		3		8.3
	Δ Peak / eV	0.9	1.1	1	1.1		0.8		1.1		1.8
Peak 6	BE / eV	861.3	861.6	861.4	861.6		861.5		861.5		861.6
	FWHM / eV	3.5	3.5	3.4	3.5		3.5		3.1		2.8
	%	24	22.8	19.4	23.5		28.3		27.1		28.2
	Δ Peak / eV	3.3	3.1	3.1	2.9		3		2.6		3.1
Peak 7	BE / eV	864.1	864.3	864.2	864.3		864.3		864.3		864.3
	FWHM / eV	2.2	2.2	2.2	2.2		2.2		2.2		2.2
	%	5	5.4	5.1	4.7		4.5		4.4		5.2
	Δ Peak / eV	2.7	2.7	2.8	2.7		2.8		2.8		2.8
Peak 8	BE / eV	865.9	866.7	866.3	866.3		866.5		866.9		866.8
	FWHM / eV	2.1	2.2	2.2	2.2		2.2		2		2.2
	%	2	2.7	1.6	1.8		1.9		1.2		2.7
	Δ Peak / eV	1.9	2.4	2.1	2		2.2		2.6		2.5

4.3.2.5. Characterization of $LiNi_{0.8-y}Mn_yCo_{0.2}O_2$ ($0 \leq y \leq 0.4$) powders using MgKα excitation

In order to independently evidence the reliability of the developed procedure to include also AlKα X-ray-induced Auger electron peaks into the template approach exemplarily $LiNi_{0.5}Mn_{0.3}Co_{0.2}O_2$ powder sample was characterized using MgKα excitation to shift the Auger peaks 233 eV, i.e. the energy difference between the characteristic Al and Mg X-ray lines towards lower binding energies (see Chapter 2.1.4). However, as the surface analysis group's spectrometer does not have the necessary performance, these experiments were done in the application lab of Thermo Fisher Scientific in East Grinstead, UK, using an ESCALAB 250 Xi instrument. Unfortunately, the change of the excitation energy causes new peak overlap problems, as the O KLL Auger peak is shifted to the energy range of Co 2p, see Figure 4-25. Therefore, only the Ni 2p and Mn 2p peaks were used to check for the correctness of the AlKα approach, the respective multiplet fits are depicted in Figure 4-25.

The Ni $2p_{3/2}$ spectra of $LiNi_{0.5}Mn_{0.3}Co_{0.2}O_2$ powder sample is fitted with the fit parameters used for the measurements done with AlKα excitation as depicted in Table 4-6 and described in Chapter 4.3.2.3. Moreover, the Ni^{2+} fraction was determined to be 54 % of the total Ni ions in comparison to the 62 % that was obtained previously for $LiNi_{0.5}Mn_{0.3}Co_{0.2}O_2$ compound via measurements by AlKα excitation. Accordingly, the deconvolution of Mn $2p_{3/2}$ spectra of $LiNi_{0.5}Mn_{0.3}Co_{0.2}O_2$ powder sample in Figure 4-25, shows that around 50 % of Mn ions can be attributed to Mn^{3+}state, which is higher than the value estimated via AlKα excitation measurements.

The discrepancy in the obtained stoichiometry of transition metals can be explained by the possible instability of the material surface that can form Li_2CO_3 (and LiOH) by time passing when it is stored in ambient air condition [68] (see Chapter 2.3.1.1). Moreover, using MgKα the information depth is smaller since all photoelectrons have 233 eV less kinetic energy. In consequence, if stoichiometric shifts occur in topmost layers, e.g. due to aging, these become more dominant with MgKα excitation. In conclusion, the templates developed for AlKα excitation comprising photoelectron and Auger peak overlaps are appropriate tools to reliably deconvolute the respective multiplet spectra with a restriction that the experiments should be repeated once the group has its own ESCALAB instrument available on site to avoid degradation/altering effects.

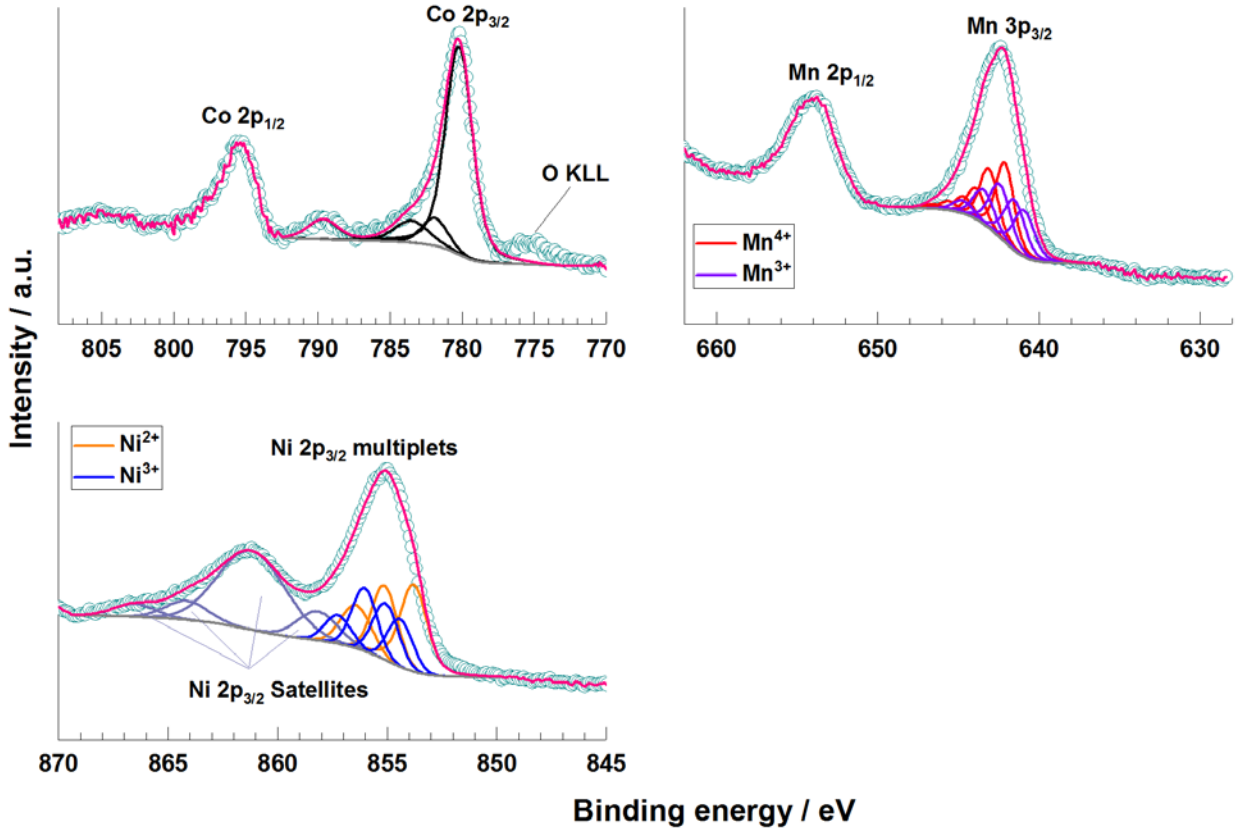

Figure 4-25: Co 2p, Mn 2p, and Ni $2p_{3/2}$ of the $LiNi0.5Mn_{0.3}Co_{0.2}O_2$ powder sample measured with MgKα X-ray excitation.

4.3.3. Characterization of pristine electrodes of the $LiNi_{0.8-y}Mn_yCo_{0.2}O_2$ ($0 \leq y \leq 0.4$)

Following the comprehensive discussion of quantitative chemical state elucidation of newly developed $LiNi_{0.8-y}Mn_yCo_{0.2}O_2$ ($0 \leq y \leq 0.4$) cathode powder materials, the XPS characterization of the pristine electrodes will be presented in this chapter. This is a further step towards the proof of the applicability of the developed template-fitting approach to practical batteries. Here the electrodes are commonly made of active powder materials in combination with a binder and carbon black, which consequently results in a dilution of the active material and herewith in a reduction of its XPS peak intensity. Moreover, additional challenges arise, as Auger peaks stemming from binder overlap with the main photoelectron peaks of the active material leading probably to misinterpretation of the existing oxidation states and degradation species. Therefore, in this chapter, besides considering the developed approach from previous chapters (Chapter 4.3.1 and Chapter 4.3.2) to deal with the complex peak structures of transition metals, the additional intensity reduction effect as well as Auger and photoelectron peak overlaps will be studied on the pristine

electrodes made of bulk stoichiometric $LiNi_{0.8-y}Mn_yCo_{0.2}O_2$ ($0 \leq y \leq 0.4$) compounds in combination with PVDF binder and carbon black in 80:10:10 concentration ratio, respectively. Moreover, the possible artifacts of using charge compensation alongside the sensitivity of electrodes to X-ray exposure as well as the pros and contras of utilizing Ar-cluster ion etching to enhance the signal intensity of the active material on LIB electrodes will be covered in this chapter.

It should be noted that in the particular case of electrodes all binding energies are referenced to C 1s = 284.4 eV originating from graphite as an internal reference.

In some cases, throughout the rest of the document, $LiNi_{0.4}Mn_{0.4}Co_{0.2}O_2$, $LiNi_{0.5}Mn_{0.3}Co_{0.2}O_2$, $LiNi_{0.6}Mn_{0.2}Co_{0.2}O_2$, $LiNi_{0.7}Mn_{0.1}Co_{0.2}O_2$, and $LiNi_{0.8}Co_{0.2}O_2$ compounds are abbreviated as NMC442, NMC532, NMC622, NMC712, and NMC802 for more convenience.

4.3.3.1. Artifacts of XPS measurements on pristine electrodes of $LiNi_{0.8-y}Mn_yCo_{0.2}O_2$ ($0 \leq y \leq 0.4$) compounds

Sputter cleaning of the Li-ion electrodes using gentle Ar-cluster ion etching might be a possible way to increase the peak intensity of the active material by removing organic contaminations from the surface without affecting the chemical state of the transition metals unlike the conventional monoatomic Ar-ion sputtering as discussed in Chapter 2.1.7 and Chapter 4.1.4. To verify this idea on pristine electrodes of $LiNi_{0.8-y}Mn_yCo_{0.2}O_2$ ($0 \leq y \leq 0.4$) compounds, the electrodes were sputter-etched by Ar clusters for 5 min using three different energy and cluster sizes namely Ar_{1000}^+ at 4 keV, Ar_{500}^+ at 4 keV, and Ar_{300}^+ at 8 keV clusters which provide a nominal energy of 4 eV, 8 eV, and 27 eV per single Ar atom. The percentage of NMC active material at the surface of electrodes before and after etching was calculated considering the characterization approaches, that will be discussed in Chapter 4.3.3.2, and illustrated in Figure 4-26. The most intensive etching with around 27 eV energy per Ar atom, reveals 26 %, 42 %, 71 %, 152 %, 108 % increase of intensity with respect to the as-received surface, for NMC442, NMC532, NMC622, NMC712, and NMC802 respectively. However, even the intensity-gain of 152 % doesn't provide enough improvement for the NMC712 sample to solve the fine structure of transition metals' 2p spectra. This can be more understood by considering the low signal to noise ratio of NMC662, NMC712, NMC802 samples' as-received surfaces in Chapter 4.3.3.2. The irregularity of intensity-gain for the different NMC materials with respect to the per-atom-energy of cluster ions (cf. Figure 4-26) can be attributed to microscopic inhomogeneity of the electrode surfaces. It is easy to be seen, that for NMC622, NMC712, and NMC802 the binder/carbon black amount dramatically dominates the

XPS information volume and, in consequence, sputter cleaning cannot improve the overall intensity of the active material.

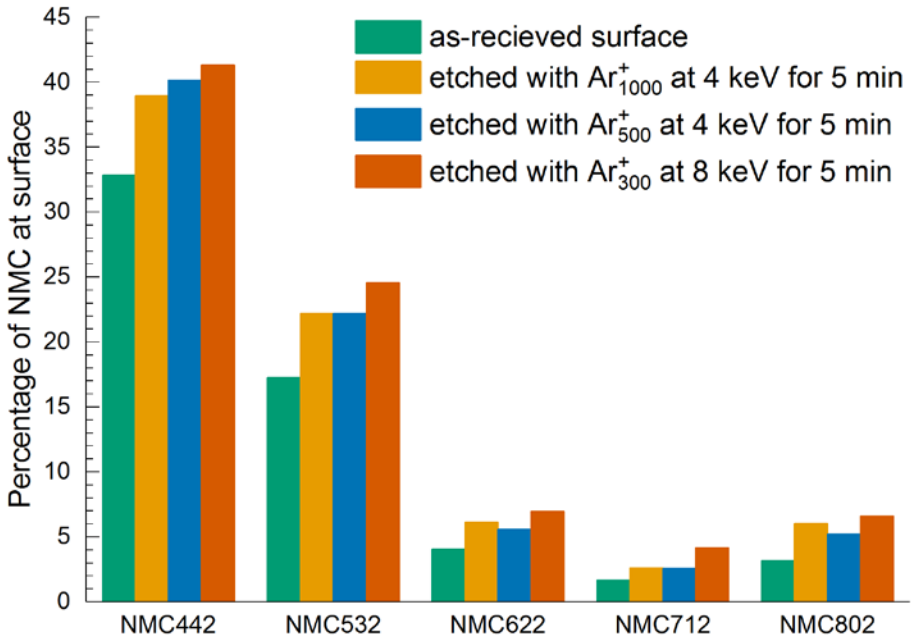

Figure 4-26: Intensity gain for pristine electrodes of $LiNi_{0.8-y}Mn_yCo_{0.2}O_2$ ($0 \leq y \leq 0.4$) compounds after different cluster sputtering conditions.

Nevertheless, this study reveals important information in general on the Ar-cluster ion beam parameters to be chosen for a non-destructive sputter cleaning of transition metal compounds. This has been checked only for $LiNi_{0.4}Mn_{0.4}Co_{0.2}O_2$ and $LiNi_{0.5}Mn_{0.3}Co_{0.2}O_2$ pristine electrodes that exhibit sufficient signal intensity and is shown in Figure 4-27.

The degradation effect via Ar-cluster ion etching is most noticeable from the increase of Co 2p peak intensity at around 785.5 eV attributed to the characteristic satellite of Co^{2+} ions (cf. Chapter 4.2.2) in Co 2p spectra as indicated by the blue arrow in Figure 4-27c and Figure 4-27χ for both $LiNi_{0.4}Mn_{0.4}Co_{0.2}O_2$ and $LiNi_{0.5}Mn_{0.3}Co_{0.2}O_2$ pristine electrodes. The probable reduction of Ni and Mn ions is not much noticeable from the Ni $2p_{3/2}$ and Mn 2p spectra in Figure 4-27. However, the Mn 3s splitting for $LiNi_{0.4}Mn_{0.4}Co_{0.2}O_2$ and $LiNi_{0.5}Mn_{0.3}Co_{0.2}O_2$ samples increases from 4.6 eV and 4.9 eV (as-received) to 5.1 eV and 5.3 eV (etched with Ar_{300}^+ at 4 keV cluster ions) respectively, that proves the reduction of Mn ions as well.

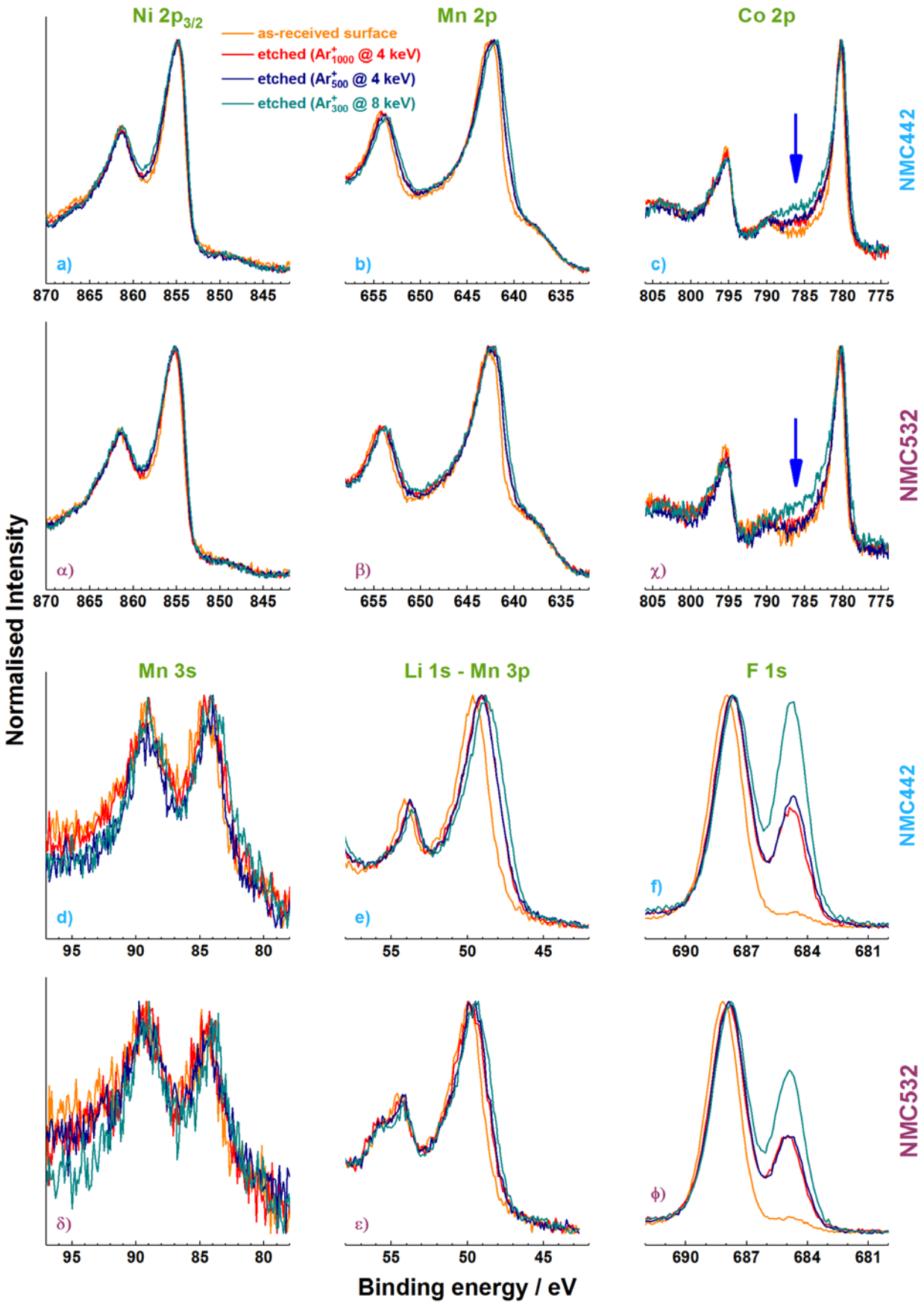

Figure 4-27: Normalized Ni $2p_{3/2}$, Mn 2p, Co 2p, Mn 3s, Li 1s, and F 1s spectra for several cluster etch conditions on NMC442 (1st and 3rd row) and NMC532 (2nd and 4th row).

Another noticeable feature in Figure 4-27 is the intensity gain of F 1s peak at 685.0 eV during the measurement, known as binding energy for LiF. F containing polymers are known to be degraded by X-ray exposure (see Figure 4-28) and sputter etching. Therefore, the increase of the component at 685.0 eV obviously might be an artifact to the binding energy of F ions of LiF compound, and it shouldn't generally stimulate the interpretations which assume more inorganic species like LiF are to be found in deeper layers.

To investigate the sensitivity of pristine electrodes of $LiNi_{0.8-y}Mn_yCo_{0.2}O_2$ ($0 \leq y \leq 0.4$) compounds to X-ray exposure, they were exposed to X-ray for one hour in the absence of any charge compensation. The results of the measurements, as depicted in Figure 4-28 exemplarily for a $LiNi_{0.4}Mn_{0.4}Co_{0.2}O_2$ pristine electrode, show that the spectra of transition metals remain mainly unaffected by one-hour X-ray exposure; neither the FWHM nor the satellite or multiplet structure of the transition metals' peaks alters under this experimental condition. The intensity-decrease of F 1s, O 1s, and C 1s species are due to degradation of C-F components as well as to the desorption of volatile species from the surface. As a conclusion, the reduction of the transition metals is doubtlessly only caused by Ar-cluster ion sputtering with the consequence that the used parameter-set has to be checked and adjusted for every single sample to guarantee surface cleaning in a non-destructive manner.

However, the intensity of some species in F 1s, O 1s and C 1s spectra (cf. Figure 4-28) reduces. This might be caused by the heating of the sample via X-rays and desorption of volatile species from the surface or eventually by the reaction of these species with produced secondary electrons. Meanwhile, the results of X-ray sensitivity measurements confirm that the reduction of transition metal elements in $LiNi_{0.8-y}Mn_yCo_{0.2}O_2$ ($0 \leq y \leq 0.4$) electrodes during sputter cleaning with Ar-cluster ions cannot be attributed to X-ray destruction, contrary to F containing species.

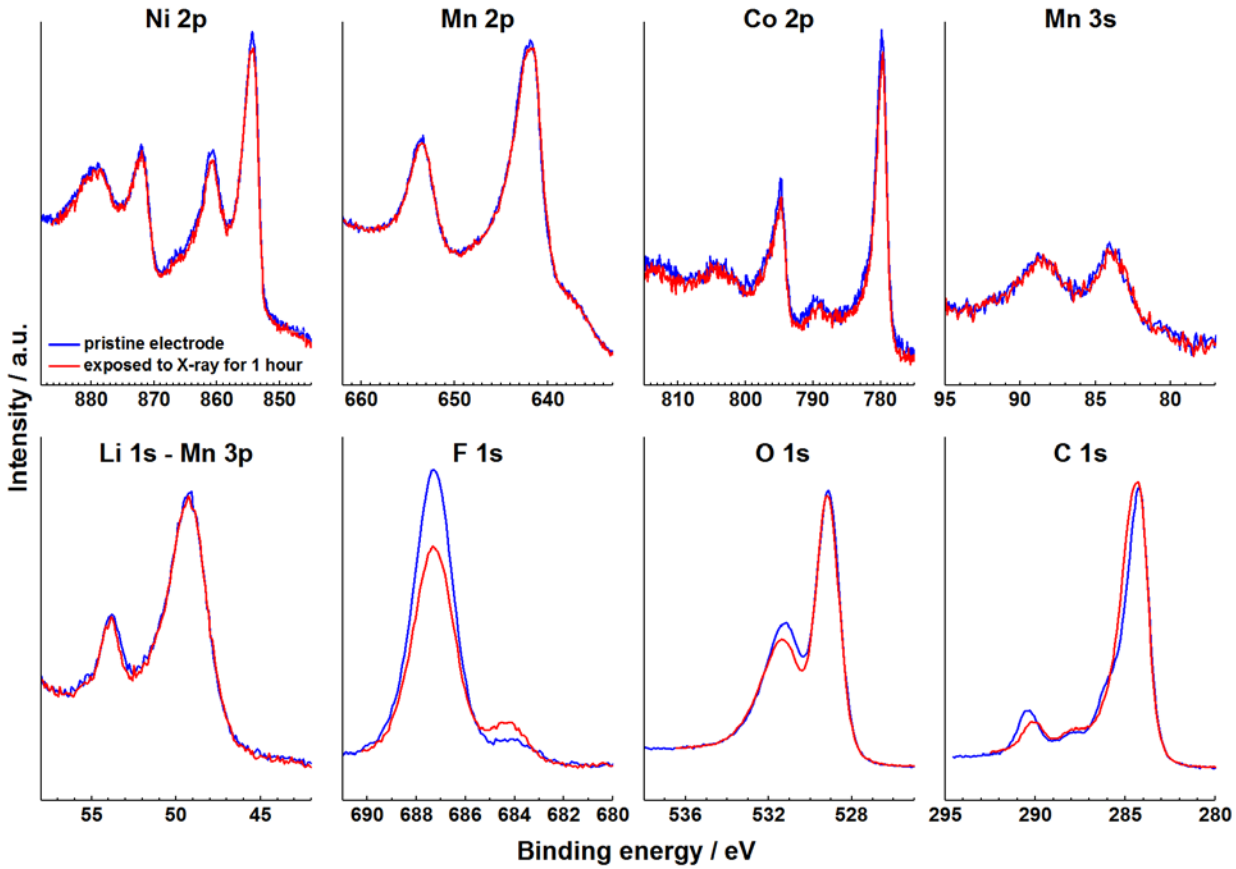

Figure 4-28: Comparison of XP spectra of pristine $LiNi_{0.4}Mn_{0.4}Co_{0.2}O_2$ electrodes to prove non-degradation after X-ray exposure for one hour.

Although the LIB electrodes containing carbon black are considered as conductive materials, the application of a flood gun is still necessary for their measurements. Since as illustrated in Figure 4-29 for the $LiNi_{0.4}Mn_{0.4}Co_{0.2}O_2$ pristine electrode, the absence of charge compensation can lead to uneven shifts for the different spectra of the same sample, that in consequence demands individual charge correction for each spectrum using external references. This might cause erroneous interpretation of the existing chemical species. The sequence of measurement in this example is C 1s, O 1s, Ni 2p, Mn 2p, Co 2p, Li 1s, Mn 3s, F 1s that leads to overall charging of 4.3, 4.2, 4.3, 4.1, 3.5, 3.8, 4.5, 4.5, for a measurement without flood gun and a repeated measurement after one hour relative to charge compensated measurement with utilizing flood gun. It might be that a time-dependent local charge-up must be considered. In consequence, for these materials, charge neutralization should always be applied to avoid artifacts.

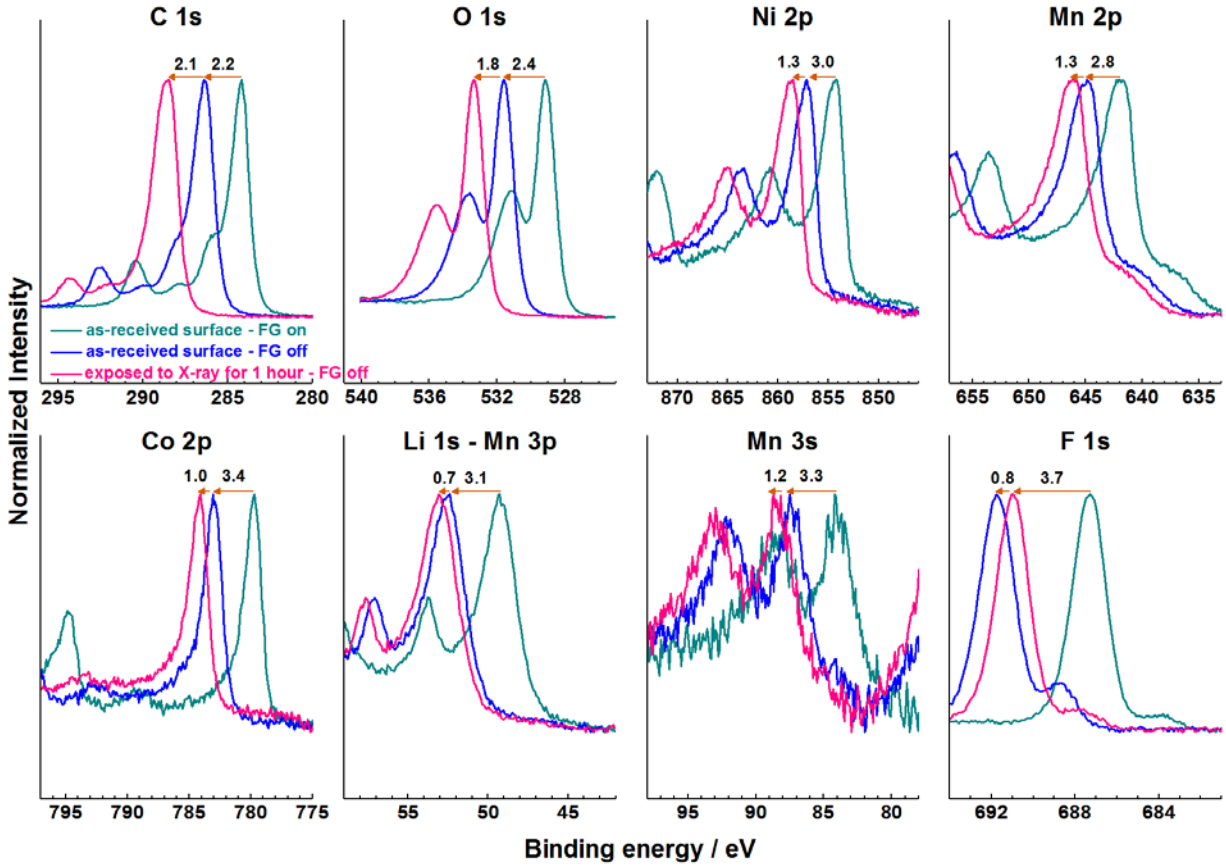

Figure 4-29: Uneven charging of $LiNi_{0.4}Mn_{0.4}Co_{0.2}O_2$ pristine electrodes in the absence of charge compensation.

Although it has been already shown in Chapter 4.1.3 that the spectrometers neutralization system can be used safely and without affecting the spectra, it is essential to exclude its influence also on the electrode materials since the electrodes contain accompanying components like carbon black and binder. The comparison of the normalized spectra of a $LiNi_{0.4}Mn_{0.4}Co_{0.2}O_2$ pristine electrode with (pink) and without (blue) utilizing flood gun shown in Figure 4-30, proves unambiguously that the flood gun does not affect the peak shape or FWHM of the spectra of the pristine electrodes. The weak differences in the intensity of the F 1s peaks in Figure 4-30 might originate from the sample inhomogeneity, as the different measurements were performed always on fresh surface areas.

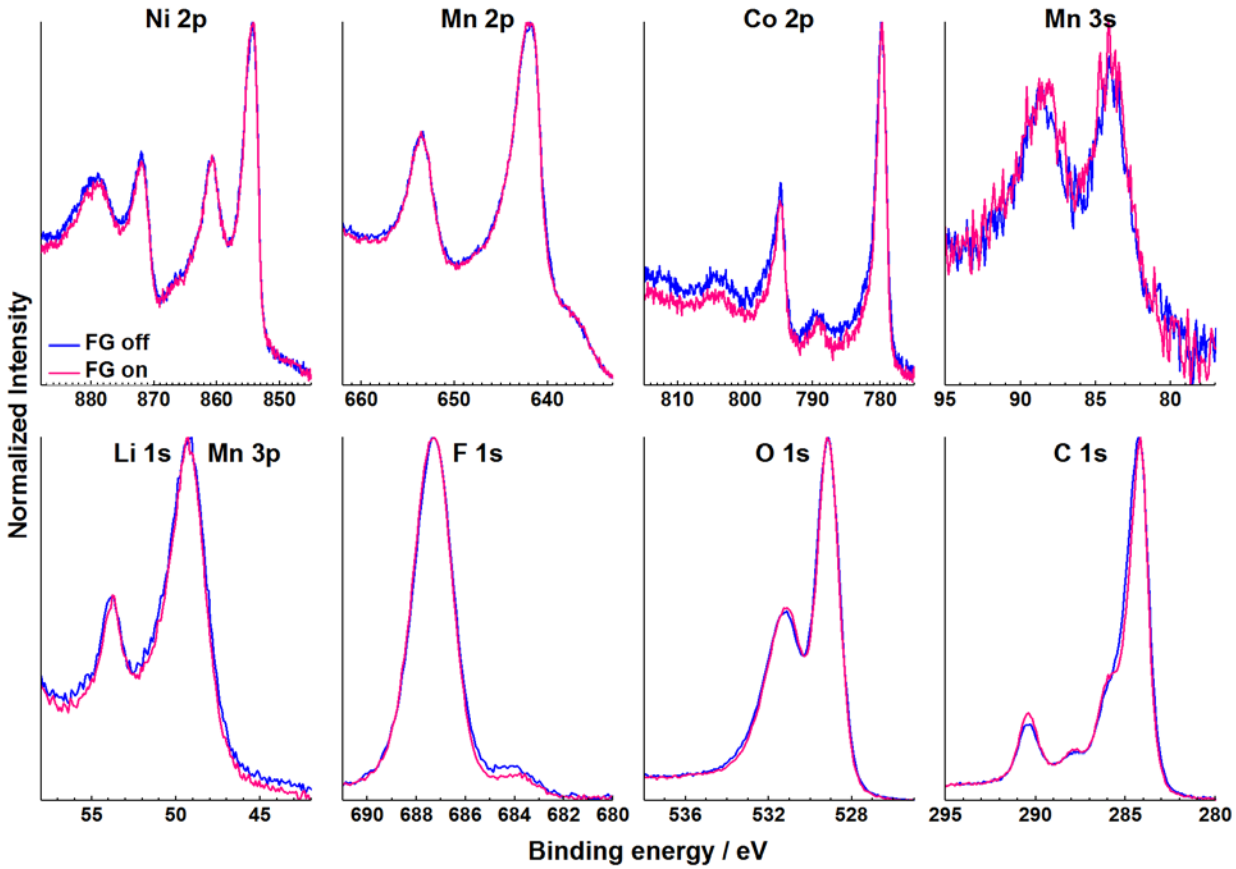

Figure 4-30: Normalized XP spectra of a $LiNi_{0.4}Mn_{0.4}Co_{0.2}O_2$ pristine electrode with (pink) and without (blue) utilizing the flood gun for surface charge compensation.

4.3.3.2. XPS characterization of the surface of pristine electrodes of $LiNi_{0.8-y}Mn_yCo_{0.2}O_2$ ($0 \leq y \leq 0.4$) compounds

Verifying the artifacts of XPS measurements on the LIB electrodes has already confirmed the applicability of the method on the electrodes without causing degradation of the samples. Therefore, based on the results of Chapter 4.3.3.1, for characterization of the electrode surfaces, the flood gun was necessarily utilized, and the spectra are referenced to the C 1s peak of graphite at 284.4 eV. Also, it is worth to mention that the fitting parameters for electrodes of $LiNi_{0.8-y}Mn_yCo_{0.2}O_2$ ($0 \leq y \leq 0.4$) compounds are kept firmly the same as for the powder materials.

Figure 4-31 shows the Co 2p spectra of pristine electrodes of $LiNi_{0.8-y}Mn_yCo_{0.2}O_2$ ($0 \leq y \leq 0.4$) compounds that are quite similar to the spectra obtained for powders of the same material as shown in Figure 4-17. With the similar reasoning made for the powders in Chapter 4.3.2.1, the Co ions present in the electrodes are attributed to Co^{3+} oxidation state. However, the peak intensity for some of the samples especially for $LiNi_{0.7}Mn_{0.1}Co_{0.2}O_2$ and $LiNi_{0.8}Co_{0.2}O_2$ stoichiometries is too

weak to make a precise evaluation of oxidation states. In those cases, the fitting is only a replication of what is already done on the samples with higher peak intensity, for example on the sample with a $LiNi_{0.4}Mn_{0.4}Co_{0.2}O_2$ nominal stoichiometry of the active material.

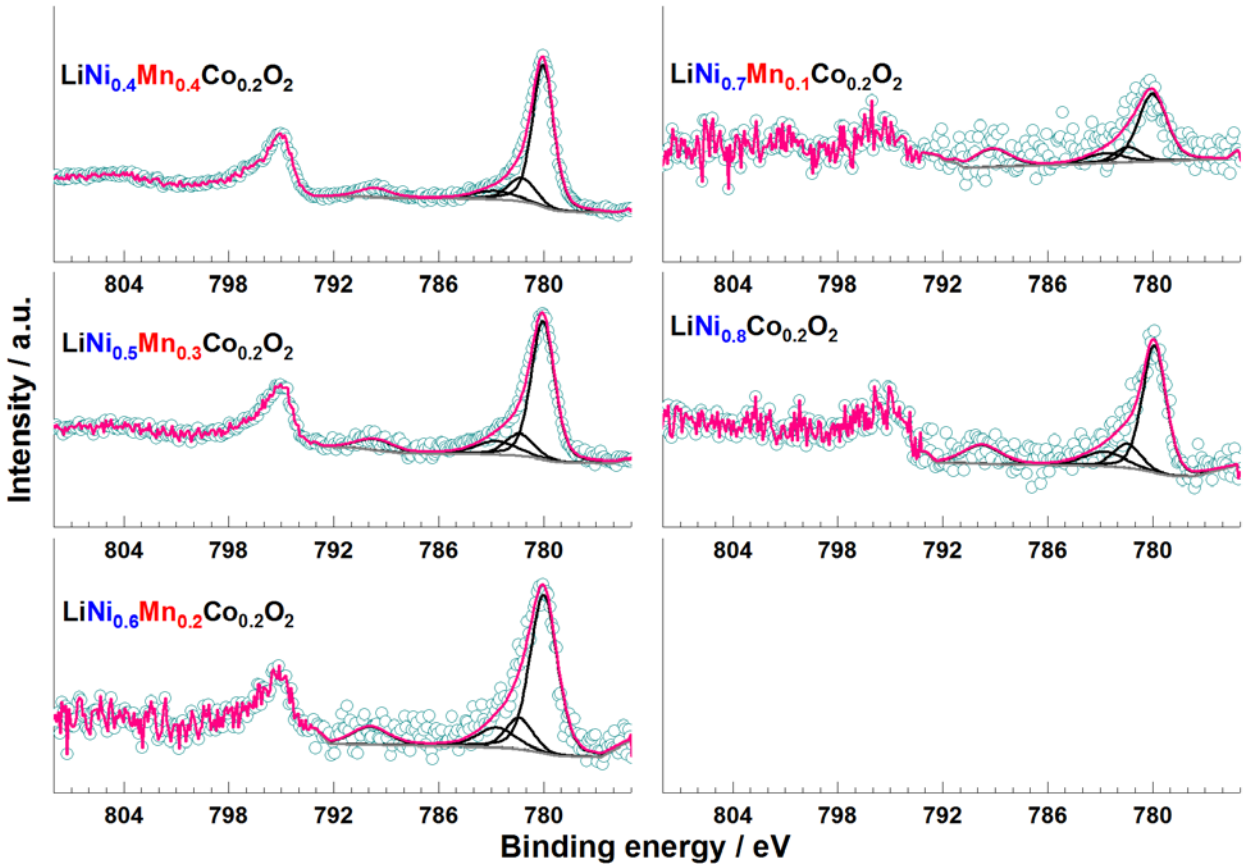

Figure 4-31: Co 2p spectra of pristine electrodes of the various $LiNi_{0.8-y}Mn_yCo_{0.2}O_2$ ($0 \leq y \leq 0.4$) compounds.

Similarly, as shown in Figure 4-32, the results of deconvolution of Mn 2p spectra of pristine electrodes of $LiNi_{0.8-y}Mn_yCo_{0.2}O_2$ ($0 \leq y \leq 0.4$) compounds are comparable to the analysis of their powders described in Chapter 4.3.2.2. Very few Mn^{3+} (10 % of total Mn ions) is resolved for the $LiNi_{0.4}Mn_{0.4}Co_{0.2}O_2$ stoichiometry in comparison to $LiNi_{0.5}Mn_{0.3}Co_{0.2}O_2$ (30 % of total Mn ions). The peak intensity coming from $LiNi_{0.6}Mn_{0.2}Co_{0.2}O_2$ and $LiNi_{0.7}Mn_{0.1}Co_{0.2}O_2$ stoichiometries is again so weak and hampers any precise judgment on the oxidation state of Mn ions.

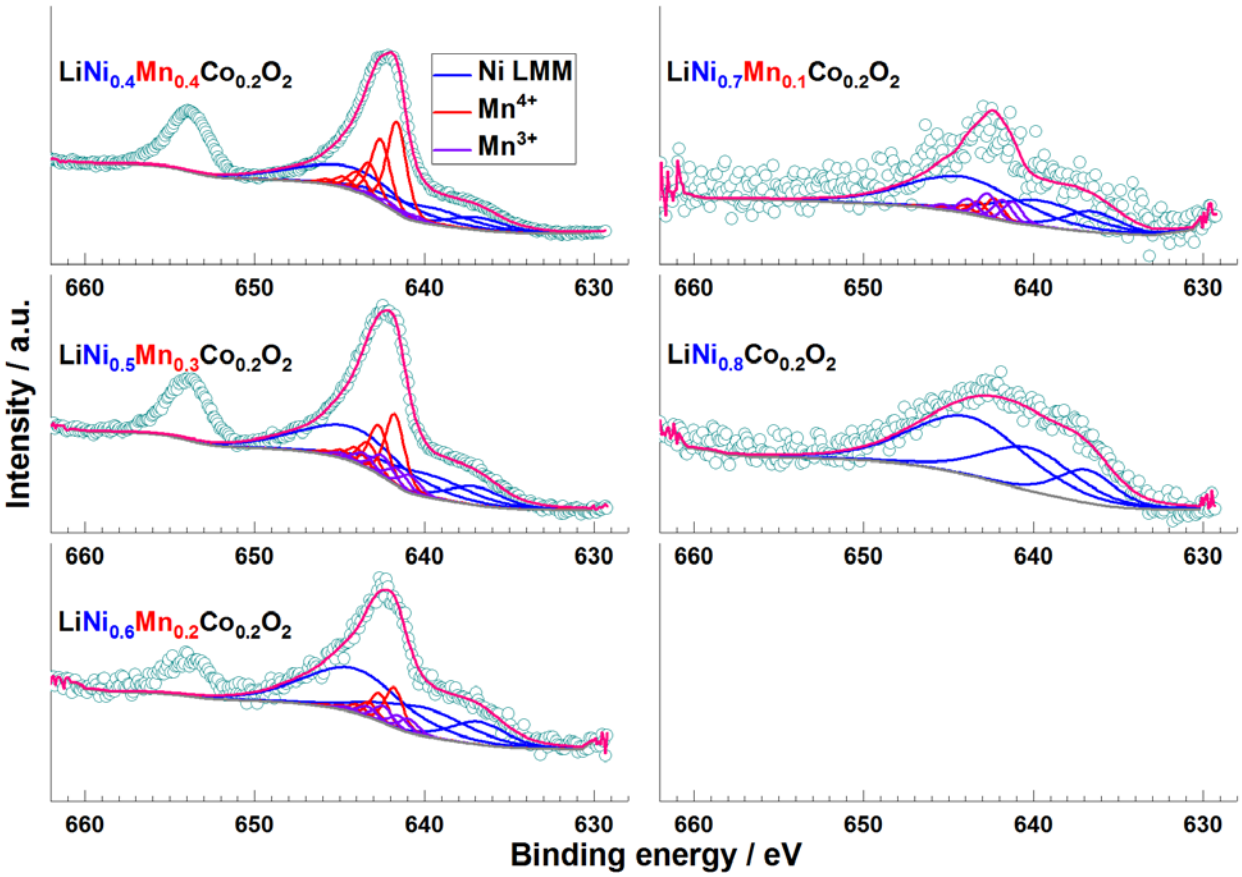

Figure 4-32: Mn 2p spectra of pristine electrodes of the various $LiNi_{0.8-y}Mn_yCo_{0.2}O_2$ ($0 \leq y \leq 0.4$) compounds.

The Mn 3s splitting of $LiNi_{0.4}Mn_{0.4}Co_{0.2}O_2$ and $LiNi_{0.5}Mn_{0.3}Co_{0.2}O_2$ stoichiometries which is around 4.6 and 4.9 eV respectively, cf. Figure 4-33, confirms the increasing amount of Mn^{3+} ions obtained from Mn 2p deconvolution. The increasing of splitting energy is a signature of increasing Mn^{3+} ions as stated in Chapter 4.2.1. Splitting energies obtained for $LiNi_{0.6}Mn_{0.2}Co_{0.2}O_2$ and $LiNi_{0.7}Mn_{0.1}Co_{0.2}O_2$ stoichiometries are not reliable for the characterization due to the very low signal to noise ratio.

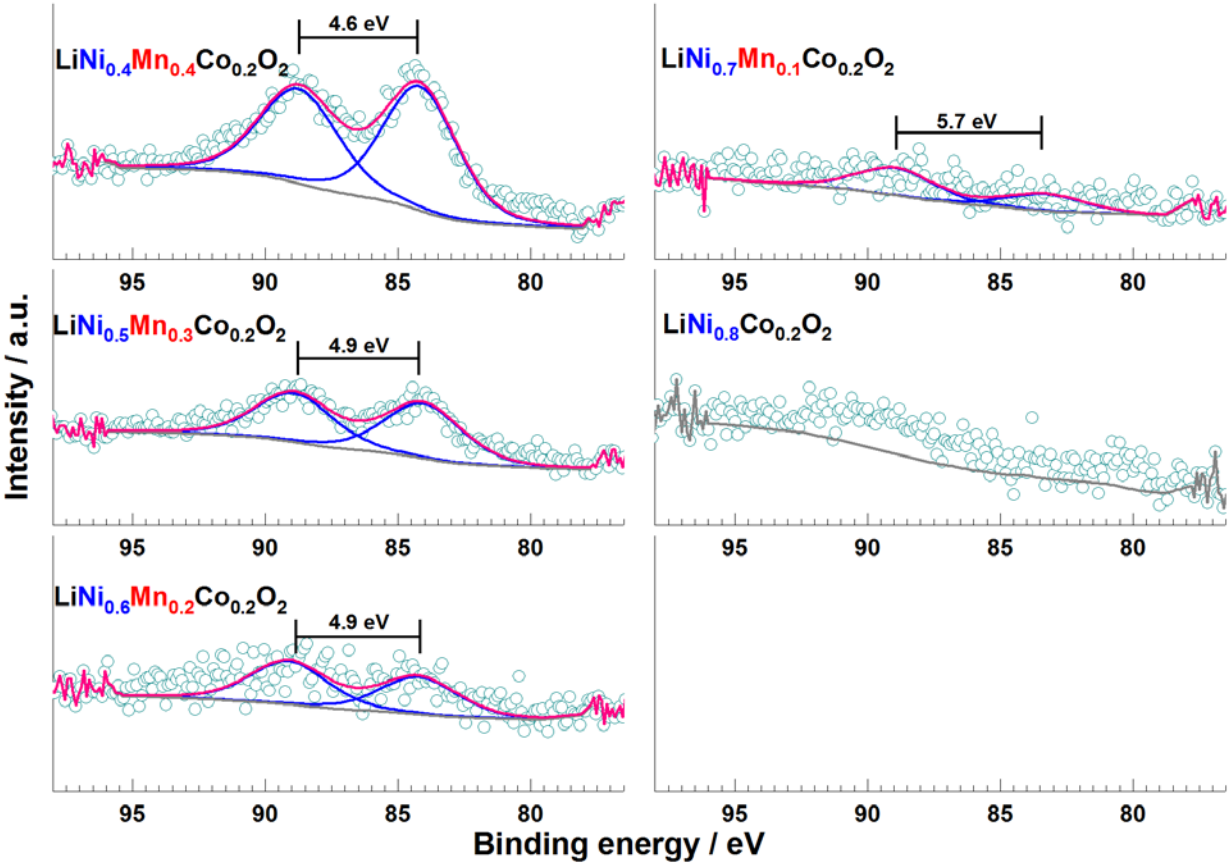

Figure 4-33: Mn 3s spectra of pristine electrodes of the various $LiNi_{0.8-y}Mn_yCo_{0.2}O_2$ ($0 \leq y \leq 0.4$) compounds.

Also, the Li species in pristine electrodes of $LiNi_{0.8-y}Mn_yCo_{0.2}O_2$ ($0 \leq y \leq 0.4$) compounds as depicted in Figure 4-34 show a similar trend to the Li species found in the powder materials cf. Figure 4-20 and Chapter 4.3.2.4, which could mean that the process of electrode preparation has hardly influenced the formation of Li_2CO_3 on the surface of these compounds. The samples with higher Ni content contain more Li_2CO_3 as the ratio of Li in Li_2CO_3 per Li in $LiNi_{0.8-y}Mn_yCo_{0.2}O_2$ ($0 \leq y \leq 0.4$) electrodes increases from 0.1 and 0.5, for NMC442, NMC532, to 2.0, 5.9, and 3.4 for NMC622, NMC712, and NMC802, respectively.

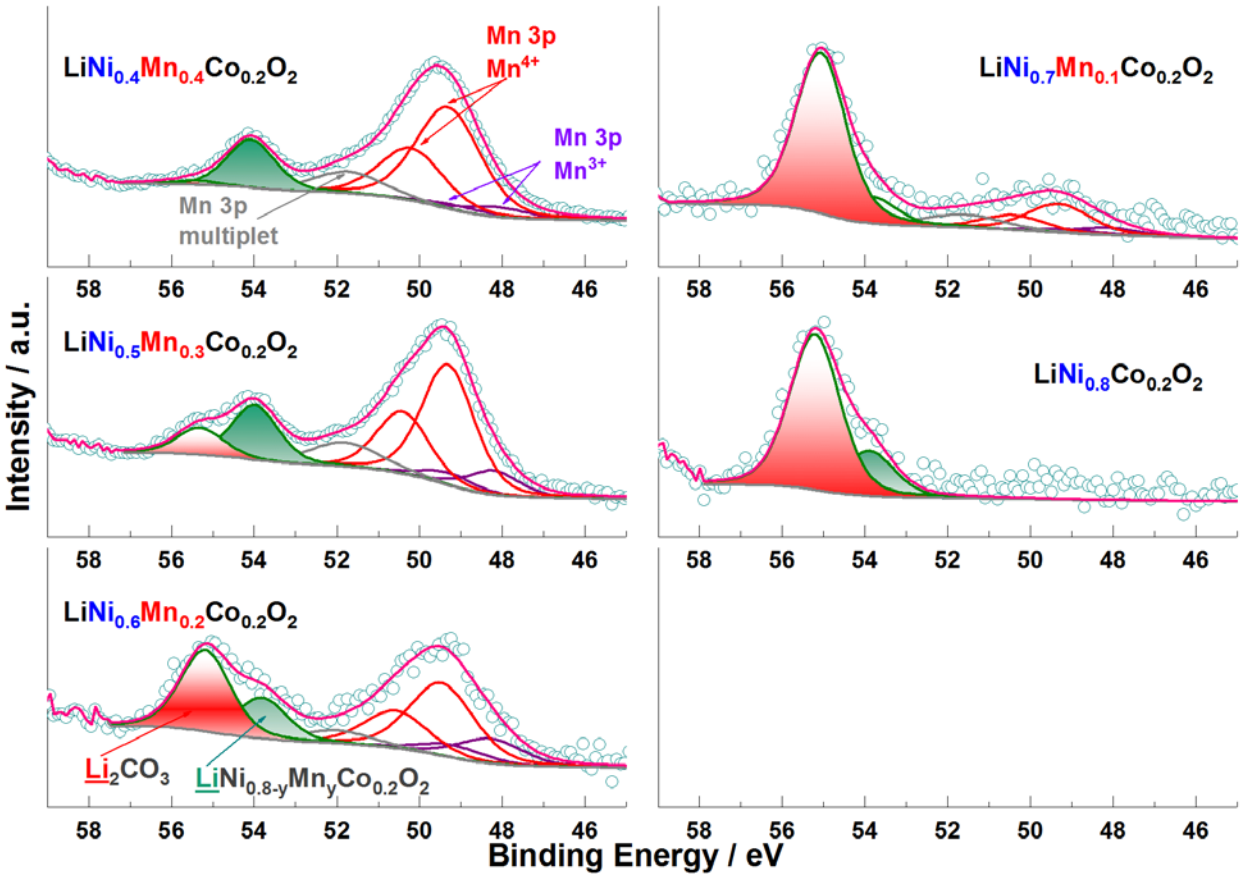

Figure 4-34: Mn 3p and Li 1s spectra of pristine electrodes of the various $LiNi_{0.8-y}Mn_yCo_{0.2}O_2$ ($0 \leq y \leq 0.4$) compounds.

As already shown for the powder samples (cf. Chapter 4.3.2.4), the presence of Li_2CO_3 is supported by the C 1s peak at 289.7 eV and O 1s peak at 531.7 eV, exemplarily shown for the $LiNi_{0.6}Mn_{0.2}Co_{0.2}O_2$ pristine electrode in Figure 4-35. The O 1s peak at 529.2 eV is assigned to the oxygen found in the lattice structure of the $LiNi_{0.8-y}Mn_yCo_{0.2}O_2$ ($0 \leq y \leq 0.4$) compounds whereas the peaks at higher binding energies are assigned to oxygen in $Li_2C\underline{O}_3$ at 531.7 eV and other contaminations like $Si\underline{O}_2$ and $S\underline{O}_4^{2-}$, C-O (at 533.0 eV) and C=O (at 530.9 eV) containing compounds. These contaminations are present in negligible quantities so that Si 2p and S 2p are not shown here. As described in Chapter 4.3.2.4, the Si and S impurities were also detected in the powder materials stemming from annealing and grinding process of the active material. The possible LiF formation is excluded by hardly detectable F 1s peak at 684.1 eV. The atomic percent of the deconvoluted C 1s peak at 290.8 eV amounting to 4.4 % is in a good agreement to the corresponding F 1s at 687.8 eV amounting to 9.6 % that reflects the $-CF_2-$ bonding of PVDF binder, cf, Figure 4-35a and Figure 4-35c.

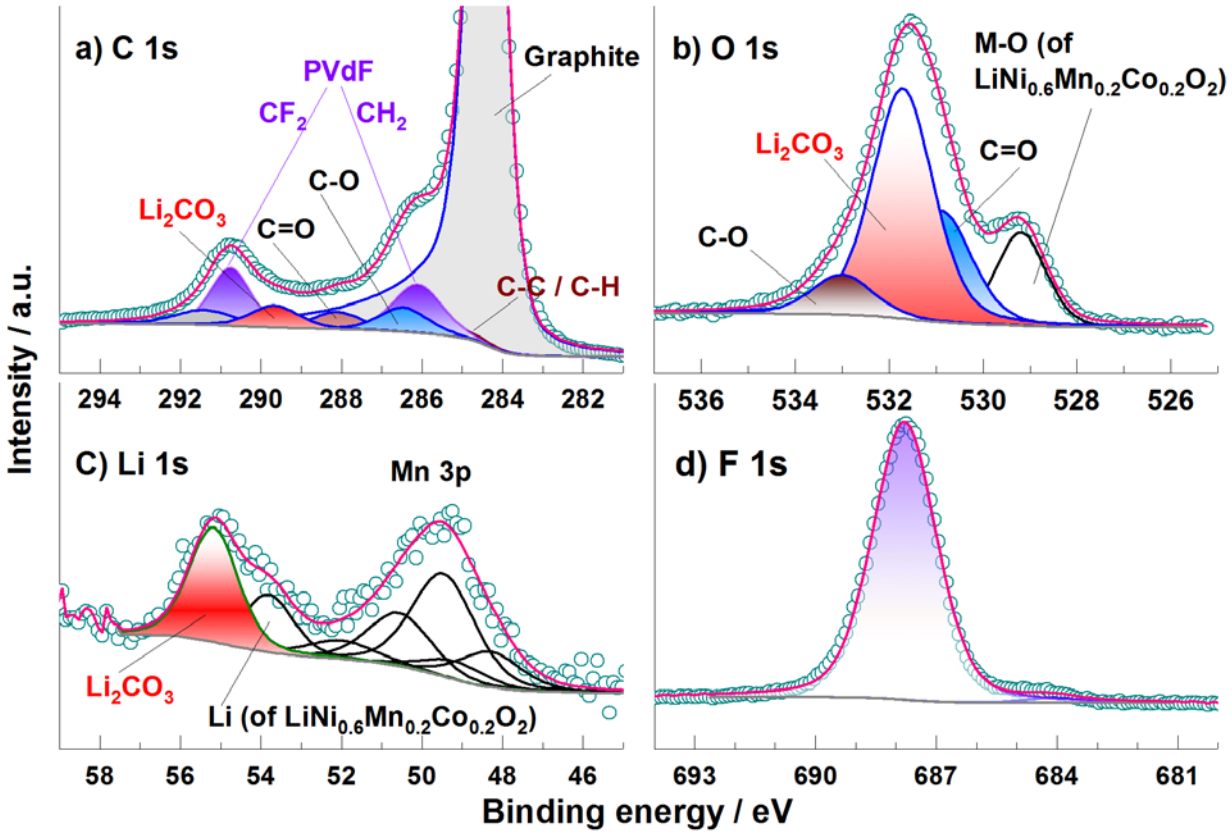

Figure 4-35: C 1s, Li 1s, O 1s, and F 1s spectra of the pristine $LiNi_{0.6}Mn_{0.2}Co_{0.2}O_2$ electrode.

Finally, the Ni $2p_{3/2}$ spectra of pristine electrodes of $LiNi_{0.8-y}Mn_yCo_{0.2}O_2$ ($0 \leq y \leq 0.4$) compounds are shown in Figure 4-36. The additional complexity of deconvoluting Ni 2p spectra of pristine electrodes in comparison to the pure powders originates from the overlapping F KLL peak of the PVDF binder with the Ni 2p energy range. The contribution of F KLL to the Ni $2p_{3/2}$ spectra is separated using an F KLL template obtained from the PVDF reference measurements described in Chapter 4.2.6. The peaks shaded in blue color in Figure 4-14 overlap with Ni 2p spectra of $LiNi_{0.8-y}Mn_yCo_{0.2}O_2$ ($0 \leq y \leq 0.4$) compounds. The very low intensity of active material in the samples with higher Ni content makes the evaluation of oxidation state of Ni in these stoichiometries very difficult and unreliable. However, the adapted fitting procedure indicates a decreasing fraction of the Ni^{2+} oxidation state by increasing Ni content in the active material namely $LiNi_{0.8-y}Mn_yCo_{0.2}O_2$ ($0 \leq y \leq 0.4$) compound series, reflecting the already identified chemical states for pure powders in Chapter 4.3.2.3.

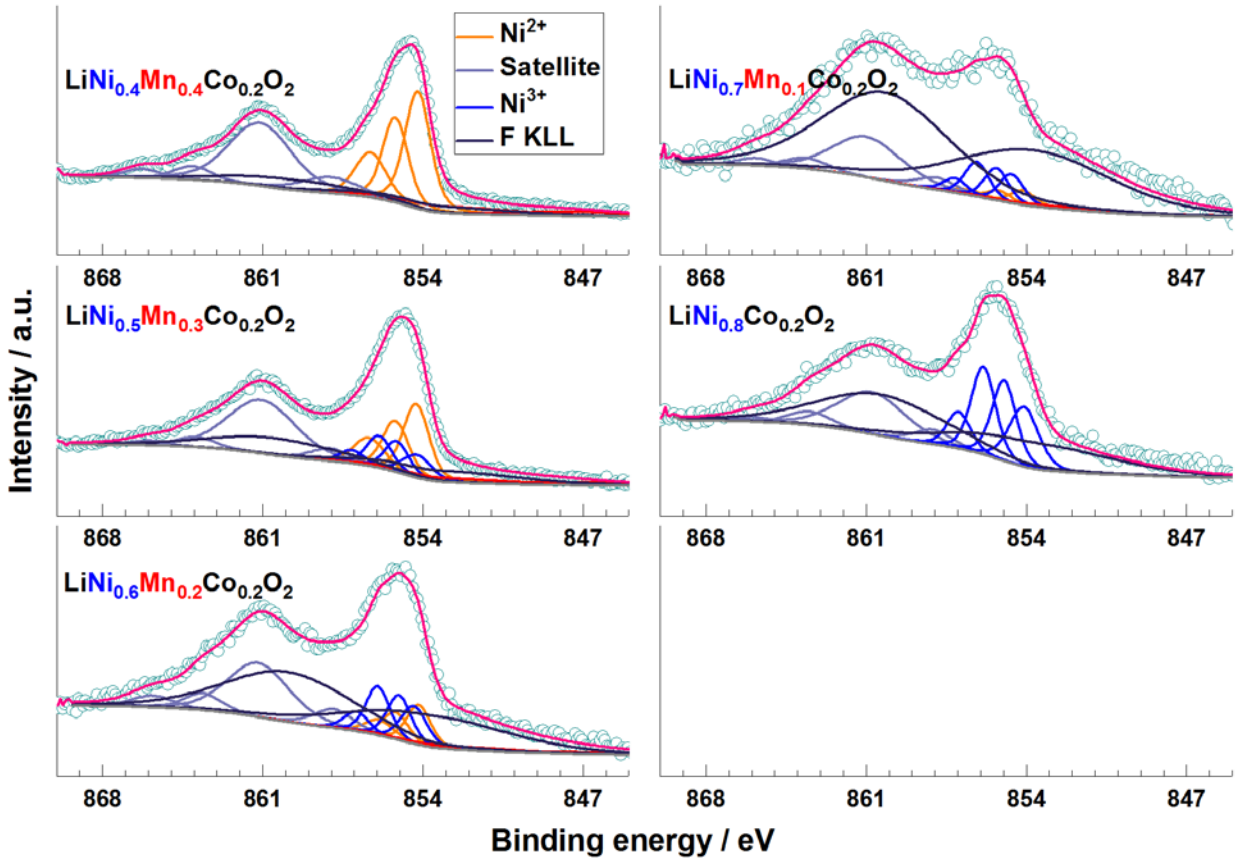

Figure 4-36: Ni $2p_{3/2}$ spectra of pristine electrodes of the various $LiNi_{0.8-y}Mn_yCo_{0.2}O_2$ ($0 \leq y \leq 0.4$) compounds.

Since all the fitting parameters are kept consistent in transferring from powders to the electrodes of $LiNi_{0.8-y}Mn_yCo_{0.2}O_2$ ($0 \leq y \leq 0.4$) compounds, only the fit parameters for Ni $2p_{3/2}$ spectra of pristine NMC electrodes are presented in Table 4-7 due to the addition of F KLL to the fitting procedure.

Table 4-7: Fit parameters for Ni $2p_{3/2}$ spectra of $LiNi_{0.8-y}Mn_yCo_{0.2}O_2$ ($0 \leq y \leq 0.4$) active materials in pristine electrodes.

Photoelectron Ni $2p_{3/2}$		$LiNi_{0.8}Co_{0.2}O_2$		$LiNi_{0.7}Mn_{0.1}Co_{0.2}O_2$			$LiNi_{0.6}Mn_{0.2}Co_{0.2}O_2$			$LiNi_{0.5}Mn_{0.3}Co_{0.2}O_2$			$LiNi_{0.4}Mn_{0.4}Co_{0.2}O_2$	
		Ni^{3+}	F KLL	Ni^{2+}	Ni^{3+}	F KLL	Ni^{2+}	Ni^{3+}	F KLL	Ni^{2+}	Ni^{3+}	F KLL	Ni^{2+}	F KLL
Peak 1	BE / eV	854.1	853.6	854.2	854.7	853.6	854.2	854.4	853.6	854.3	854.3	853.0	854.2	853.8
	FWHM / eV	1.5	8.1	1.3	1.3	8.1	1.3	1.4	8.1	1.3	1.3	7.9	1.3	8.1
	%	16.3	43.5	5.0	9.3	43.5	8.7	8.8	43.5	16.5	6.0	43.5	24.5	43.5
Peak 2	BE / eV	855.0	860.4	855.2	855.3	860.2	855.2	855.0	859.9	855.2	855.2	860.4	855.2	859.8
	FWHM / eV	1.3	6.6	1.3	1.3	6.6	1.3	1.3	6.6	1.4	1.3	6.6	1.3	6.7
	%	17.9	56.5	3.5	10.3	56.5	6.2	9.7	56.5	11.7	6.6	56.5	17.4	56.5
Δ Peak / eV		0.9	6.8	1.1	0.7	6.6	1.0	0.6	6.3	0.9	0.9	7.4	1.0	6.0
Peak 3	BE / eV	855.9		856.5	856.2		855.9	856.0		856.4	855.9		856.3	
	FWHM / eV	1.3		1.6	1.3		1.5	1.3		1.6	1.3		1.6	
	%	19.5		2.3	11.2		4.1	10.6		7.7	7.2		11.5	
Δ Peak / eV		0.9		1.3	0.9		0.7	1.0		1.1	0.8		1.1	
Peak 4	BE / eV	857.0		857.1			856.9			857.1				
	FWHM / eV	1.3		1.3			1.3			1.3				
	%	8.1		4.7			4.4			3.0				
Δ Peak / eV		1.1		1.0			0.9			1.2				
Peak 5	BE / eV	858.1		857.9			857.9			858.1			858.0	
	FWHM / eV	2.0		2.0			2.0			2.0			3.0	
	%	5.1		6.3			6.6			4.3			7.4	
Δ Peak / eV		1.1		0.8			1.0			1.0			1.7	
Peak 6	BE / eV	860.8		861.0			861.2			861.1			861.1	
	FWHM / eV	3.5		3.6			3.3			3.0			3.3	
	%	25.9		37.4			30.3			32.0			32.1	
Δ Peak / eV		2.7		3.1			3.3			3.0			3.1	
Peak 7	BE / eV	863.5		863.7			863.6			863.9			864.1	
	FWHM / eV	2.2		2.2			2.0			2.0			2.0	
	%	5.5		6.2			5.9			3.5			4.3	
Δ Peak / eV		2.7		2.7			2.4			2.9			3.0	
Peak 8	BE / eV	865.9		865.8			865.8			865.9			866.3	
	FWHM / eV	2.0		2.0			2.2			2.0			2.0	
	%	1.7		3.8			4.6			1.6			2.9	
Δ Peak / eV		2.4		2.1			2.2			2.0			2.2	

In conclusion, it can be confirmed that despite the complexity increase in the peak shape analysis of NMC pristine electrodes' XP spectra, for example due to overlapping of F KLL spectra stemming from PVDF binder with Ni 2p energy region, the developed approach for the identification of chemical states of transition metals in LIB materials considering all spectral features like multiplet splitting and characteristic satellites is applicable also on the electrodes. However, a major prerequisite is a highly homogeneous distribution of active material and binder/carbon black across the complete electrode to avoid a non-representative decrease in the active material at the topmost surfaces analyzed by XPS. This all is ready to be seen in Figure 4-26. Although all electrodes of the different $LiNi_{0.8-y}Mn_yCo_{0.2}O_2$ ($0 \leq y \leq 0.4$) compounds are processed in the same way, the intensity of peak stemming from the active material is dramatically varying among the electrodes. In consequence, the signal to noise ratio of Co, Ni, and Mn spectra (cf. Figure 4-31, Figure 4-32, and Figure 4-36) decrease by increasing the Ni content within the active material, which is obviously due to the fact that the total amount of detectable active material in the XPS information volume is decreasing. Figure 4-37 illustrates this for all surface compounds within the sampling depth indicating that the amount of active material at the surface can be drop down to 2 %. This issue will be discussed in more detail in Chapter 4.3.3.3. Nevertheless, an overall amount of around 17 % active material (and even a few percents less than that) can be reliably characterized.

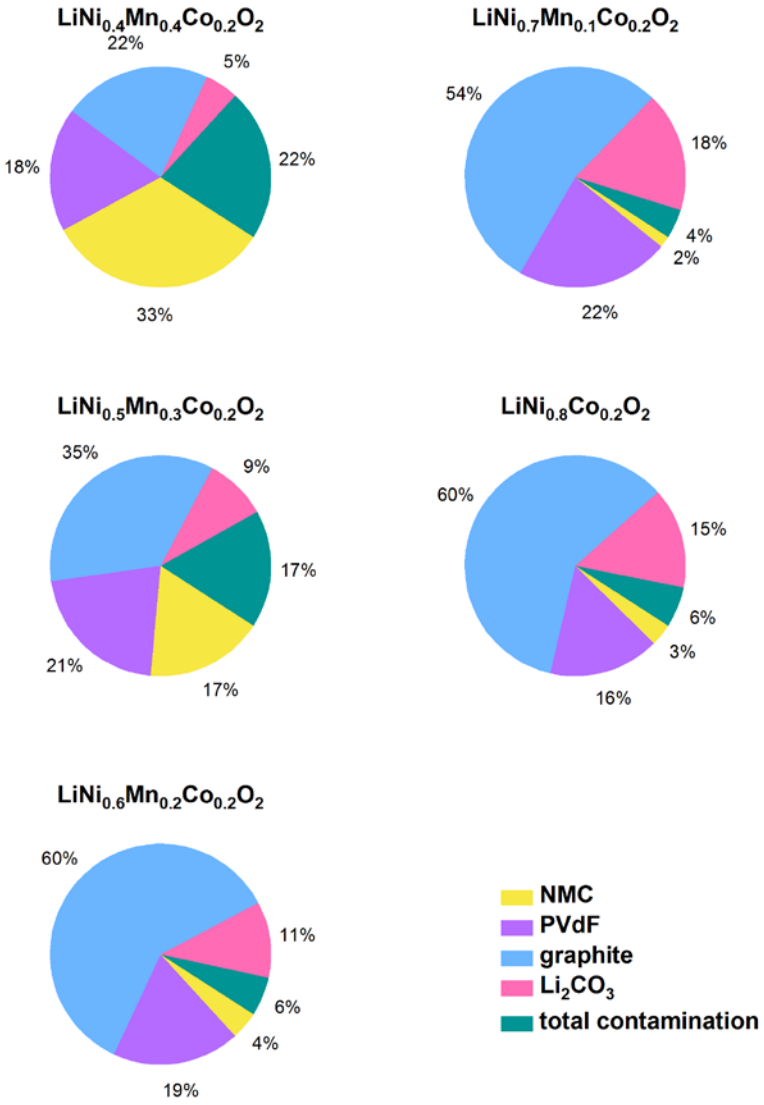

Figure 4-37: Distribution of identified components on the surface of pristine electrodes of the various $LiNi_{0.8-y}Mn_yCo_{0.2}O_2$ ($0 \leq y \leq 0.4$) compounds.

An interim conclusion of this chapter is that even under intensity limitations and based on the consistent fitting of 2p spectra of transition metals and with consideration of the F KLL Auger in the peak fitting of Ni 2p spectra, presented in Figure 4-31, Figure 4-32, and Figure 4-36, a quantification of Ni, Mn, and Co, in pristine electrodes of $LiNi_{0.8-y}Mn_yCo_{0.2}O_2$ ($0 \leq y \leq 0.4$) compounds is feasible. For a better visualization, the quantitative comparison in Figure 4-38 is based exclusively on the active material, i.e. binder and carbon black contributions are not taken into account. It is clearly to be seen that the expected trends and values as found for pure powders (cf. Figure 4-24) are similarly present in $LiNi_{0.4}Mn_{0.4}Co_{0.2}O_2$ and $LiNi_{0.5}Mn_{0.3}Co_{0.2}O_2$ pristine electrodes. Equally, the amount of Li is more, and the oxygen content is less than expected for the stoichiometric $LiNi_{0.8-y}Mn_yCo_{0.2}O_2$ ($0 \leq y \leq 0.4$) compounds (cf. Figure 4-38).

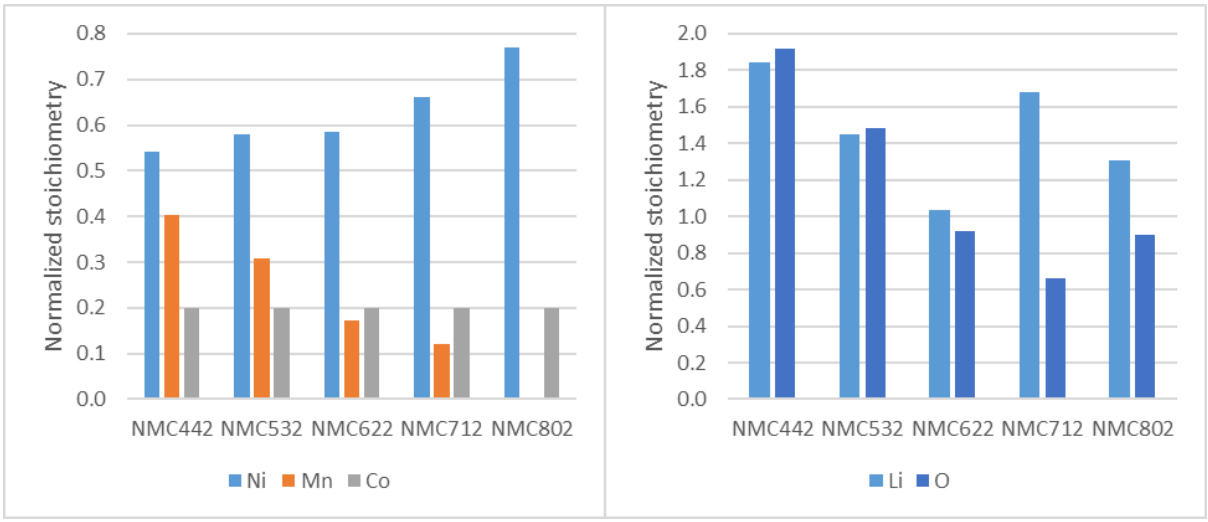

Figure 4-38: XPS quantification of transition metals (left) and Li and Oxygen (right) on the surfaces of $LiNi_{0.8-y}Mn_yCo_{0.2}O_2$ ($0 \leq y \leq 0.4$) compounds, normalized to Co=0.2.

Additionally, Table 4-8 summarizes the oxidation state of each of the transition metals and the overall oxidation state for transition metals in pristine electrodes compiled in respect to their normalized stoichiometry obtained from XPS analysis. As already discussed above, the uncertainty level of the resolved oxidation states for the samples with higher Ni content, namely NMC622, NMC712, and NMC802, is high because of the low active material's content within the XPS sampling depth. Nevertheless, and as a rule of thumb estimated from Figure 4-26 and Figure 4-37, an overall active material concentration of about 10 % in minimum within the information depth is sufficient to achieve a reliable XPS chemical state evaluation. This crucial point of active material's concentration gradients on topmost electrode surfaces in comparison to theoretically homogeneous bulk concentrations will be discussed in the next chapter.

Table 4-8: Compilation of oxidation states for $LiNi_{0.8-y}Mn_yCo_{0.2}O_2$ ($0 \leq y \leq 0.4$) pristine electrodes based on XPS data.

	NMC442	NMC532	NMC622	NMC712	NMC802
Ni^{3+} / Ni_{total} (%)	0	39	64	77	100
Mn^{3+} / Mn_{total} (from Mn 2p fit) (%)	10	31	38	70	
Co	Determined as Co^{3+} for all of the compounds				
Total oxidation state	+3.26	+3.12	+2.77	+2.83	+2.91

4.3.3.3. SEM and ToF-SIMS characterization of the surface of pristine electrodes of $LiNi_{0.8-y}Mn_yCo_{0.2}O_2$ ($0 \leq y \leq 0.4$) compounds

As already shown in the previous Chapter 4.3.3.2, the quantitative XPS characterization of the surface of the pristine $LiNi_{0.8-y}Mn_yCo_{0.2}O_2$ ($0 \leq y \leq 0.4$) electrodes strongly depends on the homogeneity of the dedicated active materials content across the electrode's thickness. Therefore, ToF-SIMS and SEM studies were additionally performed to investigate the active material's distribution.

The SEM images of the surface of pristine electrodes of $LiNi_{0.8-y}Mn_yCo_{0.2}O_2$ ($0 \leq y \leq 0.4$) compounds are shown in Figure 4-39. The enhanced material contrast by utilizing energy selective backscattered electron imagining (ESB) enables easily the differentiation between active material (high Z value, bright) and accompanying carbon black and binder (low Z value, dark) and finally the quantification of the active material at the electrode surface by image analysis. This analysis results in a decreasing active material's surface area of 63 %, 51 %, 24 %, 21 %, and 18 % for NMC442, NMC532, NMC622, NMC712 and NMC802 active materials, respectively, which strongly corroborates the XPS findings (cf. Figure 4-37).

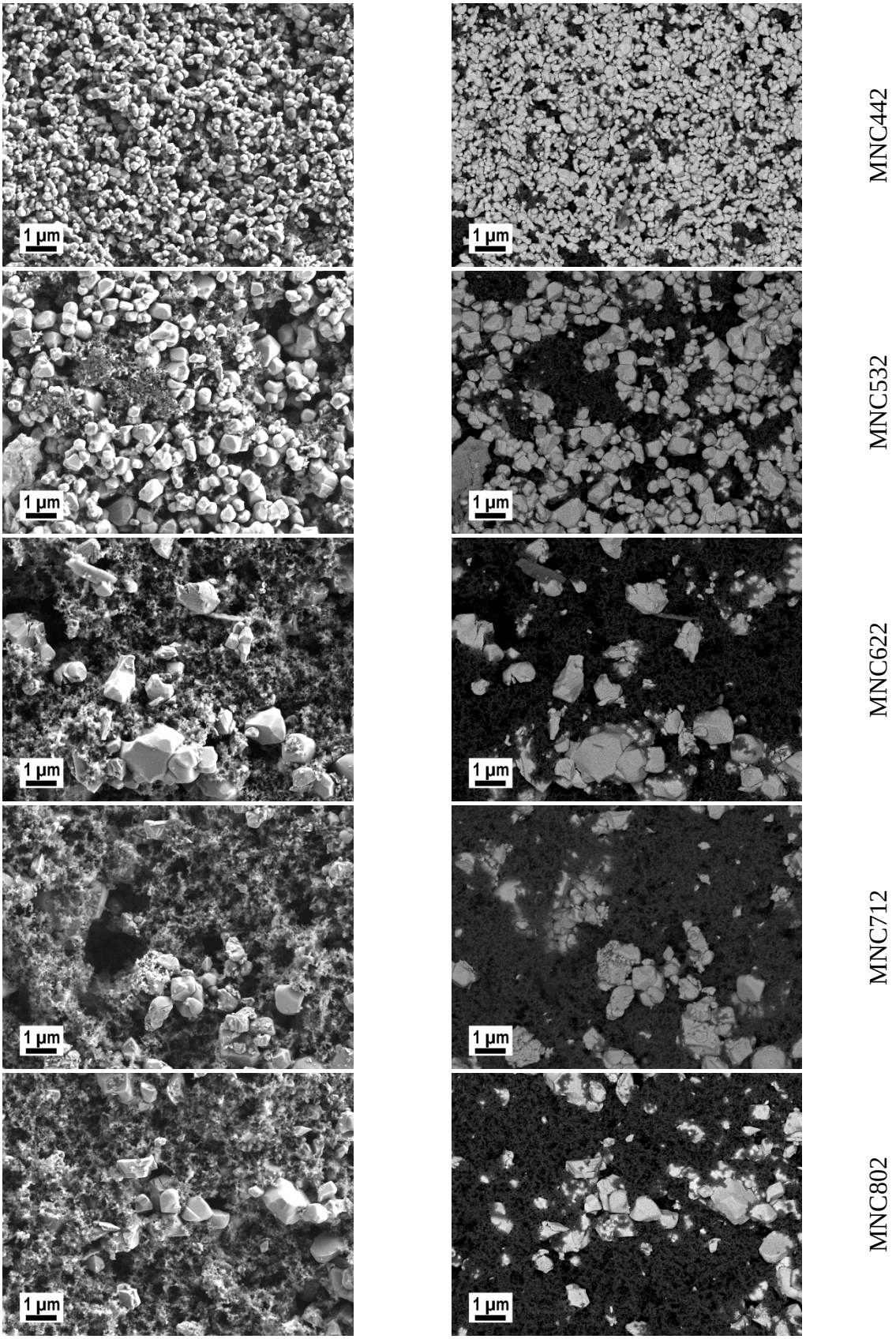

Figure 4-39: SEM images of $LiNi_{0.8-y}Mn_yCo_{0.2}O_2$ $(0 \leq y \leq 0.4)$ pristine electrodes, using secondary electrons (SE) at the left column and energy selective backscattered electrons (ESB) at the right column.

Finally, ToF-SIMS chemical images at a spatial resolution of < 1 µm again prove the inhomogeneous lateral distribution of the active material across the electrodes surfaces. This is shown for the pristine electrodes of $LiNi_{0.8-y}Mn_yCo_{0.2}O_2$ ($0 \leq y \leq 0.4$) compounds in Figure 4-40 for the transition metals in negative polarity using NiO_2^-, MnO_2^-, and CoO_2^- fragments whereas the chemical mapping of Li is depicted in Figure 4-41 in positive polarity using Li_3O^+ and Li_2OH^+ fragments. However, since the images were acquired using the delayed extraction mode (see details in Chapter 2.2.2.1), it is indispensable to use fresh or as-received area of the sample surface for both of the polarities due to the unavoidable method-induced damages (cf. Chapter 2.2) and, therefore, the respective images are stemming from adjacent areas.

The SEM images in Figure 4-39 suggest that the amount of available NMC active material at the electrode's surface changes depending on the size of the crystalline NMC particles, which is directly supported by the ToF-SIMS chemical images in Figure 4-40 and Figure 4-41. The small-sized NMC particles such as the particles in NMC442 sample (< 1 µm) obviously can be homogeneously distributed across the surface during coating and drying of the electrode. In contrast, large NMC particles probably can easily be displaced and forwarded by the doctor blade during the knife coating process whereas the space behind them is filled up with the low viscosity slurry, i.e. mainly carbon black. Additionally, the sedimentation of big particles can occur, which is already a known issue in the electrode coating procedure [128], [129].

In conclusion, an improved electrode fabrication resulting in homogeneous active material distribution across the overall electrode surface should open-up in general the applicability of the template approach of multiplet fitting of first-row transition metal XP spectra even for electrodes with a high amount of binder and carbon black.

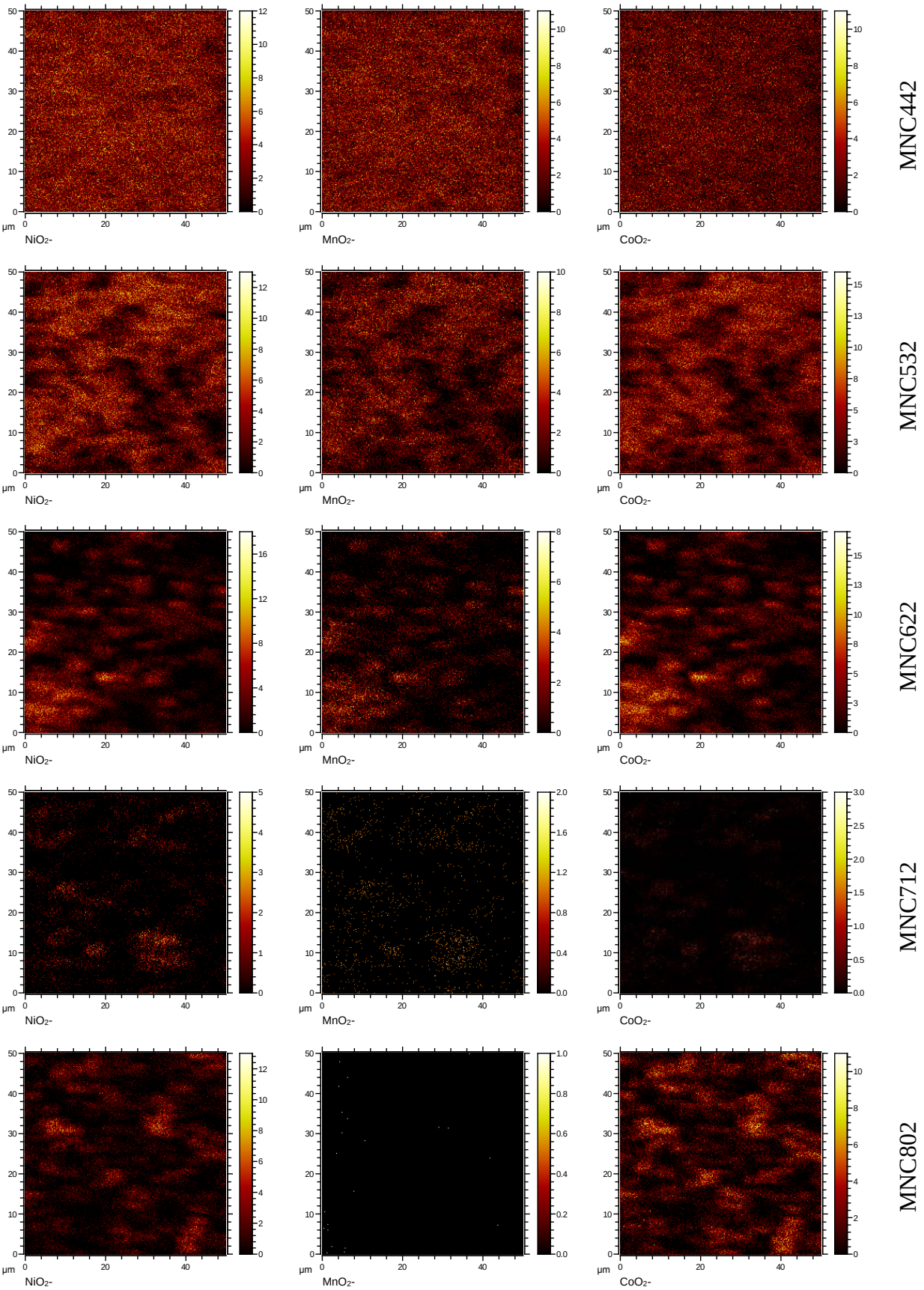

Figure 4-40: ToF-SIMS chemical images of $LiNi_{0.8-y}Mn_yCo_{0.2}O_2$ $(0 \leq y \leq 0.4)$ pristine electrode surfaces, using NiO_2^-, MnO_2^-, and CoO_2^- fragments.

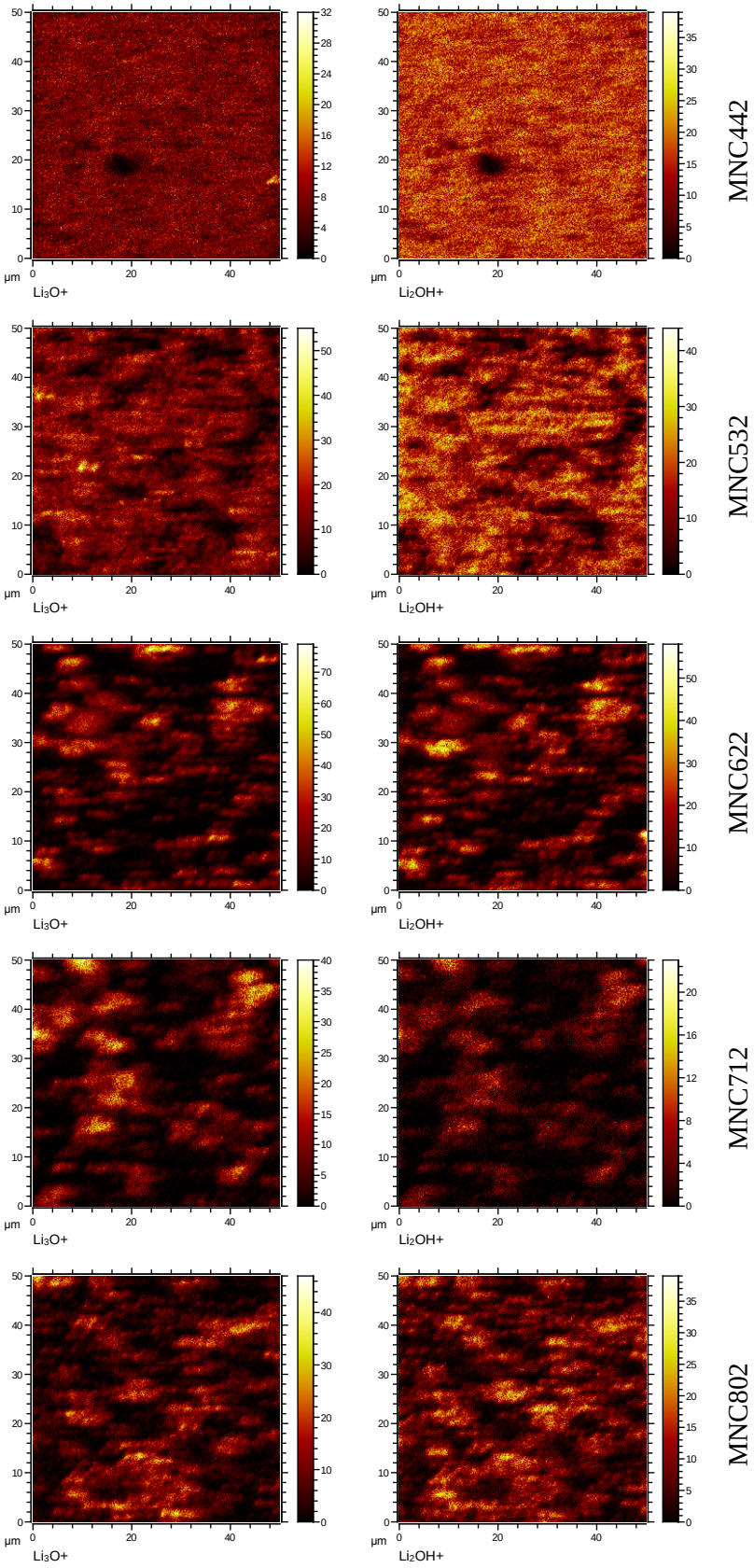

Figure 4-41: ToF-SIMS chemical images of Li on $LiNi_{0.8-y}Mn_yCo_{0.2}O_2$ ($0 \leq y \leq 0.4$) pristine electrodes surfaces, using Li_3O^+ and Li_2OH^+ fragments.

4.3.4. XPS characterization of cycled electrodes of the Li-Ni-Mn-Co-O system

The final step to prove the applicability of the developed fitting procedure using templates for transition metal 2p XP spectra deconvolution is the feasibility study on cycled electrodes of $LiNi_{0.8-y}Mn_yCo_{0.2}O_2$ ($0 \leq y \leq 0.4$) compounds, which is very important for the development and degradation studies on the LIBs. In addition to the complex spectral features of transition metals (i.e. multiplets, satellites, Auger peaks, and cross-talking) and the dilution of the active material via binder and carbon black in pristine electrodes, the major challenge in characterization of cycled electrodes is the protective layer which is also formed on the cathode's surface analogous to the anode's solid electrolyte interphase (SEI) and is termed the cathode electrolyte interphase (CEI). This CEI generally should consist of similar solvent and salt decomposition products as those found for negative electrodes, including LiF, $ROCO_2Li$, $ROCO_2M$, ROLi, MCO_3, Li_2CO_3, MF_2 (M = transition metal, R = alkyl group), polycarbonates, and poly(ethylene oxide) [130]–[132] and, as an additional topmost layer, might cause further decreases of the XPS peak intensity of the active material's constituents.

For this study, the pristine electrodes of $LiNi_{0.8-y}Mn_yCo_{0.2}O_2$ ($0 \leq y \leq 0.4$) compounds presented in Chapter 4.3.3 were cycled under the conditions described in detail in the experimental Chapter 3.4.3. For each stoichiometry of the $LiNi_{0.8-y}Mn_yCo_{0.2}O_2$ ($0 \leq y \leq 0.4$) compound series, two electrochemical cells were prepared and cycled up to the 5^{th} cycle. The cells subsequently were dismounted at 4.2 V (charged state) and 3.0 V (discharged state) potentials to be analyzed with XPS. However, the discharged $LiNi_{0.4}Mn_{0.4}Co_{0.2}O_2$ sample failed to deliver any voltage after the second cycle, cf. Chapter 3.4.3, Figure 3-1. Nevertheless, to track any degradation reasons which could be detectable by XPS, it was not sorted out of the measured samples. Due to time constraints, the necessary repeats, unfortunately, could not be carried out in this work. However, this is not decisive, since this study shall only prove the applicability of the fit procedure to XPS spectra of cycled electrode surfaces in principle. On the other hand, these results underpin the applicability of XPS in LIB failure analysis to elucidate degradation mechanism's details.

In order to elucidate the chemical state of transition metals in cycled electrodes, the XPS spectra were fitted with the same parameters and procedure as in Chapter 4.3.3.2 for the pristine electrodes. Fortunately, no significant reduction of the signal intensity due to CEI was observed for the cycled samples as shown in Figure 4-42 to Figure 4-46.

Only the Ni $2p_{3/2}$ spectra of cycled electrodes' surface of NMC442 and NMC 532 in Figure 4-42 indeed have sufficient intensity to determine Ni^{2+} and Ni^{3+} states for charged and discharged states when applying the developed template approach for the multiplet evaluation. In particular,

$LiNi_{0.5}Mn_{0.3}Co_{0.2}O_2$ in the discharged state is fitted with mixed Ni^{2+} and Ni^{3+} multiplet templates while in the charged state, the Ni^{3+} template alone is sufficient to properly fit the multiplet. According to literature [68], [133]–[135], in the NMC cathode materials, Ni^{2+} and Co^{3+} are the electrochemically active ions and the charge compensation during lithium extraction (i.e. charging) must be accompanied by the oxidation of Ni^{2+} to Ni^{3+} and Ni^{4+}, and Co^{3+} to Co^{4+}; however considering the cut-off potential of 4.2 V applied on $LiNi_{0.8-y}Mn_yCo_{0.2}O_2$ ($0 \leq y \leq 0.4$) electrodes, the activation of Co^{3+}/Co^{4+} redox couple is unlikely. However, in the absence of proper reference material for Ni^{4+} and Co^{4+} chemical states, this theory hardly can be proved experimentally by XPS measurements. Nevertheless, the differentiation between Ni ions in discharged (i.e. mixed oxidation state in powder, pristine electrode, and discharged cathode) and charged electrodes (Ni^{3+}) is already a major step towards comprehensive and reliable LIB characterization based on the deconvolution of such complex spectra especially in coherence with the theoretical expectation. The fitting parameters of Ni 2p spectra are compiled exemplarily for the charged and discharged electrodes of $LiNi_{0.5}Mn_{0.3}Co_{0.2}O_2$ in Table 4-9. The Ni 2p spectra of the failed discharged NMC442 cell in Figure 4-42 is more dominated by F KLL spectra in comparison to other samples, the respective high fluorine content might be a result of this failure.

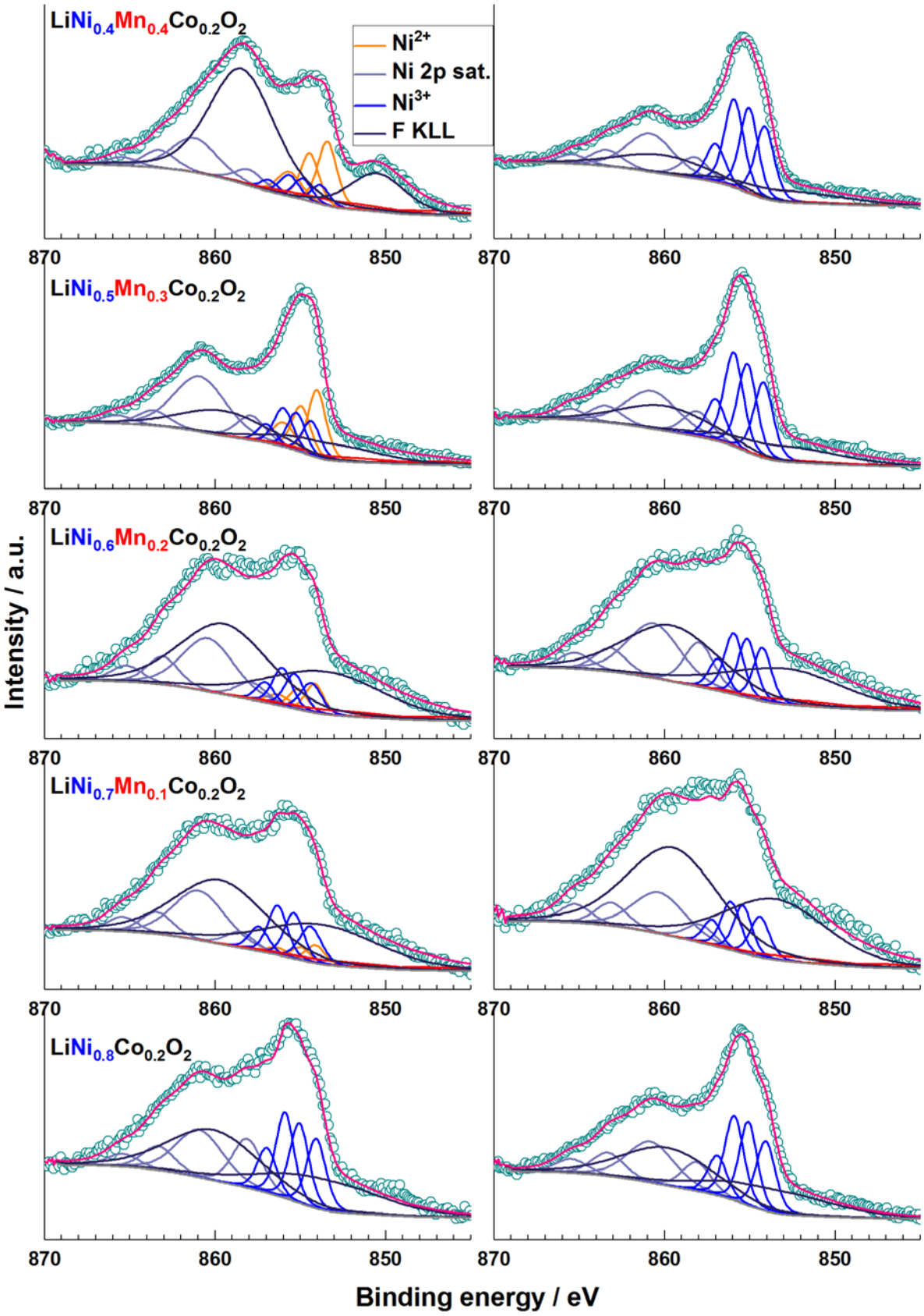

Figure 4-42: Comparison of the Ni $2p_{3/2}$ spectra of cycled electrode surfaces of $LiNi_{0.8-y}Mn_yCo_{0.2}O_2$ ($0 \leq y \leq 0.4$) compounds in the discharged (left column) and charged (right column) state.

For both the charged and discharged samples of all stoichiometries the Co 2p spectra in Figure 4-43, clearly indicate the Co^{3+} oxidation state, as the peak intensity allows for reliable resolving of the peak structure (even for the failed discharged $LiNi_{0.4}Mn_{0.4}Co_{0.2}O_2$ cell). These results confirm that under 4.2 V cut-off potential, no oxidation of Co ions happens, although probable Co^{4+}, in general, is difficult to be identified by XPS. Moreover, these results are in a good agreement with the theoretically expected Co^{3+} state for $LiNi_{0.8-y}Mn_yCo_{0.2}O_2$ ($0 \leq y \leq 0.4$) compounds in charged and discharged electrodes when the cut-off potential is 4.2 V.

As already seen for the pristine electrodes in Chapter 4.3.3.2, the intensity of all Mn photoelectron peaks (Mn 2p, Mn 3s, Mn 3p) necessary to reliably elucidate the chemical state of Mn is only sufficient for the $LiNi_{0.4}Mn_{0.4}Co_{0.2}O_2$ and $LiNi_{0.5}Mn_{0.3}Co_{0.2}O_2$ compositions (cf. Figure 4-44 to Figure 4-46). Finally, only the NMC532 data are appropriate for the fitting procedure. Here the majority of Mn ions in discharged NMC532 are in the Mn^{4+} state while the majority in charged NMC532 belongs to Mn^{3+} ions. This is actually surprising, since for such compositions, theoretically, the Mn ions should preserve their oxidation state in the cycling window of 3 V to 4.2 V selected for these samples. In principle one could speculate that X-ray-induced reduction might be the reason for this behavior, however, this would be contradictory to the behavior of e.g. Ni and must remain an open question. Nevertheless, the important major proof of the applicability of the developed template approach for chemical state evaluation of first-row transition metals by means of XPS was also doubtlessly demonstrated for Mn compounds in cycled electrodes.

The behavior of Li is shown in Figure 4-46. The failed discharged $LiNi_{0.4}Mn_{0.4}Co_{0.2}O_2$ cell shows a high amount of a Li 1s component at 55.6 eV attributed to Li_2CO_3 and LiF contrary to the very low amount of Li_2CO_3 detected for a pristine electrode of the same compound, cf. Figure 4-35 and Figure 4-37. The existence of the high LiF amount in this particular sample is confirmed by the corresponding F 1s peak at 685.1 eV.

For all other components, the expected trend of low lattice Li concentration (Li 1s = 54.0 eV) in charged electrodes compared to discharged electrodes is traceable from the normalization of Li 1s peak at 54.0 eV to the detected Co concentration of the active material in the cycled electrodes. The estimated Li normalized stoichiometry for charged samples is almost around 0.7 whereas it is more than 1.0 for the discharged samples. In addition, the discharged samples again show a high amount of lattice Li (compared to the expected bulk stoichiometry) similar to the powders and pristine electrodes of $LiNi_{0.8-y}Mn_yCo_{0.2}O_2$ ($0 \leq y \leq 0.4$) compounds.

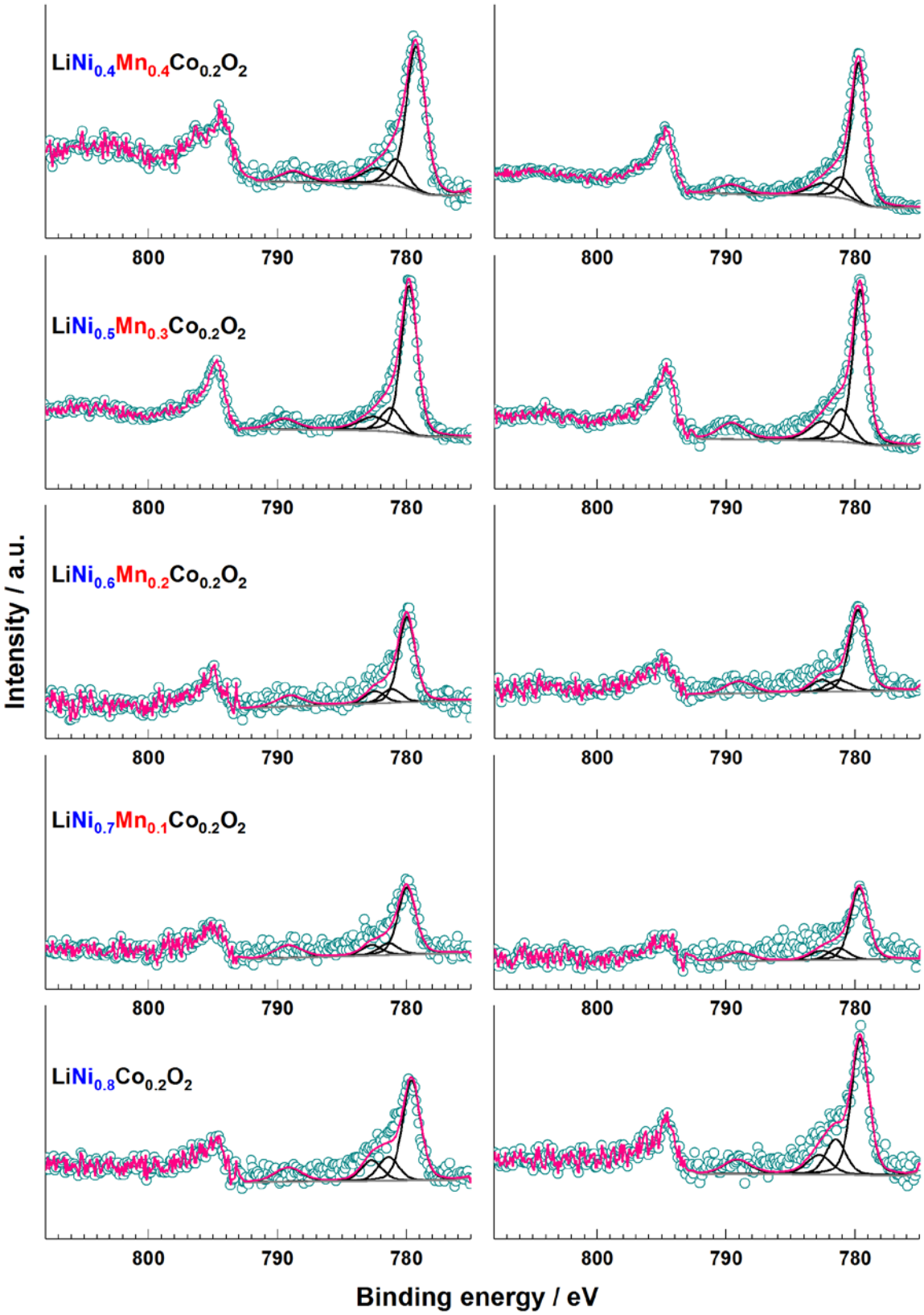

Figure 4-43: Comparison of the Co 2p spectra of cycled electrode surfaces of $LiNi_{0.8-y}Mn_yCo_{0.2}O_2$ ($0 \leq y \leq 0.4$) compounds in the discharged (left column) and charged (right column) state.

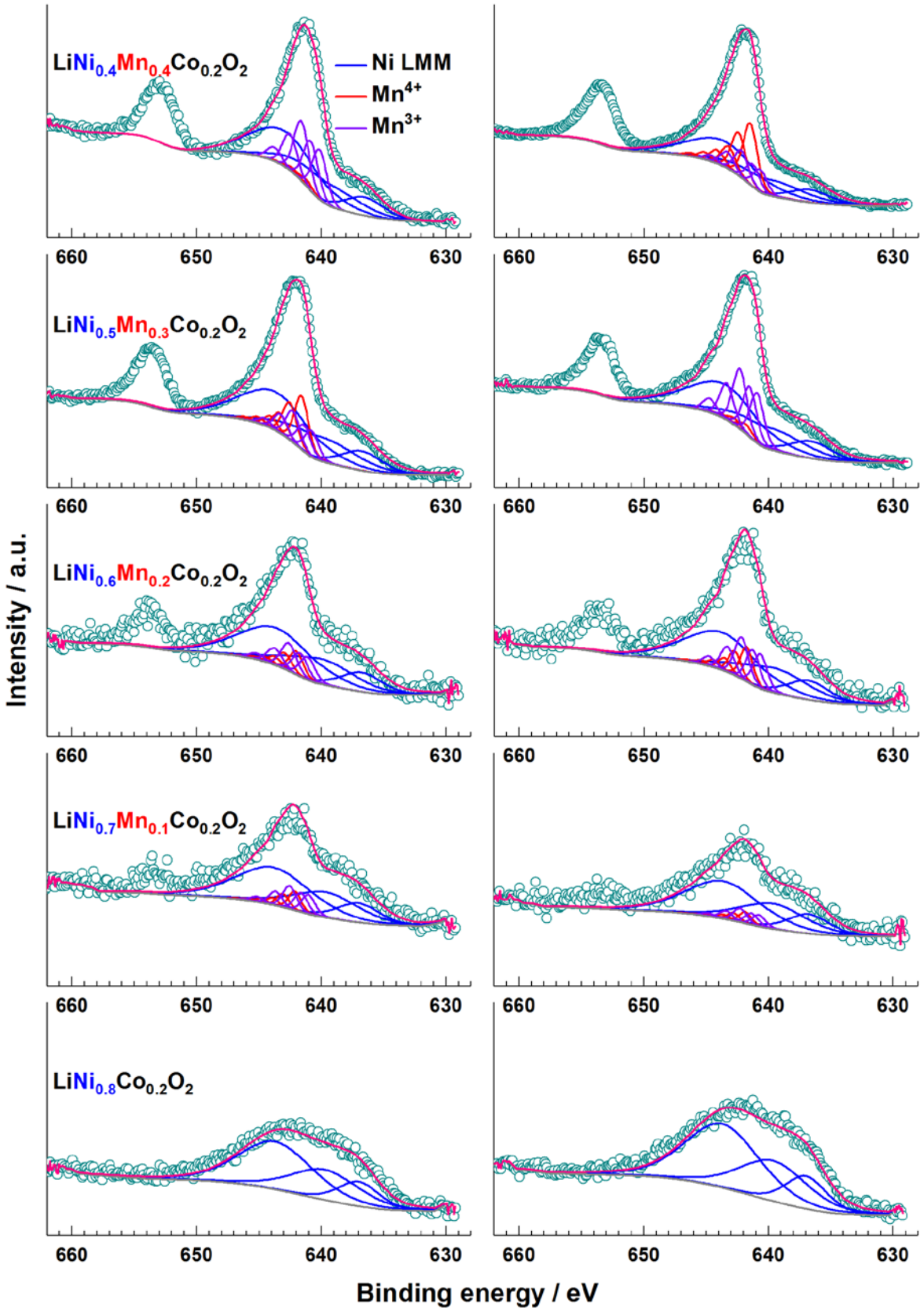

Figure 4-44: Comparison of the Mn 2p spectra of cycled electrode surfaces of $LiNi_{0.8-y}Mn_yCo_{0.2}O_2$ ($0 \leq y \leq 0.4$) compounds in the discharged (left column) and charged (right column) state.

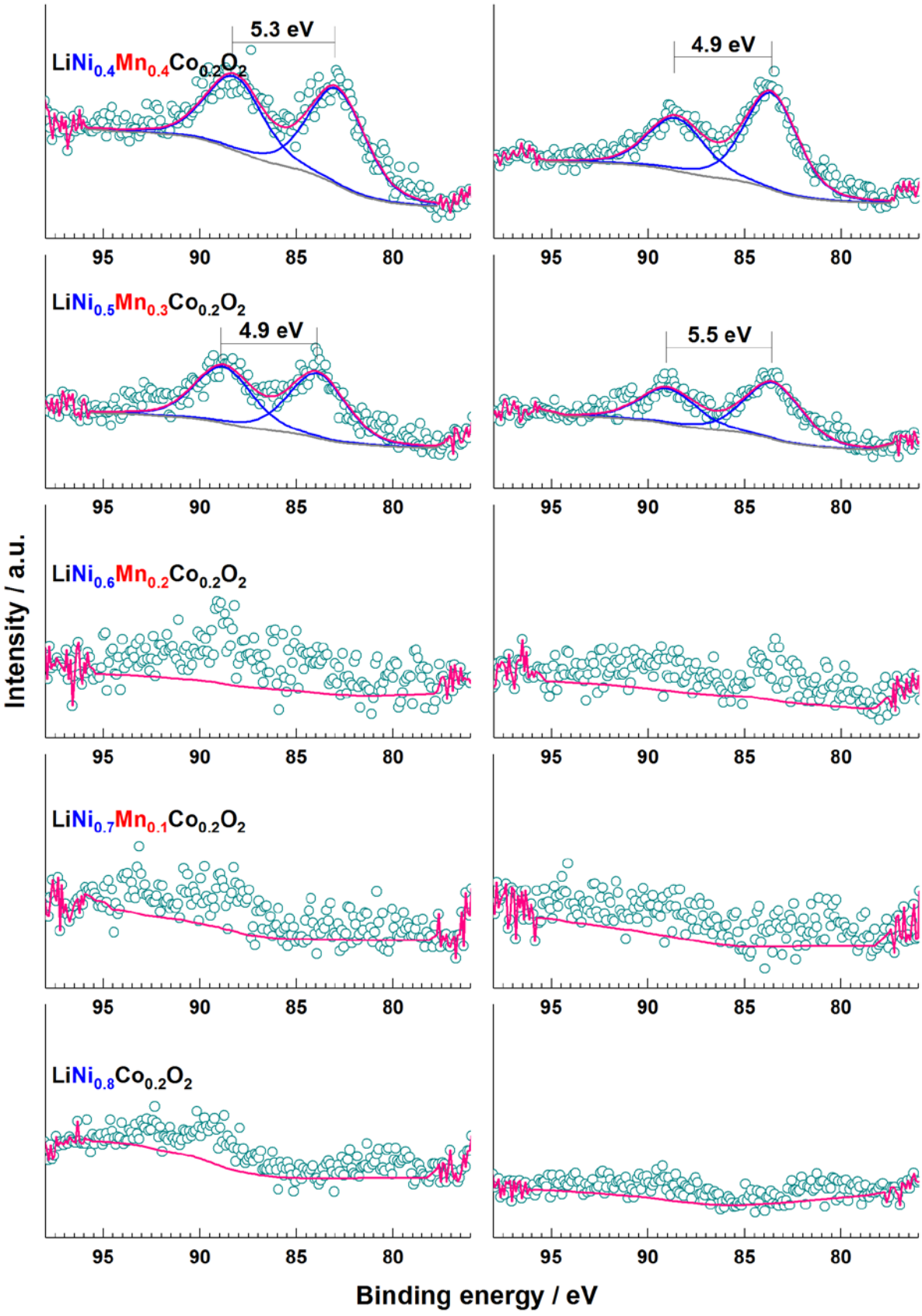

Figure 4-45: Comparison of the Mn 3s spectra of cycled electrode surfaces of $LiNi_{0.8-y}Mn_yCo_{0.2}O_2$ ($0 \leq y \leq 0.4$) compounds in the discharged (left column) and charged (right column) state.

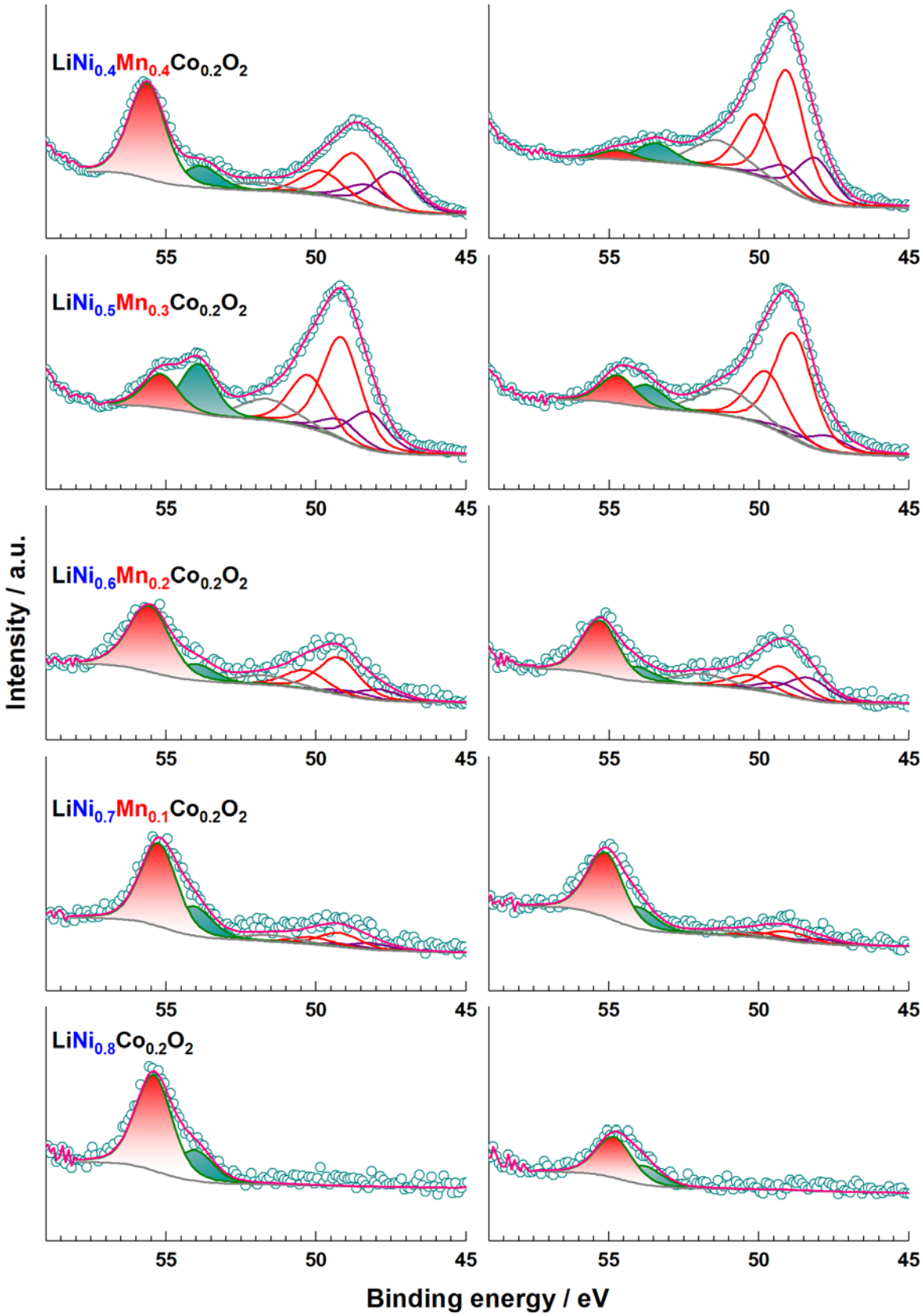

Figure 4-46: Comparison of the Mn 3p and Li 1s spectra of cycled electrode surfaces of $LiNi_{0.8-y}Mn_yCo_{0.2}O_2$ ($0 \leq y \leq 0.4$) compounds in the discharged (left column) and charged (right column) state.

Table 4-9: Fit parameters for the Ni $2p_{3/2}$ spectra of charged and discharged $LiNi_{0.5}Mn_{0.3}Co_{0.2}O_2$ electrodes.

Photoelectron Ni $2p_{3/2}$		$LiNi_{0.5}Mn_{0.3}Co_{0.2}O_2$ (discharged)			$LiNi_{0.5}Mn_{0.3}Co_{0.2}O_2$ (charged)	
		Ni^{3+}	Ni^{2+}	F KLL	Ni^{3+}	F KLL
Peak 1	BE / eV	854.4	584.0	853.5	854.2	853.0
	FWHM / eV	1.3	1.3	7.1	1.3	8.1
	%	6.7	12.9	43.5	14.6	43.5
Peak 2	BE / eV	855.2	855.0	859.5	855.2	859.9
	FWHM / eV	1.3	1.3	56.5	1.3	6.3
	%	7.3	9.2	6.0	16.6	56.5
Δ Peak / eV		0.9	1.0	6.0	0.9	6.9
Peak 3	BE / eV	856.0	856.0		856.0	
	FWHM / eV	1.3	1.6		1.3	
	%	8.0	6.1		18.1	
Δ Peak / eV		0.8	1.0		0.8	
Peak 4	BE / eV	857.0			857.0	
	FWHM / eV	1.3			1.3	
	%	3.7			8.0	
Δ Peak / eV		1.0			1.0	
Peak 5	BE / eV	857.9			858.1	
	FWHM / eV	2.0			2.0	
	%	7.6			7.3	
Δ Peak / eV		0.9			1.1	
Peak 6	BE / eV	860.9			860.8	
	FWHM / eV	3.7			3.7	
	%	30.6			19.6	
Δ Peak / eV		3.0			2.7	
Peak 7	BE / eV	863.6			863.5	
	FWHM / eV	2.2			2.2	
	%	5.3			5.4	
Δ Peak / eV		2.7			2.7	
Peak 8	BE / eV	865.8			865.5	
	FWHM / eV	2.2			2.0	
	%	2.8			3.2	
Δ Peak / eV		2.1			2.0	

Complementary ToF-SIMS analysis

As already stated above and in Chapter 4.3.3 for the pristine electrodes, the quantification and oxidation state identification for $LiNi_{0.6}Mn_{0.2}Co_{0.2}O_2$, $LiNi_{0.7}Mn_{0.1}Co_{0.2}O_2$, and $LiNi_{0.8}Co_{0.2}O_2$ charged and discharged electrodes are extremely hampered by the low signal intensity and, therefore, could lead to enormous errors. In consequence, complementary ToF-SIMS was applied to achieve reliable information on the in-depth Li distribution of charged and discharged electrode surfaces, based on the ToF-SIMS' high Li sensitivity. In particular, metal-Cs cluster fragments were detected by sputter depth profiling of the electrodes' surfaces, utilizing a raster-scanned Cs-ion beam for materials removal. This approach diminishes the ToF-SIMS inherent matrix effect and results in the sputter depth profiles in Figure 4-47 exemplarily shown for $CsLi^+$ cluster ions of charged and discharged $LiNi_{0.5}Mn_{0.3}Co_{0.2}O_2$ electrodes normalized to the $CsNi^+$, $CsMn^+$, and $CsCo^+$ cluster ions of interest. For all transition metal references both the high Li content in discharged samples and the respective low Li content at charged surfaces can be directly proved. Moreover, the increasing Li gradient towards the bulk of the charged active material doubtlessly proves that only surface-near regions are involved in electrochemical delithiation. Finally, it also confirms the stoichiometry of the $LiNi_{0.5}Mn_{0.3}Co_{0.2}O_2$ compound (by positioning of the $CsLi^+$ profile in respect to the $CsNi^+$, $CsMn^+$, and $CsCo^+$ profiles) since Ni:Mn:Co are in 5:3:2 ratio.

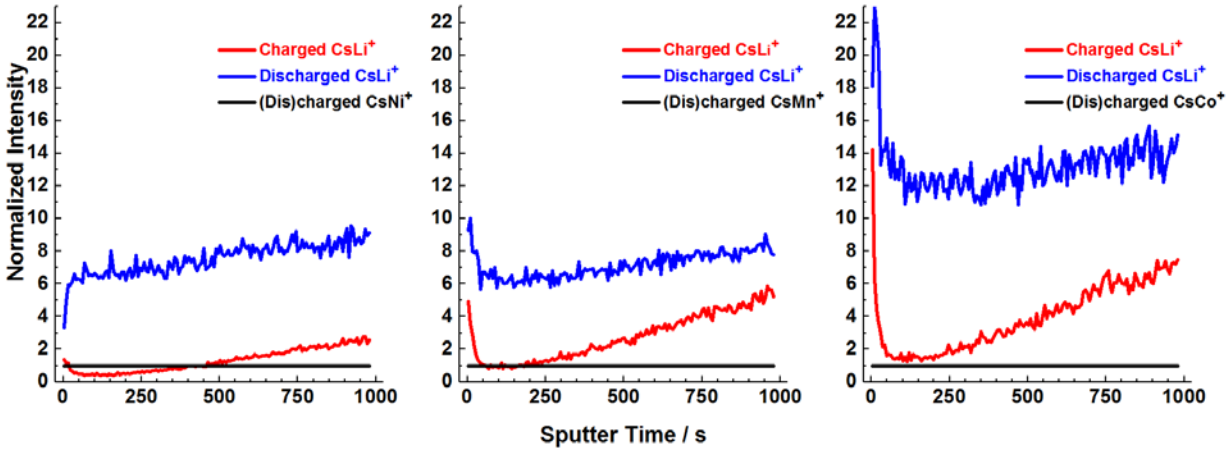

Figure 4-47: ToF-SIMS sputter depth profiles of $LiNi_{0.5}Mn_{0.3}Co_{0.2}O_2$ electrode surfaces using $CsLi^+$ normalized to the transition metal $CsNi^+$, $CsMn^+$, and $CsCo^+$ cluster ions.

Finally, for further research on the cathode electrolyte interface, it is interesting to consider the average of bindings energies obtained for identified lithium and fluoride species on cycled NMC

electrode surfaces. The average of binding energies obtained for Li species that can be attributed to the Li within the crystal structure of NMC active material is 53.9 eV, this value is 687.5 eV for F 1s peak of PVDF. However, the average binding energy obtained for Li 1s and F 1s peaks attributed mainly to LiF differs around 0.5 eV between charged and discharged electrodes, namely the average binding energy of Li 1s peak for LiF is 55.4 eV in discharged electrodes, and 54.9 eV in charged electrodes, similarly the average binding energy of F 1s peak for LiF is 684.8 eV and 684.3 eV in discharged and charged electrodes respectively. Nevertheless, it should be considered that the F 1s peak for LiF and PVDF is not a characteristic peak and they contain also the species of electrolyte salt (degradation products or not well-rinsed species) with the general formula of $Li_xPO_yF_z$, which can shift the binding energies according to the strength of the ligands.

4.4. General applicability of the developed XPS template approach

The previous comprehensive XPS characterization of Li-Ni-Mn-Co-O cathode systems enables the extension of the gained knowledge on other LIB cathode materials. Therefore, and to prove the general applicability of the developed template fitting procedure for XPS spectra of transition metal compounds, several doped active materials of the Li-Ni-Mn-O system in a spinel structure, which is crystallographically different from layered oxides of Li-Ni-Mn-Co-O system, were studied. The respective preparation methods are given in related chapters: from Chapter 3.4.4 to Chapter 3.4.7. However, some of these material systems are still in the development phase and, therefore, not in optimized stoichiometries available. In consequence, only a proof of principle for the XPS fitting procedures can be provided here and any quantification has not been carried out.

4.4.1. XPS characterization of Fe, Co, and Cu doped $LiNi_{0.5}Mn_{1.5}O_4$ powders

$LiNi_{0.5}Mn_{1.5}O_4$ (LNMO) spinel cathode material has been reviewed in several works due to its attractive electrochemical properties such as high rate capability and high operating voltage [71]. Ni^{2+} is the only electrochemically active species in this material and the electrochemical redox reaction takes place at ~4.7 V against Li^+/Li and results in a high energy density and makes this material a very promising candidate for an application as positive electrode in Li-ion batteries [71], [74], [82], [83], [136].

Even though the ideal oxidation state of Mn is 4+ in the LNMO, there usually exists additional Mn^{3+} due to the oxygen loss resulting from the high-temperature synthesis route. Slight oxygen deficiency in the LNMO results in a face-centered cubic spinel phase, which is more attractive with respect to the electrochemical performance in comparison to its not oxygen-deficient compound. However, Mn^{3+} is a Jahn-Teller ion and causes structural instability in the spinel structure. Moreover, Mn^{3+} undergoes disproportionation to form divalent Mn ions which may dissolve in the commercial carbonate-based battery electrolytes and adversely affect the cell performance [82]. Doping of LNMO using cations and anions is found to be a highly promising approach to improve its electrochemical performance. It has been already reported that appropriate cation doping on LNMO spinel enhances the obtainable capacity, cycling stability and rate capability [71], [74], [82], [83], [136]–[138]. Therefore, the identification of the oxidation states by XPS is again crucial for the development of these materials.

The above-mentioned introduction indicates the importance of oxidation state determination for doped $LiNi_{0.5}Mn_{1.5}O_4$ materials that are presented in the next paragraphs. The XPS characterization of the oxidation state of Mn ions in $LiNi_{0.5}Mn_{1.5}O_4$, $LiNi_{0.4}Co_{0.2}Mn_{1.4}O_4$,

$LiNi_{0.4}Cu_{0.2}Mn_{1.4}O_4$, $LiNi_{0.4}Fe_{0.2}Mn_{1.4}O_4$ spinel compounds (abbreviated respectively as LNMO, $LNCo_{0.2}MO$, $LNCu_{0.2}MO$, $LNF_{0.2}MO$) is shown in Figure 4-48. Using the same peak fitting parameters as for the powders of the $LiNi_{0.8-y}Mn_yCo_{0.2}O_2$ ($0 \leq y \leq 4$) series depicted in Table 4-5, the Mn 2p spectra of these compounds can successfully be fitted with Mn^{4+} multiplets and minor amount of Mn^{3+} (20 % of total Mn ions), the fitting is also confirmed by considering Mn 3s splitting (see Chapter 4.2.1 for more detail on XPS characterization of Mn ions).

The Li 1s peak in Fe doped $LiNi_{0.5}Mn_{1.5}O_4$ has severely overlapped with Fe 3p peak, as shown in Figure 4-48 with light blue shaded peaks. Nevertheless, according to the developed peak fitting procedure, the Li and Fe contributions can be clearly identified.

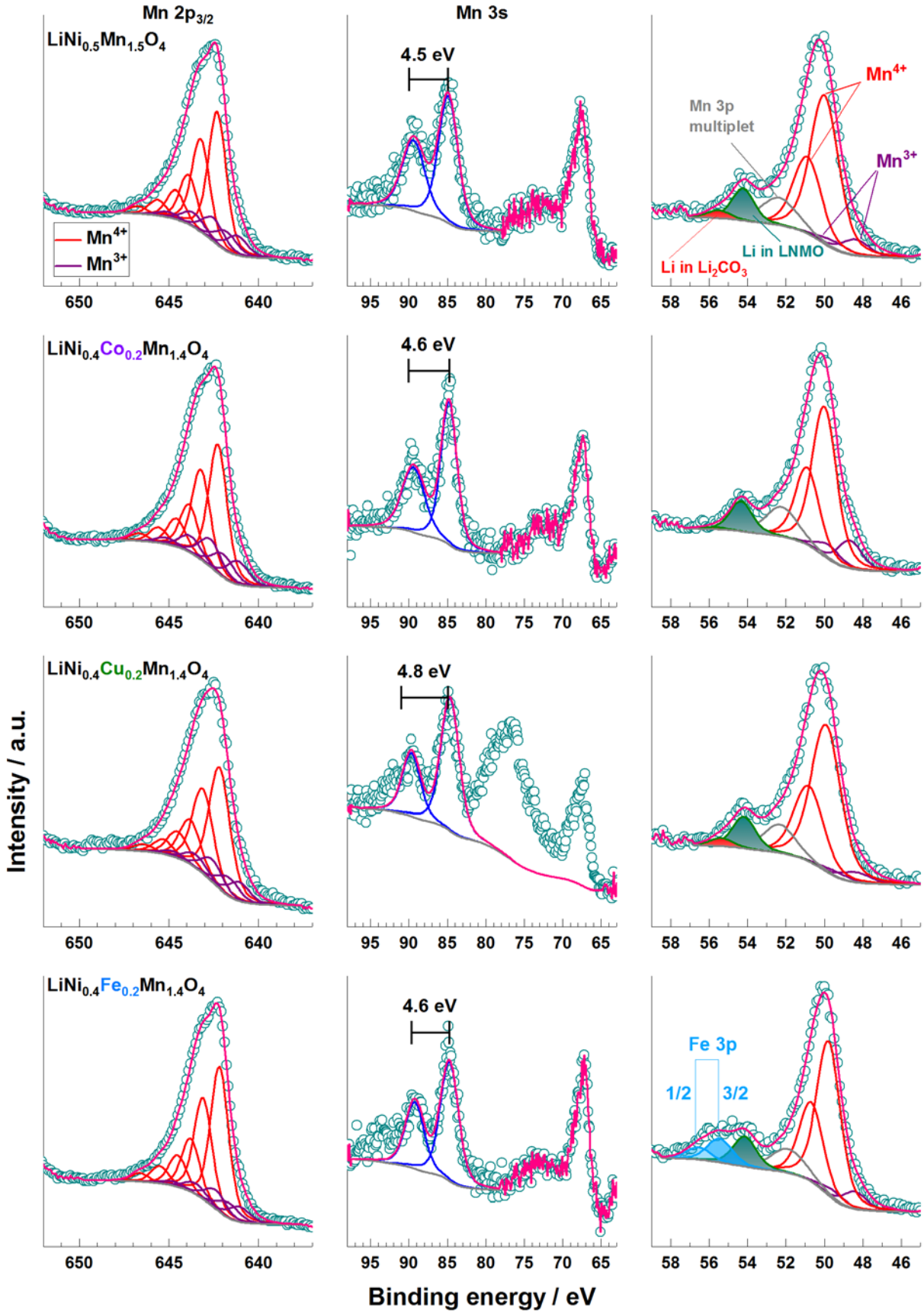

Figure 4-48: Mn 2p, Mn 3s, Mn 3p and Li 1s spectra of $LiNi_{0.5}Mn_{1.5}O_4$ (top row), $LiNi_{0.4}Co_{0.2}Mn_{1.4}O_4$ (2nd row), $LiNi_{0.4}Cu_{0.2}Mn_{1.4}O_4$ (3rd row), & $LiNi_{0.4}Fe_{0.2}Mn_{1.4}O_4$ (bottom).

The peak fitting of Ni 2p spectra of the doped $LiNi_{0.5}Mn_{1.5}O_4$ compounds is shown in Figure 4-49 together with the Co 2p, Cu 2p, Fe 2p spectra of dopants. Ni ions in these compounds are attributed to the Ni^{2+} oxidation state, however it should be considered that the relative intensity of multiplets of Ni^{2+} ions in Ni 2p spectra of spinels could not be fitted sufficiently with the same peak ratios as Ni^{2+} set of multiplets for $LiNi_{0.8-y}Mn_yCo_{0.2}O_2$ ($0 \leq y \leq 4$) compounds as depicted in Table 4-6. Therefore, the doped samples were fitted with the same parameters as for the undoped $LiNi_{0.5}Mn_{1.5}O_4$ material, the respective peak parameters are summarized in Table 4-10. Furthermore, the contribution of Mn LMM Auger peaks in Ni 2p spectra of $LiNi_{0.5}Mn_{1.5}O_4$ spinels can no longer be neglected due to the higher Mn concentration and, therefore, have to be considered in peak fitting approach as shown in Figure 4-49 (brown peaks in Ni 2p spectra).

Table 4-10: Fit parameters for Ni $2p_{3/2}$ spectra of $LiNi_{0.5}Mn_{1.5}O_4$ powder.

Photo-/Auger- electron	Ni $2p_{3/2}$	Mn LMM	Peak 1			Peak 2			Δ Peak BE / eV	Peak 3			Δ Peak BE / eV	Peak 4			Δ Peak BE / eV	Peak 5			Δ Peak BE / eV	Peak 6			Δ Peak BE / eV	Peak 7			Δ Peak BE / eV
BE / eV	854.7	847.7	BE / eV	FWHM / eV	%	BE / eV	FWHM / eV	%		BE / eV	FWHM / eV	%		BE / eV	FWHM / eV	%		BE / eV	FWHM / eV	%		BE / eV	FWHM / eV	%		BE / eV	FWHM / eV	%	
FWHM / eV	1.3	5.0	854.7	1.3	28.0	855.5	1.3	16.8	0.8	856.8	1.5	8.4	1.3	858.5	2.5	9.3	1.7	861.4	3.1	27.6	2.9	864.0	2.2	5.5	2.6	866.6	2.2	4.3	2.6
%	28.0	31.3	1.3	28.0		855.5	1.3	16.8	0.8	856.8	1.5	8.4	1.3	858.5	2.5	9.3	1.7	861.4	3.1	27.6	2.9	864.0	2.2	5.5	2.6	866.6	2.2	4.3	2.6
Δ Peak BE / eV	0.8	4.8																											
Peak 1	854.7	847.7																											
FWHM / eV	1.3	5.0																											
%	28.0	31.3																											
Peak 2	855.5	852.5																											
FWHM / eV	1.3	7.2																											
%	16.8	68.7																											
Δ Peak BE / eV	0.8	4.8																											
Peak 3	856.8																												
FWHM / eV	1.5																												
%	8.4																												
Δ Peak BE / eV	1.3																												
Peak 4	858.5																												
FWHM / eV	2.5																												
%	9.3																												
Δ Peak BE / eV	1.7																												
Peak 5	861.4																												
FWHM / eV	3.1																												
%	27.6																												
Δ Peak BE / eV	2.9																												
Peak 6	864.0																												
FWHM / eV	2.2																												
%	5.5																												
Δ Peak BE / eV	2.6																												
Peak 7	866.6																												
FWHM / eV	2.2																												
%	4.3																												
Δ Peak BE / eV	2.6																												

Co dopant

Co ions as a dopant in $LNCo_{0.2}MO$ compound show dominantly the Co^{3+} oxidation state with a minor Co^{2+} contribution (35 % of total Co ions) as shown in Figure 4-49. The fitting is done in accordance with Co 2p fit parameters indicated in Table 4-4 for Co^{3+} ions of powder $LiNi_{0.8-y}Mn_yCo_{0.2}O_2$ ($0 \leq y \leq 4$) compounds. The parameters for Co^{2+} ions are adapted from the work of Biesinger et al. in [15]. Due to the similarity to the $LiNi_{0.8-y}Mn_yCo_{0.2}O_2$ ($0 \leq y \leq 4$) series, no further challenges regarding the multiplet fitting were expected and indeed could easily be done.

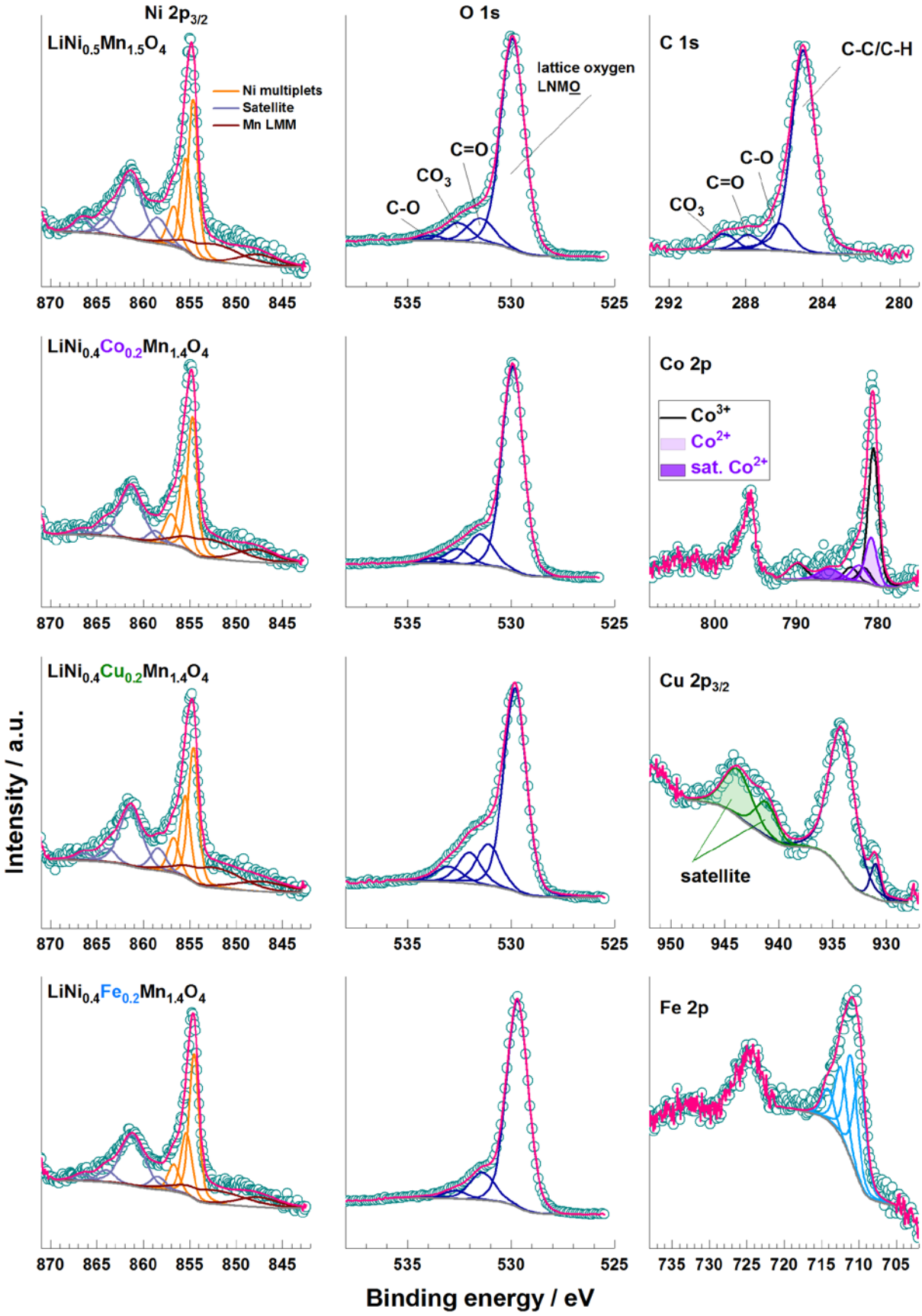

Figure 4-49: Ni 2p, O 1s, and C 1s spectra of $LiNi_{0.5}Mn_{1.5}O_4$ (top row), $LiNi_{0.4}Co_{0.2}Mn_{1.4}O_4$ (2nd row), $LiNi_{0.4}Cu_{0.2}Mn_{1.4}O_4$ (3rd row), and $LiNi_{0.4}Fe_{0.2}Mn_{1.4}O_4$ (bottom) together with the Co 2p, Cu 2p, Fe 2p spectra of the respective dopants.

Cu dopant

As indicated in the literature [139], the Cu ions do not show extensive multiplet splitting and normally the presence of the well-known shake-up satellite found in Cu 2p spectra is used as an indication of the presence of Cu^{2+} species [139]. These satellites are also present in the Cu 2p spectra of $LNCu_{0.2}MO$ at 941.2 and 943.8 eV as shown in Figure 4-49, therefore Cu^{2+} ions are identified as the main oxidation state of Cu ions in this compound. Moreover, the binding energy of the main Cu 2p peak at 934.1 eV is comparable to the binding energy of Cu^{2+} in $Cu(OH)_2$ at 934.7 eV and in CuO at 933.1 eV, as depending on the binding partner an energy gap of around 1 eV can be found similar to Ni^{2+} compounds, see Chapter 4.2.3 and [139]. However, due to the relatively weak concentration, the correct evaluation of the composition will remain an open question, as the necessary increase of measuring time simultaneously would lead to the well-known X-ray-induced reduction of Cu^{2+} components and, therefore, result into artifacts [88]. This method-induced degradation probably is already the reason for the small peak at 931.0 eV. Nevertheless, also $Cu(OH)_2$ formation at the topmost particle surfaces seems to be reasonable due to atmospheric contact.

Fe dopant

The 2p spectrum of the Fe dopant ions in $LNFe_{0.2}MO$ is fitted with the parameter set of $NiFe_2O_4$ from Biesinger et al. [15] and is shown in Figure 4-49. The precise evaluation of oxidation state of Fe ions in $LNFe_{0.2}MO$ is hampered by the low intensity of the Fe 2p spectra, however, the fitting suggests Fe^{3+} oxidation state for these ions.

C 1s peak of LNMO in Figure 4-49 is shown just as an example. The C 1s peaks of all doped systems are similar to $LiNi_{0.5}Mn_{1.5}O_4$ and show only small surface contaminations at the topmost surface in a sum-up amount of 25.5 %, 30.5 %, 33.2 %, and 30.8 % for LNMO, $LNCo_{0.2}MO$, $LNCu_{0.2}MO$, and $LNFe_{0.2}MO$ respectively.

As a partial conclusion, the above-characterized differently doped spinel materials can be sufficiently described by the developed template approach for 2p transition metal XP spectra and only minor additional peak overlapping must be considered; which is namely the Mn Auger peak in the Ni 2p region cannot be neglected and the overlap of Li 1s and Fe 3p should be properly fitted.

4.4.2. XPS characterization of Ru/Ti-doped $LiNi_{0.5}Mn_{1.5}O_4$ powders

The developed peak fitting approach is also applicable to XP spectra of compounds with additional transition metal dopants like the Ru/Ti-doped LNMO (LNMRTO), e.g. to tune its properties. This is in addition to the complex Ni and Mn templates really challenging due to further peak overlaps (Ru 3d / C1s and Ru 2p / Ti 2p), together with the very weak concentration of the dopants. Figure 4-50 in this regard shows the respective XP spectra of the as-prepared ($LNMRTO_{AP}$) and the annealed ($LNMRTO_{HT}$) powder samples.

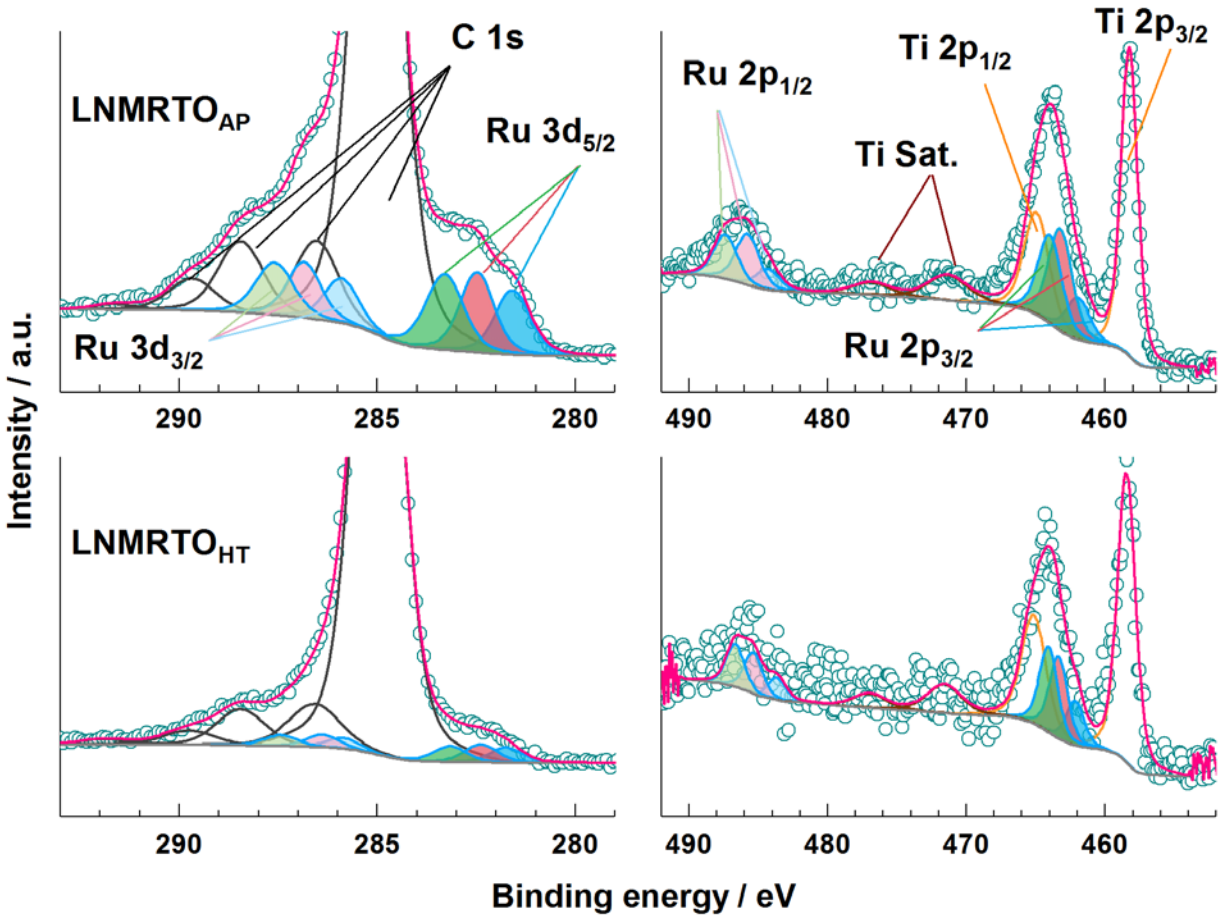

Figure 4-50: C 1s, Ru 3d, and Ti 2p spectra of Ru/Ti-doped $LiNi_{0.5}Mn_{1.5}O_4$.

In particular, the XP high-resolution spectrum of the Ru 3d region of LNMRTO powders is complex due to the overlapping of the C 1s signal and Ru 3d spin-orbit doublet. Three Ru 3d doublets have to be considered to reasonably fit the multiplet, namely Ru $3d_{5/2}$ at 281.6, 282.5, 283.3 eV with an FWHM of 1.0 eV. However, the assignment of different chemical states is very

difficult since the interpretation of Ru XP core level spectra is still controversially discussed in the literature. According to reference [140], the Ru $3d_{5/2}$ peak at 281.6 eV can be assigned to Ru^{4+} ions. The two other resolved peaks can be assigned to higher oxidation states of Ru, probably to Ru^{6+} and Ru^{8+}. The assignment of the Ru $3d_{5/2}$ peak at 283.3 eV to a satellite structure is impeded by the fact that the intensity of all peaks is approximately the same (all are within the range of 0.1-0.2 at. %) in contrast to the usual findings in literature that indicate the intensity of satellites is much smaller than the intensity of the main peak [141], [142]. Due to the very weak concentration of the dopant, the final clarification is subject to future work, especially a complete reference samples series fundamentally has to be studied and, therefore, is beyond the scope of this work.

In the case of double doping of LNMO with Ru and Ti, the relevant Ti 2p energy region is partly cross-talked by Ru 3p peaks, cf. Figure 4-50, right column. However, the nearly free-standing Ti $2p_{3/2}$ peak at around 458.3 eV can be assigned to Ti^{4+} ions [139].

Figure 4-51 proves Ni in Ru/Ti-doped LNMO to appear as Ni^{2+} ions only since it is very similar to the above-mentioned Co, Cu, or Fe doped LNMO powders (Chapter 4.4.1). Moreover, the major chemical state of Mn ions was found to be Mn^{4+}, like in NMC compounds (see Chapter 4.3.2.2) and the O 1s peak at 530.0 eV is attributed to lattice oxygen (see Chapter 4.2.5).

Table 4-11 summarizes the quantification of the LNMRTO samples normalized to Ni = 0.5 content and the binding energy assignments. According to the results of the bulk chemical analysis in [83], the stoichiometry of $Li_{1.0}Ni_{0.5}Mn_{1.4}Ru_{0.1}Ti_{0.027}O_4$ could be proven. Hence, XPS quantification depicted in Table 4-11 shows a very good agreement to the bulk analysis except for the Li, due to its extremely weak cross-section for the photoionization and the Li 1s peak overlaps with transition metal peaks as described in Chapter 4.2.4.

Overall the Ru/Ti-doped LNMO materials can be characterized properly when utilizing the developed principal template approach for XP spectra. However, the major problem is the weak concentration of the dopants, especially in case of Ru when considering the high carbon (binder and carbon black) amount of LIB electrodes, where it seems to be almost impossible to achieve reliable chemical state elucidation for the Ru components.

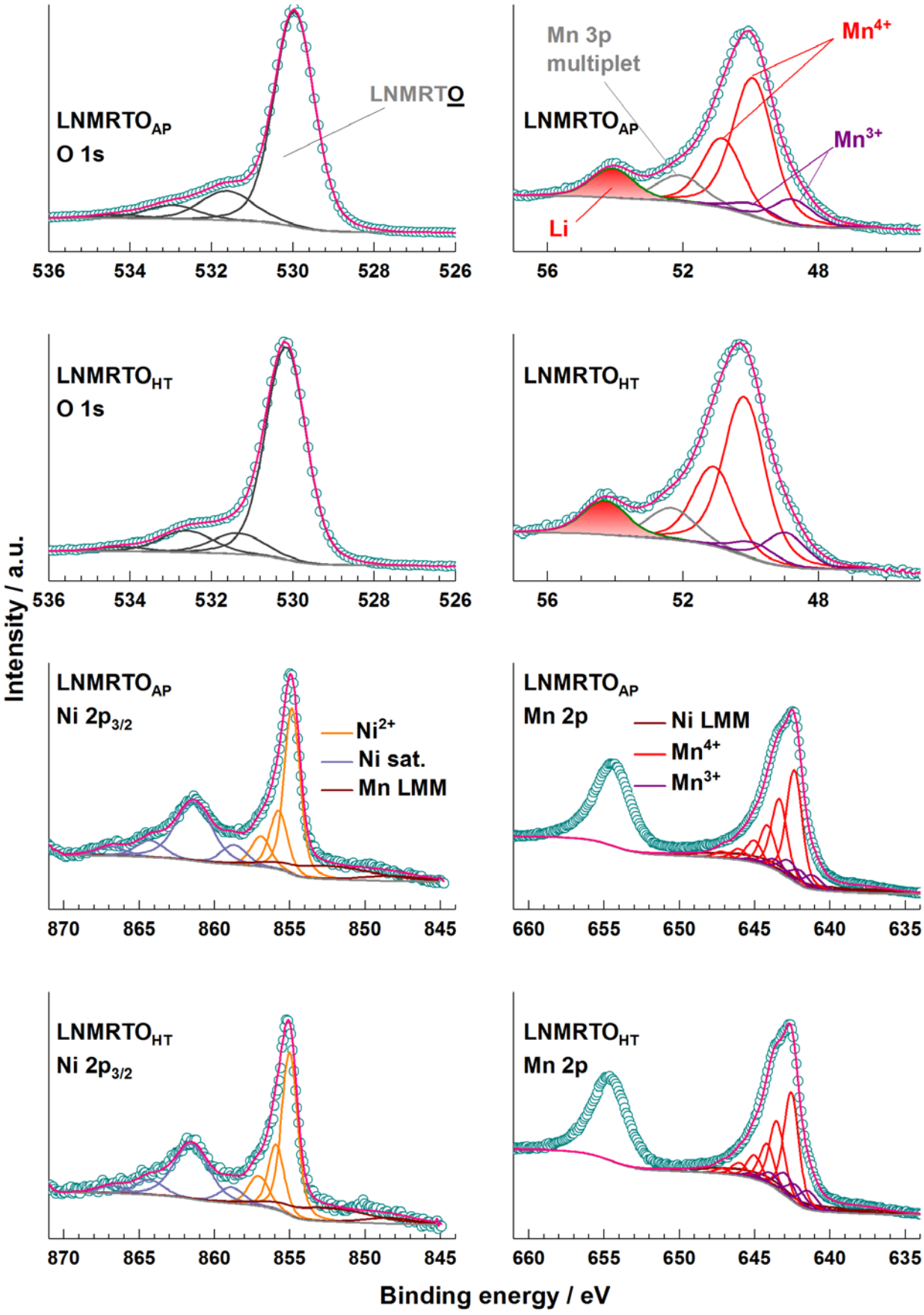

Figure 4-51: O 1s, Li 1s, Mn 3p, Ni $2p_{3/2}$ and Mn 2p spectra of $LNMRTO_{AP}$ (1st and 3rd row) and $LNMRTO_{HT}$ (2nd and 4th row) surfaces.

Table 4-11: Peak assignments and atomic concentrations (normalized to the Ni = 0.5 content) of Ru/Ti-doped LNMRTO samples.

Elements / Photoelectron peaks	$LNMRTO_{AP}$	$LNMRTO_{HT}$
Stoichiometry by XPS (normalized to the Ni = 0.5 content)		
Li	2.8	3.5
Ni	0.5	0.5
Mn	1.3	1.4
Ru	0.06	0.03
Ti	0.08	0.06
O	3.6	4.0
Binding energies / eV		
Li 1s	54.1	54.3
Ni $2p_{3/2}$	854.9	855.0
Mn^{4+} $2p_{3/2}$	642.4	642.6
Mn^{3+} $2p_{3/2}$	641.2	641.5
Ru $3d_{5/2}$	281.6 / 282.5 / 283.3	281.8 / 282.4 / 283.2
Ti $2p_{3/2}$	458.3	458.5
O 1s	530.0	530.2
Mn 3p	49.9	50.2
Mn 3s split	4.6	4.5
Mn^{3+}/total Mn from 2p fit	20 %	30 %

4.4.3. XPS characterization of mesoporous spinel-type MCo_2O_4 (M = Co, Zn, and Ni) rods

Supercapacitors are a new category of energy storage devices. They have attracted much attention because of their fast charge/discharge rate, high power density, high reliability, and long life-cycle. Various spinel-type binary metal oxides $A^{2+}B_2^{3+}O_4$ where A is a divalent cation (Zn, Ni, Mn, Cu, etc.) and B is a trivalent cation (Co, Fe, Mn, etc.) have been recently investigated as pseudocapacitors. Among the spinel-type metal oxides, the cobalt-based metal oxides show better electrochemical properties [33], [34].

To prove the applicability of the template approach concept for XPS multiplet fitting on such material, naturally self-assembled porous spinel-type MCo_2O_4 rods (M = Co, Ni, and Zn), see Chapter 3.4.6 and [33], were studied in detail with respect to the elemental composition and the component's oxidation state. The respective transition metal 2p spectra are shown in Figure 4-52. The corresponding main O 1s peaks at 530.3, 529.9, and 529.8 eV are attributed to the spinel lattice oxygen of $CoCo_2O_4$, $ZnCo_2O_4$, and $NiCo_2O_4$, respectively, and are shown in Figure 4-53 together with the C 1s spectra to prove the only weak topmost contamination [100], [120], [121]. In particular, templates of pure Co^{2+} and Co^{3+} 2p multiplets were used to describe the $CoCo_2O_4$ compound in Figure 4-52a, see 4.2.2. Because of the strong overlap of the respective photoelectron peaks, the sole attempt to distinguish between the two binding states is to utilize the respective satellite features around 785.6 eV (Co^{2+}) and 789.7 eV (Co^{3+}) as guiding peaks for the respective multiplets. This is corroborated by the pure Co^{3+} multiplet of $ZnCo_2O_4$ in Figure 4-52c. The overall Co quantification for $CoCo_2O_4$ finally results in a Co^{3+} amount of 62 % (of overall Co content) which is close to the expected content. The Co 2p spectrum of $ZnCo_2O_4$ in Figure 4-52c reveals, as already stated above, a pure Co^{3+} multiplet justified by the absence of the Co^{2+} satellite. By contrast, the corresponding Zn $2p_{3/2}$ multiplet in Figure 4-52d results in two Zn^{2+} components at 1021.4 and 1022.8 eV which indicate Zn^{2+} in tetrahedral and octahedral oxygen coordination, respectively [143] [144]. This is supported by the fact that an almost random arrangement of the different cations on tetrahedral and octahedral cation sites is often observed in nanostructured oxide spinels [145] [146]. The chemical state of Zn^{2+} additionally corroborated by the Zn LMM Auger peaks in Figure 4-52b.

The Co 2p spectrum of $NiCo_2O_4$ in Figure 4-52e was again fitted using the developed templates (considering $CoCo_2O_4$ and $ZnCo_2O_4$ compounds). In conclusion, we have to consider the presence of a certain amount of Co^{2+} in $NiCo_2O_4$ compound because of the pronounced satellite feature at 785.4 eV. Finally, the Co^{3+} concentration amounts to 59 % of the overall Co content. As already mentioned in Chapter 4.2.3, an unambiguous XPS chemical state identification of Ni ions demand

a careful multiplet fitting. For Ni^{2+} in pure NiO (see Figure 4-10), the ratio between the peaks at 855.9 and at 854.3 eV amounts to 1.5. In the case of the $NiCo_2O_4$ rods, the mentioned ratio is about 2.8; hence, in conclusion, a distinct amount of Ni^{3+} has to be considered because the main peak for Ni^{3+} is expected at around 856.0 eV. Therefore, the corresponding Ni 2p spectrum in Figure 4-52f was fitted using the adapted template reported in Chapter 4.3.2.3 for pure powders of $LiNi_{0.8-y}Mn_yCo_{0.2}O_2$ ($0 \leq y \leq 0.4$) compound series. According to the provided deconvolution in Figure 4-52f, 60 % of overall Ni content is assigned to Ni^{3+} ions and it is in good agreement to the corresponding amount of Co^{2+}, suggesting some Co/Ni exchange.

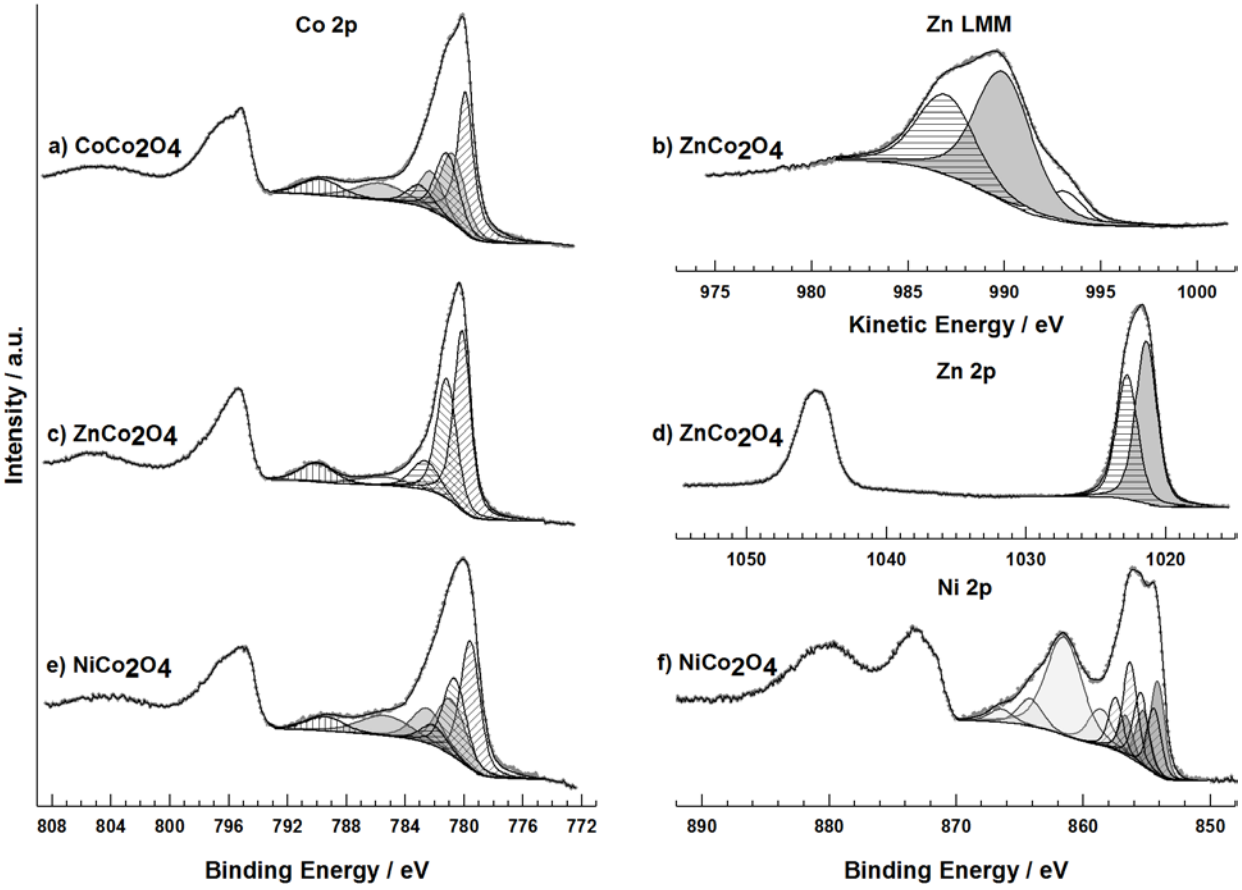

Figure 4-52: Co 2p, Ni 2p, Zn 2p, and Zn LMM spectra of $CoCo_2O_4$ (a), $ZnCo_2O_4$ (b−d), and $NiCo_2O_4$ (e, f) mesoporous rods. In particular, (a, c, e) Co^{3+} peaks and satellites: shaded and Co^{2+} peaks and satellites: gray; (b, d) Zn^{2+} tetrahedral coordination: gray and octahedral coordination: shaded; and (f) Ni^{2+} multiplets: gray and Ni^{3+} multiplets: shaded and Ni 2p satellite/loss features: light gray.

From the results described above, the following conclusions can be drawn: (i) The Co^{3+} content of 62 % found for $CoCo_2O_4$ is to some extent smaller than 2/3 and might hint at some oxygen

deficiency; (ii) $NiCo_2O_4$ shows mixed valences for both the transition metal elements, which compensate each other; (iii) $ZnCo_2O_4$ shows site exchange for Zn and Co, that is, a partially inverse spinel.

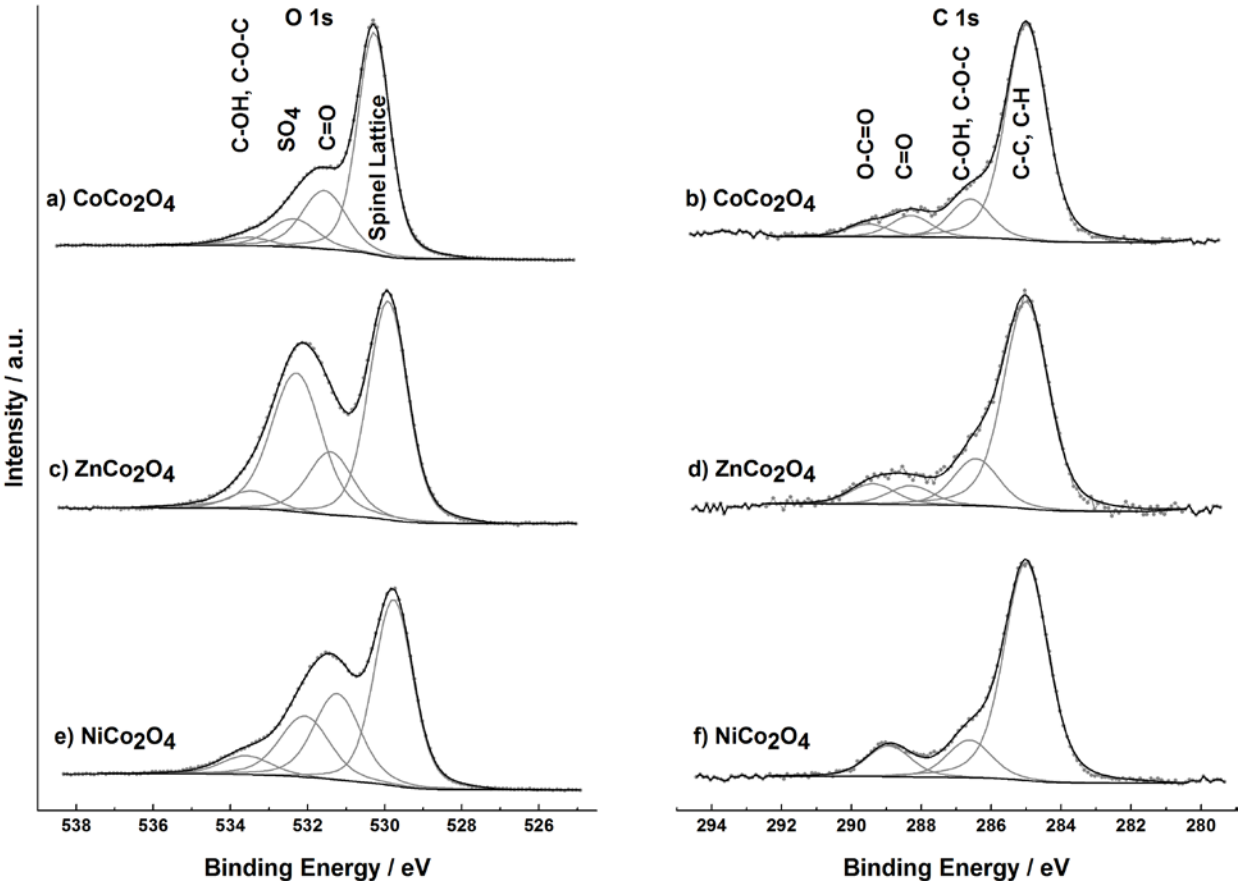

Figure 4-53: O 1s (a, c, e), and C 1s (b, d, f), spectra of $CoCo_2O_4$ (a, b), $ZnCo_2O_4$ (c, d), and $CoNi_2O_4$ (e, f).

4.4.4. Characterization of 3D highly porous spinel-type $Zn_{0.2}Ni_{0.8}Co_2O_4$ microspheres

In a normal spinel structure ($ZnCo_2O_4$), the divalent (Zn^{2+}) cations occupy the tetrahedral sites exhibiting semiconductor behavior, whereas, in an inverse spinel structure ($NiCo_2O_4$), the divalent (Ni^{2+}) cations occupy the octahedral sites and show semi-metallic behavior. Hence it is possible to combine their competitive advantages by partially replacing Ni with Zn or vice versa and investigate them as electrodes in supercapacitor and LIB applications [34]. More information about the oxidation state of different first-row transition metals in highly porous $Zn_{0.2}Ni_{0.8}Co_2O_4$ microspheres (for synthesis detail see Chapter 3.4.7) was achieved by X-ray photoelectron spectroscopy, using successful application of the developed template approach.

Following this approach, the Co $2p_{3/2}$ spectra were fitted with templates of pure Co^{2+} and Co^{3+} 2p multiplets (cf. Chapter 4.2.2), as shown in Figure 4-54 left. Again, the characteristic satellite features around 785.6 eV (Co^{2+}) and 789.8 eV (Co^{3+}) were utilized as guiding peaks to resolve the strong overlap of the respective photoelectron peaks. As a result, 76 % of the total Co content could be attributed to Co^{3+} ions and 24 % to Co^{2+} ions. The corresponding Ni 2p spectrum (deconvoluted according to Chapter 4.3.2.3) reveals a mixed oxidation state of 31 % Ni^{2+} and 69 % Ni^{3+} ions of the overall Ni content. The results of quantification for the fractions of Ni^{3+} (69 %) and Co^{2+} (24 %) are in agreement with the factor Ni:Co = 2:0.8 expected from the chemical composition of the sample, i.e. the amount of Ni^{3+} is compensated by the same absolute amount of Co^{2+}.

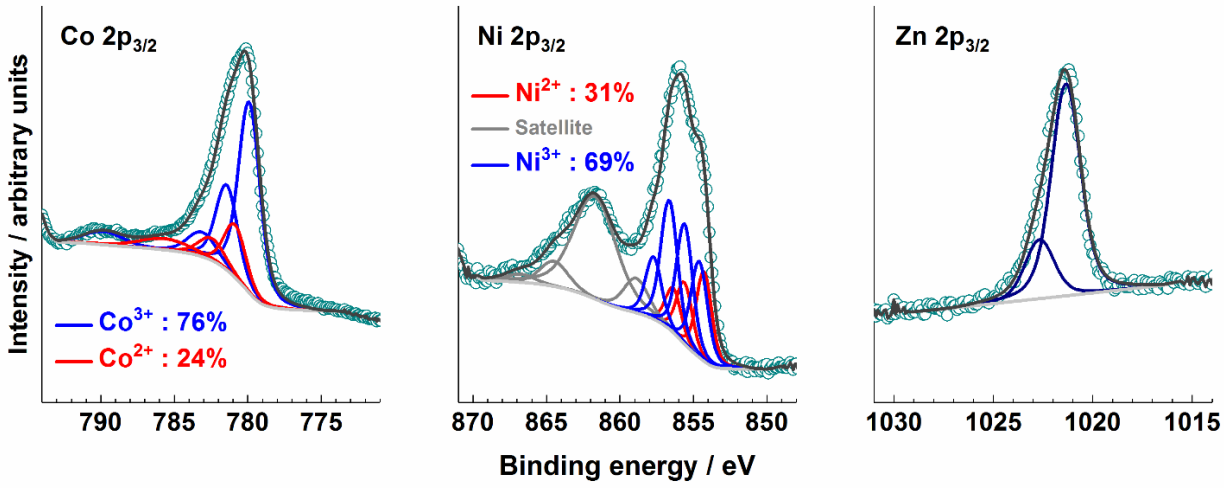

Figure 4-54: Co $2p_{3/2}$, Ni $2p_{3/2}$, and Zn $2p_{3/2}$ XP spectra of highly porous $Zn_{0.2}Ni_{0.8}Co_2O_4$ microspheres.

Finally, the corresponding Zn $2p_{3/2}$ spectrum in Figure 4-54 (right) reveals two Zn^{2+} components at 1021.4 eV and 1022.7 eV, which indicate Zn^{2+} in tetrahedral and octahedral oxygen coordination, respectively. This is supported by the fact that in nanostructured oxide spinels, an almost random arrangement of the different cations on the tetrahedral and octahedral cation sites is commonly observed. The results are in good agreement with the findings on spinel-type MCo_2O_4 (M = Co, Zn, and Ni) rods in Chapter 4.4.3.

5. Conclusion

The aim of this work was to develop a novel tool to reliably deconvolute XP spectra of compounds comprising various combinations of transition metals regarding quantitative chemical state elucidation. The necessity of this development resulted directly from the fact that the worldwide-practice to utilize simplifying approaches for interpretation of transition metal XPS core level multiplets via either using only raw data sets and solely assigning expected oxidation states or reducing the complex multiplet splitting to single Voigt peak shapes, could lead at least to uncertainties or even errors regarding the quantitative chemical state information. In particular, it is essential to consequently address the complex multiplet splitting, photoelectron and Auger peak overlaps, and additional shake-up and plasmon features in the respective 2p XP spectra to finally achieve a comprehensive and quantitative information on the transitions metals' chemical states.

The materials chosen for the development phase were several novel Li-Ni-Mn-Co-O (NMC) compounds designed for Lithium-ion battery (LIB) application. For the first time in a consecutive way, reference materials, NMC thin-films, NMC powders with various stoichiometry and finally LIB cathodes, thereof in the pristine and cycled state, were systematically characterized to achieve templates for each photoelectron peak of the respective transition metals and their different oxidation states.

As an essential prerequisite, data acquisition strategies have been developed to avoid potential artifacts due to probable contamination during sample handling and transport from synthesis to analysis under inert gas conditions and, moreover, method-induced decomposition (reduction, depletion, etc.) of the samples during the different characterization steps. Herewith the desired multiplet fitting approach for 2p spectra containing at least three transition metals was developed, using magnetron sputtered Li-Co-Mn-O thin-films as a model system to exclude any intensity minimizing effects due to topography and dilution by carbon black and binder.

For the first time, complete parameter sets comprising peak shapes, FWHM, energy gaps, and intensity ratios of the single peak components originating from the 2p core level multiplet splitting now are available considering, in addition, photoelectron peak overlaps and cross-talks of X-ray-induced Auger electron peaks. The careful consideration of Auger electron peaks, in particular, is essential if the utilized XPS instruments do not provide a second excitation energy, such as MgKα irradiation, to shift the Auger peaks out of the respective photoelectron's energy range. For all overlaps (e.g. Mn 2p / Ni LMM, Ni 2p / F KLL, etc.) it could be doubtlessly

demonstrated that the developed templates allow to clearly separate the photoelectron peaks from the Auger contributions.

Subsequently, it could unambiguously be proven, that the elaborated parameter set is highly suitable to elucidate the chemical state changes due to systematically tuning the stoichiometry of pure NMC powder system series. Moreover, and although it is often denied in the literature, the present work, in principle, evidences the applicability of multiplet splitting approaches to XP spectra of LIB cathodes, i.e. after diluting the maximal active materials concentration by mixing with carbon black and binder. Here the major constraint is the necessary homogeneous distribution of the active material within the XPS information depth. However, this is more a problem based on the electrode's fabrication processes and in no way diminishes the feasibility in principle. In conclusion, an improved electrode fabrication resulting in homogeneous active material distribution across the overall electrode's surface should open-up in general the applicability of the new XPS template approach also for electrodes with a high amount of binder and carbon black. Even after the electrode's cycling, it could be exemplarily justified that the developed fitting procedure leads to reliable quantitative chemical state information. Nevertheless, the overall stoichiometry evaluation of the respective compounds will remain erroneous due to the poor quantifiability of Li.

The general applicability of the new template approach was evidenced by the application of the developed procedures to spectra of different novel transition metal powder compounds comprising various combinations of Co, Ni, or Mn and additional dopants, such as Cu, Fe, Ru, Ti, and Zn. This successful justification opens-up the possibility of reliable XPS characterization of transition metal compounds within the high diversity of materials development. However, the fundamental elucidation of the XPS core level multiplet splitting behavior of every additional transition metal as a prerequisite has to be done carefully prior to the desired characterization.

6. Literature

[1] R. Wagner, N. Preschitschek, S. Passerini, J. Leker, and M. Winter, “Current research trends and prospects among the various materials and designs used in lithium-based batteries,” *J. Appl. Electrochem.*, vol. 43, no. 5, pp. 481–496, May 2013.

[2] R. Marom, S. F. Amalraj, N. Leifer, D. Jacob, and D. Aurbach, “A review of advanced and practical lithium battery materials,” *J. Mater. Chem.*, vol. 21, no. 27, p. 9938, 2011.

[3] B. Scrosati and J. Garche, “Lithium batteries: Status, prospects and future,” *J. Power Sources*, vol. 195, no. 9, pp. 2419–2430, May 2010.

[4] J. B. Goodenough and K. Park, “The Li-Ion Rechargeable Battery: A Perspective,” *J. Am. Chem. Soc.*, vol. 135, no. 4, pp. 1167–1176, Jan. 2013.

[5] D. Deng, “Li-ion batteries: basics, progress, and challenges,” *Energy Sci. Eng.*, vol. 3, no. 5, pp. 385–418, Sep. 2015.

[6] V. Etacheri, R. Marom, R. Elazari, G. Salitra, and D. Aurbach, “Challenges in the development of advanced Li-ion batteries: a review,” *Energy Environ. Sci.*, vol. 4, no. 9, p. 3243, 2011.

[7] K. M. Abraham, “Prospects and Limits of Energy Storage in Batteries,” *J. Phys. Chem. Lett.*, vol. 6, no. 5, pp. 830–844, Mar. 2015.

[8] M. Winter, “The solid electrolyte interphase - The most important and the least understood solid electrolyte in rechargeable Li batteries,” *Zeitschrift für Phys. Chemie*, vol. 223, no. 10–11, pp. 1395–1406, Dec. 2009.

[9] P. Verma, P. Maire, and P. Novák, “A review of the features and analyses of the solid electrolyte interphase in Li-ion batteries,” *Electrochim. Acta*, vol. 55, no. 22, pp. 6332–6341, Sep. 2010.

[10] K. Ciosek Högström, S. Malmgren, M. Hahlin, M. Gorgoi, L. Nyholm, H. Rensmo, and K. Edström, “The Buried Carbon/Solid Electrolyte Interphase in Li-ion Batteries Studied by Hard X-ray Photoelectron Spectroscopy,” *Electrochim. Acta*, vol. 138, pp. 430–436, Aug. 2014.

[11] V. Winkler, T. Hanemann, and M. Bruns, “Comparative surface analysis study of the solid

electrolyte interphase formation on graphite anodes in lithium-ion batteries depending on the electrolyte composition," *Surf. Interface Anal.*, vol. 49, no. 5, pp. 361–369, May 2017.

[12] F. Liao, J. Światowska, V. Maurice, A. Seyeux, L. H. Klein, S. Zanna, and P. Marcus, "Electrochemical lithiation and passivation mechanisms of iron monosulfide thin-film as negative electrode material for lithium-ion batteries studied by surface analytical techniques," *Appl. Surf. Sci.*, vol. 283, pp. 888–899, 2013.

[13] J. T. Li, J. Światowska, V. Maurice, A. Seyeux, L. Huang, S. G. Sun, and P. Marcus, "XPS and ToF-SIMS study of electrode processes on Sn-Ni alloy anodes for Li-ion batteries," *J. Phys. Chem. C*, vol. 115, no. 14, pp. 7012–7018, 2011.

[14] C. Pereira-Nabais, J. Światowska, A. Chagnes, F. Ozanam, A. Gohier, P. Tran-Van, C. S. Cojocaru, M. Cassir, and P. Marcus, "Interphase chemistry of Si electrodes used as anodes in Li-ion batteries," *Appl. Surf. Sci.*, vol. 266, pp. 5–16, 2013.

[15] M. C. Biesinger, B. P. Payne, A. P. Grosvenor, L. W. M. Lau, A. R. Gerson, and R. S. C. Smart, "Resolving surface chemical states in XPS analysis of first row transition metals, oxides and hydroxides: Cr, Mn, Fe, Co and Ni," *Appl. Surf. Sci.*, vol. 257, no. 7, pp. 887–898, Jan. 2010.

[16] R. P. Gupta and S. K. Sen, "Calculation of multiplet structure of core p-vacancy levels," *Phys. Rev. B*, vol. 10, no. 1, pp. 71–77, Jul. 1974.

[17] R. P. Gupta and S. K. Sen, "Calculation of multiplet structure of core p-vacancy levels. II," *Phys. Rev. B*, vol. 12, no. 1, pp. 15–19, Jul. 1975.

[18] T. Eriksson, A. M. Andersson, A. G. Bishop, C. Gejke, T. Gustafsson, and J. O. Thomas, "Surface Analysis of LiMn[sub 2]O[sub 4] Electrodes in Carbonate-Based Electrolytes," *J. Electrochem. Soc.*, vol. 149, no. 1, p. A69, 2002.

[19] S. K. Martha, J. Nanda, G. M. Veith, and N. J. Dudney, "Surface studies of high voltage lithium rich composition: Li1.2Mn0.525Ni0.175Co0.1O2," *J. Power Sources*, vol. 216, pp. 179–186, Oct. 2012.

[20] R. A. Quinlan, Y.-C. Lu, Y. Shao-Horn, and A. N. Mansour, "XPS Studies of Surface Chemistry Changes of LiNi0.5Mn0.5O2 Electrodes during High-Voltage Cycling," *J. Electrochem. Soc.*, vol. 160, no. 4, pp. A669–A677, Feb. 2013.

[21] L. Baggetto, N. J. Dudney, and G. M. Veith, “Surface chemistry of metal oxide coated lithium manganese nickel oxide thin-film cathodes studied by XPS,” *Electrochim. Acta*, vol. 90, pp. 135–147, Feb. 2013.

[22] E. Castel, E. J. Berg, M. El Kazzi, P. Novák, and C. Villevieille, “Differential Electrochemical Mass Spectrometry Study of the Interface of x Li 2 MnO 3 ·(1– x)LiMO 2 (M = Ni, Co, and Mn) Material as a Positive Electrode in Li-Ion Batteries,” *Chem. Mater.*, vol. 26, no. 17, pp. 5051–5057, Sep. 2014.

[23] S. Doubaji, B. Philippe, I. Saadoune, M. Gorgoi, T. Gustafsson, A. Solhy, M. Valvo, H. Rensmo, and K. Edström, “Passivation Layer and Cathodic Redox Reactions in Sodium-Ion Batteries Probed by HAXPES,” *ChemSusChem*, vol. 9, no. 1, pp. 97–108, Jan. 2016.

[24] N. Andreu, D. Flahaut, R. Dedryvère, M. Minvielle, H. Martinez, and D. Gonbeau, “XPS Investigation of Surface Reactivity of Electrode Materials: Effect of the Transition Metal,” *ACS Appl. Mater. Interfaces*, vol. 7, no. 12, pp. 6629–6636, Apr. 2015.

[25] K. Edström, T. Gustafsson, and J. O. Thomas, “The cathode–electrolyte interface in the Li-ion battery,” *Electrochim. Acta*, vol. 50, no. 2–3, pp. 397–403, Nov. 2004.

[26] J. Li, S. Xiong, Y. Liu, Z. Ju, and Y. Qian, “Uniform LiNi1/3Co1/3Mn1/3O2 hollow microspheres: Designed synthesis, topotactical structural transformation and their enhanced electrochemical performance,” *Nano Energy*, vol. 2, no. 6, pp. 1249–1260, Nov. 2013.

[27] E. Talik, L. Lipińska, P. Zajdel, A. Załóg, M. Michalska, and A. Guzik, “Electronic structure and magnetic properties of LiMn1.5M0.5O4 (M=Al, Mg, Ni, Fe) and LiMn2O4/TiO2 nanocrystalline electrode materials,” *J. Solid State Chem.*, vol. 206, pp. 257–264, Oct. 2013.

[28] W. Ahn, S. N. Lim, K.-N. Jung, S.-H. Yeon, K.-B. Kim, H. S. Song, and K.-H. Shin, “Combustion-synthesized LiNi0.6Mn0.2Co0.2O2 as cathode material for lithium ion batteries,” *J. Alloys Compd.*, vol. 609, pp. 143–149, Oct. 2014.

[29] D. Tang, L. Ben, Y. Sun, B. Chen, Z. Yang, L. Gu, and X. Huang, “Electrochemical behavior and surface structural change of LiMn 2 O 4 charged to 5.1 V,” *J. Mater. Chem. A*, vol. 2, no. 35, p. 14519, Jun. 2014.

[30] M. Sachs, M. Gellert, M. Chen, H.-J. Drescher, S. R. Kachel, H. Zhou, M. Zugermeier, M. Gorgoi, B. Roling, and J. M. Gottfried, “LiNi 0.5 Mn 1.5 O 4 high-voltage cathode coated

with Li 4 Ti 5 O 12 : a hard X-ray photoelectron spectroscopy (HAXPES) study," *Phys. Chem. Chem. Phys.*, vol. 17, no. 47, pp. 31790–31800, 2015.

[31] R. Azmi, V. Trouillet, M. Strafela, S. Ulrich, H. Ehrenberg, and M. Bruns, "Surface analytical approaches to reliably characterize lithium ion battery electrodes," *Surf. Interface Anal.*, vol. 50, no. 1, pp. 43–51, Jan. 2018.

[32] R. Azmi, M. Masoumi, H. Ehrenberg, V. Trouillet, and M. Bruns, "Surface analytical characterization of LiNi 0.8- y Mn y Co 0.2 O 2 ($0 \leq y \leq 0.4$) compounds for lithium-ion battery electrodes," *Surf. Interface Anal.*, no. September 2017, pp. 6–11, Mar. 2018.

[33] V. Kumar, C. R. Mariappan, R. Azmi, D. Moock, S. Indris, M. Bruns, H. Ehrenberg, and G. Vijaya Prakash, "Pseudocapacitance of Mesoporous Spinel-Type MCo 2 O 4 (M = Co, Zn, and Ni) Rods Fabricated by a Facile Solvothermal Route," *ACS Omega*, vol. 2, no. 9, pp. 6003–6013, Sep. 2017.

[34] C. R. Mariappan, V. Kumar, R. Azmi, L. Esmezjan, S. Indris, M. Bruns, and H. Ehrenberg, "High electrochemical performance of 3D highly porous Zn 0.2 Ni 0.8 Co 2 O 4 microspheres as an electrode material for electrochemical energy storage," *CrystEngComm*, vol. 20, no. 15, pp. 2159–2168, 2018.

[35] Q. Fu, R. Azmi, A. Sarapulova, D. Mikhailova, S. Dsoke, A. Missiul, V. Trouillet, M. Knapp, N. Bramnik, and H. Ehrenberg, "Electrochemical and structural investigations of different polymorphs of TiO 2 in magnesium and hybrid lithium/magnesium batteries," *Electrochim. Acta*, vol. 277, pp. 20–29, Jul. 2018.

[36] W. Hua;, M. Chen;, B. Schwarz;, S. Indris;, M. Bruns;, J. Barthel;, X. Yang;, F. Sigel;, R. Azmi;, M. Knapp;, A. Senyshyn;, A. Missiul;, L. Simonelli;, X. Mu;, A. Fiedler;, J. R., Binder;, X. Guo;, Shulei Chou;, Benhe Zhong;, and H. Ehrenberg, "Unlocking the secrets of spinel/layered heterostructured cathode materials to build high performance Li-ion batteries," *Nano Energy*.

[37] H. Hertz, "Ueber einen Einfluss des ultravioletten Lichtes auf die electrische Entladung," *Ann. Phys.*, vol. 267, no. 8, pp. 983–1000, 1887.

[38] W. V. Gmbh and C. Kgaa, "© Wiley-VCH Verlag GmbH & Co. KGaA, Weinheim," vol. 47, pp. 229–247, 2005.

[39] P. van der Heide, *X-ray Photoelectron Spectroscopy: An Introduction to Principles and*

Practices. Wiley, 2011.

[40] C. S. Fadley, “X-ray photoelectron spectroscopy: Progress and perspectives,” *J. Electron Spectros. Relat. Phenomena*, vol. 178–179, pp. 2–32, May 2010.

[41] J. F. Watts and J. Wolstenholme, *An Introduction to Surface Analysis by XPS and AES*, vol. 27, no. 3. Chichester, UK: John Wiley & Sons, Ltd, 2003.

[42] M. Seah and W. Dench, “Quantitative Electron Spectroscopy of Surfaces,” *Surf. Interface Anal.*, vol. 2, no. 1, p. 1979, 1979.

[43] M. P. Seah and W. A. Dench, “Quantitative Electron Spectroscopy of Surfaces: A Standard Data Base for Electron Inelastic Mean Free Paths in Solids,” *Surf. Interface Anal.*, vol. 1, no. 1, pp. 2–11, 1979.

[44] C. (Sr M. C. S.) Millholland, “Thermo Fisher Scientific (East Grinstead, UK) sales presentation for the K-Alpha instrument,” 2014. [Online]. Available: https://www.slideshare.net/cmillholland?utm_campaign=profiletracking&utm_medium=ssite&utm_source=ssslideview.

[45] W. Heisenberg, “Über den anschaulichen Inhalt der quantentheoretischen Kinematik und Mechanik,” *Zeitschrift für Phys.*, vol. 43, no. 3–4, pp. 172–198, Mar. 1927.

[46] F. Müller, R. de Masi, D. Reinicke, P. Steiner, S. Hüfner, and K. Stöwe, “Epitaxial growth of MnO/Ag(001) films,” *Surf. Sci.*, vol. 520, no. 3, pp. 158–172, Dec. 2002.

[47] M. A. Arenas, I. García, and J. de Damborenea, “X-ray photoelectron spectroscopy study of the corrosion behaviour of galvanised steel implanted with rare earths,” *Corros. Sci.*, vol. 46, no. 4, pp. 1033–1049, 2004.

[48] R. Hesse, “Verbesserung der qualitativen und quantitativen Analyse von Photoelektronenspektren und deren Verifizierung mittels mathematisch-numerischer Verfahren – Entwicklung und Test einer Bearbeitungs- und Analyse-Software,” 2006.

[49] D. K. R. Philip Bevington, *Data Reduction and Error Analysis for the Physical Sciences.pdf*, 3rd ed. Mcgraw Hill Book Co.

[50] M. P. Seah, “The quantitative analysis of surfaces by XPS: A review,” *Surf. Interface Anal.*, vol. 2, no. 6, pp. 222–239, 1980.

[51] J. H. Scofield, “Hartree-Slater subshell photoionization cross-sections at 1254 and 1487 eV,” *J. Electron Spectros. Relat. Phenomena*, vol. 8, no. 2, pp. 129–137, Jan. 1976.

[52] S. Tanuma, C. J. Powell, and D. R. Penn, “Calculations of electron inelastic mean free paths. IX. Data for 41 elemental solids over the 50 eV to 30 keV range,” *Surf. Interface Anal.*, vol. 43, no. 3, pp. 689–713, Mar. 2011.

[53] S. Tougaard and C. Jansson, “Comparison of validity and consistency of methods for quantitative XPS peak analysis,” *Surf. Interface Anal.*, vol. 20, no. 13, pp. 1013–1046, 1993.

[54] T. K. Claus, B. Richter, V. Hahn, A. Welle, S. Kayser, M. Wegener, M. Bastmeyer, G. Delaittre, and C. Barner-Kowollik, “Simultaneous Dual Encoding of Three-Dimensional Structures by Light-Induced Modular Ligation,” *Angew. Chemie Int. Ed.*, vol. 55, no. 11, pp. 3817–3822, Mar. 2016.

[55] R. A. De Souza and M. Martin, “Secondary ion mass spectrometry (SIMS) – a powerful tool for studying mass transport over various length scales,” *Phys. Status Solidi*, vol. 4, no. 6, pp. 1785–1801, 2007.

[56] J. C. Vickerman and D. Briggs, *ToF-SIMS: Materials Analysis by Mass Spectrometry*. IM Publications, 2013.

[57] S. C. Lee and W. Y. Jung, “Analogical understanding of the Ragone plot and a new categorization of energy devices,” *Energy Procedia*, vol. 88, pp. 526–530, 2016.

[58] B. D. McCloskey, “Expanding the Ragone Plot: Pushing the Limits of Energy Storage,” *J. Phys. Chem. Lett.*, vol. 6, no. 18, pp. 3592–3593, 2015.

[59] M. Winter, R. J. Brodd, and E. Capacitors, “What are batteries, fuel cells, and supercapacitors?,” *Chem. Rev.*, vol. 104, no. 10, pp. 4245–4269, 2004.

[60] R. Korthauer Hrsg, *Handbuch Lithium-Ionen-Batterien*. Berlin, Heidelberg: Springer Berlin Heidelberg, 2013.

[61] J. B. Goodenough and Y. Kim, “Challenges for rechargeable Li batteries,” *Chem. Mater.*, vol. 22, no. 3, pp. 587–603, 2010.

[62] M. Winter, J. O. Besenhard, M. E. Spahr, and P. Novák, “Insertion electrode materials for rechargeable lithium batteries,” *Adv. Mater.*, vol. 10, no. 10, pp. 725–763, 1998.

[63] M. S. Whittingham, “Lithium Batteries and Cathode Materials,” *Chem. Rev.*, vol. 104, no. 10, pp. 4271–4302, Oct. 2004.

[64] A. Manthiram, “An Outlook on Lithium Ion Battery Technology,” *ACS Cent. Sci.*, vol. 3, no. 10, pp. 1063–1069, 2017.

[65] R. Chen, T. Zhao, X. Zhang, L. Li, and F. Wu, “Advanced cathode materials for lithium-ion batteries using nanoarchitectonics,” *Nanoscale Horizons*, vol. 1, no. 6, pp. 423–444, 2016.

[66] R. Hausbrand, G. Cherkashinin, H. Ehrenberg, M. Gröting, K. Albe, C. Hess, and W. Jaegermann, “Fundamental degradation mechanisms of layered oxide Li-ion battery cathode materials: Methodology, insights and novel approaches,” *Mater. Sci. Eng. B*, vol. 192, pp. 3–25, Feb. 2015.

[67] X. Li, Y. Xu, and C. Wang, “Suppression of Jahn-Teller distortion of spinel LiMn2O4 cathode,” *J. Alloys Compd.*, vol. 479, no. 1–2, pp. 310–313, 2009.

[68] A. Manthiram, B. Song, and W. Li, “A perspective on nickel-rich layered oxide cathodes for lithium-ion batteries,” *Energy Storage Mater.*, vol. 6, no. October 2016, pp. 125–139, Jan. 2017.

[69] F. Schipper, E. M. Erickson, C. Erk, J.-Y. Shin, F. F. Chesneau, and D. Aurbach, “Review—Recent Advances and Remaining Challenges for Lithium Ion Battery Cathodes,” *J. Electrochem. Soc.*, vol. 164, no. 1, pp. A6220–A6228, 2017.

[70] K. M. Shaju, G. V. Subba Rao, and B. V. R. Chowdari, “Performance of layered Li(Ni1/3Co1/3Mn1/3)O2 as cathode for Li-ion batteries,” *Electrochim. Acta*, vol. 48, pp. 145–151, 2002.

[71] A. Bhaskar, D. Mikhailova, N. Kiziltas-Yavuz, K. Nikolowski, S. Oswald, N. N. Bramnik, and H. Ehrenberg, “3d-Transition metal doped spinels as high-voltage cathode materials for rechargeable lithium-ion batteries,” *Progress in Solid State Chemistry*, vol. 42, no. 4, Elsevier Ltd, pp. 128–148, 2014.

[72] J. M. Tarascon, “The Spinel Phase of LiMn[sub 2]O[sub 4] as a Cathode in Secondary Lithium Cells,” *J. Electrochem. Soc.*, vol. 138, no. 10, p. 2859, 1991.

[73] B. Xu, D. Qian, Z. Wang, and Y. S. Meng, “Recent progress in cathode materials research

for advanced lithium ion batteries," *Mater. Sci. Eng. R Reports*, vol. 73, no. 5–6, pp. 51–65, 2012.

[74] N. Kiziltas-Yavuz, A. Bhaskar, D. Dixon, M. Yavuz, K. Nikolowski, L. Lu, R.-A. Eichel, and H. Ehrenberg, "Improving the rate capability of high voltage lithium-ion battery cathode material LiNi0.5Mn1.5O4 by ruthenium doping," *J. Power Sources*, vol. 267, pp. 533–541, Dec. 2014.

[75] J. Wang and X. Sun, "Olivine LiFePO $_4$: the remaining challenges for future energy storage," *Energy Environ. Sci.*, vol. 8, no. 4, pp. 1110–1138, 2015.

[76] D. A. Shirley, "High-resolution x-ray photoemission spectrum of the valence bands of gold," *Phys. Rev. B*, vol. 5, no. 12, pp. 4709–4714, 1972.

[77] K. L. Parry, A. G. Shard, R. D. Short, R. G. White, J. D. Whittle, and A. Wright, "ARXPS characterisation of plasma polymerised surface chemical gradients," *Surf. Interface Anal.*, vol. 38, no. 11, pp. 1497–1504, Nov. 2006.

[78] L. Pfaffmann, S. Jaiser, M. Müller, P. Scharfer, W. Schabel, W. Bauer, F. Scheiba, and H. Ehrenberg, "New method for binder and carbon black detection at nanometer scale in carbon electrodes for lithium ion batteries," *J. Power Sources*, vol. 363, pp. 460–469, 2017.

[79] A. Garitagoitia Cid, R. Rosenkranz, and E. Zschech, "Optimization of the SEM Working Conditions: EsB Detector at Low Voltage," *Adv. Eng. Mater.*, vol. 18, no. 2, pp. 185–193, 2016.

[80] M. Masoumi, D. M. Cupid, T. L. Reichmann, K. Chang, D. Music, J. M. Schneider, and H. J. Seifert, "Enthalpies of formation of layered LiNi x Mn x Co 1–2 x O 2 ($0 \leq x \leq 0.5$) compounds as lithium ion battery cathode materials," *Int. J. Mater. Res.*, vol. 2, p. 146.111553, Sep. 2017.

[81] M. Ma, N. A. Chernova, B. H. Toby, P. Y. Zavalij, and M. S. Whittingham, "Structural and electrochemical behavior of LiMn0.4Ni0.4Co0.2O2," *J. Power Sources*, vol. 165, no. 2, pp. 517–534, 2007.

[82] N. Kiziltas-Yavuz, M. Yavuz, S. Indris, N. N. Bramnik, M. Knapp, O. Dolotko, B. Das, H. Ehrenberg, and A. Bhaskar, "Enhancement of electrochemical performance by simultaneous substitution of Ni and Mn with Fe in Ni-Mn spinel cathodes for Li-ion batteries," *J. Power Sources*, vol. 327, pp. 507–518, 2016.

[83] A. Höweling, A. Stoll, D. O. Schmidt, H. Geßwein, U. Simon, and J. R. Binder, “Influence of Synthesis, Dopants and Cycling Conditions on the Cycling Stability of Doped LiNi 0.5 Mn 1.5 O 4 Spinels,” *J. Electrochem. Soc.*, vol. 164, no. 1, pp. A6349–A6358, Jan. 2017.

[84] K. N. R. Wuest, V. Trouillet, R. Köppe, P. W. Roesky, A. S. Goldmann, M. H. Stenzel, and C. Barner-Kowollik, “Direct light-induced (co-)grafting of photoactive polymers to graphitic nanodiamonds,” *Polym. Chem.*, vol. 8, no. 5, pp. 838–842, 2017.

[85] G. Kilibarda, D. V. Szabó, S. Schlabach, V. Winkler, M. Bruns, and T. Hanemann, “Investigation of the degradation of SnO2 electrodes for use in Li-ion cells,” *J. Power Sources*, vol. 233, pp. 139–147, Jul. 2013.

[86] V. Winkler, G. Kilibarda, S. Schlabach, D. V. Szabó, T. Hanemann, and M. Bruns, “Surface Analytical Study Regarding the Solid Electrolyte Interphase Composition of Nanoparticulate SnO 2 Anodes for Li-Ion Batteries,” *J. Phys. Chem. C*, vol. 120, no. 43, pp. 24706–24714, Nov. 2016.

[87] J. Cazaux, “A physical approach to the radiation damage mechanisms induced by X-rays in X-ray microscopy and related techniques,” *J. Microsc.*, vol. 188, no. 2, pp. 106–124, 1997.

[88] W. M. Skinner, C. a Prestidge, and R. S. C. Smart, “Irradiation Effects During XPS Studies of Cu (I1) Activation of Zinc Sulphide,” vol. 24, no. November 1995, pp. 620–626, 1996.

[89] B. Wallbank, C. Johnson, and I. Main, “Surface reduction of solid 3d transition metal compounds during X-ray photoelectron spectroscopy,” *J. Electron Spectros. Relat. Phenomena*, vol. 4, pp. 263–269, 1974.

[90] D. Briggs and A. B. Wootton, “Analysis of polymer surfaces by SIMS 1. An investigation of practical problems,” *Surf. Interface Anal.*, vol. 4, no. 3, pp. 109–115, Jun. 1982.

[91] D. Briggs, “Analysis of polymer surfaces by SIMS. 2-fingerprint spectra from simple polymer films,” *Surf. Interface Anal.*, vol. 4, no. 4, pp. 151–155, Aug. 1982.

[92] E. Alizadeh, P. Cloutier, D. Hunting, and L. Sanche, “Soft X-ray and Low Energy Electron-Induced Damage to DNA under N_2 and O_2 Atmospheres,” *J. Phys. Chem. B*, vol. 115, no. 15, pp. 4523–4531, 2011.

[93] H. Nykänen, P. Mattila, S. Suihkonen, J. Riikonen, and M. Sopanen, “Low energy electron beam induced damage on gallium nitride based materials,” *Phys. Status Solidi*, vol. 9, no.

7, pp. 1563–1565, 2012.

[94] Z. J. W. A. Leijten, A. D. A. Keizer, G. de With, and H. Friedrich, “Quantitative Analysis of Electron Beam Damage in Organic Thin-films,” *J. Phys. Chem. C*, vol. 121, no. 19, pp. 10552–10561, 2017.

[95] R. Simpson, R. G. White, J. F. Watts, and M. A. Baker, “XPS investigation of monatomic and cluster argon ion sputtering of tantalum pentoxide,” *Appl. Surf. Sci.*, vol. 405, pp. 79–87, 2017.

[96] A. T. Kozakov, A. G. Kochur, A. V. Nikolsky, K. a. Googlev, V. G. Smotrakov, and V. V. Eremkin, “Valence and magnetic state of transition-metal and rare-earth ions in single-crystal multiferroics RMn2O5 (R=Y, Bi, Eu, Gd) from X-ray photoelectron spectroscopy data,” *J. Electron Spectros. Relat. Phenomena*, vol. 184, no. 8–10, pp. 508–516, Nov. 2011.

[97] A. J. Nelson, J. G. Reynolds, and J. W. Roos, “Core-level satellites and outer core-level multiplet splitting in Mn model compounds,” *J. Vac. Sci. Technol. A*, vol. 18, no. 4, pp. 1072–1076, Jul. 2000.

[98] B. D. Hermsmeier, C. S. Fadley, B. Sinkovic, M. O. Krause, J. Jimenez-Mier, P. Gerard, T. A. Carlson, S. T. Manson, and S. K. Bhattacharya, “Energy dependence of the outer core-level multiplet structures in atomic Mn and Mn-containing compounds,” *Phys. Rev. B*, vol. 48, no. 17, pp. 12425–12437, Nov. 1993.

[99] J. L. Junta and M. F. Hochella, “Manganese (II) oxidation at mineral surfaces: A microscopic and spectroscopic study,” *Geochim. Cosmochim. Acta*, vol. 58, no. 22, pp. 4985–4999, Nov. 1994.

[100] N. Zydziak, C. Hübner, M. Bruns, and C. Barner-Kowollik, “One-Step Functionalization of Single-Walled Carbon Nanotubes (SWCNTs) with Cyclopentadienyl-Capped Macromolecules via Diels−Alder Chemistry,” *Macromolecules*, vol. 44, no. 9, pp. 3374–3380, May 2011.

[101] H. W. Nesbitt and D. Banerjee, “Interpretation of XPS Mn(2p) spectra of Mn oxyhydroxides and constraints on the mechanism of MnO 2 precipitation,” *Am. Mineral.*, vol. 83, no. 3–4, pp. 305–315, Apr. 1998.

[102] Q.-H. Wu, J.-M. Xu, Q.-C. Zhuang, and S.-G. Sun, “X-ray photoelectron spectroscopy of LiM0.05Mn1.95O4 (M=Ni, Fe and Ti),” *Solid State Ionics*, vol. 177, no. 17–18, pp. 1483–

1488, Jul. 2006.

[103] C. S. Fadley and D. A. Shirley, “Multiplet Splitting of Metal-Atom Electron Binding Energies,” *Phys. Rev. A*, vol. 2, no. 4, pp. 1109–1120, Oct. 1970.

[104] S. P. Kowalczyk, L. Ley, F. R. McFeely, and D. A. Shirley, “Multiplet splitting of the manganese 2p and 3p levels in MnF2 single crystals,” *Phys. Rev. B*, vol. 11, no. 4, pp. 1721–1727, Feb. 1975.

[105] J. Töpfer, A. Feltz, D. Gräf, B. Hackl, L. Raupach, and P. Weissbrodt, “Cation Valencies and Distribution in the Spinels NiMn2O4 and MzNiMn2−zO4 (M = Li, Cu) Studied by XPS,” *Phys. Status Solidi*, vol. 134, no. 2, pp. 405–415, Dec. 1992.

[106] C. A. F. Vaz, D. Prabhakaran, E. I. Altman, and V. E. Henrich, “Experimental study of the interfacial cobalt oxide inCo3O4/α -Al2O3(0001) epitaxial films,” *Phys. Rev. B*, vol. 80, no. 15, p. 155457, Oct. 2009.

[107] J.-G. Kim, D. L. Pugmire, D. Battaglia, and M. A. Langell, “Analysis of the NiCo2O4 spinel surface with Auger and X-ray photoelectron spectroscopy,” *Appl. Surf. Sci.*, vol. 165, no. 1, pp. 70–84, Sep. 2000.

[108] J. C. Dupin, D. Gonbeau, I. Martin-Litas, P. Vinatier, and A. Levasseur, “Lithium intercalation/deintercalation in transition metal oxides investigated by X-ray photoelectron spectroscopy,” *J. Electron Spectros. Relat. Phenomena*, vol. 120, no. 1–3, pp. 55–65, Oct. 2001.

[109] N. V. Kosova, E. T. Devyatkina, and V. V. Kaichev, “LiMn2O4 and LiCoO2 composite cathode materials obtained by mechanical activation,” *Russian Journal of Electrochemistry*, vol. 45, no. 3. pp. 277–285, 2009.

[110] L. Dahéron, H. Martinez, R. Dedryvère, I. Baraille, M. Ménétrier, C. Denage, C. Delmas, and D. Gonbeau, “Surface Properties of LiCoO 2 Investigated by XPS Analyses and Theoretical Calculations,” *J. Phys. Chem. C*, vol. 113, no. 14, pp. 5843–5852, Apr. 2009.

[111] Y. C. Lu, A. N. Mansour, N. Yabuuchi, and Y. Shao-Horn, “Probing the origin of enhanced stability of AlPO4 nanoparticle coated liCoO2 during cycling to high voltages: Combined XRD and XPS studies,” *Chem. Mater.*, vol. 21, no. 19, pp. 4408–4424, 2009.

[112] J. C. Dupin, D. Gonbeau, H. Benqlilou-Moudden, P. Vinatier, and A. Levasseur, “XPS

analysis of new lithium cobalt oxide thin-films before and after lithium deintercalation," *Thin Solid Films*, vol. 384, no. 1, pp. 23–32, 2001.

[113] M. Oku, "X-ray photoelectron spectrum of low-spin Co(III) in LiCoO2," *J. Solid State Chem.*, vol. 23, no. 1–2, pp. 177–185, Jan. 1978.

[114] T. J. Chuang, C. R. Brundle, and D. W. Rice, "Interpretation of the x-ray photoemission spectra of cobalt oxides and cobalt oxide surfaces," *Surf. Sci.*, vol. 59, no. 2, pp. 413–429, Oct. 1976.

[115] J. Haber and L. Ungier, "On chemical shifts of ESCA and Auger lines in cobalt oxides," *J. Electron Spectros. Relat. Phenomena*, vol. 12, no. 3, pp. 305–312, Jan. 1977.

[116] T. Ivanova, A. Naumkin, A. Sidorov, I. Eremenko, and M. Kiskin, "X-ray photoelectron spectra and electron structure of polynuclear cobalt complexes," *J. Electron Spectros. Relat. Phenomena*, vol. 156–158, pp. 200–203, May 2007.

[117] A. P. Grosvenor, M. C. Biesinger, R. S. C. Smart, and N. S. McIntyre, "New interpretations of XPS spectra of nickel metal and oxides," *Surf. Sci.*, vol. 600, no. 9, pp. 1771–1779, May 2006.

[118] A. W. Moses, H. G. G. Flores, J.-G. Kim, and M. A. Langell, "Surface properties of LiCoO2, LiNiO2 and LiNi1−xCoxO2," *Appl. Surf. Sci.*, vol. 253, no. 10, pp. 4782–4791, Mar. 2007.

[119] C. Loho, R. Djenadic, M. Bruns, O. Clemens, and H. Hahn, "Garnet-Type Li7La3Zr2O12 Solid Electrolyte Thin-films Grown by CO2 -Laser Assisted CVD for All-Solid-State Batteries," *J. Electrochem. Soc.*, vol. 164, no. 1, pp. A6131–A6139, Nov. 2017.

[120] G. Cherkashinin, K. Nikolowski, H. Ehrenberg, S. Jacke, L. Dimesso, and W. Jaegermann, "The stability of the SEI layer, surface composition and the oxidation state of transition metals at the electrolyte–cathode interface impacted by the electrochemical cycling: X-ray photoelectron spectroscopy investigation," *Phys. Chem. Chem. Phys.*, vol. 14, no. 35, p. 12321, 2012.

[121] L. Baggetto, R. R. Unocic, N. J. Dudney, and G. M. Veith, "Fabrication and characterization of Li–Mn–Ni–O sputtered thin-film high voltage cathodes for Li-ion batteries," *J. Power Sources*, vol. 211, pp. 108–118, Aug. 2012.

[122] M. Strafela, H. Leiste, K. Seemann, H. J. Seifert, and S. Ulrich, “Influence of substrate surface roughness on microstructural and electrical properties of Lithium-rich Li-Ni-Mn-Co-O thin-film cathodes,” *Vacuum*, vol. 131, pp. 240–245, Sep. 2016.

[123] J. K. Ngala, N. A. Chernova, M. Ma, M. Mamak, P. Y. Zavalij, and M. S. Whittingham, “The synthesis, characterization and electrochemical behavior of the layered LiNi0.4Mn0.4Co0.2O2 compound,” *J. Mater. Chem.*, vol. 14, no. 2, p. 214, 2004.

[124] Y. Gu, Y. Chen, H. Liu, Y.-M. Wang, C. Wang, and H. Wu, “Structural characterization of layered LiNi0.85?xMnxCo0.15O2 with x=0, 0.1, 0.2 and 0.4 oxide electrodes for Li batteries,” *J. Alloys Compd.*, vol. 509, no. 30, pp. 7915–7921, Jul. 2011.

[125] D. Kim, J.-M. Lim, Y. Lim, J. Yu, M. Park, M. Cho, and K. Cho, “Design of Nickel-rich Layered Oxides Using d Electronic Donor for Redox Reactions,” *Chem. Mater.*, vol. 27, no. 18, pp. 6450–6456, Sep. 2015.

[126] P. Y. Liao, J. G. Duh, and S. R. Sheen, “Effect of Mn Content on the Microstructure and Electrochemical Performance of LiNi[sub 0.75-x]Co[sub 0.25]Mn[sub x]O[sub 2] Cathode Materials,” *J. Electrochem. Soc.*, vol. 152, no. 9, p. A1695, 2005.

[127] N. V. Kosova, E. T. Devyatkina, and V. V. Kaichev, “Optimization of Ni2+/Ni3+ ratio in layered Li(Ni,Mn,Co)O2 cathodes for better electrochemistry,” *J. Power Sources*, vol. 174, no. 2, pp. 965–969, Dec. 2007.

[128] A. Etiemble, N. Besnard, A. Bonnin, J. Adrien, T. Douillard, P. Tran-Van, L. Gautier, J.-C. Badot, E. Maire, and B. Lestriez, “Multiscale morphological characterization of process induced heterogeneities in blended positive electrodes for lithium–ion batteries,” *J. Mater. Sci.*, vol. 52, no. 7, pp. 3576–3596, Apr. 2017.

[129] F. Buss, C. C. Roberts, K. S. Crawford, K. Peters, and L. F. Francis, “Effect of soluble polymer binder on particle distribution in a drying particulate coating,” *J. Colloid Interface Sci.*, vol. 359, no. 1, pp. 112–120, 2011.

[130] S. Nowak and M. Winter, “Elemental Analysis of Lithium Ion Batteries,” *J. Anal. At. Spectrom.*, vol. 32, no. 10, pp. 1833–1847, 2017.

[131] M. Xu, N. Tsiouvaras, A. Garsuch, H. A. Gasteiger, and B. L. Lucht, “Generation of cathode passivation films via oxidation of lithium bis(oxalato) borate on high voltage spinel (LiNi0.5Mn 1.5O4),” *J. Phys. Chem. C*, vol. 118, no. 14, pp. 7363–7368, 2014.

[132] Y.-M. Liu, B. G. Nicolau, J. L. Esbenshade, and A. A. Gewirth, “Characterization of the Cathode Electrolyte Interface in Lithium Ion Batteries by Desorption Electrospray Ionization Mass Spectrometry,” *Anal. Chem.*, vol. 88, no. 14, pp. 7171–7177, 2016.

[133] J. Zheng, P. Yan, J. Zhang, M. H. Engelhard, Z. Zhu, B. J. Polzin, S. Trask, J. Xiao, C. Wang, and J. Zhang, “Suppressed oxygen extraction and degradation of LiNixMnyCozO2cathodes at high charge cut-off voltages,” *Nano Res.*, vol. 10, no. 12, pp. 4221–4231, 2017.

[134] S.-M. Bak, E. Hu, Y. Zhou, X. Yu, S. D. Senanayake, S.-J. Cho, K.-B. Kim, K. Y. Chung, X.-Q. Yang, and K.-W. Nam, “Structural Changes and Thermal Stability of Charged LiNi $_x$ Mn $_y$ Co $_z$ O $_2$ Cathode Materials Studied by Combined *In Situ* Time-Resolved XRD and Mass Spectroscopy,” *ACS Appl. Mater. Interfaces*, vol. 6, no. 24, pp. 22594–22601, 2014.

[135] C. Julien, A. Mauger, K. Zaghib, and H. Groult, “Optimization of layered cathode materials for lithium-ion batteries,” *Materials (Basel).*, vol. 9, no. 7, 2016.

[136] M. Yavuz, N. Kiziltas-Yavuz, A. Bhaskar, M. Scheuermann, S. Indris, F. Fauth, M. Knapp, and H. Ehrenberg, “Influence of Iron on the Structural Evolution of LiNi 0.4 Fe 0.2 Mn 1.4 O 4 during Electrochemical Cycling Investigated by in situ Powder Diffraction and Spectroscopic Methods,” *Zeitschrift für Anorg. und Allg. Chemie*, vol. 640, no. 15, pp. 3118–3126, 2014.

[137] J. Xiao, X. Chen, P. V. Sushko, M. L. Sushko, L. Kovarik, J. Feng, Z. Deng, J. Zheng, G. L. Graff, Z. Nie, D. Choi, J. Liu, J.-G. Zhang, and M. S. Whittingham, “High-Performance LiNi 0.5 Mn 1.5 O 4 Spinel Controlled by Mn 3+ Concentration and Site Disorder,” *Adv. Mater.*, vol. 24, no. 16, pp. 2109–2116, Apr. 2012.

[138] G. B. Zhong, Y. Y. Wang, Y. Q. Yu, and C. H. Chen, “Electrochemical investigations of the LiNi0.45M0.10Mn1.45O4 (M=Fe, Co, Cr) 5V cathode materials for lithium ion batteries,” *J. Power Sources*, vol. 205, pp. 385–393, May 2012.

[139] M. C. Biesinger, L. W. M. Lau, A. R. Gerson, and R. S. C. Smart, “Resolving surface chemical states in XPS analysis of first row transition metals, oxides and hydroxides: Sc, Ti, V, Cu and Zn,” *Appl. Surf. Sci.*, vol. 257, no. 3, pp. 887–898, Nov. 2010.

[140] D. J. Morgan, “Resolving ruthenium: XPS studies of common ruthenium materials,” *Surf. Interface Anal.*, vol. 47, no. 11, pp. 1072–1079, 2015.

[141] H. Do Kim, H. J. Noh, K. H. Kim, and S. J. Oh, “Core-level x-ray photoemission satellites in ruthenates: A new mechanism revealing the Mott transition,” *Phys. Rev. Lett.*, vol. 93, no. 12, pp. 10–13, 2004.

[142] H. Over, A. P. Seitsonen, E. Lundgren, M. Smedh, and J. N. Andersen, “On the origin of the Ru-3d5/2 satellite feature from RuO2(1 1 0),” *Surf. Sci.*, vol. 504, no. 1–3, pp. L196–L200, 2002.

[143] V. Šepelák, S. M. Becker, I. Bergmann, S. Indris, M. Scheuermann, A. Feldhoff, C. Kübel, M. Bruns, N. Stürzl, A. S. Ulrich, M. Ghafari, H. Hahn, C. P. Grey, K. D. Becker, and P. Heitjans, “Nonequilibrium structure of Zn2SnO4 spinel nanoparticles,” *J. Mater. Chem.*, vol. 22, no. 7, p. 3117, 2012.

[144] V. Sepelak, S. Indris, P. Heitjans, and K. D. Becker, “Direct determination of the cation disorder in nanoscale spinels by NMR , XPS , and Mössbauer spectroscopy,” *J. Alloys Compd.*, vol. 435, pp. 776–778, 2007.

[145] V. Sepelak, I. Bergmann, S. Indris, A. Feldhoff, H. Hahn, K. D. Becker, C. P. Grey, and P. Heitjans, “High-resolution 27 Al MAS NMR spectroscopic studies of the response of spinel aluminates to mechanical action,” *J. Mater. Chem.*, vol. 21, pp. 8332–8337, 2011.

[146] S. Permien, H. Hain, M. Scheuermann, S. Mangold, V. Mereacre, A. K. Powell, S. Indris, U. Schürmann, L. Kienle, V. Duppel, S. Harm, and W. Bensch, “Electrochemical insertion of Li into nanocrystalline MnFe2O4: a study of the reaction mechanism,” *RSC Adv.*, vol. 3, no. 45, p. 23001, 2013.

Publications

Articles in Scientific Journals

† R. Azmi, V. Trouillet, M. Strafela, S. Ulrich, H. Ehrenberg, M. Bruns, *Surface analytical approaches to reliably characterize lithium ion battery electrodes*, Surface and Interface Analysis. 50 (2018) 43–51. doi:10.1002/sia.6330.

† R. Azmi, M. Masoumi, H. Ehrenberg, V. Trouillet, M. Bruns, *Surface analytical characterization of* $LiNi_{0.8-y}Mn_yCo_{0.2}O_2$ $(0 \leq y \leq 0.4)$ *compounds for lithium-ion battery electrodes*, Surface and Interface Analysis. (2018) 6–11. doi:10.1002/sia.6415.

† Q. Fu, R. Azmi, A. Sarapulova, D. Mikhailova, S. Dsoke, A. Missiul, V. Trouillet, M. Knapp, N. Bramnik, H. Ehrenberg, *Electrochemical and structural investigations of different polymorphs of* TiO_2 *in magnesium and hybrid lithium/magnesium batteries*, Electrochimica Acta. 277 (2018) 20–29. doi:10.1016/j.electacta.2018.04.200.

† V. Kumar, C.R. Mariappan, R. Azmi, D. Moock, S. Indris, M. Bruns, H. Ehrenberg, G. Vijaya Prakash, *Pseudocapacitance of Mesoporous Spinel-Type* MCo_2O_4 *(M = Co, Zn, and Ni) Rods Fabricated by a Facile Solvothermal Route*, ACS Omega. 2 (2017) 6003–6013. doi:10.1021/acsomega.7b00709.

† C.R. Mariappan, V. Kumar, R. Azmi, L. Esmezjan, S. Indris, M. Bruns, H. Ehrenberg, *High electrochemical performance of 3D highly porous* $Zn_{0.2}Ni_{0.8}Co_2O_4$ *microspheres as an electrode material for electrochemical energy storage*, CrystEngComm. 20 (2018) 2159–2168. doi:10.1039/C7CE02161E.

† W. Hua, M. Chen, B. Schwarz, S. Indris, M. Bruns, J. Barthel, X. Yang, F. Sigel, R. Azmi, M. Knapp, A. Senyshyn, A. Missiul, L. Simonelli, X. Mu, A. Fiedler, J. R., Binder, X. Guo, Shulei Chou, Benhe Zhong, H. Ehrenberg, *Unlocking the secrets of spinel/layered heterostructured cathode materials to build high performance Li-ion batteries*, Nano Energy. (under review, 2018).

Conference Contributions

† R. Azmi, "Surface Analysis of $LiCoMnO_4$ Spinel Type Cathode Material", in *ECASIA2015*, 2015, Granada, *Oral presentation*.

† R. Azmi, "Surface Analysis of Cathode Materials for Li-ion Batteries", in *5th XPS workshop*, 2016, Eggenstein-Leopoldshafen, *Oral presentation*.

† R. Azmi, M. Strafela, S.O. Steinmueller, H. Ehrenberg, H.J. Seifert, S. Ulrich, M. Bruns, "ToF-SIMS and XPS Characterization of R. F. Magnetron Sputtered Li-Ni-Mn-Co-O Thin-films for Li-ion Batteries", in *ECOSS32*, 2016, Grenoble, *Poster presentation*.

† R. Azmi, "Surface Analytical Approaches to Characterize Cathode Materials for Li-ion Batteries", in *ECASIA2017*, 2017, Montpellier, *Oral presentation*.

† R. Azmi, "Surface Analytical Approaches to Characterize Cathode Materials for Li-ion Batteries", in *6th XPS workshop*, 2018, Eggenstein-Leopoldshafen, *Oral presentation*.

Declaration

I hereby declare that this submission is my own work and that, to the best of my knowledge and belief, it contains no material previously published or written by another person nor material which to a substantial extent has been accepted for the award of any other degree or diploma of the university or another institute of higher learning, except where the acknowledgment has been made in the text.

Furthermore, I declare that doctoral procedures outside the Faculty of Mechanical Engineering of the KIT are neither pending for me nor have been unsuccessfully completed by me.

(signature)

Raheleh Azmi

18.07.2018

Acknowledgments

Although It is often very difficult to put one's gratitude into words, I like to take this opportunity to thank all the people who have made a decisive contribution to the success of this work, especially …

I would like to thank Prof. Dr. Helmut Ehrenberg for enabling me to complete this work at his institute. I would also like to thank Prof. Dr. Michael J. Hoffmann for agreeing to be the first referee of this work. Thank you for giving me space, time, further financing and many tools to complete this work.

I would like to express my sincere thanks to Dr. Michael Bruns, who as the direct initiator and supervisor of this work put his trust in me and made this work possible. Many thanks for numerous constructive discussions, the networking, the encouragement, and the perspectives, as well as the support through the completion of the work. Without your help and the great interest in the topic of work, it would not have come this far.

My special thanks go to Vanessa Trouillet, who not only actively supported me in practicing XPS but also become my best friend motivating me in learning the German language and many other aspects of living and working in Germany. Thank you very much.

I would like to thank Udo Geckle for carrying out the SEM measurements. I would also like to thank Dr. Lukas Pfaffmann for his helpful advice on many SEM measurements and for being available at all times for fruitful discussions.

I would like to thank my colleagues at IAM-ESS, and especially the surface analysis group for their creative, humorous and pleasant atmosphere. Thanks for the time together.

I would like also to thank financial support from the Federal Ministry of Education and Research (BMBF) within the DESIREE project, grant no. 03SF0477B, as well as the financial support from the Federal Ministry of Economics and Energy (BMWi) on the basis of a decision by the German Bundestag for the financing of the K-Alpha+ instrument.

My thanks also go to my family who accompanied me during this time and supported me in various ways.

Rasoul, thank you for all your tireless support and encouragement over the years.